MAXIMAL-RATIO EIGEN-COMBINING FOR SMARTER ANTENNA ARRAY WIRELESS COMMUNICATION RECEIVERS

by

Constantin Siriteanu

A thesis submitted to the
Department of Electrical and Computer Engineering
in conformity with the requirements
for the degree of Doctor of Philosophy

Queen's University
Kingston, Ontario, Canada
August, 2006

Abstract

The conventional single-antenna receiver suffers in wireless fading channels from limitations that preclude deployment of envisioned wireless applications. By increasing complexity, improvements are possible using multi-branch receivers. In particular, smart antenna arrays employ maximal-ratio combining (MRC) or statistical beamforming (BF) to exploit diversity and array gain. However, varying azimuth spread creates unfavorable spatial correlation conditions that diminish these gains, while BF and MRC complexity remains constant. On the other hand, adaptive eigen-combining can yield near-optimum performance for more efficient resource usage. This motivates our study of maximal-ratio eigen-combining (MREC).

We unravel the relationship between MREC, BF, and MRC performance, and evaluate their complexity. Outage and average error probability expressions are derived for MREC assuming perfectly and imperfectly known channel gains. These results are specialized to MRC and BF, as well as to well-accepted pilot-symbol-based channel estimation techniques. In the process, new performance analyses are provided.

Numerical results for typical urban scenarios with variable correlation demonstrate MREC's advantages. Existing criteria for optimum eigen-mode selection in MREC are reviewed, and a new adaptation approach that accounts for channel condition, algorithm complexity, resource availability, and intended performance level, is proposed and evaluated.

These single- and multi-branch receivers are then evaluated on a field-programmable gate array (FPGA) in terms of symbol-detection performance and resource and power consumption.

MREC flexibility is shown to yield near-optimum performance for half of the hardware and power requirements of MRC, or, equivalently, a doubling of the number of users which can be handled with the same hardware. Smarter antennas, i.e., array receivers aware of the channel-statistics, resource availability, and required performance, can thus be deployed.

Finally, for code-division multiple access (CDMA) systems, we specify an eigen-combining approach. A recently-developed signal despreading method, which eliminates the intended signal, is exploited for interference-plus-noise correlation matrix calculation. After some transformations, combining can once again be relegated to a few eigen-modes, for lower complexity and improved performance.

Acknowledgments

Foremost, I would like to thank my supervisor, Dr. Steven D. Blostein, for his guidance and financial support during my Ph.D. program at Queen's University. From him I learned great skills required for intelligent research work. I have to thank Dr. Blostein also for accepting my joining his lab when my first supervisor here — Dr. Frederick W. Fairman — retired, and then allowed me the time to become familiar with the new research area of Communications Systems. I also want to acknowledge Dr. Fairman for the great opportunity of studying at Queen's, and for his financial support and guidance while I worked with him on Control Systems.

My appreciation goes to the Thesis Defense Committee members: committee Chair, ; external examiner, Dr. Ravi Adve from the University of Toronto; Head delegate, Dr. John C. Cartledge; ELEC Examiner, Dr. Peter J. McLane; MATH Examiner, Dr. Glen K. Takahara.

Thanks for the help they provided and the good times we shared go to present and past members of the Information Processing and Communications Laboratory (IPCL), especially Minhua Ding, Leon Lee, Edmund Tam, Yu Cao, Wei Sheng, Jinsong Wu, Neng Wang, Joseph Chou, Yi Song, as well as to the many Persian friends I made at Queen's.

My family deserves big thanks for their patience, understanding, and moral support. This thesis is dedicated to my mother.

Contents

List of Tables

List of Figures

Acronyms

2G	2nd Generation
3G	3rd Generation
3GPP	3rd Generation Partnership Project
a.c.f.	auto-correlation function
AEP	Average Error Probability
AoA	Angle-of-Arrival
AS	Azimuth Angle Spread
ASIC	Application-Specific Integrated Circuit
AWGN	Additive White Gaussian Noise
BF	Beamforming (statistical, stochastic)
BPSK	Binary Phase-Shift Keying
BVTC	Bias–Variance Tradeoff Criterion
CDMA	Code-Division Multiple Access
c.f.	characteristic function
DSP	Digital Signal Processor
e.p.m.	eigenbranch processing module/s
EVTC	EigenValue-based Tradeoff Criterion
FPGA	Field-Programmable Gate Array
IEEE	Institute of Electrical Electronics Engineers

HDL	Hardware description language
HIL	Hardware-in-the-loop
i.i.d.	independent and identically distributed
i.k.c.	imperfectly known channel/s
IP	Intellectual property
KLT	Karhunen-Loève Transform
LE	Logic Elements
LoS	Line-of-Sight
m.g.f.	moment generating function
MIMO	Multiple-Input Multiple-Output
MISO	Multiple-Input Single-Output
ML	Maximum-Likelihood
MMSE	Minimum Mean Squared Error
MMSEC	Minimum Mean Squared Error Criterion
MPSK	*M*-ary Phase-Shift Keying
MRC	Maximal-Ratio Combining
MREC	Maximal-Ratio Eigen-Combining
OFDM	orthogonal frequency division multiplexing
p.a.s.	power azimuth spectrum
PCTC	Performance–Complexity Tradeoff Criterion
p.d.f.	probability density function
p.k.c.	perfectly known channel/s
PSAM	Pilot-Symbol-Aided Modulation
p.s.d.	power spectral density
QPSK	Quadrature Phase-Shift Keying

r.m.g.f.	reversed moment generating function
RMSE	Root Mean Squared Error
SIMO	Single-Input Multiple-Output
SINC	stands for sinc interpolation
SINR	Signal-to-Interference-Plus-Noise Ratio
SISO	Single-Input Single-Output
SOPC	System-on-a-programmable-chip
SNR	Signal-to-Noise Ratio
TU	Typical Urban (scenario)
ULA	Uniform Linear Array
WCDMA	Wideband code-division multiple access
WLAN	Wireless local area network

List of Important Symbols

$\stackrel{\triangle}{=}$	Defined as
$k = 1:N$	$k = 1, 2, \ldots, N-1, N$
$(\cdot)^T$	Matrix or vector transpose
$(\cdot)^*$	Complex conjugate
$(\cdot)^H$	Matrix or vector conjugate transpose
$(\cdot)_{i,j}$	(i, j)th entry of a matrix
$\lvert x \rvert$	Absolute value (modulus) of the scalar x
$\lVert \mathbf{x} \rVert_2$	Euclidian or 2-norm of vector $\mathbf{x}$: $\lVert \mathbf{x} \rVert_2 = (\mathbf{x}^H \mathbf{x})^{1/2}$
$\mathbb{C}^L$	The set of all length-L complex-valued vectors
$\mathbb{C}^{L \times L}$	The set of all $L \times L$ complex-valued matrices
$\breve{\cdot}$	Indicates perfectly known channel/s
$\propto$	Proportional to
$\binom{n}{k}$	Binomial coefficient: $\frac{n!}{k!(n-k)!}$
$n!$	Factorial operator: $n! = (n-1) \cdot (n-2) \ldots 3 \cdot 2 \cdot 1$
σ_x^2	Autocorrelation, variance, power, of zero-mean random process x
$\sigma_{x,z}^2$	Cross-correlation of zero-mean random variables x and z
$\mu_{x,z}$	Correlation coefficient of zero-mean random variables x and z
γ_b	Average SNR per received information bit
γ_th	Threshold SNR

$\widetilde{\gamma}$, γ	Instantaneous effective combiner SNR before, after the KLT
$\widetilde{\gamma}_i$, γ_i	Instantaneous effective SNR at ith branch/eigenbranch before/after the KLT
$\delta_{i,j}$	Discrete Kronecker delta function
θ_c	Average AoA
$\lambda(\mathbf{R})$	Spectrum, i.e., the set of eigenvalues of matrix $\mathbf{R}$
$\widetilde{\mathbf{\Phi}}$, $\mathbf{\Phi}$	Pilot-sample vector correlation matrix before, after the KLT
$\widetilde{\boldsymbol{\phi}}$, $\boldsymbol{\phi}$	Correlation of pilot-sample vector and actual channel gain/eigengain before, after the KLT
$\widetilde{\Gamma}$, Γ	Average effective combiner SNR before, after the KLT
$\widetilde{\Gamma}_i$, Γ_i	Average effective SNR at ith branch/eigenbranch before/after the KLT
Ξ_k, $k = 1 : N_d$	Distinct values in the set $\{\Gamma_1\, g_{\text{PSK}}\,, \Gamma_2\, g_{\text{PSK}}\,, \ldots\,, \Gamma_N\, g_{\text{PSK}}\}$
$\Phi(\cdot)$	Characteristic function of random variable
$\widetilde{\mathbf{n}}$, $\mathbf{n}$	Noise vector before, after the KLT
$\widetilde{n}_i$, n_i	ith element of the noise vector before, after the KLT
$\widetilde{\mathbf{h}}$, $\mathbf{h}$	Channel gain vector before, after the KLT
$\widetilde{h}_i$, h_i	ith element of the channel gain/eigengain vector before, after the KLT
$\widetilde{\mathbf{g}}$, $\mathbf{g}$	Channel gain/eigengain vector estimate before, after the KLT
$\widetilde{g}_i$, g_i	ith element of the channel gain/eigengain vector estimate before, after the KLT
$\widetilde{\mathbf{e}}$, $\mathbf{e}$	Channel gain/eigengain vector estimation error before, after the KLT
$\widetilde{\boldsymbol{\nu}}$, $\boldsymbol{\nu}$	Effective noise vector before, after the KLT
$\widetilde{\mathbf{y}}$, $\mathbf{y}$	Received signal vector before, after the KLT
$\widetilde{\mathbf{u}}$, $\mathbf{u}$	Interference-plus-noise signal vector before, after the KLT
$\widetilde{\mathbf{r}}$, $\mathbf{r}$	Vector formed with pilot samples before, after the KLT
$\widetilde{\mathbf{w}}$, $\mathbf{w}$	Combiner vector before, after the KLT

$\widetilde{\mathbf{v}}$, $\mathbf{v}$	Interpolation vector before, after the KLT
b, $\hat{b}$	Transmitted symbol, detected symbol
b, $\hat{b}$	Transmitted symbol, detected symbol
$\widetilde{q}, q$	Symbol test statistic (decision variable) before, after KLT
E_{s}	Energy transmitted per information symbol
E_{p}	Energy transmitted per pilot symbol
K_{p}	$E_{\mathrm{p}}/E_{\mathrm{s}}$
T_{s}	Symbol duration and period
f_{s}	Symbol rate
c	Transmitted chip
E_{c}	Energy transmitted per chip
T_{c}	Chip duration
PG	Processing, or spreading, gain: PG $\stackrel{\triangle}{=} T_{\mathrm{s}}/T_{\mathrm{c}}$
$\mathrm{diag}\{\lambda_i\}_{i=1}^{N}$	Diagonal matrix with λ_i, $i = 1:N$, on its main diagonal
$\det(\cdot)$	Determinant of a matrix
$\mathrm{tr}(\cdot)$	Trace of a matrix
$\Pr(\cdot)$	Probability of event
P_e	(Average) Error probability
P_o	Outage probability
$E\{\cdot\}$	Expectation of random variables
$\mathcal{N}_c(\cdot,\cdot)$	Complex-valued Gaussian distribution
$\mathbf{I}_L$	$L \times L$ identity matrix
$\mathbf{0}$	vector with all elements equal to 0
$\mathrm{S}_z(\cdot)$	Power spectral density of random process z
N_0	Complex-valued-noise variance

$\mathbf{R}_{\mathbf{x}}$	Correlation matrix of complex-valued random vector $\mathbf{x}$
$\mathbf{E}_N$	Matrix formed with N dominant eigenvectors
$\mathbf{\Lambda}_N$	Diagonal matrix formed with N dominant eigenvalues, sorted decreasingly
λ_i	ith dominant eigenvalue, when sorted in decreasing order
$\mathbf{e}_i$	Eigenvector corresponding to λ_i
L	Number of receive antennas or branches
N	Number of eigenbranches, or MREC order
N_{u}	Number of actively transmitting mobiles, or users
N_d	Number of distinct eigenvalues of a matrix
M	Modulation constellation size
g_{PSK}	$\sin^2 \frac{\pi}{M}$
M_{s}	Slot length
T	Interpolator size
(t, m_{s})	temporal indexing for channel estimation
t	slot position: $t = 0$ for currently detected slot
m_{s}	$m_{\mathrm{s}} = 0$ for pilot symbol, $m_{\mathrm{s}} \neq 0$ for information symbol
f_{c}	Carrier signal frequency
λ_{c}	Carrier signal wavelength
v	Mobile velocity
f_{D}	Maximum Doppler shift
T_{C}	Coherence time due to Doppler spread
f_{m}	Maximum normalized Doppler shift
d_{n}	ULA inter-element distance, normalized to half-wavelength
d_{C}	Coherence distance due to Doppler spread
d_{AS}	Azimuth spread decorrelation distance

$\Re(\cdot)$	Real part of a complex number
$\Im(\cdot)$	Imaginary part of a complex number
$u(\cdot)$	Heaviside unit-step function
$\mathscr{O}(\cdot)$	Numerical complexity order
$M(\cdot)$	Moment generating function of random variable
$F(\cdot)$	Reversed moment generating function of random variable
$J_i(\cdot)$	ith order Bessel function of the first kind
$\mathscr{G}(\cdot,\cdot)$	Incomplete gamma function $\frac{1}{(n-1)!}\int_0^x e^{-t}\,t^{n-1}\,dt$
Q-function	$Q(x) \triangleq \int_x^\infty \frac{1}{\sqrt{2\pi}} e^{-y^2/2} dy = \frac{1}{\pi}\int_0^{\pi/2} \exp\left\{-\frac{x^2}{2\sin^2\phi}\right\} d\phi$

Chapter 1

Introduction

1.1 Motivation

Envisioned applications for current and future mobile and fixed wireless communications systems [44, 92] will require data rates, area coverage, symbol-detection performance, and user capacities which surpass the capabilities of conventional, single-input single-output (SISO) implementations, comprising one transmitting and one receiving antenna. Multi-branch transceivers exploiting the single-input multiple-output (SIMO) or the multiple-input single-output (MISO) concepts, also known as smart antennas [79, 80], have been promoted to improve the performance at no need for expensive new bandwidth [62, 106, 115, 123]. Therefore they have been specified for implementation in mobile communications systems by the 3rd Generation Partnership Project (3GPP) [3, 4], as well as in Local and Metropolitan Area Networks by the IEEE 802.11 and IEEE 802.16 standards [73, 79, 80]. More recently, the multiple-input multiple-output (MIMO) concept has been proposed to enhance the spectral efficiency [57, 73, 106, 140].

In this thesis, we focus on cost-effective and power-efficient receivers that employ antenna

array signal combining. Without loss of generality and for greater clarity, the results are described in the context of SIMO systems. However, with appropriate additional processing, the same concepts can be straightforwardly generalized to MIMO receivers.

The SIMO smart-antenna concept has been attracting research interest and has been extensively developed over the past four decades [23, 33, 35, 36, 42, 43, 61, 62, 79, 80, 83, 87, 99–101, 107, 134, 147]. SIMO processing can be classified into two conceptually-distinct classes, each optimizing performance for certain channel conditions, as described next. If there exists line-of-sight communication between transmitter and receiver, antenna array received signals tend to be highly correlated. Then, maximum average signal-to-noise ratio (SNR), i.e., statistical, beamforming (BF) is known to enhance symbol-detection performance, due to array gain [99] [106, Section 1.2.1], over the SISO system. Conversely, when rich scattering [106] occurs in the channel, maximal-ratio combining [34] (MRC) can yield significant diversity gain [106, Sections 1.2.2, 5.3, Table 5.1, p. 101].

Nevertheless, for actual rural, sub/urban, and indoor channels, signals received with an antenna array are never perfectly correlated (coherent) or decorrelated [130]. (Such a situation is also characteristic of other multi-branch receivers, e.g., the taps of a CDMA RAKE [104] [106, Section 5.7].) In this case of medium correlation, BF and MRC performance is worse than that achievable with a pre-selected number of branches which are coherent or uncorrelated, respectively [42, 125, 128, 130]. Channel estimation [39, 90] inaccuracy will further degrade performance [123, Section 9.9].

In actual mobile communications scenarios spatial branch correlation varies, although slowly compared to the channel fading, due to changing azimuth angle spread (AS) [8]. Employing BF or MRC then maintains high computational requirements, whereas performance varies. The high complexity of multi-branch transceiver signal processing algorithms has been impeding their deployment in actual systems [79, 80] because it translates into high equipment

cost and power consumption. Smarter processing that adapts to channel statistics is thus expected to provide manufacturers, operators, and users with high-performing yet cost-effective and power-efficient base-stations and mobile terminals.

Recently, eigen-combining, also known as eigen-beamforming, was proposed for receiving antenna arrays as a more versatile approach in which both performance and complexity can follow the channel statistics [35, 36, 42, 47, 48, 76, 77, 83, 106, 125, 128, 130]. Ideally, eigen-combining would exploit only those eigen-modes of the channel that yield most of the available performance gain. Eigen-combining has previously been proposed as an enhancement to BF for scenarios with non-zero azimuth spread [35, 36, 42, 83], as well as a lower complexity alternative to MRC for scenarios with non-rich scattering [35, 36, 47, 48, 76, 77]. MISO and MIMO eigen-mode-based combining has also been analyzed [60, 106, 140, 154] and specified for implementation by the 3GPP [3].

In this work we focus on receiver-side maximal-ratio eigen-combining (MREC), which consists of two steps [125, 128, 130]:

1. The received signal vector is passed through the Karhunen-Loève Transform [59, 68] (KLT), using a number of eigenvectors of the channel gain vector correlation matrix.

2. The elements of the KLT output signal vector are then linearly combined so as to maximize the SNR conditioned on the fading [34].

Since the channel statistics can vary as much as three orders of magnitude more slowly than the fading [130], the computations involved in eigen-decomposition can be distributed over long intervals, and thus do not represent a significant load, as opposed to the channel-fading-rate and symbol-rate operations involved in channel estimation and signal combining [1, 35, 36, 130].

Previous studies have not clearly stated the relationships between MREC, BF, and MRC,

nor have these studies compared their optimum and suboptimum implementations given channel estimates [35, 36, 42, 47, 48, 76, 77, 83, 125]. Furthermore, eigen-combining performance evaluations have mainly relied on simulation [35,36,42,47,76,77,83], or analysis for unrealistic power azimuth spectrum (p.a.s.) models [47, 48]. In addition, even when eigen-combining was proposed for problem-dimension reduction, the channel statistics alone controlled the computational savings [47, 76, 77]. The tradeoff between eigen-combining complexity and performance has not been considered in detail thus far. However, as base-station receiver resources become scarcer due to high system load, one may be satisfied with eigen-combining performance achieved by considering only very few eigen-modes for certain users. On the other hand, when resources are readily available, one could achieve better performance by exploiting additional eigen-modes. Graceful controlled performance adjustments can then yield more flexible upper limits on user capacities.

Formulas for BF and MRC performance measures such as average error probability (AEP) and outage probability (OP) have not been readily available, even for perfectly known channels (p.k.c.). For instance, [89] considers MRC performance measures for the case of correlated branches which can have unequal variances, but does not cover the case when some eigenvalues of the channel correlation matrix coincide. The recent MRC study from [123] considers only special correlation cases. The newer results from [48] suffer from similar limitations as those from [89], although they apply for imperfectly known channels (i.k.c.). Furthermore, performance measure expressions proposed by other authors specifically for BF are not readily available.

Comparative assessments by other authors of actual, fixed-point, implementations of MREC, BF, and MRC, in terms of performance and receiver resource/power consumption averaged over the channel statistics, are not available. Such evaluations are of utmost importance as they

can reveal issues which are not addressed by typical theoretical performance analysis. Of special importance are implementations which rely on field-programmable gate arrays (FPGAs) to cope with heavy computational loads [129].

FPGAs have recently moved from the level of simple glue logic for embedded systems into the realm of intensive signal processing where they are quickly becoming very strong competitors to digital signal processors (DSPs) and application-specific integrated circuits (ASICs). FPGA producers boast significant on-chip enhancements, e.g., embedded DSP blocks and memory [15, 149], that can speed-up algorithm execution several-fold over DSPs, through hardware parallelism [17, 72]. Furthermore, FPGAs reprogrammability and integrated design flows [11, pp. 55 - 56] can shorten the time-to-market as well as reduce the costs and risk of new-product development, compared to ASICs, which are fully customized very-large-scale integration (VLSI) chips [27]. FPGAs are thus very suitable for prototyping newly developed signal processing algorithms. Numerous examples of such FPGA-based implementations of advanced communications signal processing algorithms are presented in the current EURASIP "*Journal on Applied Signal Processing*" volume, and the upcoming "Special Issue on Field-Programmable Gate Arrays in Embedded Systems", of the EURASIP "*Journal on Embedded Systems*", to appear in the 4th quarter of 2006. Finally, the hardware reconfigurability allowed by FPGA-based implementations permits optimization of systems already operational, and can yield longer lifespan for deployed systems in an era of fast-changing standards, markets, and applications [27].

FPGA chips are designed and fabricated to minimize power consumption whether in stand-by or operation modes [82]. Nevertheless, power-aware application design can also make a significant impact because consistently underutilized and underperforming implementations waste resources and power [31, 121, 135, 150]. For multi-branch communications receivers, frequently the channel does not offer performance-maximizing conditions for BF or MRC,

given the complexity of these algorithms, and the resources and power their implementations consume. Although eigen-combining has been previously proposed for complexity reduction and performance improvement, there does not seem to be research comparing actual performance and resource/power consumption for FPGA-based implementations of BF and MRC, and adaptive MREC. The actual power consumption and receiver cost savings, or the user processing capacity increases achievable with MREC, have not been quantified.

Finally, code-division multiple access (CDMA) is commonly exploited in 2nd- and 3rd-generation (2G and 3G) wireless cellular communications systems [33, 71, 132, 134] to improve the user capacity [134]. However, CDMA systems are interference-limited and so significant performance improvements are possible with smart antenna array receivers employing optimum combining [100, 101] or statistical beamforming [43], which, however, increase the complexity. Lower complexity and further improvements have been claimed possible with eigen-combining [36, 42]. Nevertheless, previously proposed algorithms [43, 100, 101] rely on the front-end, pre-correlation, received signal, which is generally quantized with low precision [122]. Furthermore, their performance depends on the actual chip-pulse waveform, and their convergence may be slow.

1.2 Thesis Overview

Within the following five chapters of this thesis we investigate the single- and multi-branch receivers introduced above. We summarize our results and indicate possible future work in the last chapter. The appendix sections provide reference material and further details on certain issues discussed in the main body of the text, which is organized as follows.

Chapter 2 provides the background on SISO communications systems, to demonstrate the need for performance improvements. It takes us from the transmitted M-ary Phase Shift Keying

(MPSK) signal model, through the performance-degrading effects of receiver noise, multipath fading (with a focus the Rayleigh distribution), and channel gain estimation inaccuracy.

Chapter 3 introduces the multi-branch receiver signal model, and presents methods employed thereafter for symbol-detection performance analysis, i.e., to determine formulas for the average error probability and the outage probability. The traditional signal combining methods, i.e., BF and MRC, are then described for p.k.c., along with the derivation of their performance measures. Numerical results indicate that significant performance improvements are possible due to antenna and diversity gains. Nevertheless, the fading distribution parameters and correlation can change that. MREC is described next and analyzed for p.k.c. The fact that MREC is a superset of BF and MRC is documented. It is then shown that SIMO performance gains over SISO can be seriously diminished by channel estimation inaccuracy. For two common channel estimation techniques, and for optimum and suboptimum eigen-/combining we then find that BF and MRC are still performance-equivalent to special cases of MREC. These equivalencies are used to derive performance measures for BF and MRC in fairly general cases, e.g., when the channel gains have the same distribution type, but have non-zero correlation and non-equal variances. Finally, the numerical complexity is evaluated for BF, MRC, and MREC.

Chapter 4 introduces the more realistic Laplacian power azimuth spectrum (p.a.s.) and the azimuth angle spread (AS) model for typical mobile wireless channels. BF, MRC, and MREC performance dependence on azimuth spread is evaluated. The need for adaptive use of MREC is demonstrated. Existing as well as new criteria for MREC adaptation are then described. Promising performance improvements and complexity reductions are shown to be possible.

Chapter 5 presents our FPGA implementations of the conventional, single-branch, receiver,

as well as the multi-branch receivers discussed. Comparisons are made between their floating-point, computer-based, simulations and their fixed-point FPGA realizations. Parallelism-enabling FPGA implementations of BF, MRC, and MREC are evaluated comparatively for performance and resource/power consumption.

Finally, Chapter 6 discusses multi-branch receiver combining for CDMA systems. The benefits of a recently-proposed CDMA signal despreading approach which can readily provide the interference-plus-noise correlation matrix are described from the optimum-combining perspective. Then, eigen-combining for this multi-user scenario is described.

1.3 Summary of Contributions

This thesis makes the following contributions:

- A unified analysis of diversity combining, statistical beamforming, and eigen-combining is performed. Maximal-ratio eigen-combining (MREC) is shown to be a superset of statistical beamforming (BF) and maximal-ratio combining (MRC). AEP and OP formulas are derived for p.k.c. and i.k.c. Optimum and sub-optimum eigen-/combining are considered and compared. The resulting expressions are important since they quantify the performance of statistical beamforming and combining for the more practical cases when channel gains are correlated and have non-identical variances.

- The numerical complexities of BF, MRC, and MREC are evaluated. The performance advantages of MREC over BF and MRC are documented for typical actual mobile communications scenarios, based on both analysis and simulations. For small complexity increases, MREC is shown to greatly outperform BF. MREC is shown to have the potential to significantly lower complexity and even improve performance compared to MRC in practical situations where uncertainty in channel state information exists.

- FPGA implementations of the conventional single-branch receiver and of the enhanced, BF, MRC, and MREC, receivers confirm significant performance improvements with multi-branch receivers, at the price of higher resource requirements including power consumption. Among the enhanced receivers, MREC is shown to appropriately adapt to the slow variations in the channel eigen-modes and to yield resource- and power-efficient, i.e., smarter, antenna array receivers that can attain performance targets.

- A possible eigen-combining implementation for CDMA systems is proposed. A CDMA signal despreading technique which helps to accurately compute the interference-plus-noise correlation matrix for any chip-pulse waveform is employed. The proposed eigen-combining approach promises wider applicability, faster convergence, and controllable performance–complexity tradeoff.

Chapter 2

Background on Conventional SISO Systems

2.1 Chapter Overview

In this background chapter we first present the model for M-ary phase-shift keying (MPSK) transmitted signals and evaluate the symbol-detection performance for additive white Gaussian noise (AWGN) and nonfading channel. A versatile performance analysis method described by Simon and Alouini in their seminal book [123] is then used to quantify a very significant potential deterioration due to channel multipath fading. Finally, we study the negative effect of channel gain estimation inaccuracy on performance. We focus on pilot-symbol-aided modulation (PSAM) at the transmitter and pilot-sample interpolation at the receiver, and evaluate the system symbol-detection performance as a function of relative pilot-symbol transmitted power. This background chapter on wireless impairments and their effects on SISO communications system performance is provided to demonstrate the need for improvements. Such improvements can be achieved efficiently, as described in subsequent chapters, with adaptive multi-branch receivers. Antenna arrays can for example combat channel fading, improve channel estimation accuracy, enhance coverage, and cancel interference. They would also require lower-cost power amplifiers than single-antenna counterparts for similar coverage [80].

2.2 Signal Model

2.2.1 Transmitted Signal

Throughout this work we will consider M-ary phase-shift keying (MPSK) transmitted waveforms, unless stated otherwise, where M is the constellation size. At time intervals of length T_s seconds, the MPSK modulator transforms a new group of

$$k = \log_2 M \tag{2.1}$$

equiprobable 0 and 1 information bits into one of the M deterministic, finite-energy, temporal waveforms described by [115, Eqn. 4.3-11, p. 171]

$$\begin{aligned} s_m(t) &= \Re\left[p(t)\, e^{j\,2\pi(m-1)/M}\, e^{j\,2\pi f_\mathrm{c} t}\right], \quad m = 1:M, \quad t \in [0, T_\mathrm{s}], && (2.2)\\ &= p(t)\cos\left[\frac{2\pi}{M}(m-1) + 2\pi f_\mathrm{c} t\right] && (2.3)\\ &= p(t)\cos\left[\frac{2\pi}{M}(m-1)\right]\cos 2\pi f_\mathrm{c} t - p(t)\sin\left[\frac{2\pi}{M}(m-1)\right]\sin 2\pi f_\mathrm{c} t, && (2.4) \end{aligned}$$

where $\Re$ stands for the real part of a complex-valued number, t stands for time, T_s is the transmitted symbol duration, f_c is the carrier frequency, and $p(t)$ is the transmitted pulse waveform, herein assumed to be non-zero only in $[0, T_\mathrm{s}]$. Then, for all possible waveforms, the *transmitted energy per symbol* is [115, Eqn. 4.3-3, p. 170]

$$E_\mathrm{s} \stackrel{\triangle}{=} \int_0^{T_\mathrm{s}} s_m^2(t)\,dt, \tag{2.5}$$

which is related to the energy in the pulse waveform,

$$\varepsilon_p \stackrel{\triangle}{=} \int_0^{T_\mathrm{s}} p^2(t)\,dt, \tag{2.6}$$

as [115, Eqn. 4.3-12, p. 172]

$$E_\mathrm{s} = \frac{1}{2}\,\varepsilon_p. \tag{2.7}$$

The transmitted signal can be written as the orthogonal-function expansion [115, Eqns. (4.3-13 – 16), pp.172-173]

$$s_m(t) = s_{m,1} \cdot f_1(t) + s_{m,2} \cdot f_2(t), \tag{2.8}$$

where the transmitted signal coordinates, i.e., $s_{m,1}$ and $s_{m,2}$, are given by

$$s_{m,1} = \sqrt{\frac{\varepsilon_p}{2}} \cos\left[\frac{2\pi}{M}(m-1)\right] = \sqrt{E_s} \cos\left[\frac{2\pi}{M}(m-1)\right], \tag{2.9}$$

$$s_{m,2} = \sqrt{\frac{\varepsilon_p}{2}} \sin\left[\frac{2\pi}{M}(m-1)\right] = \sqrt{E_s} \sin\left[\frac{2\pi}{M}(m-1)\right], \tag{2.10}$$

and the functions

$$f_1(t) \triangleq \sqrt{\frac{2}{\varepsilon_p}}\, p(t) \cos 2\pi f_c t = \sqrt{\frac{1}{E_s}}\, p(t) \cos 2\pi f_c t \tag{2.11}$$

$$f_2(t) \triangleq -\sqrt{\frac{2}{\varepsilon_p}}\, p(t) \sin 2\pi f_c t = -\sqrt{\frac{1}{E_s}}\, p(t) \sin 2\pi f_c t \tag{2.12}$$

are orthonormal [115, Eqn. 4.2-21, p. 161], i.e.,

$$\int_{-\infty}^{\infty} f_i(t)\, f_j(t) dt = \delta_{i,j}, \tag{2.13}$$

where

$$\delta_{i,j} \triangleq \begin{cases} 1 & , \quad \text{for } i = j, \\ 0 & , \quad \text{for } i \neq j. \end{cases} \tag{2.14}$$

The electrical signal produced by the modulator, described by (2.2), is sent to a transmitting antenna [29], which transforms it into an electromagnetic wave.

2.2.2 Received Signal

The transmitted electromagnetic wave propagates over the wireless channel from the transmitting antenna to a receiving antenna. The latter picks up the signal and inputs it to a filter [115, p. 157] which outputs the real-valued random process

$$r(t) = p(t)\, a(t) \cos\left[\frac{2\pi}{M}(m-1) + 2\pi f_c t + \alpha(t)\right] + z(t) \tag{2.15}$$

where the amplitude gain $a(t)$ and the phase shift $\alpha(t)$ are real-valued channel effects, and $z(t)$ is the real-valued noise added by the receiver [115, Sect. 4.1.4]. Throughout this work, $a(t)$ and $\alpha(t)$ are assumed to vary more slowly than the symbol rate, $f_s \stackrel{\triangle}{=} 1/T_s$. Further, $z(t)$ is considered to be a Gaussian distributed process with zero-mean and double-sided power spectral density (p.s.d.) given by [115, Fig. 4.1-3, p. 158]

$$S_z(f) = \begin{cases} \frac{N_0}{2} & , \quad \text{for } |f \pm f_c| \leq \frac{B}{2} \\ 0 & , \quad \text{otherwise.} \end{cases} \tag{2.16}$$

The band-limited random process $z(t)$ is referred to as *additive white Gaussian noise (AWGN)*, since, when the bandwidth B is large, temporally-separated samples of $z(t)$ will be nearly uncorrelated.

Let us consider a correlation demodulator as described in [115, Sect. 5.1.1, p. 232]. Without constraining the generality of the ensuing discussion, the time required by the electromagnetic wave to propagate from the transmitter to the receiver is disregarded and the correlation demodulator is assumed to be synchronized perfectly with the received waveform. For notational simplicity it is assumed that transmission of the symbol starts at time 0 (and ends at time T_s). Nevertheless, since in practice symbols are sent successively from the transmitter, the discrete-time received signal will be indexed accordingly, when necessary. Then, at the end of each symbol interval, the components of the received signal along the two orthonormal functions defined earlier are

$$r_1 \stackrel{\triangle}{=} \int_0^{T_s} r(t)\, f_1(t) dt = \sqrt{E_s}\, a \cos\left[\frac{2\pi}{M}(m-1) + \alpha\right] + z_1, \tag{2.17}$$

and

$$r_2 \stackrel{\triangle}{=} \int_0^{T_s} r(t)\, f_2(t) dt = \sqrt{E_s}\, a \sin\left[\frac{2\pi}{M}(m-1) + \alpha\right] + z_2, \tag{2.18}$$

where

$$z_i \stackrel{\triangle}{=} \int_0^{T_s} z(t)\, f_i(t) dt, \tag{2.19}$$

is zero-mean Gaussian with variance (auto-correlation) $\sigma_{z_i}^2 \stackrel{\triangle}{=} E\{z_i^2\} = N_0/2$, $i = 1,2$ [115, Eqn. 5.1.7, p. 235], with $E\{\cdot\}$ denoting statistical averaging. Since temporally-separated samples of the noise process $z(t)$ are uncorrelated, and $f_1(t)$ and $f_2(t)$ defined in (2.11), (2.12) are orthonormal, (2.19) yields

$$E\{z_1\, z_2\} = 0. \tag{2.20}$$

For a more compact mathematical representation, the equivalent complex-valued received signal is commonly employed, i.e.,

$$\begin{aligned} \widetilde{y} &\stackrel{\triangle}{=} r_1 + j\, r_2 \\ &= \sqrt{E_{\rm s}}\, a\, e^{j\left[\frac{2\pi}{M}(m-1)+\alpha\right]} + z_1 + j\, z_2 \\ &= \sqrt{E_{\rm s}}\, e^{j\frac{2\pi}{M}(m-1)}\, a\, e^{j\alpha} + z_1 + j\, z_2, \\ &= \sqrt{E_{\rm s}}\, b\, \widetilde{h} + \widetilde{n}, \end{aligned} \tag{2.21}$$

where

$$b \stackrel{\triangle}{=} e^{j\frac{2\pi}{M}(m-1)} \tag{2.22}$$

is the complex notation of the MPSK transmitted symbol,

$$\widetilde{h} \stackrel{\triangle}{=} a\, e^{j\alpha} \tag{2.23}$$

is the equivalent complex-valued *channel gain,* and

$$\widetilde{n} \stackrel{\triangle}{=} z_1 + j\, z_2 \tag{2.24}$$

is the equivalent complex-valued, zero-mean AWGN. From (2.20) it follows that the real and imaginary parts of the receiver noise are independent, due to their joint Gaussianity. Then

$$\sigma_{\widetilde{n}}^2 \stackrel{\triangle}{=} E\{\widetilde{n}\,\widetilde{n}^*\} = E\{|\widetilde{n}|^2\} = \sigma_{z_1}^2 + \sigma_{z_2}^2 = N_0. \tag{2.25}$$

2.3 Nonfading Channel with Receiver AWGN

2.3.1 Signal Model

Let us assume for now that in (2.21) the channel gain is fixed at $\widetilde{h} = 1$. The received signal model is then

$$\widetilde{y} = \sqrt{E_s}\, b + \widetilde{n}, \tag{2.26}$$

The probability density function (p.d.f.) of the complex-valued zero-mean AWGN $\widetilde{n}$ is given by [102, Eqn. 8-62a, p. 199]

$$\text{p.d.f.}(\widetilde{n}) = \frac{1}{\pi N_0} e^{-|\widetilde{n}|^2/N_0}. \tag{2.27}$$

This distribution is further denoted with $\mathcal{N}_c(0, N_0)$.

2.3.2 Performance

The *signal-to-noise ratio (SNR) per symbol* is then given by

$$\widetilde{\Gamma} \stackrel{\triangle}{=} \frac{E_s}{N_0}, \tag{2.28}$$

and, since one transmitted symbol corresponds to $k = \log_2 M$ information bits, the *SNR per bit* is

$$\gamma_b \stackrel{\triangle}{=} \frac{\widetilde{\Gamma}}{\log_2 M}. \tag{2.29}$$

The bit error probability for BPSK modulation is [115, Eqn. 5.2-57, p. 268]

$$P_e = Q\left(\sqrt{2\widetilde{\Gamma}}\right) = \frac{1}{2}\,\text{erfc}\left(\sqrt{\widetilde{\Gamma}}\right), \tag{2.30}$$

where $Q(\cdot)$ is the Gaussian Q-function [123, Eqn. 4.1, p. 70]

$$Q(x) \stackrel{\triangle}{=} \int_x^\infty \frac{1}{\sqrt{2\pi}} e^{-y^2/2} dy, \tag{2.31}$$

and erfc is the *complementary error function* given by [115, Eqn. 2.1-95, p. 39]

$$\operatorname{erfc}(x) = \frac{2}{\sqrt{\pi}} \int_x^\infty e^{-y^2} dy. \tag{2.32}$$

Furthermore, a symbol error probability expression for MPSK modulation is [46, Eqn. 5, p. 25.5.2] [123, Eqn. 4.2, p. 71]

$$P_e = \frac{1}{\pi} \int_0^{\frac{M-1}{M}\pi} \exp\left\{ -\widetilde{\Gamma} \frac{g_{\mathrm{PSK}}}{\sin^2 \phi} \right\} d\phi, \tag{2.33}$$

where

$$g_{\mathrm{PSK}} \stackrel{\triangle}{=} \sin^2 \frac{\pi}{M}. \tag{2.34}$$

That (2.33) reduces for BPSK modulation (i.e., $M = 2$) to (2.30) can easily be shown using the equivalent representations of the Q-function [46, Eqn. 9, p. 25.5.2] [123, Eqn. 8.22, p. 198]

$$Q(x) = \frac{1}{\pi} \int_0^{\pi/2} \exp\left\{ -\frac{x^2}{2 \sin^2 \phi} \right\} d\phi \tag{2.35}$$

and of the erfc function [46, Eqn. 10, p. 25.5.2]

$$\operatorname{erfc}(x) = \frac{2}{\pi} \int_0^{\pi/2} \exp\left\{ -\frac{x^2}{\sin^2 \phi} \right\} d\phi. \tag{2.36}$$

The performance of a SISO communication system with AWGN is presented for BPSK modulation in Fig. 2.1. The theoretical bit error probability from (2.30) — equivalent to (2.33) for $M = 2$ — and that obtained by simulating $4 \cdot 10^6$ noise samples are plotted vs. the SNR per symbol γ_b defined in (2.29) on page 15. Fig. 2.2 shows results obtained with (2.33) and by simulation for QPSK modulation.

2.4 Multipath Fading

2.4.1 Fading Channel Gain Model

In actual wireless communications, an additional, very significant, phenomenon affects the transmitted signal before it arrives at the receiver: the transmitted electromagnetic waves can

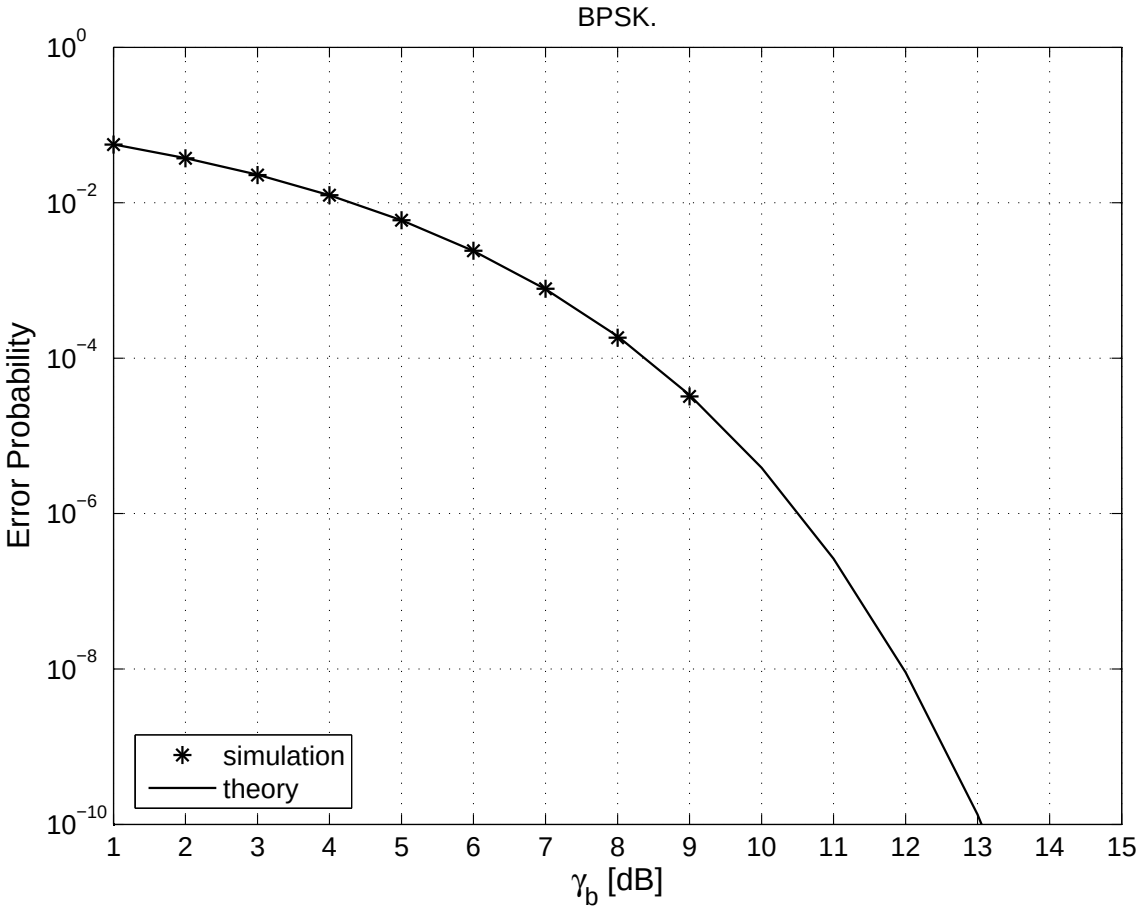

Figure 2.1. Performance for BPSK modulation and channel with AWGN.

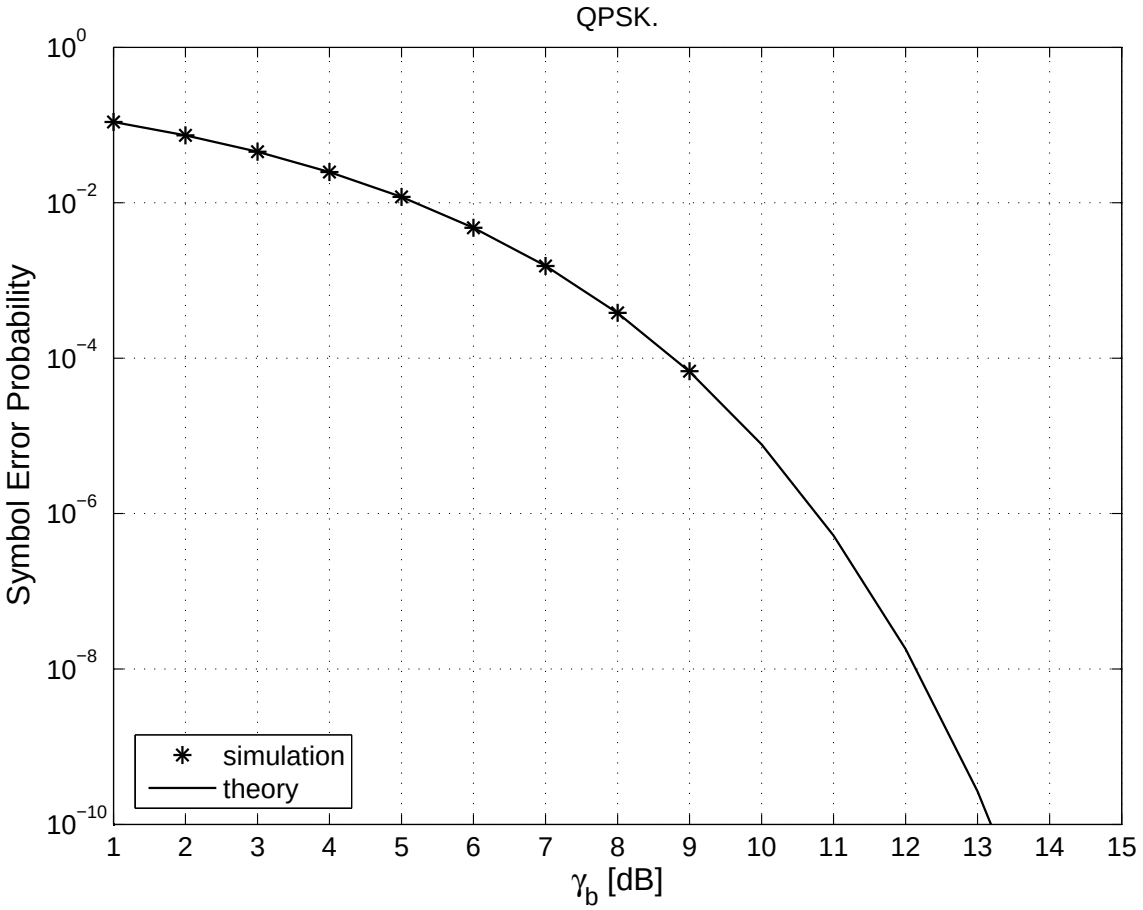

Figure 2.2. Performance for QPSK modulation and channel with AWGN.

propagate over numerous different paths, overlapping constructively or destructively at different instances in time and space. This phenomenon is known as *multipath fading* [75, 89, 123, 133, 145]. The continuous-time random real-valued processes $a(t)$ and $\alpha(t)$ from (2.15) and the corresponding discrete-time complex-valued process $\widetilde{h}$ from (2.21) denote the effect of multipath fading on the transmitted signal, assuming frequency-flat fading.

Unless stated otherwise, for the analytical and numerical results presented in this work we will consider that the channel gain is a complex-valued random variable with Gaussian distribution, which is approximately the case when the transmitted signal propagates to the receiver over a large number of paths [75, p. 14]. The complex gains of these paths are assumed to have phases which are uniformly distributed in $[0, 2\pi]$. Furthermore, the amplitudes and the phases are statistically independent. Furthermore, unless specified otherwise, we will assume that the channel gain is zero-mean, i.e.,

$$E\{\widetilde{h}\} = 0, \tag{2.37}$$

and denote its variance (autocorrelation) with

$$\sigma_{\widetilde{h}}^2 \triangleq E\{|\widetilde{h}|^2\}, \tag{2.38}$$

so that, $\widetilde{h} \sim \mathcal{N}_c(0, \sigma_{\widetilde{h}}^2)$. Then, the p.d.f. of the channel gain is given by [102, Eqn. 8-62a, p. 199]

$$p(\widetilde{h}) = \frac{1}{\pi \sigma_{\widetilde{h}}} e^{-|\widetilde{h}|^2/\sigma_{\widetilde{h}}^2}. \tag{2.39}$$

The real and imaginary parts of $\widetilde{h}$ are mutually independent, real-valued random variables described by [75, pp. 16,17] [102, p. 198] $\widetilde{h}_{re}, \widetilde{h}_{im} \sim \mathcal{N}(0, \sigma_{\widetilde{h}}^2/2)$. The amplitude of the channel gain, i.e., $|\widetilde{h}| = \sqrt{\widetilde{h}_{re}^2 + \widetilde{h}_{im}^2}$, is a real-valued random variable with Rayleigh distribution [75, pp. 16,17] [85, p. 100] described by the p.d.f. [75, Eqn. 1.1-12] [85, Eqn. 4.15]

$$p(|\widetilde{h}|) = 2\,|\widetilde{h}|/\sigma_{\widetilde{h}}^2\, e^{-|\widetilde{h}|^2/\sigma_{\widetilde{h}}^2}, \tag{2.40}$$

justifying the commonly used title for this type of fading model.

Let us now consider that there is relative motion between the transmitter and the receiver, with velocity v. Then, due to the phenomenon called *Doppler shift* [75, p. 20], the carrier frequency for the arriving signal will be distributed in the interval $[f_c - f_D, f_c + f_D]$, where f_D is called maximum Doppler rate [75, 89, 145], and can be computed with

$$f_D = f_c \frac{v}{c}, \tag{2.41}$$

where $c \approx 3 \cdot 10^8$ m/s is the speed of electromagnetic waves in free space.

The maximum Doppler rate is related to the channel *coherence time* T_C which is "a statistical measure of the time duration over which the channel impulse response is essentially invariant" [116, p. 165]. More exactly, if the coherence time is defined as the "time over which the time correlation is above 0.5" [116, p. 165], then it can be computed as [116, Eqn. 4.40.b, p. 165]

$$T_C \approx \frac{9}{16\pi f_D^2} \approx \frac{0.179}{f_D}. \tag{2.42}$$

A channel *coherence distance* can also be defined as

$$d_C \triangleq T_C \, v \approx 0.179 \, \lambda_c, \tag{2.43}$$

where λ_c is the carrier-signal wavelength, defined as $\lambda_c \triangleq c/f_c$. Channel gains at two time or space instances separated by more than T_C or d_C, respectively, can differ substantially as will be observed in the example provided shortly.

Jakes' model [75, Ch. 1] accounts for channel gain temporal correlation with the following as autocorrelation function (a.c.f.)

$$R_{\tilde{h}}(t_1, t_2) \triangleq E\{\tilde{h}(t_1)\tilde{h}^*(t_2)\} = \sigma_{\tilde{h}}^2 J_0(2\pi f_D |t_1 - t_2|), \tag{2.44}$$

where t_1 and t_2 index the discrete time, and $J_0(\cdot)$ is the *zero-order Bessel function of the first*

kind [6, §9.1.18, p. 360], given by

$$J_0(x) \stackrel{\triangle}{=} \frac{1}{\pi} \int_0^{\pi} \cos(x \sin\theta) d\,\theta. \tag{2.45}$$

Since the a.c.f. from (2.44) only depends on the time delay $\tau = t_1 - t_2$, and since $E\{\widetilde{h}(t)\} = 0$, $\forall t$, the fading process is wide sense stationary [102, p. 298]. The theoretical a.c.f. for Jakes' fading model can then be rewritten simpler as

$$R_{\widetilde{h}}(\tau) \stackrel{\triangle}{=} E\{\widetilde{h}(t)\widetilde{h}^*(t+\tau)\} = \sigma_{\widetilde{h}}^2 J_0(2\pi f_{\mathrm{D}} |\tau|). \tag{2.46}$$

The *power spectral density* (p.s.d.) of the channel gain, i.e., the Fourier transform [19] of $R_{\widetilde{h}}(\tau)$, is given by [75, Eqn. 1.2-11, p. 21]

$$S_{\widetilde{h}}(f) \stackrel{\triangle}{=} \mathscr{F}\{R_{\widetilde{h}}(\tau)\} = \frac{\sigma_{\widetilde{h}}^2}{\pi f_{\mathrm{D}}} \left[1 - \left(\frac{f - f_{\mathrm{c}}}{f_{\mathrm{D}}}\right)^2\right]^{-1/2}. \tag{2.47}$$

Generating realistic temporally-correlated Rayleigh fading by numerical means is an important research area and numerous methods have been proposed (see [25, 105, 152, 153] and references therein). Unless stated otherwise, for numerical results shown in this work we employ the method described in [152, 153].

Let us assume, for example, that $f_{\mathrm{c}} = 1.8$ GHz and $v = 60$ km/h. Then the carrier wavelength is $\lambda_{\mathrm{c}} \approx 16.7$ cm and, from the above equations, the maximum Doppler shift, coherence time, and coherence distance are $f_{\mathrm{D}} = 100$ Hz, $T_{\mathrm{C}} \approx 1.8$ ms, and $d_{\mathrm{C}} \approx 2.98$ cm, respectively. Fig. 2.3 shows the variation of the real and imaginary parts of Rayleigh fading channel gain, its amplitude and phase, generated as indicated in [152, 153], for $\sigma_{\widetilde{h}}^2 = 1$. The figure depicts the well-known fact [132, p. 4] that channel gain fades are separated by about $\lambda_{\mathrm{c}}/2$.

Let the symbol rate be denoted as f_{s}. It is related to the symbol period as $f_{\mathrm{s}} = T_{\mathrm{s}}^{-1}$. Let us define the *normalized maximum Doppler rate* as

$$f_{\mathrm{m}} \stackrel{\triangle}{=} \frac{f_{\mathrm{D}}}{f_{\mathrm{s}}}. \tag{2.48}$$

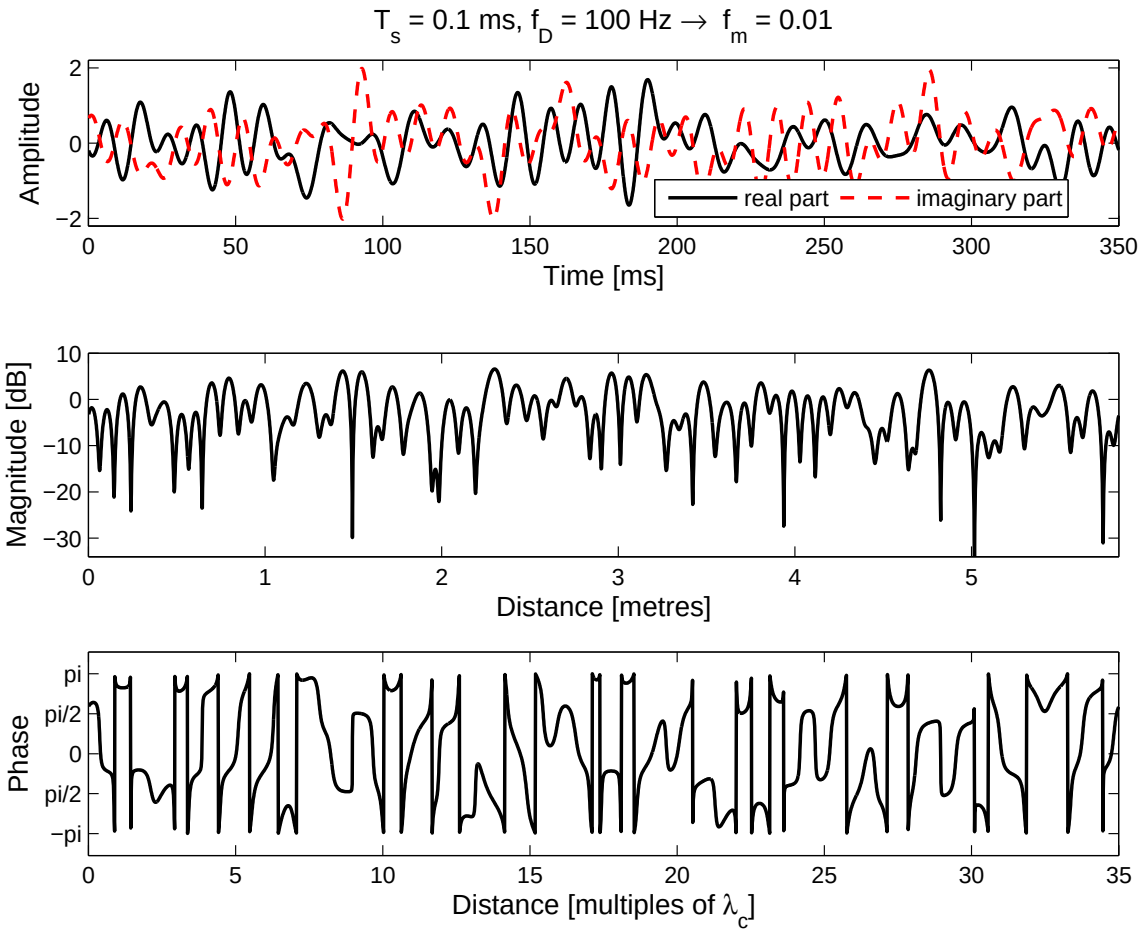

Figure 2.3. Temporally-correlated Rayleigh fading channel gain: amplitudes of the real and imaginary parts, and magnitude and phase.

and the *normalized coherence time* (measured in symbol periods) as

$$T_{C,\text{norm}} \stackrel{\triangle}{=} \frac{T_\text{C}}{T_\text{s}} \approx \frac{0.179}{f_\text{D}\, T_\text{s}} = 0.179\, \frac{f_\text{s}}{f_\text{D}} \approx \frac{0.179}{f_\text{m}}. \tag{2.49}$$

If we assume that the symbol period is $T_\text{s} = 10^{-4}$ seconds [s], the symbol rate will be $f_\text{s} = 10,000$ [sps – symbols per second], so that $f_\text{m} = 0.01$. Then, we can expect that the fading correlation decreases significantly over inter-symbol spacings larger than $T_{C,\text{norm}}$, i.e., about 18 symbols ($T_{C,\text{norm}} \approx 0.179/0.01 = 17.9$). In Fig. 2.4, we plot the theoretical a.c.f. from (2.44), and the empirical a.c.f. computed using 10^6 samples of the Rayleigh fading process generated as in [152, 153]. We find that

- The empirical a.c.f. approximates closely the theoretical a.c.f.
- The correlation is 0.5 at a lag of about 24 symbols, which is fairly close to the theoretical value of $T_{C,\text{norm}}$ computed above.
- The a.c.f. looks like a damped oscillation, whose first zero occurs at a lag of about 39 symbols. This lag corresponds to a distance of about $0.4\,\lambda_\text{c}$, as also observed in [63, p. 74].

For the same parameters, Fig. 2.5 shows a good match between the theoretical p.s.d. of (2.47) for Jakes' fading model [75, Eqn. 1.2-11, p. 21], and the empirical p.s.d. obtained by simulation from the generated channel gain samples, using Welch's method [146]. Clearly, the generated channel gain is a bandlimited process [102, Sect. 11-5] of bandwidth f_D, and can therefore be reconstructed from samples taken at a rate equal or greater than twice its bandwidth [102, Theorem, p. 378].

Actual fading can sometimes be described by the Nakagami-*m* distribution [123, Eqn. 2.20, p. 22] of which the Rayleigh distribution is particular case. The Nakagami-*m* distribution is

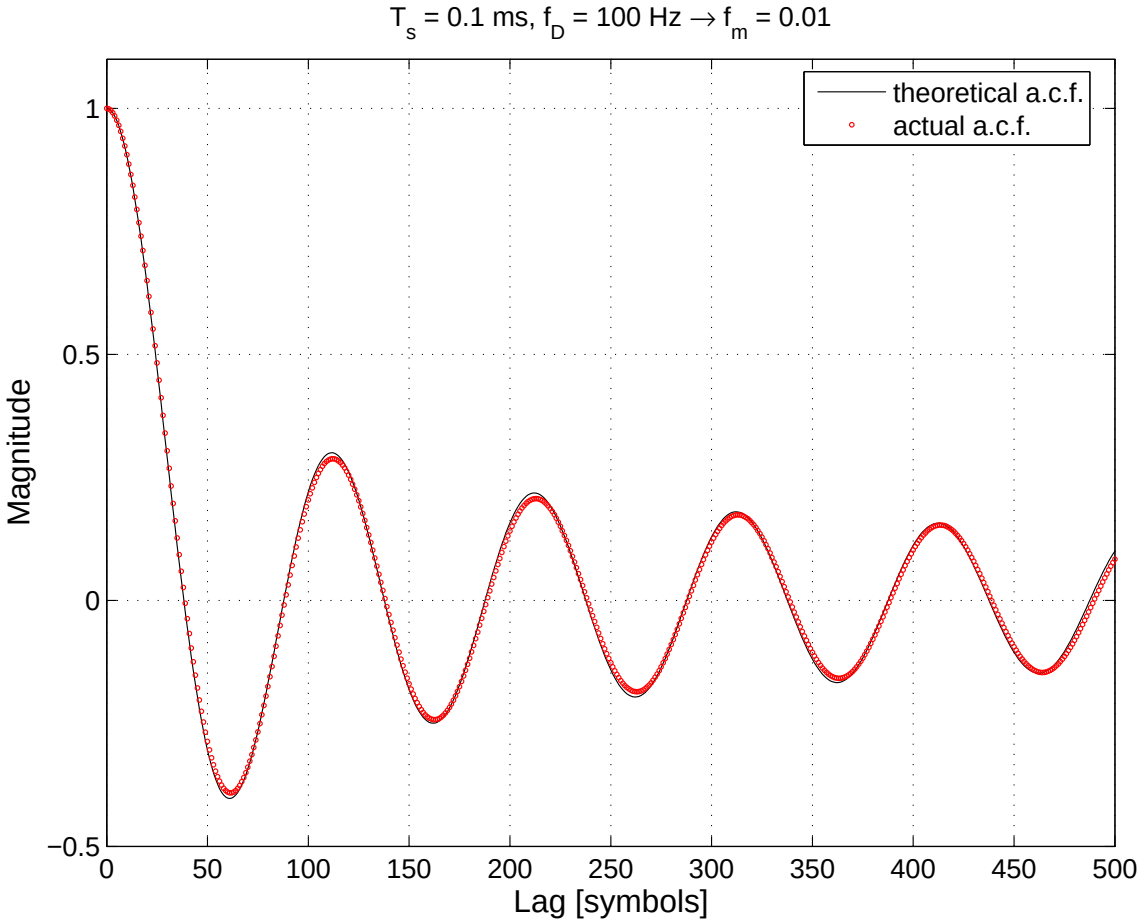

Figure 2.4. Autocorrelation function for Rayleigh fading with $f_{\mathrm{m}} = 0.01$, obtained from theory, using (2.46), and by simulation, from samples of temporally-correlated Rayleigh fading channel gain.

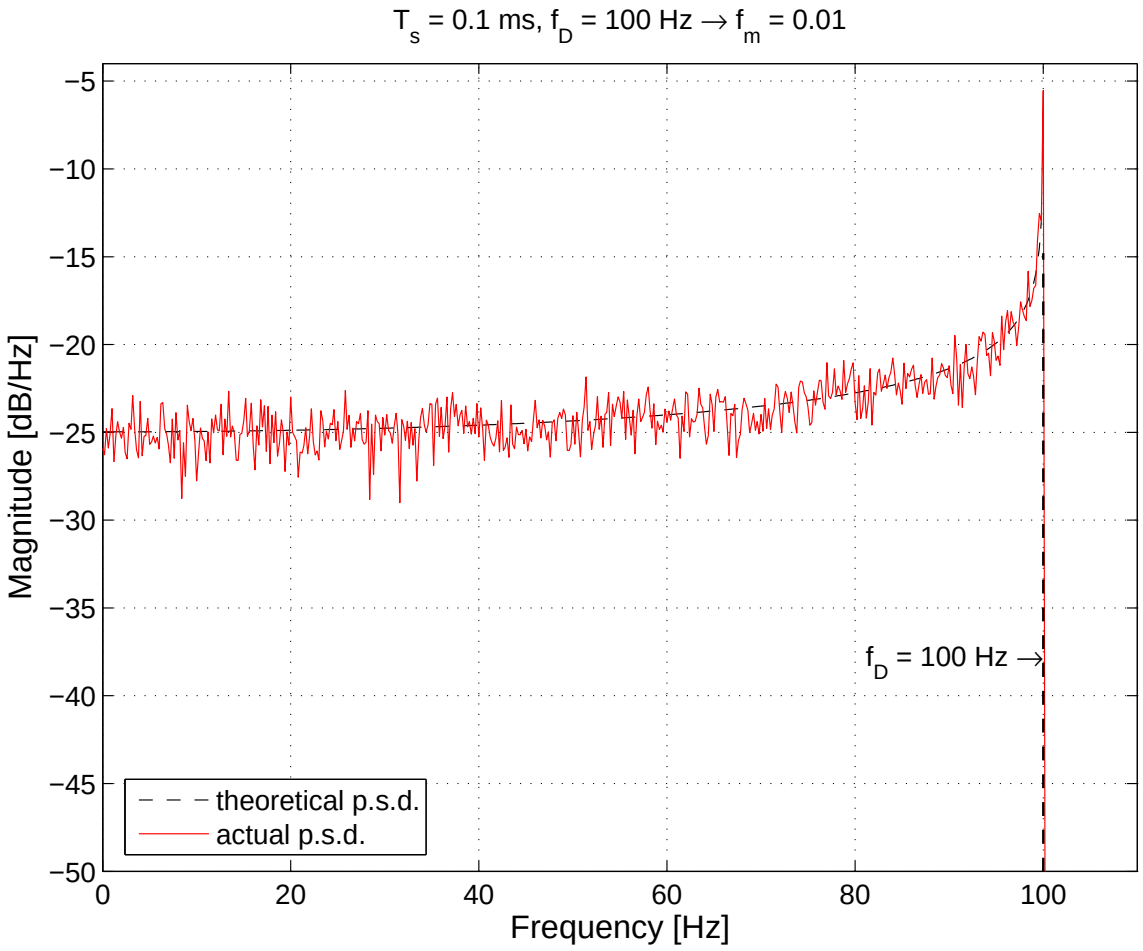

Figure 2.5. Power spectral densities obtained from theory, using (2.47), and by simulation, from samples of temporally-correlated Rayleigh fading channel gain.

characterized by

$$p(|\widetilde{h}|) = \frac{2\,m^m |\widetilde{h}|^{2m-1}}{\left[\sigma^2_{\widetilde{h}}\right]^m \mathscr{G}(m)} \exp\left\{-\frac{m\,|\widetilde{h}|^2}{\sigma^2_{\widetilde{h}}}\right\}, \tag{2.50}$$

where m is referred to as the *fading parameter*, ranging from $\frac{1}{2}$ to ∞, and $\mathscr{G}(m)$ is the so-called Gamma function defined as [115, Eqn. 2.1-111, p. 42]

$$\mathscr{G}(m) \stackrel{\triangle}{=} \int_0^\infty t^{m-1} e^{-t}\, dt. \tag{2.51}$$

It can be shown that for integer m, $\mathscr{G}(m) = (m-1)! \stackrel{\triangle}{=} (m-1)\cdot(m-2)\ldots 3\cdot 2\cdot 1$. Notice that for $m = 1$, the Nakagami-m distribution reduces to the Rayleigh distribution.

2.4.2 Performance

The symbol-detection performance analysis shown in this section relies on the approach from [123, Section 8.2.1]. For MPSK modulation, reception performance over a non-fading AWGN channel is characterized by (2.33). Since a non-fading channel can also be viewed as a fading channel with fixed unit fading gain, the *instantaneous* symbol error probability for MPSK and a fading channel with AWGN, i.e., the error probability obtained by averaging over noise, conditioned on the fading, is simply

$$P_e(|\widetilde{h}|) = \frac{1}{\pi}\int_0^{\frac{M-1}{M}\pi} \exp\left(-\frac{E_\mathrm{s}}{N_0}|\widetilde{h}|^2\,\frac{g_\mathrm{PSK}}{\sin^2\phi}\right) d\phi, \tag{2.52}$$

which is therefore affected by channel gain fades which occur as depicted in the middle subplot in Fig. 2.3. Due to the concavity of P_e-vs.-SNR plots — see Figs. 2.1 and 2.2 — these deep fades can lead to very significant performance degradation when averaging over the fading, as shown next.

Formula (2.52) actually describes the error probability for the maximum-likelihood (ML) estimate of the transmitted MPSK symbol for the signal model in (2.21) from page 14, given

perfect knowledge of the channel gain. For BPSK this is

$$\widehat{b}_{\mathrm{ML}} = \mathrm{sign}\left[\Re\left(\widetilde{w}_{\mathrm{ML}}^{*}\widetilde{y}\right)\right], \tag{2.53}$$

where

$$\widetilde{w}_{\mathrm{ML}} = \widetilde{h}. \tag{2.54}$$

Since knowledge of the channel phase is required, this approach is referred to as *coherent detection* [123, Chapter 3].

For perfect knowledge of the channel gain, the average symbol error probability (AEP) for the ML detector is determined by averaging the instantaneous error probability given by (2.52) over the fading distribution, i.e.,

$$P_e \stackrel{\triangle}{=} E\{P_e(|\widetilde{h}|)\} = \int_0^{\infty} \frac{1}{\pi} \int_0^{\frac{M-1}{M}\pi} \exp\left(-\frac{E_{\mathrm{s}}}{N_0}|\widetilde{h}|^2 \frac{g_{\mathrm{PSK}}}{\sin^2\phi}\right) d\phi \,\mathrm{p.d.f.}(|\widetilde{h}|)\, d|\widetilde{h}|. \tag{2.55}$$

Let us define the *instantaneous SNR per symbol*, at the receiver, as [123, p. 18]

$$\widetilde{\gamma} \stackrel{\triangle}{=} \frac{E_{\mathrm{s}}}{N_0}|\widetilde{h}|^2. \tag{2.56}$$

For Rayleigh fading, $\widetilde{\gamma}$ is an exponentially distributed random variable, i.e., [123, Table 2.2, p. 19]

$$\mathrm{p.d.f.}(\widetilde{\gamma}) = \begin{cases} 1/\widetilde{\Gamma}\, e^{-\widetilde{\gamma}/\widetilde{\Gamma}} & , \quad \text{for } \widetilde{\gamma} \geq 0 \\ 0 & , \quad \text{otherwise,} \end{cases} \tag{2.57}$$

where

$$\widetilde{\Gamma} \stackrel{\triangle}{=} E\{\widetilde{\gamma}\} = \frac{E_{\mathrm{s}}}{N_0}\sigma_{\widetilde{h}}^2 \tag{2.58}$$

is *the average SNR per symbol* at the receiver. Another measure commonly used in plotting numerical results is the receiver *average SNR per information bit*, or simply, the *SNR per bit*, defined as [115, Ch. 14] [123, Ch. 9]

$$\gamma_{\mathrm{b}} \stackrel{\triangle}{=} \frac{\widetilde{\Gamma}}{\log_2 M}. \tag{2.59}$$

This average receive SNR per information bit will be used in plotting numerical results.

Using (2.56) and (2.57), the AEP expression from (2.55) becomes

$$\begin{aligned} P_e = E\{P_e(\widetilde{\gamma})\} &= \int_0^{\infty} \frac{1}{\pi} \int_0^{\frac{M-1}{M}\pi} \exp\left(-\widetilde{\gamma}\frac{g_{\text{PSK}}}{\sin^2\phi}\right) d\phi \, \text{p.d.f.}(\widetilde{\gamma})\, d\widetilde{\gamma} \\ &= \frac{1}{\pi} \int_0^{\frac{M-1}{M}\pi} \int_0^{\infty} \exp\left(-\widetilde{\gamma}\frac{g_{\text{PSK}}}{\sin^2\phi}\right) \text{p.d.f.}(\widetilde{\gamma})\, d\widetilde{\gamma} d\phi. \end{aligned} \tag{2.60}$$

The moment generating function (m.g.f.) of the instantaneous SNR per bit, $\widetilde{\gamma}$, is defined as [123, Eqn. 1.2, p. 4]

$$M_{\widetilde{\gamma}}(s) \stackrel{\triangle}{=} E\{e^{s\widetilde{\gamma}}\} = \int_0^{\infty} e^{s\widetilde{\gamma}} \text{p.d.f.}(\widetilde{\gamma}) d\widetilde{\gamma}, \tag{2.61}$$

which, for Rayleigh fading, can easily determined to be [123, Table 2.2, p. 19]

$$M_{\widetilde{\gamma}}(s) = \left(1 - s\widetilde{\Gamma}\right)^{-1}. \tag{2.62}$$

Therefore, P_e from (2.60) can be written as

$$P_e = \frac{1}{\pi} \int_0^{\frac{M-1}{M}\pi} M_{\widetilde{\gamma}}\left(-\frac{g_{\text{PSK}}}{\sin^2\phi}\right) d\phi = \frac{1}{\pi} \int_0^{\frac{M-1}{M}\pi} \left(1 + \widetilde{\Gamma}\frac{g_{\text{PSK}}}{\sin^2\phi}\right)^{-1} d\phi, \tag{2.63}$$

which can be easily and accurately implemented numerically for any PSK constellation. The corresponding *closed-form* expression is [123, Eqn. 5A.15, p.127]

$$P_e = \frac{M-1}{M} \cdot \left\{ 1 - \sqrt{\frac{\widetilde{\Gamma}\, g_{\text{PSK}}}{1 + \widetilde{\Gamma}\, g_{\text{PSK}}}} \frac{M}{(M-1)\,\pi} \left[\frac{\pi}{2} + \tan^{-1}\left(\sqrt{\frac{\widetilde{\Gamma}\, g_{\text{PSK}}}{1 + \widetilde{\Gamma}\, g_{\text{PSK}}}} \cot\frac{\pi}{M} \right) \right] \right\},$$

which, for $M = 2$ ($g_{\text{PSK}} = 1$), becomes the AEP expression for ML detection of BPSK symbols transmitted through Rayleigh fading channel with AWGN [123, Eqn. 8.104, p. 220]

$$P_e = \frac{1}{2}\left(1 - \sqrt{\frac{\widetilde{\Gamma}}{\widetilde{\Gamma} + 1}}\right). \tag{2.64}$$

For Nakagami-*m* fading, the instantaneous SNR per symbol $\widetilde{\gamma} \stackrel{\triangle}{=} \frac{E_s}{N_0}|\widetilde{h}|^2$ is described by [123, Table 2.2, p. 19]

$$\text{p.d.f.}(\widetilde{\gamma}) = \begin{cases} \left[m^m \widetilde{\gamma}^{m-1}\right] / \left[\widetilde{\Gamma}^m \mathscr{G}(m)\right] \exp\left(-m\widetilde{\gamma}/\widetilde{\Gamma}\right) & , \quad \text{for } \widetilde{\gamma} \geq 0 \\ 0 & , \quad \text{otherwise}, \end{cases} \tag{2.65}$$

where $\mathscr{G}(m)$ was defined in (2.51), on page 26. Then [123, Table 2.2, p. 19]

$$M_{\widetilde{\gamma}}(s) = \left(1 - \frac{s\widetilde{\Gamma}}{m}\right)^{-m}, \tag{2.66}$$

and, following a similar procedure to the one that led to the AEP expression from (2.63) for Rayleigh fading, the AEP expression for Nakagami-*m* fading can be determined as

$$P_e = \frac{1}{\pi}\int_0^{\frac{M-1}{M}\pi}\left(1 + \frac{\widetilde{\Gamma}}{m}\frac{g_{\text{PSK}}}{\sin^2\phi}\right)^{-m} d\phi. \tag{2.67}$$

Accurate numerical computation of finite-limit integral AEP expressions such as (2.63) and (2.67) is fairly simple. For MPSK and Nakagami fading the AEP expression from (2.67) can also be written as an (involved) closed-form, using [123, Eqns. 5A.17-19, pp. 127-128]. Similar results can be obtained for Ricean fading [123, Table 2.2, p. 19].

Let us now quantify the effects of channel fading on symbol-detection performance. Consider the following cases:

- a fading channel with unit variance, i.e., $\sigma_{\widetilde{h}}^2 = 1$, and
  - Nakagami-*m* distribution with fading parameter $m = \frac{1}{2}$; AEP given by (2.67).
  - Rayleigh distribution; AEP given by (2.63), which is equivalent to (2.67) for $m = 1$.
  - Nakagami-*m* distribution with fading parameter $m = 10$; AEP given by (2.67).
- a nonfading AWGN channel (i.e., $\widetilde{h} = 1$); the AEP is given by (2.33).

Figs. 2.6, 2.7, and 2.8 show the average error probabilities for BPSK, QPSK, and 8-PSK, respectively. On the horizontal axis is the average SNR per bit γ_b from (2.59). Notice from these figures that, as the fading parameter for the Nakagami-*m* distribution increases, the performance for the fading channel approaches the performance for the nonfading channel. Actually, by taking $\lim_{m\to\infty}$ in (2.67) we obtain

$$\lim_{m\to\infty} P_e = \frac{1}{\pi}\int_0^{\frac{M-1}{M}\pi}\exp\left\{-\widetilde{\Gamma}\frac{g_{\text{PSK}}}{\sin^2\phi}\right\} d\phi, \tag{2.68}$$

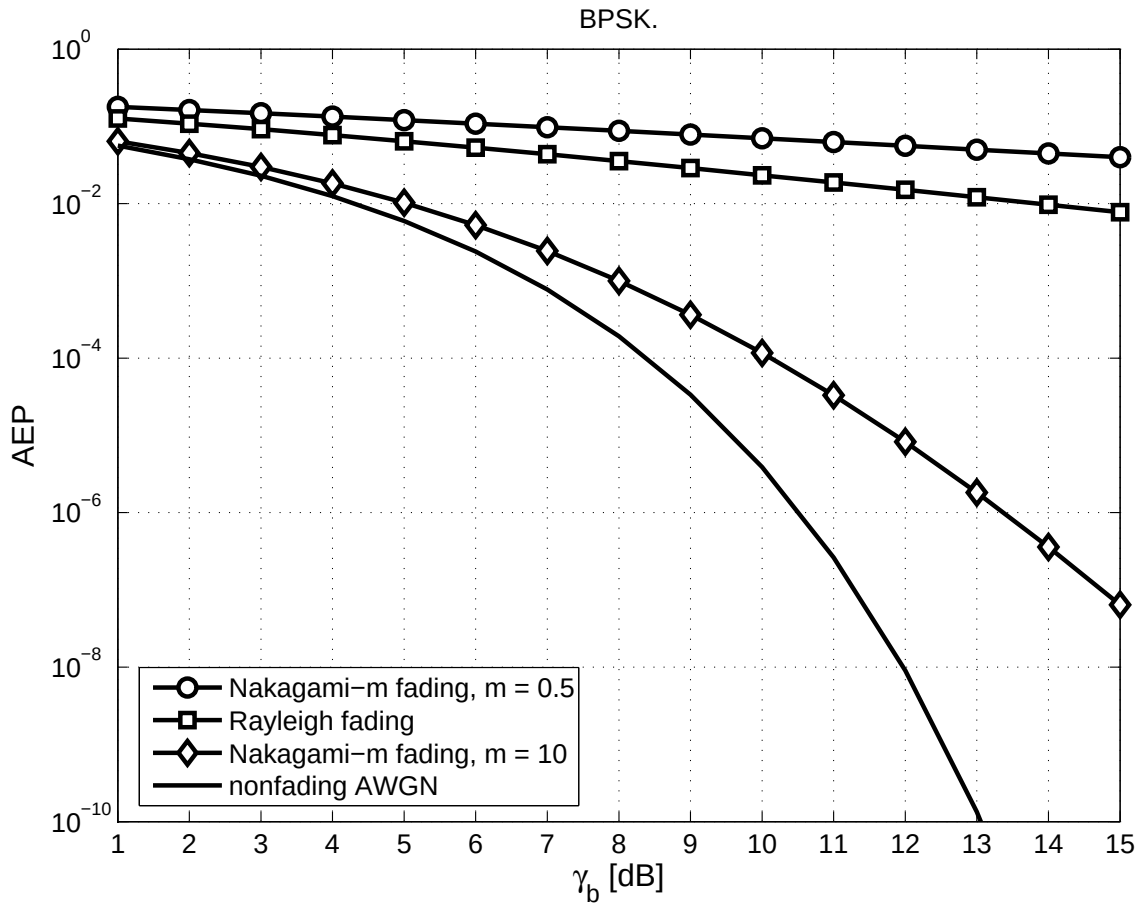

Figure 2.6. Performance for BPSK signal transmitted over a nonfading channel with receiver AWGN, as well as over fading Rayleigh and Nakagami-*m* channels.

which, considering (2.33) on page 16, is the error probability for a nonfading channel with receiver AWGN, whose SNR per symbol is given by $\widetilde{\Gamma}$, explaining the above observation.

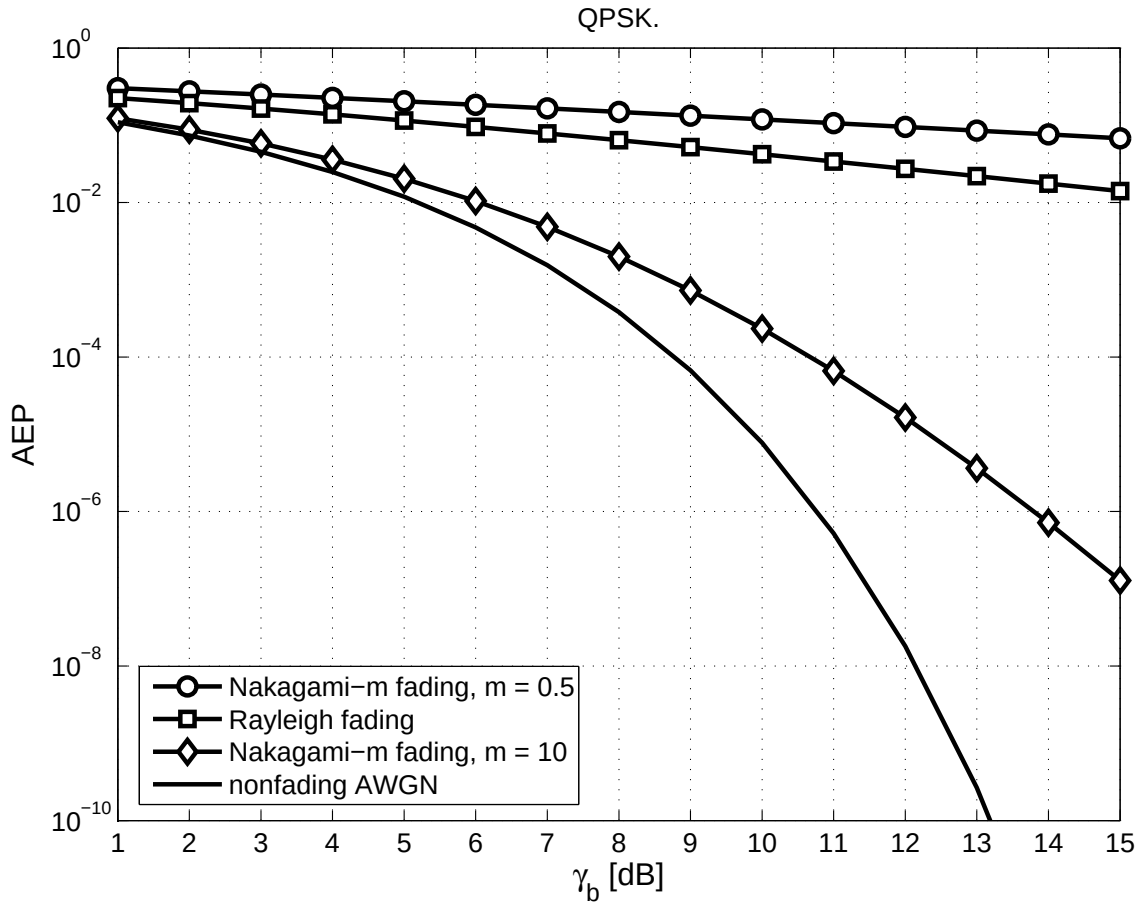

Figure 2.7. Performance for QPSK signal transmitted over a nonfading channel with receiver AWGN, as well as over fading Rayleigh and Nakagami-*m* channels.

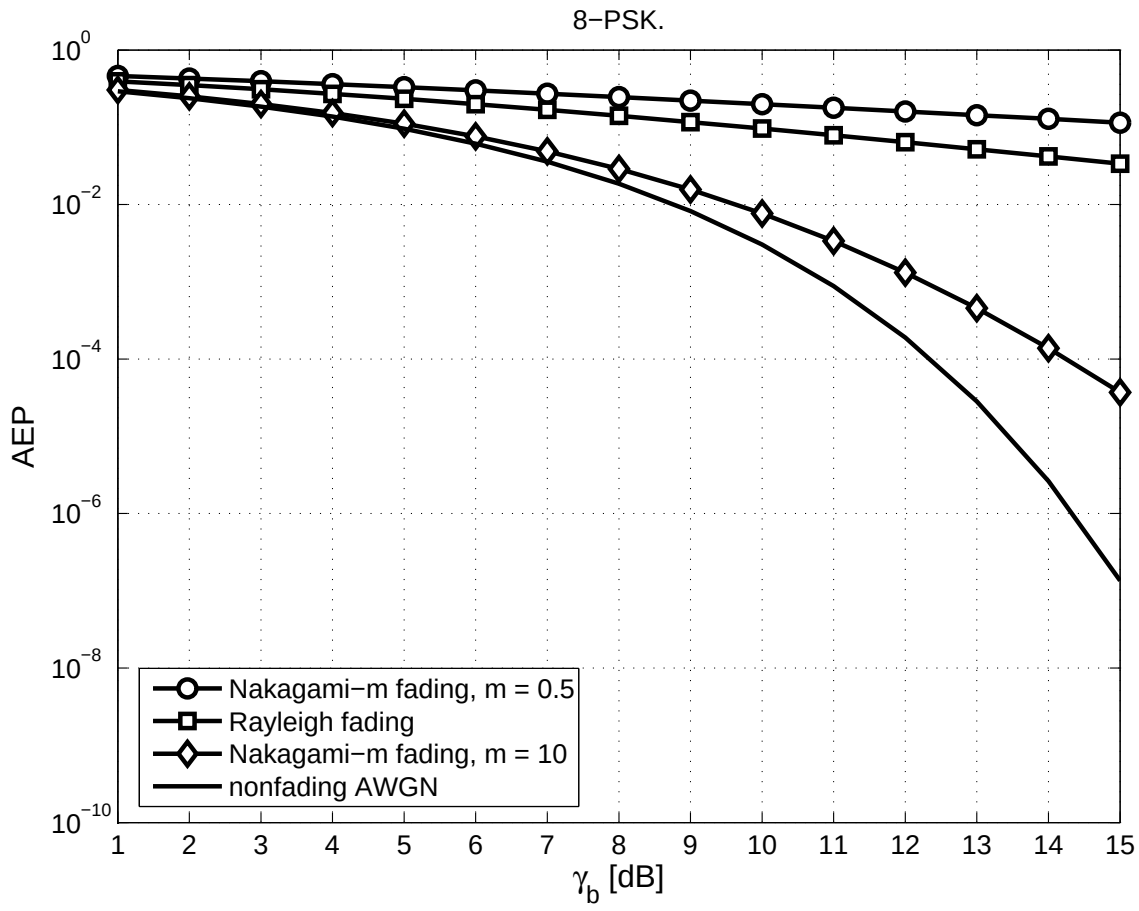

Figure 2.8. Performance for 8-PSK signal transmitted over a nonfading channel with receiver AWGN, as well as over fading Rayleigh and Nakagami-*m* channels.

2.5 Channel Estimation with PSAM and Interpolation

2.5.1 Pilot-Symbol-Aided Modulation (PSAM)

The ideal coherent receiver discussed above assumed perfectly known channel (p.k.c.), i.e., the complex-valued channel gain $\widetilde{h}$ is perfectly known at the receiver. Performance degradation then occurred due to fading as well as AWGN. As we shall see next, in practice symbol detection performance can deteriorate even further due to the fact that the channel gain is never perfectly known. Actual (pseudo-)coherent receivers then require channel gain estimation, which can be done efficiently by employing pilot-symbol-aided modulation [39, 90] (PSAM) at the transmitter, followed by interpolation [19] at the receiver.

The structure of the transmitted signal is herein assumed as shown in Fig. 2.9. Time dependence is conveniently represented by the index pair (t, m_s), where

- $t = -T_1 : T_2$ is the slot index with $t = 0$ corresponding to the slot in which channel estimation and symbol detection currently takes place, and
- $m_s = 0 : M_s - 1$ is the symbol index within the slot of length M_s; $m_s = 0$ corresponds to the pilot symbol and $m_s = 1 : M_s - 1$ corresponds to information symbols.

2.5.2 Interpolation

The channel gain estimate at the m_sth data symbol position in the slot of symbols to be detected can then be obtained by interpolation as follows [39, 90] [19, Sec. 11.3, pp. 473-478]

$$\widetilde{g}(0, m_s) = \widetilde{\mathbf{v}}(m_s)^H \widetilde{\mathbf{r}}, \tag{2.69}$$

where $\widetilde{\mathbf{v}}(m_s)$ is the *interpolation filter* vector, and $\widetilde{\mathbf{r}}$ is a vector formed with $T = T_1 + T_2 + 1$ pilot signal samples, i.e., T_1 "past" samples, the sample from the slot of symbols to be detected,

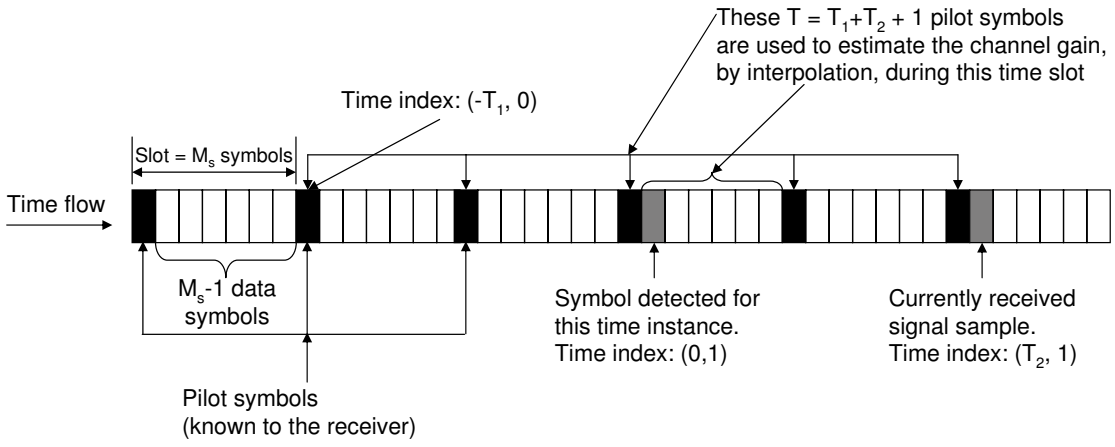

Figure 2.9. PSAM signal slot structure, and interpolation procedure description.

and T_2 "future" samples, as follows

$$\widetilde{\mathbf{r}} \stackrel{\triangle}{=} \frac{1}{\sqrt{E_{\mathrm{p}}}\, b_p} \left[\widetilde{y}(-T_1,0)\ \widetilde{y}\ (-T_1+1,0)\ \ldots\ \widetilde{y}(0,0)\ \ldots \widetilde{y}(T_2-1,0)\ \widetilde{y}(T_2,0)\right]^{\mathrm{T}}, \qquad (2.70)$$

where E_{p} is the pilot symbol waveform energy, b_p is the pilot symbol, and

$$\widetilde{y}(t,0) = \sqrt{E_{\mathrm{p}}}\, b_p\, \widetilde{h}\,(t,0) + \widetilde{n}\,(t,0), \quad t = -T_1 : T_2, \qquad (2.71)$$

are the received signal samples corresponding to transmitted pilot signals. Notice that the received signal has to be stored for T_2 slots ahead of the slot in which estimation and symbol detection is then executed.

Since the channel gain estimates are obtained from pilot samples of the received signal, $\widetilde{h}$ and $\widetilde{g}$ are jointly Gaussian [102, Eqn. 8-56, p. 197]. The joint Gaussianity of the channel gain and its estimate is often assumed in previous work [21, 58, 113, 115].

Interpolation filters can be classified as:

1. **data-independent**, e.g., the filter with brick-wall-type frequency response, which is optimum in the absence of noise [19]; we will refer to this filter, after truncating and tapering its impulse-response with a raised-cosine window [90] [19, Table 11.2, p. 476],

Table 2.1. Interpolation filters

Interpolation Method	Interpolation Vector
SINC	$[\widetilde{\mathbf{v}}(m_s)]_t = \text{sinc}\left(\frac{m_s}{M_s} - t\right) \frac{\cos\left[\pi\beta\left(\frac{m_s}{M_s} - t\right)\right]}{1-\left[2\beta\left(\frac{m_s}{M_s} - t\right)\right]^2}$
MMSE	$\widetilde{\mathbf{v}}(m_s) = \widetilde{\mathbf{\Phi}}^{-1}\widetilde{\boldsymbol{\phi}}(m_s)$

as the SINC filter (because the computation of its coefficients involves the sinc function, defined below), and the corresponding estimation approach as SINC PSAM.

2. **data-dependent**, e.g., the Wiener filter, which is minimum mean squared error (MMSE) optimum in the presence of noise, but requires knowledge of the second-order statistics of the received signals [39]; this filter is referred to as the MMSE filter, and the corresponding estimation approach as MMSE PSAM.

Table 2.1 specifies the SINC [90, Eqns. 9, 10, p. 639] [19, Table 11.2, p. 476] and MMSE [39] interpolation filters, where

$$\text{sinc}(x) = \frac{\sin \pi x}{\pi x}, \tag{2.72}$$

and β is the *rolloff factor* [19, p. 478], for which the typical value $\beta = 0.2$ is chosen for all the numerical results shown herein. The elements of the $T \times T$ matrix

$$\widetilde{\mathbf{\Phi}} \stackrel{\triangle}{=} E\{\widetilde{\mathbf{r}}\,\widetilde{\mathbf{r}}^H\}, \tag{2.73}$$

and of the $T \times 1$ vector

$$\widetilde{\boldsymbol{\phi}}(m_s) \stackrel{\triangle}{=} E\{\widetilde{\mathbf{r}}\widetilde{h}^*(0, m_s)\} \tag{2.74}$$

are expressed in Table 2.2 for Jakes' model of temporal correlation [75] described earlier.

Since the channel gain is a process bandlimited to f_D (see discussion related to Fig. 2.5 shown on page 25), pilot symbols have to be inserted at time intervals no longer than $\frac{1}{2f_D}$ [90,

Table 2.2. Elements of $\widetilde{\mathbf{\Phi}}$ and $\widetilde{\boldsymbol{\phi}}(m_s)$

$\left[\widetilde{\mathbf{\Phi}}\right]_{t_1,t_2}$	$\sigma_{\tilde{h}}^2 J_0(2\pi f_{\mathrm{m}} \lvert t_1 - t_2 \rvert M_s) + \frac{N_0}{E_{\mathrm{p}} \lvert b_p \rvert^2} \delta_{t_1,t_2}$
$\left[\widetilde{\boldsymbol{\phi}}(m_s)\right]_t$	$\sigma_{\tilde{h}}^2 J_0(2\pi f_{\mathrm{m}} \lvert t M_s - m_s \rvert)$

Eqn. 5, p. 638] [39, p. 689], i.e.,

$$M_{\mathrm{s}} T_{\mathrm{s}} \leq \frac{1}{2 f_{\mathrm{D}}} \tag{2.75}$$

which leads to

$$M_{\mathrm{s}} \leq \frac{1}{2} \frac{f_{\mathrm{s}}}{f_{\mathrm{D}}} = \frac{1}{2 f_{\mathrm{m}}}. \tag{2.76}$$

Cavers showed in [39, Fig. 3, p. 689] that increasing M_{s} above this limit can lead to significant performance degradation. In practice, the slot length is chosen by trading-off data throughput and symbol detection performance, e.g., larger M_{s} improves data throughput due to less frequent pilot insertion.

2.5.3 The Average SNR per Information Bit

2.5.3.1 The Case of Ideal Receiver

For an ideal receiver, i.e., a receiver with perfectly known channel, in Figs. 2.6, 2.7, and 2.8 we have already plotted the analytical error probability from (2.67) vs. the average SNR per bit, γ_{b}, which is related to the average SNR per symbol, $\widetilde{\Gamma}$, through (2.59), and to the energy transmitted per symbol, E_{s}, the noise variance, N_0, and channel gain variance, $\sigma_{\tilde{h}}^2$, as described by (2.58) and (2.59).

For an ideal receiver, i.e, with p.k.c., simulations that match analytical results can be done as described next:

- first, we write the signal model from (2.21) in equivalent form as

$$\begin{aligned}\sqrt{\frac{1}{N_0}}\,\widetilde{y} &= \sqrt{\frac{E_\mathrm{s}}{N_0}\,\sigma^2_{\widetilde{h}}}\,b\,\widetilde{h}_\mathrm{norm}+\widetilde{n}_\mathrm{norm}\\ &= \sqrt{\widetilde{\Gamma}}\,b\,\widetilde{h}_\mathrm{norm}+\widetilde{n}_\mathrm{norm},\end{aligned} \tag{2.77}$$

  where $\widetilde{h}_\mathrm{norm}$ and $\widetilde{n}_\mathrm{norm}$ are normalized versions of the channel gain and noise, respectively, i.e., $\sigma^2_{\widetilde{h}_\mathrm{norm}} = \sigma^2_{\widetilde{n}_\mathrm{norm}} = 1$;

- then, generate a sufficiently large number of transmitted symbols, b, and $\widetilde{h}_\mathrm{norm}$ and $\widetilde{n}_\mathrm{norm}$ samples;

- afterward, for each value of γ_b,

  - determine the corresponding $\widetilde{\Gamma}$ value using (2.59),
  - compute the right-hand side (RHS) of (2.77) for each transmitted symbol and the corresponding $\widetilde{h}_\mathrm{norm}$ and $\widetilde{n}_\mathrm{norm}$ samples,
  - employ ML symbol detection based on $\widetilde{h}^*_\mathrm{norm}\,\sqrt{\frac{1}{N_0}}\,\widetilde{y}$,
  - compare the transmitted symbols with the detected ones and compute the AEP.

2.5.3.2 The Case of PSAM-based Receivers

The situation is slightly more complicated when the channel gain is estimated using PSAM. Let us denote the ratio between the energy transmitted in the waveform corresponding to a pilot symbol, E_p, and the energy transmitted in the waveform corresponding to an information-encoding symbol, E_s, with K_p, i.e.,

$$K_\mathrm{p} \stackrel{\triangle}{=} \frac{E_\mathrm{p}}{E_\mathrm{s}}. \tag{2.78}$$

The *actual average SNR per received information symbol* is

$$\widetilde{\Gamma} = \frac{E_\mathrm{s}}{N_0}\,\sigma^2_{\widetilde{h}}, \tag{2.79}$$

and the *actual average SNR per received information bit* is

$$\gamma_{b,\text{actual}} = \frac{\widetilde{\Gamma}}{\log_2 M}. \tag{2.80}$$

This coincides with γ_b from (2.59) on page 27, i.e., the average SNR per bit for the ideal receiver, which does not require transmission of pilot symbols.

However, it is inequitable to compare the performance of an ideal receiver (with p.k.c.) for a given γ_b with a practical PSAM-based receiver for an equal value of $\gamma_{b,\text{actual}}$, simply because the latter requires additional energy for the transmission of a pilot symbol devoid of encoded information. A fair comparison can be done as described next [39, Sect. II.D, p. 687].

For the practical PSAM-based receiver, the total energy transmitted during a slot, i.e., in an interval of length $M_\text{s}\, T_\text{s}$, is

$$E_t \;\stackrel{\triangle}{=}\; E_\text{p} + (M_\text{s}-1)\, E_\text{s} = \left[K_\text{p} + (M_\text{s}-1)\right] E_\text{s}, \tag{2.81}$$

However, information-encoding symbols are only transmitted during the interval of duration $(M_\text{s}-1)\, T_\text{s}$. Therefore, from the total transmitted energy only

$$E_{s,\text{virtual}} \stackrel{\triangle}{=} \frac{E_t}{M_\text{s}-1} = \frac{K_\text{p} + (M_\text{s}-1)}{M_\text{s}-1}\, E_\text{s} \tag{2.82}$$

is virtually transmitted per information-encoding symbol. Therefore, for PSAM, the virtual *average SNR per information symbol* is

$$\widetilde{\Gamma}_\text{virtual} \stackrel{\triangle}{=} \frac{E_{s,\text{virtual}}}{N_0}\, \sigma_{\tilde{h}}^2 = \left(\frac{1}{M_\text{s}-1} K_\text{p} + 1\right) \frac{E_\text{s}}{N_0}\, \sigma_{\tilde{h}}^2 = \left(\frac{1}{M_\text{s}-1} K_\text{p} + 1\right) \widetilde{\Gamma}, \tag{2.83}$$

so that the *virtual average SNR per information bit* is

$$\begin{aligned} \gamma_{b,\text{virtual}} \;&\stackrel{\triangle}{=}\; \frac{\widetilde{\Gamma}_\text{virtual}}{\log_2 M} = \left(\frac{1}{M_\text{s}-1} K_\text{p} + 1\right) \frac{\widetilde{\Gamma}}{\log_2 M} \\ &\stackrel{(2.80)}{=}\; \left(\frac{1}{M_\text{s}-1} K_\text{p} + 1\right) \gamma_{b,\text{actual}}. \end{aligned} \tag{2.84}$$

Performance comparisons of ideal and PSAM-based practical receivers are equitable when γ_b for the former — see (2.59) on page 27 — coincides with $\gamma_{b,\text{virtual}}$ for the latter — see (2.84).

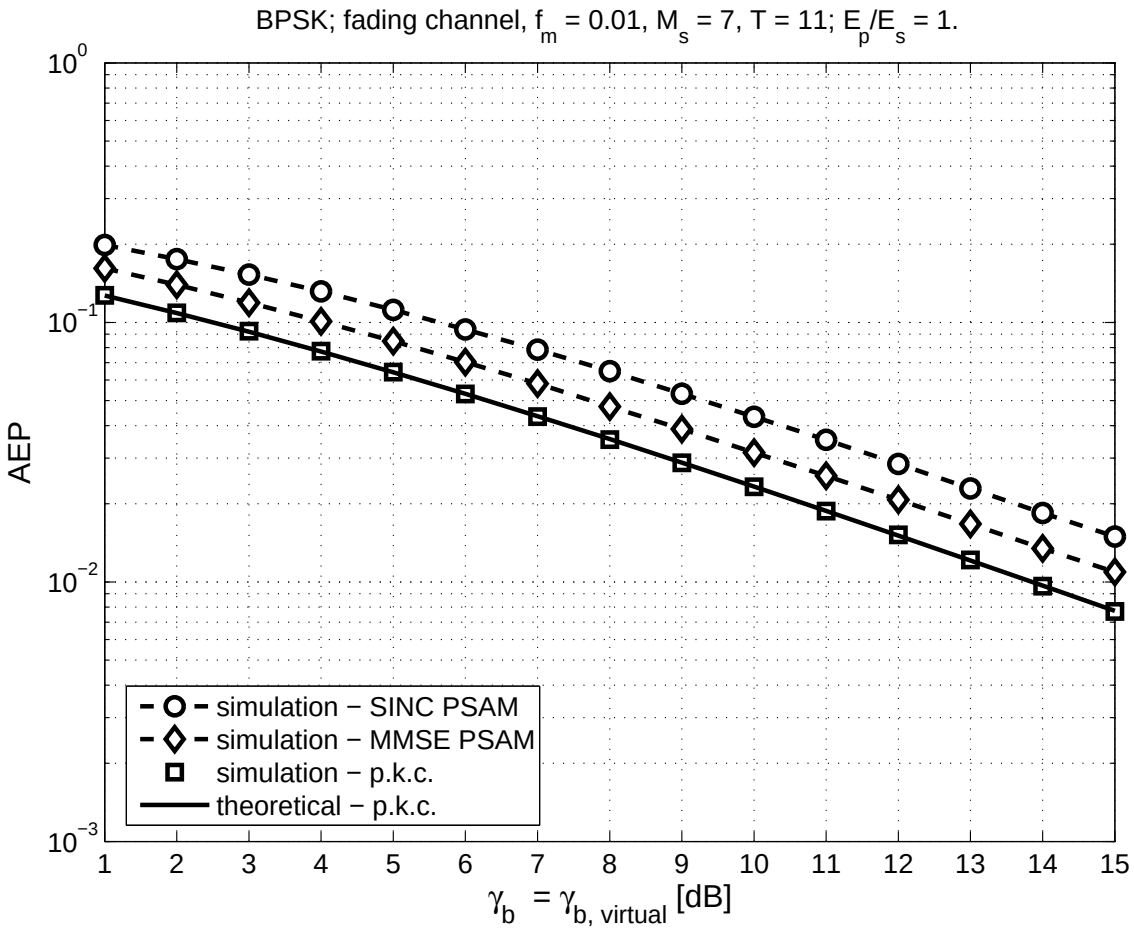

Figure 2.10. Equitable performance comparison between ideal receiver, i.e., with p.k.c., (from theory — Eqn. (2.63) — and simulations), and PSAM-based receivers (from simulations).

Such a comparison is presented for BPSK modulation, $f_{\mathrm{m}} = 0.01$, $E_{\mathrm{p}} = E_{\mathrm{s}}$, i.e., $K_{\mathrm{p}} = 1$, in Fig. 2.10, for the ideal receiver and for the two PSAM-based receivers, where the slot and interpolator lengths were $M_{\mathrm{s}} = 7$ and $T = 11$, respectively, based on the suggestions from [39]. Fig. 2.11 shows an inequitable performance comparison, where γ_{b} for the ideal receiver equals $\gamma_{b,\mathrm{actual}}$ for the non-ideal receivers. Comparing for the PSAM-based receivers the AEP curves from Figs. 2.10 and 2.11 for a given AEP value, we notice that $\gamma_{b,\mathrm{virtual}}/\gamma_{b,\mathrm{actual}}$ is about 0.7 dB, which is consistent with (2.84).

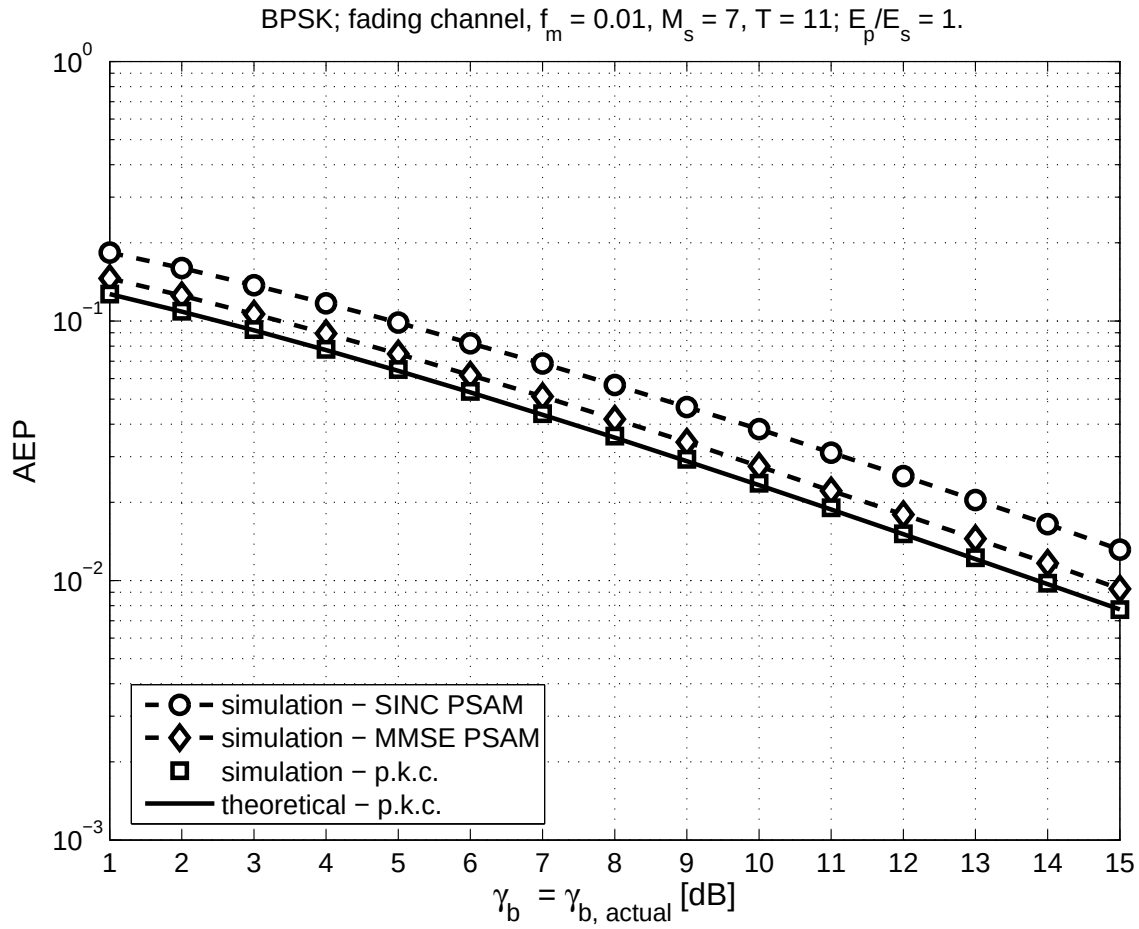

Figure 2.11. Inequitable performance comparison between ideal receiver, i.e., with p.k.c., (from theory — Eqn. (2.63) — and simulations), and PSAM-based receivers (from simulations).

The equitable performance comparisons presented hereafter follow the procedure:

- first, set the range of interest for the SNR per bit;
- then, for the ideal receiver, each such SNR per bit value corresponds to γ_{b} from (2.59), and analytical and simulation results are obtained as described in Section 2.5.3.1;
- finally, for the PSAM-based receivers, the SNR per bit will stand for $\gamma_{b,\mathrm{virtual}}$ from (2.84)
  - from above relations, the total energy transmitted per slot can be computed as

$$E_t = \frac{\gamma_{b,\mathrm{virtual}}}{\sigma_{\widetilde{h}}^2/N_0}\,(M_{\mathrm{s}}-1)\log_2 M. \tag{2.85}$$

  - compute E_{p} and E_{s} from

$$\begin{cases} E_t = E_{\mathrm{p}} + (M_{\mathrm{s}}-1)\,E_{\mathrm{s}} \\ E_{\mathrm{p}} = K_{\mathrm{p}}\,E_{\mathrm{s}}, \end{cases} \tag{2.86}$$

    i.e., from

$$E_{\mathrm{s}} = E_t\,\frac{1}{K_{\mathrm{p}}+M_{\mathrm{s}}-1} \tag{2.87}$$

$$E_{\mathrm{p}} = E_t\,\frac{K_{\mathrm{p}}}{K_{\mathrm{p}}+M_{\mathrm{s}}-1}. \tag{2.88}$$

  - compute the interpolation vectors $\widetilde{\mathbf{v}}(m_s)$, $m_{\mathrm{s}} = 1 : M_{\mathrm{s}}-1$, based on Tables 2.1 and 2.2; note that they can be computed *a priori*, even for MMSE PSAM if the channel fading and receiver noise have stationary statistics;
  - generate a sufficiently-large number of symbols, and the corresponding channel gain and noise samples; the following steps are executed on a slot-by-slot basis:
    - compute the received signal corresponding to transmitted pilot symbols, defined in (2.71), and update the vector $\widetilde{\mathbf{r}}$ defined in (2.70); store the received signal samples corresponding to information-encoding symbols;

- using (2.69), compute the estimated channel gain $\widetilde{g}(0, m_s)$, $m_\mathrm{s} = 1 : M_\mathrm{s} - 1$;
- step back T_2 slots and retrieve the stored received signal corresponding to transmitted data symbols

$$\widetilde{y}(0, m_\mathrm{s}) = \sqrt{E_\mathrm{s}}\, b(0, m_\mathrm{s})\, \widetilde{h}(0, m_\mathrm{s}) + \widetilde{n}(0, m_\mathrm{s}), \quad m_\mathrm{s} = 1 : M_\mathrm{s} - 1; \quad (2.89)$$

- detect the m_sth symbol in the current slot based on $\widetilde{g}^*(0, m_s)\ \widetilde{y}(0, m_\mathrm{s})$;

– compare the detected symbols with the transmitted ones, and compute the AEP.

For notation simplicity only γ_b will appear in subsequent figure abscissas or as parameter for numerical results. However, it will be understood that for the ideal receiver this label stands for γ_b defined in (2.59), whereas for PSAM-based receivers this label stands for $\gamma_{b,\mathrm{virtual}}$ defined in (2.84), so that performance comparisons are equitable.

2.5.4 Performance

Using the AEP expressions from (2.63), page 28, and (2.33), page 16, we showed in Fig. 2.6 on page 30 that the theoretical performance of an ideal coherent receiver for a Rayleigh fading channel can be much worse than for a non-fading channel. For fading channel and ideal receiver, the numerical results shown in Fig. 2.10, on page 39, indicate good agreement between theory and simulation. The AEP plots for PSAM-based receivers shown in Fig. 2.10 indicate that channel estimation inaccuracy can lead to significant further performance deterioration. Due to its optimality, MMSE PSAM ensures better performance than SINC PSAM. However, unlike SINC interpolation, MMSE interpolation relies on assumptions about the temporal correlation of the channel gain. Furthermore, MMSE PSAM requires knowledge about the maximum Doppler shift, channel gain, and noise variance, which are rarely available in practice. SINC PSAM is simple but yields poor performance in low SNR.

Furthermore, the equitable performance comparisons from Figs. 2.12 and 2.13 indicate (for BPSK and QPSK, respectively) that symbol detection using channel gain estimates leads to an *irreducible error floor*, i.e., the level under which the error rate cannot be decreased by increasing the SNR per bit. Clearly, symbol detection performance of SISO systems over fading channels can be very poor in practice.

Figs. 2.14 and 2.15 describe the system performance for $K_p = 10$ and $K_p = 0.1$, respectively. For the PSAM-based receivers, comparing these figures and Fig. 2.10 from page 39 suggests that there is an optimum value of K_p which maximizes performance. Fig. 2.16 further illustrates this claim for $\gamma_b = 10$ dB. AEP is minimized for K_p equal to about 1.5 and 2.7 for MMSE and SINC interpolation, respectively.

2.6 Objectives

Above we found that actual SISO symbol-detection performance/power efficiency may not enable the enhancements required in future wireless systems in terms of voice quality, coverage, data rate, and user capacity. To achieve high symbol-detection performance for reasonable transmitted power, a SISO system will require powerful channel coding [115, Ch. 8], which reduces effective data rate. To achieve desired area coverage significant amounts of power will have to be transmitted, resulting in short battery life and increased interference level.

Important concepts that will enable future communications systems are those of array gain and diversity gain, obtained, respectively, through statistical beamforming [42, 43, 83, 99] and diversity combining [34] [75, Ch. 5, 6] [89, Ch. 9, 10] [123, 133]. Therein, a number of signals carrying the same transmitted information are combined appropriately so that to improve performance. Beamforming and diversity combining are described subsequently in this work, along with a newer, more versatile, approach to which we refer as eigen-combining.

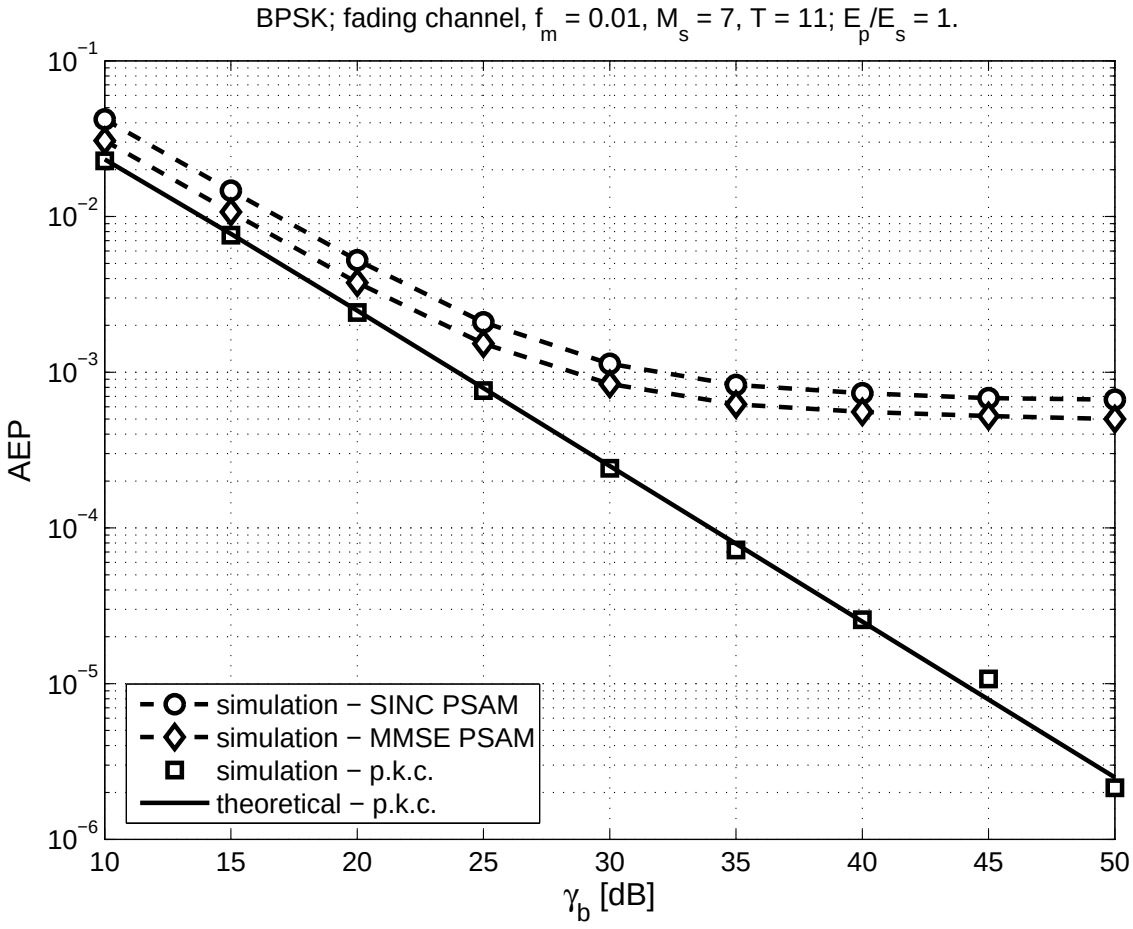

Figure 2.12. Equitable performance comparison for BPSK between ideal receiver, i.e., with p.k.c., (from theory — Eqn. (2.63) — and simulations), and PSAM-based receivers (from simulations), for high SNR per bit.

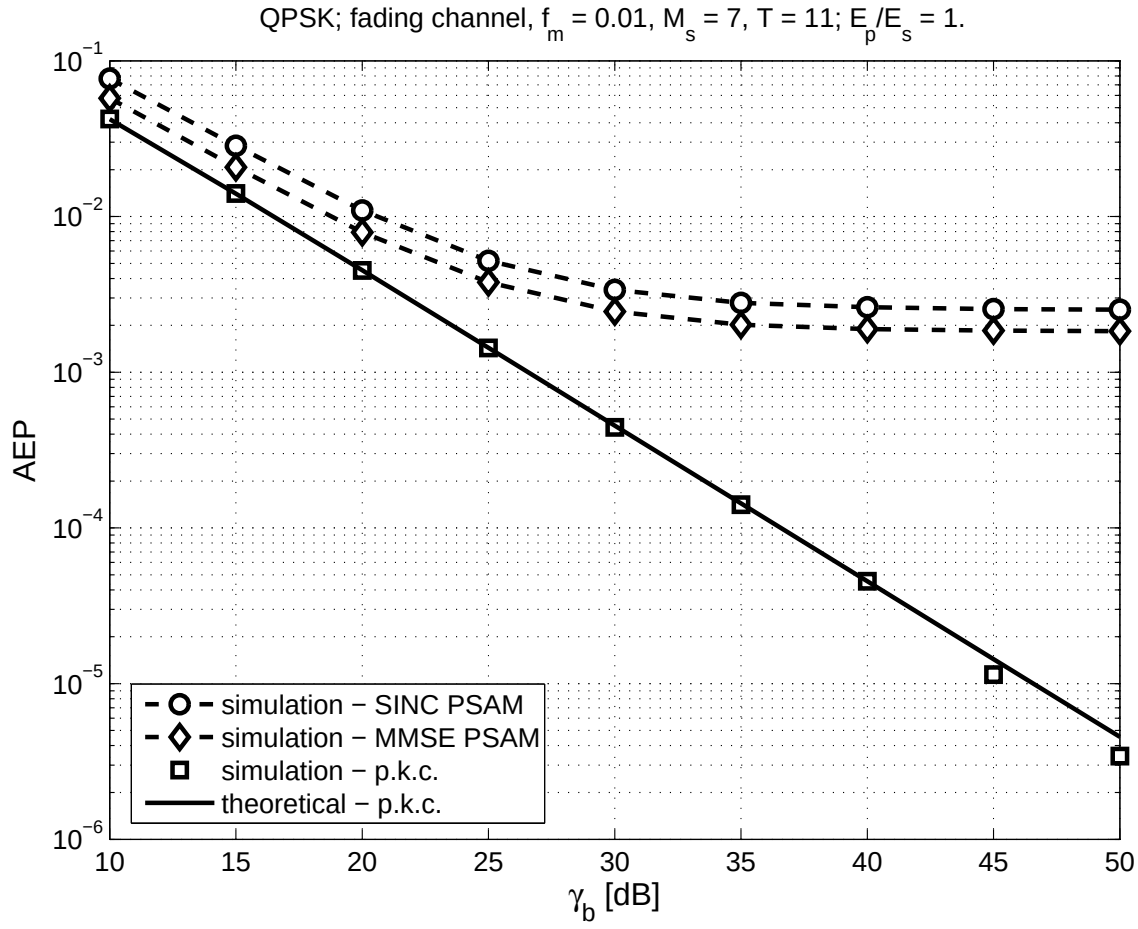

Figure 2.13. Equitable performance comparison for QPSK between ideal receiver, i.e., with p.k.c., (from theory — Eqn. (2.63) — and simulations), and PSAM-based receivers (from simulations), for high SNR per bit.

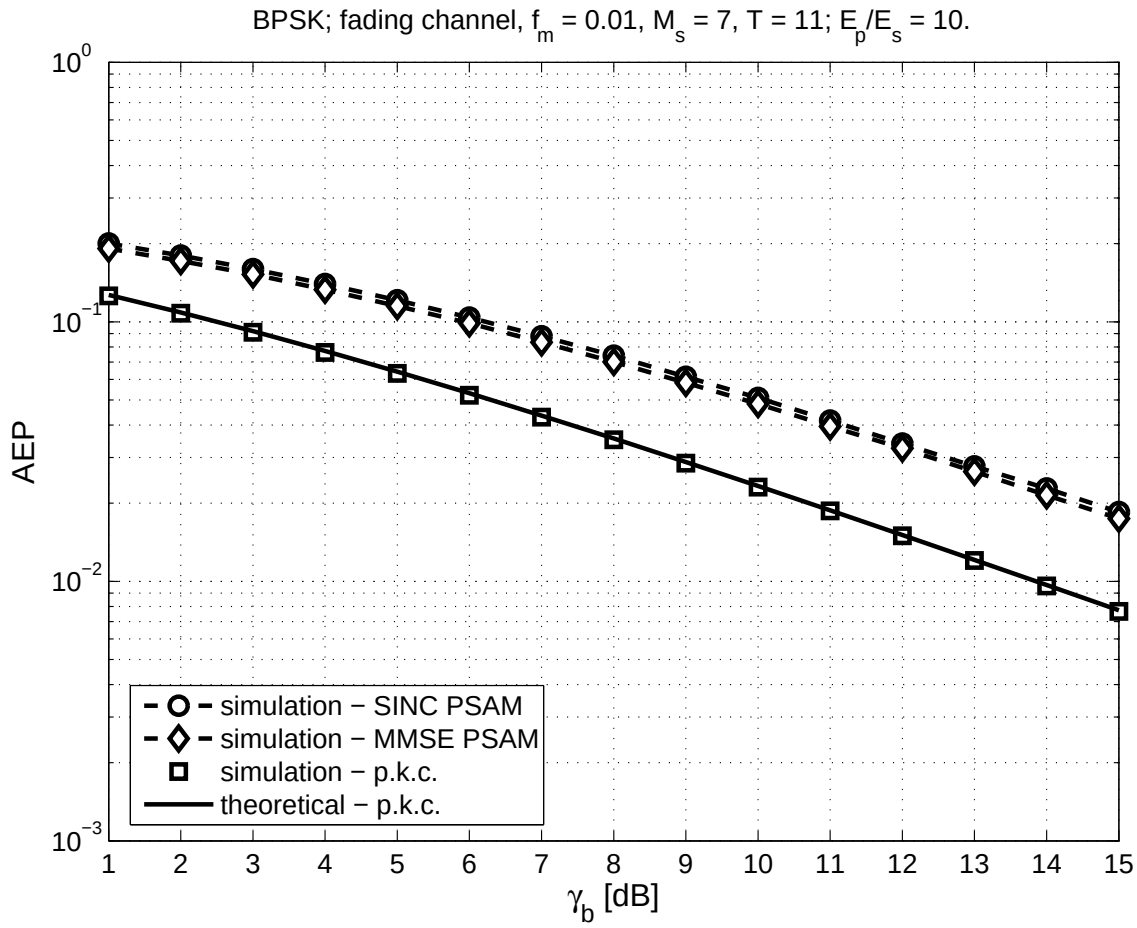

Figure 2.14. Equitable performance comparison for BPSK between ideal receiver, i.e., with p.k.c., (from theory — Eqn. (2.63) — and simulations), and PSAM-based receivers (from simulations), for large $E_{\mathrm{p}}/E_{\mathrm{s}}$.

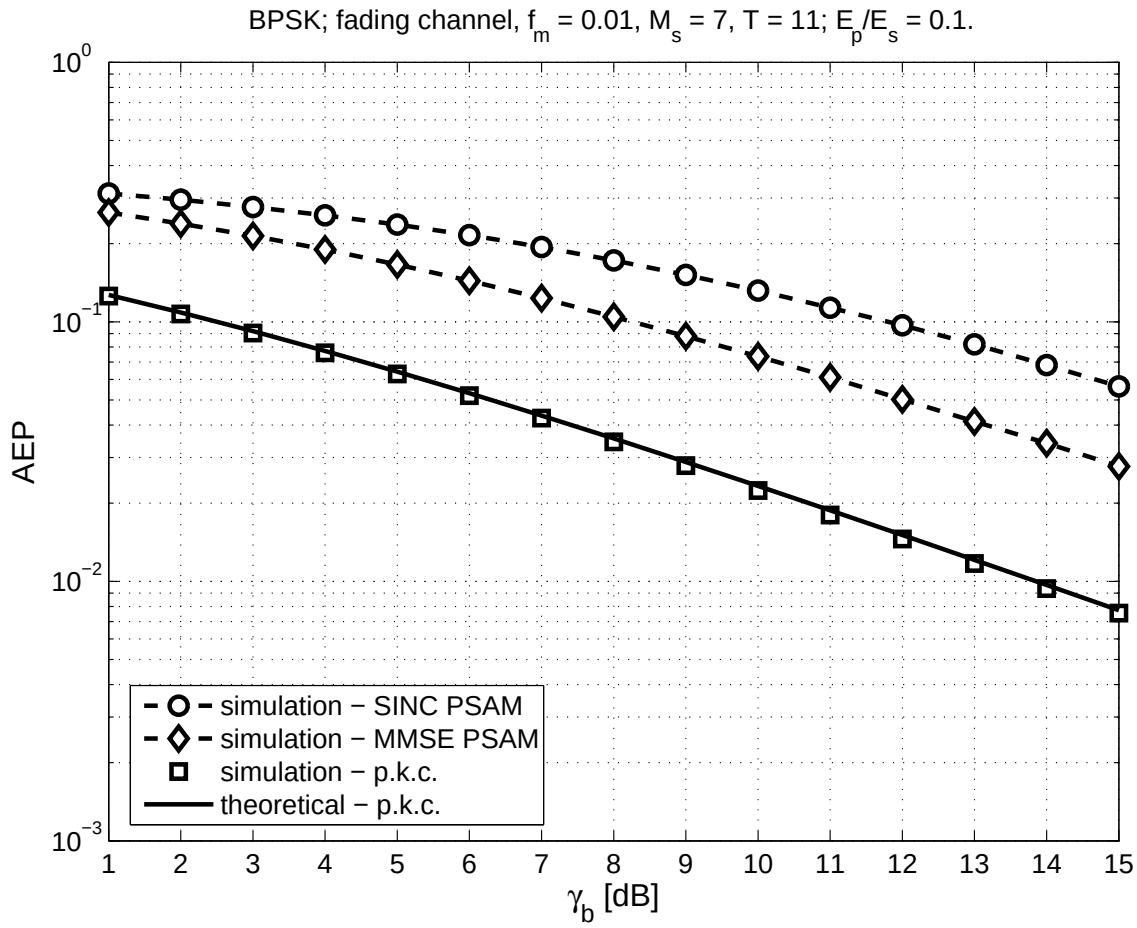

Figure 2.15. Equitable performance comparison for BPSK between ideal receiver, i.e., with p.k.c., (from theory — Eqn. (2.63) — and simulations), and PSAM-based receivers (from simulations), for small $E_{\mathrm{p}}/E_{\mathrm{s}}$.

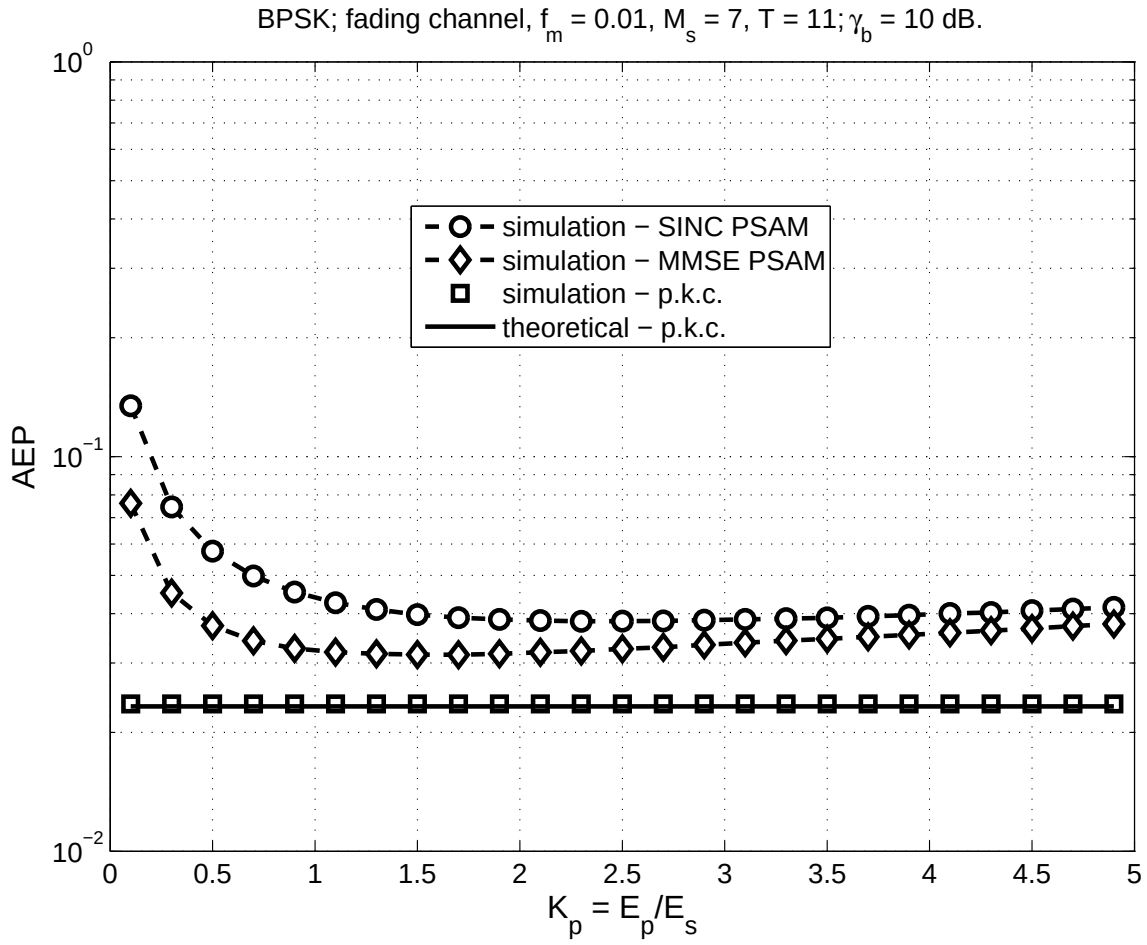

Figure 2.16. Equitable performance comparison for BPSK between ideal receiver, i.e, with p.k.c., (from theory — Eqn. (2.63) — and simulations), and PSAM-based receivers (from simulations), for variable $E_{\mathrm{p}}/E_{\mathrm{s}}$.

Chapter 3

Signal Combining Approaches

3.1 Chapter Overview

In this chapter we analyze conventional multi-branch receiver signal processing methods — statistically optimum beamforming [43] (BF), and maximal-ratio combining [34] (MRC) — as well as eigen-combining, which was recently proposed for complexity reduction and performance enhancement [1, 36, 42, 48, 76, 77].

After presenting the signal model and properties of the channel gain correlation matrix eigen-decomposition, the methods employed herein for symbol-detection performance analysis are described in Section 3.4. Maximal-ratio eigen-combining (MREC) and its special cases, BF and MRC, are analyzed for perfectly known channels in Section 3.5.

Channel estimation based on pilot-symbol-aided modulation (PSAM) and interpolation is presented in Section 3.6. Eigen-/combining approaches for imperfectly known channels are described in Section 3.7. There we provide a detailed implementation description, as well as a performance evaluation based on simulation, for optimum and suboptimum eigen-/combining.

Equivalences between MREC and BF and MRC are demonstrated in Section 3.9. Optimum, or exact, eigen-combining is analyzed based on the effective combiner-output SNR in

Section 3.10. A new, simple, non-closed-form, MREC AEP expression is derived therein — see (3.151), on page 109. This provides, to the best of our knowledge, a new means to evaluate the performance achievable with BF and MRC for imperfectly known channels which may have correlated branches with unequal variances. Also for the first time, completely-specified closed-form exact-MREC (BF, MRC) AEP expressions are provided, even for the case when some eigenvalues of the channel gain correlation matrix coincide.

Suboptimum, or approximate, MREC (BF, MRC) is analyzed in Section 3.11, using the symbol-detection test variable. Although much simpler in terms of implementation than the optimum approach, analysis of approximate MREC proves to be much more complex. A new, yet involved, closed-form AEP expression for approximate MREC (BF, MRC) is derived as (3.189), on page 120. Using the performance equivalence between approximate and exact MRC, which holds for any constellation size for independent and identically distributed (i.i.d.) branches, simple new performance measure expressions are derived for approximate MRC in Section 3.11.4.

MREC is found to promise improved performance and reduced complexity vs. BF and MRC. Subsequent chapters will provide the methodology for achieving these benefits.

3.2 Vector Signal Model

Numerous multi-branch transmission/reception systems and combining approaches have been described and analyzed in the literature and applied in practice [53, 106, 123, 129]. The discussion in the present work focuses on receiver-side combining. Furthermore, although the core of our analysis is applicable more generally, e.g., to RAKE receiver [114] combining, our numerical examples will deal mostly with spatial combining, for smart antenna arrays [79, 80].

Subsequently, we assume that L transmitted signal replicas (*branches*) are available at the

receiver, affected by Rayleigh fading (unless stated otherwise) and additive white Gaussian noise (AWGN). Let us generalize the scalar signal model from (2.21), on page 14, to the vectorial case. Then, after demodulation, matched-filtering, and symbol-rate sampling, the complex-valued received signal vector can be written as

$$\widetilde{\mathbf{y}} = \sqrt{E_\mathrm{s}}\, b\, \widetilde{\mathbf{h}} + \widetilde{\mathbf{n}} \tag{3.1}$$

where b is the equiprobable MPSK transmitted symbol (the constellation size is M), E_s is the energy transmitted per symbol, while $\widetilde{\mathbf{h}}$ and $\widetilde{\mathbf{n}}$ are the complex-valued, mutually uncorrelated channel gain and receiver noise vectors, respectively. The vectors from (3.1) are detailed below:

$$\widetilde{\mathbf{y}} = [\widetilde{y}_1 \quad \widetilde{y}_2 \quad \ldots \quad \widetilde{y}_L]^T, \tag{3.2}$$

$$\widetilde{\mathbf{h}} = [\widetilde{h}_1 \quad \widetilde{h}_2 \quad \ldots \quad \widetilde{h}_L]^T, \tag{3.3}$$

$$\widetilde{\mathbf{n}} = [\widetilde{n}_1 \quad \widetilde{n}_2 \quad \ldots \quad \widetilde{n}_L]^T. \tag{3.4}$$

The components of the received signal vector, i.e., the branches, can be written as

$$\widetilde{y}_i = \sqrt{E_\mathrm{s}}\, b\, \widetilde{h}_i + \widetilde{n}_i, \quad i = 1:L \stackrel{\triangle}{=} 1, \ldots, L. \tag{3.5}$$

Throughout this work it is assumed that the channel gain and noise are complex Gaussian random vectors, as defined in [99, Appendix E, p. 534] [115, pp. 198-199]. In particular, the noise vector is assumed to be white, zero-mean, complex Gaussian, with variance N_0, i.e.,

$$\widetilde{\mathbf{n}} \sim \mathcal{N}_c(\mathbf{0}, N_0\, \mathbf{I}). \tag{3.6}$$

Unless stated otherwise, the channel gain vector is assumed to be zero-mean, complex Gaussian. Then, we can write

$$\widetilde{\mathbf{h}} \sim \mathcal{N}_c(\mathbf{0}, \mathbf{R}_{\widetilde{\mathbf{h}}}), \tag{3.7}$$

where

$$\mathbf{R}_{\widetilde{\mathbf{h}}} \stackrel{\triangle}{=} E\{\widetilde{\mathbf{h}}\widetilde{\mathbf{h}}^H\} \tag{3.8}$$

is the channel gain vector correlation (in this case, also covariance) matrix [99, Appendix E] [115, p. 198]. Note that $\mathbf{R}_{\tilde{\mathbf{h}}}$ is Hermitian, i.e., it equals its conjugate transpose [94, Section 9.7, p. 131] [26, Section 2.2, p. 11]

$$\mathbf{R}_{\tilde{\mathbf{h}}} = \mathbf{R}_{\tilde{\mathbf{h}}}^{H}. \tag{3.9}$$

Only for the numerical results shown throughout this work we will further assume a Toeplitz structure for $\mathbf{R}_{\tilde{\mathbf{h}}}$, i.e., the elements on each diagonal are equal. Then, the first line of $\mathbf{R}_{\tilde{\mathbf{h}}}$ provides the information on all its elements. This situation occurs when the signals are received with a uniform linear array (ULA), as discussed in Chapter 4.

The elements on the main diagonal of this matrix, i.e.,

$$\left(\mathbf{R}_{\tilde{\mathbf{h}}}\right)_{i,i} = E\{|\tilde{h}_i|^2\} \stackrel{\triangle}{=} \sigma_{\tilde{h}_i}^2, \quad i = 1:L, \tag{3.10}$$

are the autocorrelations (variances) of the individual channel gains. Only for the numerical results they will all be assumed unitary. Equality of channel gain variances is an assumption often encountered for antenna arrays [35, Section 4.2.1, p. 49].

3.3 Eigenvalue Decomposition

The channel gain correlation matrix, $\mathbf{R}_{\tilde{\mathbf{h}}}$, is positive semidefinite, i.e., $\forall \mathbf{x} \in \mathbb{C}^L$, the Hermitian form [94, p. 250] $Q(\mathbf{x}) = \mathbf{x}^H \mathbf{R}_{\tilde{\mathbf{h}}} \mathbf{x}$ is real-valued and non-negative. Therefore, $\mathbf{R}_{\tilde{\mathbf{h}}}$ has real-valued, non-negative eigenvalues [94, Section 9.7.2, §1, p. 133] [26, Section 2.2.1, p. 11], which we consider ordered as

$$\lambda_1 \geq \lambda_2 \geq \ldots \geq \lambda_L \geq 0. \tag{3.11}$$

The set

$$\lambda\left(\mathbf{R}_{\tilde{\mathbf{h}}}\right) = \{\lambda_1, \lambda_2, \ldots, \lambda_L\} \tag{3.12}$$

is denoted as *spectrum* [64, Section 7.1, p. 190] of $\mathbf{R}_{\tilde{\mathbf{h}}}$. Each eigenvalue corresponds to an eigenvector. Unique eigenvalues associate with unique orthonormal eigenvectors [103]. The eigenvectors of $\mathbf{R}_{\tilde{\mathbf{h}}}$, denoted as $\mathbf{e}_i$, $i = 1 : L$, thus form an orthonormal basis [26, Section 2.2.1] [103] in $\mathbb{C}^L$. An eigenvalue of multiplicity r_k is associated with an invariant subspace [26, Section 2.2.2] of dimension r_k.

The *spectral decomposition* [94, Section 9.7.4, §1, p. 137] or *eigen-decomposition* [26, Section 2.2.1] of $\mathbf{R}_{\tilde{\mathbf{h}}}$ is described by

$$\mathbf{R}_{\tilde{\mathbf{h}}} = \sum_{i=1}^{L} \lambda_i \, \mathbf{e}_i \, \mathbf{e}_i^H = \mathbf{E}_L \mathbf{\Lambda}_L \mathbf{E}_L^H, \tag{3.13}$$

where

$$\mathbf{\Lambda}_L \stackrel{\triangle}{=} \begin{bmatrix} \lambda_1 & 0 & 0 & \dots & 0 \\ 0 & \lambda_2 & 0 & \dots & 0 \\ \vdots & \vdots & \vdots & \ddots & \vdots \\ 0 & 0 & 0 & \dots & \lambda_L \end{bmatrix} \tag{3.14}$$

is a diagonal matrix, and

$$\mathbf{E}_L \stackrel{\triangle}{=} [\mathbf{e}_1 \quad \mathbf{e}_2 \quad \dots \quad \mathbf{e}_L] \tag{3.15}$$

is a unitary matrix, i.e., $\mathbf{E}_L^H = \mathbf{E}_L^{-1}$ [94, Section 9.15, p. 167], or

$$\mathbf{E}_L^H \mathbf{E}_L = \mathbf{E}_L \mathbf{E}_L^H = \mathbf{I}_{L \times L}, \tag{3.16}$$

i.e., its rows and columns are orthonormal

$$\mathbf{e}_i^H \mathbf{e}_j = \delta_{i,j}, \tag{3.17}$$

where $\delta_{i,j}$ is defined in (2.14) at page 12. Direct and iterative eigen-decomposition methods are surveyed in [26, Chapter 4]. Unless stated otherwise, $\mathbf{R}_{\tilde{\mathbf{h}}}$, $\mathbf{\Lambda}_L$, and $\mathbf{E}_L$ will hereafter be considered perfectly known.

Hereafter, the term *dominant eigenvector* denotes the eigenvector $\mathbf{e}_1$ corresponding to the largest (dominant) eigenvalue, i.e., λ_1. The term *dominant eigenvectors* refers to the set of eigenvectors corresponding to the largest (dominant) eigenvalues.

The *trace* of the channel vector correlation matrix is [64, Section 7.1, p. 190]

$$\mathrm{tr}(\mathbf{R}_{\widetilde{\mathbf{h}}}) \stackrel{\triangle}{=} \sum_{i=1}^{L} \left(\mathbf{R}_{\widetilde{\mathbf{h}}}\right)_{i,i} = \sum_{i=1}^{L} \sigma^2_{\widetilde{h}_l} = \lambda_1 + \lambda_2 + \ldots + \lambda_L. \tag{3.18}$$

which is a measure of the total intended-signal energy received.

The following propositions are given without their simple proofs.

Proposition 1 *The elements of* $\widetilde{\mathbf{h}}$ *are coherent, i.e.,* $\widetilde{\mathbf{h}} = h_1\,\mathbf{e}_1$ *(so that* $h_1 \stackrel{\triangle}{=} \mathbf{e}_1^H\,\widetilde{\mathbf{h}}$*), if and only if* $\lambda_1 = tr(\mathbf{R}_{\widetilde{\mathbf{h}}})$.

For the following see also [47, p. 1985]:

Proposition 2 *The elements of* $\widetilde{\mathbf{h}}$ *are uncorrelated, i.e.,* $(\mathbf{R}_{\widetilde{\mathbf{h}}})_{l_1,l_2} \stackrel{\triangle}{=} E\{\widetilde{h}_{l_1}\,\widetilde{h}^*_{l_2}\} = 0$, $\forall l_1, l_2 = 1:L, l_1 \neq l_2$, *and with equal variances* $(\mathbf{R}_{\widetilde{\mathbf{h}}})_{l,l} \stackrel{\triangle}{=} E\{|\widetilde{h}_l|^2\} = \lambda$, $l = 1:L$, *if and only if the eigenvalues of* $\mathbf{R}_{\widetilde{\mathbf{h}}}$ *are all equal, i.e.,* $\lambda_l = \lambda = \frac{1}{L}\,tr(\mathbf{R}_{\widetilde{\mathbf{h}}})$, $l = 1:L$.

For uniform eigenvalue spectrum, it is known that the columns of the unitary matrix $\mathbf{E}_L$ can be the vectors of any orthonormal basis in $\mathbb{C}^L$. Without loss of generality we will then assume that $\mathbf{E}_L = \mathbf{I}_L$.

Throughout this work we will assume that the eigen-decomposition of the channel gain vector is perfectly known. This agrees with previous claims that it can be updated accurately using samples of the received signal vector [100, 101], due to its slow variation relative to the fading [1, 36, 130].

3.4 Performance Analysis

Generally, when the signal vector from (3.1) is available, one will try to appropriately combine its components to optimize a certain criterion. Receiver performance can then be analyzed by using one of the methods described next to determine the average error probability or outage probability.

3.4.1 Average Error Probability, P_e

3.4.1.1 Obtaining Simple, Finite-Limit Integral P_e Expression Using the Detection SNR

Given the symbol-detection SNR, γ, the symbol error probability expression for MPSK is [123, Eqn. 8.22, p. 198]

$$P_e(\gamma) = \frac{1}{\pi} \int_0^{\frac{M-1}{M}\pi} \exp\left(-\gamma \frac{g_{\text{PSK}}}{\sin^2 \phi}\right) d\,\phi, \tag{3.19}$$

with g_{PSK} defined in (2.34), on page 16. Similar finite-limit integral expressions in exponential functions can describe the instantaneous symbol error probability for other modulations, e.g., Multiple Amplitude-Shift-Keying (M-ASK) or Multiple Amplitude Modulation (M-AM) [123, Eqn. 8.3, p. 194; using Eqn. 4.2, p. 71], and QAM [123, Eqn. 8.12, p. 196]. The instantaneous *bit* error probability for several modulations can also be similarly described [123, Chapter 8]. Therefore, the principle of the approach described next for MPSK can also be applied to these other modulations accordingly [123, Chapter 9].

The average (over the fading) error probability — AEP — is, by definition [115, Eqn. 14.3-4, p. 817] [123, Eqn. 8.102, p. 219],

$$P_e \stackrel{\triangle}{=} \int_0^{\infty} P_e(\gamma)\, p_\gamma(\gamma)\, d\,\gamma. \tag{3.20}$$

Substituting $P_e(\gamma)$ from (3.19) in (3.20) yields the AEP expression as

$$P_e = \frac{1}{\pi} \int_0^{\frac{M-1}{M}\pi} \int_0^{\infty} \exp\left(-\gamma \frac{g_{\text{PSK}}}{\sin^2 \phi}\right) p_\gamma(\gamma) d\gamma d\phi. \tag{3.21}$$

Since the m.g.f. of γ is $M_\gamma(s) \stackrel{\triangle}{=} E\{e^{s\gamma}\}$ [123, Eqn. 2.4, p. 18], the above becomes

$$P_e = \frac{1}{\pi}\int_0^{\frac{M-1}{M}\pi} M_\gamma\left(-\frac{g_{\text{PSK}}}{\sin^2\phi}\right)\,d\phi. \tag{3.22}$$

This derivation is actually an abridged version of the one from Section 2.4.2, starting at page 26, wherein a single-branch receiver has been considered.

For optimum combining methods studied subsequently, we will show that the output SNR (or symbol-detection SNR, generically denoted in this section with γ) is the sum of a number (N) of statistically independent individual SNRs (generically denoted with γ_i), i.e.,

$$\gamma = \sum_{i=1}^{N}\gamma_i, \tag{3.23}$$

so that

$$M_\gamma(s) = \prod_{i=1}^{N} M_{\gamma_i}(s), \tag{3.24}$$

which helps recast (3.22) as

$$P_e = \frac{1}{\pi}\int_0^{\frac{M-1}{M}\pi}\prod_{i=1}^{N} M_{\gamma_i}\left(-\frac{g_{\text{PSK}}}{\sin^2\phi}\right)d\phi. \tag{3.25}$$

For Rayleigh fading, we will see that the individual γ_i, $i = 1:N$, are exponentially distributed. Let us denote their respective averages as Γ_i. Then (3.25) becomes

$$P_e = \frac{1}{\pi}\int_0^{\frac{M-1}{M}\pi}\prod_{i=1}^{L}\left(1+\Gamma_i\frac{g_{\text{PSK}}}{\sin^2\phi}\right)^{-1}d\phi. \tag{3.26}$$

Similar results are possible for Ricean and Nakagami-m fading [123, Table 9.1, p. 269]. Note however that γ_i independence only requires uncorrelated channel gains for Rayleigh and Ricean fading, but independent channel gains for Nakagami-m fading with $m \neq 1$.

3.4.1.2 Obtaining Closed-Form P_e Expression from Symbol-Decision Variable Position in Complex Plane, for BPSK Only

By definition the characteristic function (c.f.) of a random variable x with p.d.f. $p_x(\alpha)$ is given by [115, Eqn. 2.1-71, p. 34]

$$\Phi_x(\mathrm{j}\,\omega) \;\stackrel{\triangle}{=}\; E\{e^{\mathrm{j}\,\omega x}\} = \int_{-\infty}^{\infty} e^{\mathrm{j}\,\omega\,\alpha}\, p_x(\alpha)\, d\alpha, \tag{3.27}$$

so that [115, Eqn. 2.1-72, p. 34]

$$p_x(\alpha) \;=\; \frac{1}{2\,\pi}\int_{-\infty}^{\infty} e^{-\mathrm{j}\,\omega\,\alpha}\,\Phi_x(\mathrm{j}\,\omega)\, d\omega. \tag{3.28}$$

Let us define an additional function, i.e., the Laplace transform of the p.d.f.:

$$F_x(s) \;\stackrel{\triangle}{=}\; E\{e^{-s\,x}\} = \int_{-\infty}^{\infty} e^{-s\,\alpha}\, p_x(\alpha)\, d\alpha = M_x(-s). \tag{3.29}$$

We refer to this function as the reversed moment generating function (r.m.g.f.). Its inverse Laplace transform is

$$p_x(\alpha) \;=\; \int_{-\infty}^{\infty} e^{s\,\alpha}\, F_x(s)\, ds. \tag{3.30}$$

A common communications system performance analysis procedure [30] [115] [120] [119] is to assume that a certain symbol b was transmitted, followed by decision on the received symbol based on a variable generically written herein as

$$q = \Re\{\mathbf{x}^H\,\mathbf{R}^{-1}\,\mathbf{z}\}, \tag{3.31}$$

where $\mathbf{x}$ and $\mathbf{z}$ are N-dimensional, complex-valued vectors, zero-mean, jointly Gaussian, and $\mathbf{R}$ is a non-singular, Hermitian $N \times N$ matrix (also $\mathbf{R}^{-1}$ is then Hermitian [94, Section 9.7.1, §4.c, p. 131]).

For BPSK transmitted symbol, the detected symbol is

$$\widehat{b} = \mathrm{sign}(q). \tag{3.32}$$

Assuming that $b = 1$ is the transmitted symbol, the error probability is given by [115, Appendix B, Eqn. B-2, p. 943]

$$P_e = \Pr(q < 0 \,|\, b = 1) = \int_{-\infty}^{0} p(q)\, dq. \tag{3.33}$$

When the c.f. of q, denoted as $\Phi_q(\mathrm{j}\,\omega)$, is available, the p.d.f. of q required above can be obtained as in (3.28). Then, (3.33) leads to [115, Appendix B, Eqns. B-3,4, pp. 943-944] [96, Eqn. 6, p. 2138]

$$P_e = \int_{-\infty}^{0} dq \frac{1}{2\pi} \int_{-\infty}^{\infty} e^{-\mathrm{j}\,\omega\, q} \Phi_q(\mathrm{j}\,\omega) d\omega = -\frac{1}{2\pi \mathrm{j}} \int_{-\infty+\varepsilon}^{\infty+\varepsilon} \frac{\Phi_q(\mathrm{j}\,\omega)}{\omega}\, d\omega, \tag{3.34}$$

(ε is described in [115, Appendix B, p. 944]). However, this approach is fairly complicated and can yield involved, non-closed-form error probability expressions, e.g., [115, Appendix B, Eqn. B-21, p. 947] [96, Section II.A].

Given the r.m.g.f. of q — see $F_q(s)$ defined in (3.29) — it is actually simpler to find its inverse Laplace transform, i.e., $p(q)$, using (3.30), and then find the average error probability using (3.33). An approach to computing $F_q(s)$ is described next using results from [119, Ch. 3] [120].

The decision variable from (3.31) can be recast as a (real) Hermitian form [94, p. 250]

$$\begin{aligned} q &= \frac{1}{2}\left(\mathbf{x}^H \mathbf{R}^{-1} \mathbf{z} + \mathbf{z}^H \mathbf{R}^{-1} \mathbf{x}\right) \\ &= \frac{1}{2}\begin{bmatrix} \mathbf{x}^H & \mathbf{z}^H \end{bmatrix} \begin{bmatrix} \mathbf{0} & \mathbf{R}^{-1} \\ \mathbf{R}^{-1} & \mathbf{0} \end{bmatrix} \begin{bmatrix} \mathbf{x} \\ \mathbf{z} \end{bmatrix} \\ &= \mathbf{v}^H \mathbf{B} \mathbf{v}, \end{aligned} \tag{3.35}$$

where

$$\mathbf{v} \triangleq \begin{bmatrix} \mathbf{x} \\ \mathbf{z} \end{bmatrix}, \tag{3.36}$$

is a $2N$-dimensional, zero-mean, complex Gaussian vector, with correlation matrix

$$\mathbf{R_v} \stackrel{\triangle}{=} E\{\mathbf{v}\mathbf{v}^H\} = \begin{bmatrix} E\{\mathbf{x}\mathbf{x}^H\} & E\{\mathbf{x}\mathbf{z}^H\} \\ E\{\mathbf{z}\mathbf{x}^H\} & E\{\mathbf{z}\mathbf{z}^H\} \end{bmatrix} \stackrel{\triangle}{=} \begin{bmatrix} \mathbf{R_x} & \mathbf{R_{xz}} \\ \mathbf{R_{zx}} & \mathbf{R_z} \end{bmatrix}, \text{ and} \tag{3.37}$$

$$\mathbf{B} \stackrel{\triangle}{=} \frac{1}{2}\begin{bmatrix} \mathbf{0} & \mathbf{R}^{-1} \\ \mathbf{R}^{-1} & \mathbf{0} \end{bmatrix}, \tag{3.38}$$

is a $2N \times 2N$ Hermitian matrix.

Based on the seminal work of Turin [142], if $\mathbf{R_v}$ is nonsingular then the r.m.g.f. of q is

$$F_q(s) = \frac{1}{|\mathbf{I}_{2N} + s\mathbf{R_v}\mathbf{B}|} = \prod_{n=1}^{2N} \frac{1}{1+s\,\eta_n}, \tag{3.39}$$

where η_n is the nth eigenvalue of the $2N \times 2N$ matrix

$$\mathbf{R_v}\mathbf{B} = \frac{1}{2}\begin{bmatrix} \mathbf{R_{xz}}\mathbf{R}^{-1} & \mathbf{R_x}\mathbf{R}^{-1} \\ \mathbf{R_z}\mathbf{R}^{-1} & \mathbf{R_{zx}}\mathbf{R}^{-1} \end{bmatrix}. \tag{3.40}$$

In general, these eigenvalues may need to be computed numerically. Using property [94, §6, p. 50] for the determinant of a partitioned matrix, we can also write

$$\begin{aligned} |\mathbf{I}_{2N} + s\mathbf{R_v}\mathbf{B}| &= \left|\mathbf{I}_N + \frac{1}{2}s\mathbf{R_{xz}}\mathbf{R}^{-1}\right| \\ &\times \left|\left(\mathbf{I}_N + \frac{1}{2}s\mathbf{R_{zx}}\mathbf{R}^{-1}\right) - \frac{1}{4}s^2\mathbf{R_z}\mathbf{R}^{-1}\left(\mathbf{I}_N + \frac{1}{2}s\mathbf{R_{xz}}\mathbf{R}^{-1}\right)^{-1}\mathbf{R_x}\mathbf{R}^{-1}\right| \end{aligned} \tag{3.41}$$

which holds assuming that $\left|\mathbf{I}_N + \frac{1}{2}s\mathbf{R_{xz}}\mathbf{R}^{-1}\right| \neq 0$. The remaining determinant in (3.41) is difficult to factor in closed-form unless all the correlation matrices involved in the above expressions are diagonal. In this special case the above determinant can be rewritten as

$$\begin{aligned} |\mathbf{I}_{2N} + s\mathbf{R_v}\mathbf{B}| &= \prod_{n=1}^{N}\left\{\left[1 + \frac{1}{2}s\cdot(\mathbf{R_{xz}})_{n,n}(\mathbf{R}^{-1})_{n,n}\right]\left[1 + \frac{1}{2}s\cdot(\mathbf{R_{zx}})_{n,n}(\mathbf{R}^{-1})_{n,n}\right]\right. \\ &- \left.\frac{1}{4}s^2\cdot(\mathbf{R_z})_{n,n}(\mathbf{R}^{-1})_{n,n}(\mathbf{R_x})_{n,n}(\mathbf{R}^{-1})_{n,n}\right\}. \end{aligned}$$

Then, it can be shown that (3.39) becomes [125]

$$F_q(s) = \prod_{n=1}^{N} \frac{1}{\left[-a_n^2\,(s-s_{n_1})\,(s-s_{n_2})\right]}, \tag{3.42}$$

where

$$a_n^2 = -\frac{\sigma^2_{x_n z_n}\,\sigma^2_{z_n x_n} - \sigma^2_{x_n}\,\sigma^2_{z_n}}{4\,(\sigma_n^2)^2}, \tag{3.43}$$

$$s_{n_{1,2}} = \sigma_n^2 \left\{ \frac{-\left(\sigma^2_{x_n z_n} + \sigma^2_{z_n x_n}\right) \pm \sqrt{\left[\sigma^2_{x_n z_n} - \sigma^2_{z_n x_n}\right]^2 + 4\,\sigma^2_{x_n}\,\sigma^2_{z_n}}}{\left[\sigma^2_{x_n z_n}\,\sigma^2_{z_n x_n} - \sigma^2_{x_n}\,\sigma^2_{z_n}\right]} \right\}, \tag{3.44}$$

with $\sigma_n^2 \triangleq (\mathbf{R})_{n,n}$, $\sigma^2_{x_n z_n} \triangleq (\mathbf{R_{xz}})_{n,n}$, $\sigma^2_{z_n x_n} \triangleq (\mathbf{R_{zx}})_{n,n}$, $\sigma^2_{x_n} \triangleq (\mathbf{R_x})_{n,n}$, $\sigma^2_{z_n} \triangleq (\mathbf{R_z})_{n,n}$.

Assuming that $\sigma^2_{x_n z_n} = \sigma^2_{z_n x_n}$, (3.43) and (3.44) become

$$a_n^2 = \frac{1-\mu^2_{x_n z_n}}{\mu^2_{x_n z_n}} \frac{\left(\sigma^2_{x_n z_n}\right)^2}{4\,(\sigma_n^2)^2}, \tag{3.45}$$

$$s_{n_1} = 2\frac{\sigma_n^2}{\sqrt{\sigma^2_{x_n}\,\sigma^2_{z_n}}} \frac{1}{1-\mu_{x_n z_n}} = 2\frac{\sigma_n^2}{\sigma^2_{x_n z_n}} \frac{\mu_{x_n z_n}}{1-\mu_{x_n z_n}} > 0, \tag{3.46}$$

$$s_{n_2} = -2\frac{\sigma_n^2}{\sqrt{\sigma^2_{x_n}\,\sigma^2_{z_n}}} \frac{1}{1+\mu_{x_n z_n}} = -2\frac{\sigma_n^2}{\sigma^2_{x_n z_n}} \frac{\mu_{x_n z_n}}{1+\mu_{x_n z_n}} < 0, \tag{3.47}$$

with $\mu_{x_n z_n}$ the correlation coefficient of x_n and z_n — definition and properties given below. Having $F_q(s)$, the error probability can be computed as described earlier, on page 58.

For any zero-mean random variables x and z their correlation coefficient is defined as [112, Eqn. 2.3, p. 10]

$$\mu_{xz} \triangleq \frac{\sigma^2_{xz}}{\sqrt{\sigma^2_x\,\sigma^2_z}}, \text{ with } \quad |\mu_{xz}| \in [0,1]. \tag{3.48}$$

Then [112, Eqn. 2.4, p. 10]:

- $\mu_{xz} = 0$ when x and z are uncorrelated
- $|\mu_{xz}| \in (0,1)$ when x and z are partially correlated
- $|\mu_{xz}| = 1$ when x and z are completely correlated, i.e., coherent; then, we actually have $x = \alpha z$, where α is a complex-valued, non-random, constant scalar.

3.4.2 Outage Probability, P_o

The outage probability is a performance measure more suitable than the average error probability when the fading is slow. P_o represents the probability that the instantaneous probability of error exceeds a given threshold [123, Section 1.1.2, p. 5] [84], i.e.,

$$P_o \stackrel{\triangle}{=} \Pr(P_e > P_{e,\text{th}}). \tag{3.49}$$

For γ denoting the symbol-detection instantaneous SNR, if the function $P_e(\gamma)$ can be inverted (analytically or numerically) then an equivalent definition of outage probability is

$$P_o \stackrel{\triangle}{=} \Pr(\gamma < \gamma_{\text{th}}) = \int_0^{\gamma_{\text{th}}} p_\gamma(\gamma)\, d\,\gamma. \tag{3.50}$$

The alternative P_o definition from (3.50) may appear to indicate that the outage rate is only dependent on the SNR distribution, which is untrue; P_o does depend on the modulation as well, through the threshold SNR, γ_{th}.

3.5 Combining Methods for Perfectly Known Channel Gains

3.5.1 Ideal Maximal-Ratio Combining (MRC)

3.5.1.1 Procedure

The linear combination of the received signal vector given by (3.1) with a weight vector $\widetilde{\mathbf{w}}$ yields

$$\widetilde{\mathbf{w}}^H \widetilde{\mathbf{y}} = \sqrt{E_\text{s}}\, b\, \widetilde{\mathbf{w}}^H \widetilde{\mathbf{h}} + \widetilde{\mathbf{w}}^H \widetilde{\mathbf{n}}. \tag{3.51}$$

The combiner's output power averaged over noise is

$$E\{|\widetilde{\mathbf{w}}^H \widetilde{\mathbf{y}}|^2\} \quad = \quad E_\text{s}\, |b|^2\, |\widetilde{\mathbf{w}}^H \widetilde{\mathbf{h}}|^2 + E\{|\widetilde{\mathbf{w}}^H \widetilde{\mathbf{n}}|^2\}$$

$$= \quad E_{\mathrm{s}}\,|\widetilde{\mathbf{w}}^H\,\widetilde{\mathbf{h}}|^2 + N_0\,\widetilde{\mathbf{w}}^H\widetilde{\mathbf{w}}, \tag{3.52}$$

so that the combiner's output SNR is

$$\mathrm{SNR}(\widetilde{\mathbf{w}}) \stackrel{\triangle}{=} \frac{E_{\mathrm{s}}}{N_0}\,\frac{|\widetilde{\mathbf{w}}^H\,\widetilde{\mathbf{h}}|^2}{\widetilde{\mathbf{w}}^H\widetilde{\mathbf{w}}}. \tag{3.53}$$

This SNR will also be referred to as *instantaneous* combiner SNR to distinguish it from the *average* combiner SNR which will be defined later when averaging over fading as well.

Let us define the instantaneous SNR of the ith branch as

$$\breve{\widetilde{\gamma}}_i \stackrel{\triangle}{=} \frac{E_{\mathrm{s}}}{N_0}|\widetilde{h}_i|^2, \quad i = 1:L. \tag{3.54}$$

Based on the Schwartz inequality [34, Appendix II] [99, Appendix D] we can write

$$\max_{\widetilde{\mathbf{w}}\in\mathbb{C}^L} \mathrm{SNR}(\widetilde{\mathbf{w}}) = \mathrm{SNR}(k\,\widetilde{\mathbf{h}}) = \frac{E_{\mathrm{s}}}{N_0}\,|\widetilde{\mathbf{h}}|^2 = \sum_{i=1}^{L}\frac{E_{\mathrm{s}}}{N_0}\,|\widetilde{h}_i|^2. \tag{3.55}$$

Since the proportionality factor k from (3.55) does not affect the SNR, the weight vector

$$\widetilde{\mathbf{w}}_{\mathrm{MRC}} = \widetilde{\mathbf{h}} \tag{3.56}$$

yields maximum instantaneous output SNR, given by [34, Eqn. 13] [123, Eqn. 9.1]

$$\breve{\widetilde{\gamma}} = \sum_{i=1}^{L}\breve{\widetilde{\gamma}}_i, \tag{3.57}$$

i.e., the sum of the individual branch SNRs. This justifies the appellative *maximal-ratio combining* (MRC) for this approach [34].

Then, recovery of a BPSK transmitted symbol, for instance, is attempted as follows:

$$\widehat{b}_{\mathrm{MRC}} \quad = \quad \mathrm{sign}\left\{\Re\left[\widetilde{\mathbf{w}}_{\mathrm{MRC}}^H\,\widetilde{\mathbf{y}}\right]\right\} = \mathrm{sign}\left\{\Re\left[\widetilde{\mathbf{h}}^H\,\widetilde{\mathbf{y}}\right]\right\} \tag{3.58}$$

$$= \quad \mathrm{sign}\left\{\sqrt{E_{\mathrm{s}}}\,b\,|\widetilde{\mathbf{h}}|^2 + \Re\left[\widetilde{\mathbf{h}}^H\,\widetilde{\mathbf{n}}\right]\right\}. \tag{3.59}$$

It is straightforward to show that this symbol detector actually yields the maximum likelihood (ML) symbol estimate, given the received signal model in (3.1), page 51.

3.5.1.2 Ideal MRC Error Probability Analysis for Uncorrelated Branches, based on Output SNR

For Rayleigh fading $\breve{\breve{\gamma}}_i$ can be shown to be exponentially distributed, i.e., [123, p. 19]

$$\text{pdf}(\breve{\breve{\gamma}}_i) = \begin{cases} 1/\breve{\breve{\Gamma}}_i \, e^{-\breve{\breve{\gamma}}_i/\breve{\breve{\Gamma}}_i} & , \quad \text{for } \breve{\breve{\gamma}}_i \geq 0, \\ 0 & , \quad \text{otherwise}, \end{cases} \tag{3.60}$$

where

$$\breve{\breve{\Gamma}}_i \stackrel{\triangle}{=} E\{\breve{\breve{\gamma}}_i\} = \frac{E_s}{N_0}\sigma^2_{\breve{h}_i}, \tag{3.61}$$

and m.g.f. [123, Table 2.2, p. 19]

$$M_{\breve{\breve{\gamma}}_i}(s) = \frac{1}{1 - s\breve{\breve{\Gamma}}_i}. \tag{3.62}$$

Consider the case of MPSK and uncorrelated branches that can have nonidentical variances. Since $\breve{\breve{\gamma}}$ satisfies (3.57) and $\breve{\breve{\gamma}}_i$, $i = 1 : L$, are independent, the procedure outlined in Section 3.4.1.1 at page 55 can be applied, and yields the following AEP expression [123, Section 9.2.3.2]

$$P_e = \frac{1}{\pi}\int_0^{\frac{M-1}{M}\pi} \prod_{i=1}^{L} \left(1 + \breve{\breve{\Gamma}}_i \frac{g_{\text{PSK}}}{\sin^2\phi}\right)^{-1} d\phi. \tag{3.63}$$

This same approach, along with corresponding m.g.f. formulas from [123, Table 9.1, p. 269], can yield AEP expressions for other modulations as well as for Ricean and Nakagami-*m* fading channels [123, Chapter 9]. Note, however, that in order to apply this approach for Nakagami-*m* fading *independent* (i.e., not merely uncorrelated) channel gains are required.

3.5.1.3 Particular Cases and Numerical Results

For $L = 1$, (3.63) reduces to (2.63), page 28, derived specifically for the SISO case. On the other hand, for L (independent and) identically distributed branches, i.e., when $\sigma^2_{\breve{h}_i} = \sigma^2_{\breve{h}}$, $\forall i = 1 : L$,

Eqn. (3.63) above becomes

$$P_e = \frac{1}{\pi}\int_0^{\frac{M-1}{M}\pi}\left(1+\breve{\bar{\Gamma}}\frac{g_{\text{PSK}}}{\sin^2\phi}\right)^{-L} d\phi, \tag{3.64}$$

where $\breve{\bar{\Gamma}} = \frac{E_s}{N_0}\sigma_{\tilde{h}}^2$ is the average SNR per symbol for each of the i.i.d. receiver branches. The average SNR per symbol for each of the i.i.d. receiver branches is $\gamma_b = \breve{\bar{\Gamma}}/\log_2 M$.

Recall from page 52 that we assume a Toeplitz structure for $\mathbf{R}_{\tilde{\mathbf{h}}}$. Furthermore, all numerical results shown hereafter are for $\sigma_{\tilde{h}_i}^2 = \sigma_{\tilde{h}}^2 = 1$, $i = \forall 1 : L$. Equal variance channel gains is a valid assumption for antenna arrays [35, Section 4.1.2, p. 49], but not for RAKE receivers. Nonetheless, although we will only show numerical results for equal-variance channel gains, our analytical results can readily produce results for other situations. Assuming identically distributed branches with $\sigma_{\tilde{h}}^2 = 1$, the average SNR per symbol for each of the receiver branches reduces to E_s/N_0, further denoted simply as *SNR per symbol.* Then, $\gamma_b = \frac{E_s}{N_0}\frac{1}{\log_2 M}$ is further denoted simply as *SNR per bit.*

Although the integration from (3.64) can be easily implemented with a desired degree of accuracy, an involved closed-form equivalent expression can also be derived — see Section 3.10.2.1, at page 112, Eqns. (3.155)–(3.157).

For BPSK transmitted signal and MRC of $L = 1 : 5$ independent and identically distributed (i.i.d.) branches Fig. 3.1 displays the AEP, computed using (3.64), vs. E_s/N_0, i.e., the SNR per symbol (or per bit because of BPSK modulation). These results show that, theoretically, communications systems employing ideal diversity combining can provide considerable performance gains over SISO systems. For instance, at a (raw, i.e., uncoded) error probability of 10^{-2}, 5-branch MRC yields about 15 dB gain over the single-antenna receiver. Note however that the diversity gain gradient decreases as the number of branches increases.

At large SNR values, the AEP from (3.63) can be approximated as

$$P_{e,\text{high SNR}} \approx \frac{1}{\pi}\prod_{i=1}^{L}\left(\breve{\bar{\Gamma}}_i\, g_{\text{PSK}}\right)^{-1}\int_0^{\frac{M-1}{M}\pi}\sin^{2L}\phi\, d\phi. \tag{3.65}$$

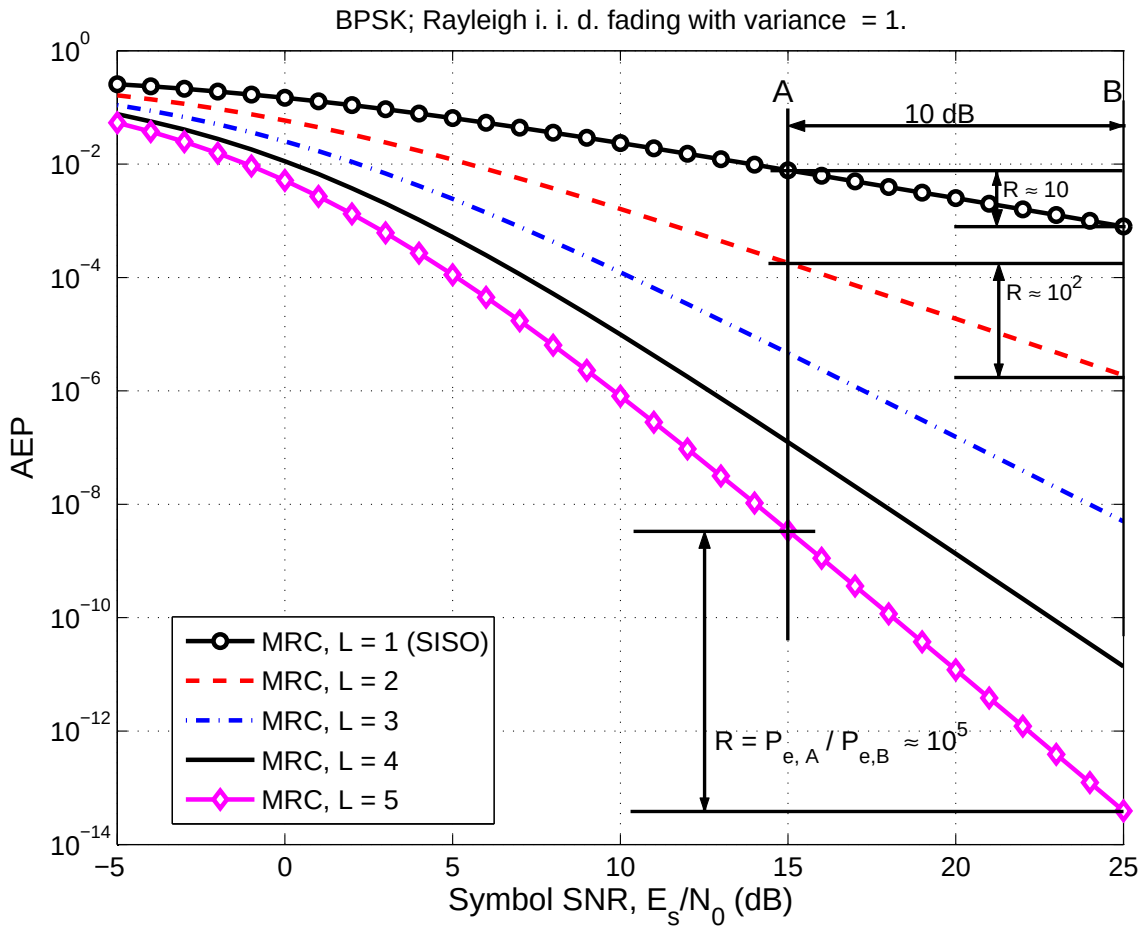

Figure 3.1. AEP vs. SNR per symbol (bit) for MRC with perfectly known channel for BPSK transmitted signal and Rayleigh i.i.d. fading branches with unit variance; the high-SNR slope stands for the diversity gain.

For BPSK, this can be written further as

$$P_{e,\text{BPSK, high SNR}} \approx \frac{(2L)!}{2^{2L+1}(L!)^2} \left[\frac{E_\text{s}}{N_0}\right]^{-L} \prod_{i=1}^{L} \left[\sigma^2_{\tilde{h}_i}\right]^{-1}. \tag{3.66}$$

The exponent of the SNR per symbol in AEP expressions is commonly referred to as *diversity order* [106, Section 5.2]. The AEP expression in (3.66) indicates a diversity order equal to the number of combined branches. Since

$$10\log_{10}\left[P_{e,\text{BPSK, high SNR}}\right] \propto -L \left[\frac{E_\text{s}}{N_0}\right]_{\text{in dB}}, \tag{3.67}$$

at large SNR values the AEP decreases by a factor of about 10^L when the SNR increases by 10 dB. This is confirmed in Fig. 3.1, where the horizontal distance between points A and B is 10 dB, and the error probability at point A is about 10^L times larger than at point B.

The expression from (3.63) can be generalized for Nakagami-*m* fading as [123, Table 9.1, p. 269]

$$P_e = \frac{1}{\pi}\int_0^{\frac{M-1}{M}\pi} \prod_{i=1}^{L} \left(1 + \frac{\breve{\bar{\Gamma}}_i}{m_i}\frac{g_\text{PSK}}{\sin^2\phi}\right)^{-m_i} d\phi, \tag{3.68}$$

which, for identically distributed branches, becomes

$$P_e = \frac{1}{\pi}\int_0^{\frac{M-1}{M}\pi} \left(1 + \frac{\breve{\bar{\Gamma}}}{m}\frac{g_\text{PSK}}{\sin^2\phi}\right)^{-mL} d\phi. \tag{3.69}$$

where $\breve{\bar{\Gamma}}$ is the common average SNR per symbol per branch. Fig. 3.2 describes the performance for QPSK transmitted signal and i.i.d. Nakagami-*m* fading branches with $m = 2$ and $\sigma^2_{\tilde{h}} = 1$.

Now let us consider the performance of MRC for an increasing number L of i.i.d. diversity branches but fixed $\text{tr}\left(\mathbf{R}_{\tilde{\mathbf{h}}}\right)$, as well as the reception performance for a non-fading AWGN channel with SNR per symbol equal to $\frac{E_\text{s}}{N_0}\text{tr}\left(\mathbf{R}_{\tilde{\mathbf{h}}}\right)$. For QPSK transmitted signal, Fig. 3.3 depicts:

- the AEP from (3.69) for MRC of i.i.d. Nakagami-*m* fading branches with $m = 2$, fixed $\text{tr}(\mathbf{R}_{\tilde{\mathbf{h}}}) = 1$, and $\sigma^2_{\tilde{h}} = \text{tr}(\mathbf{R}_{\tilde{\mathbf{h}}})/L$, for $L = 1:5$ branches, and

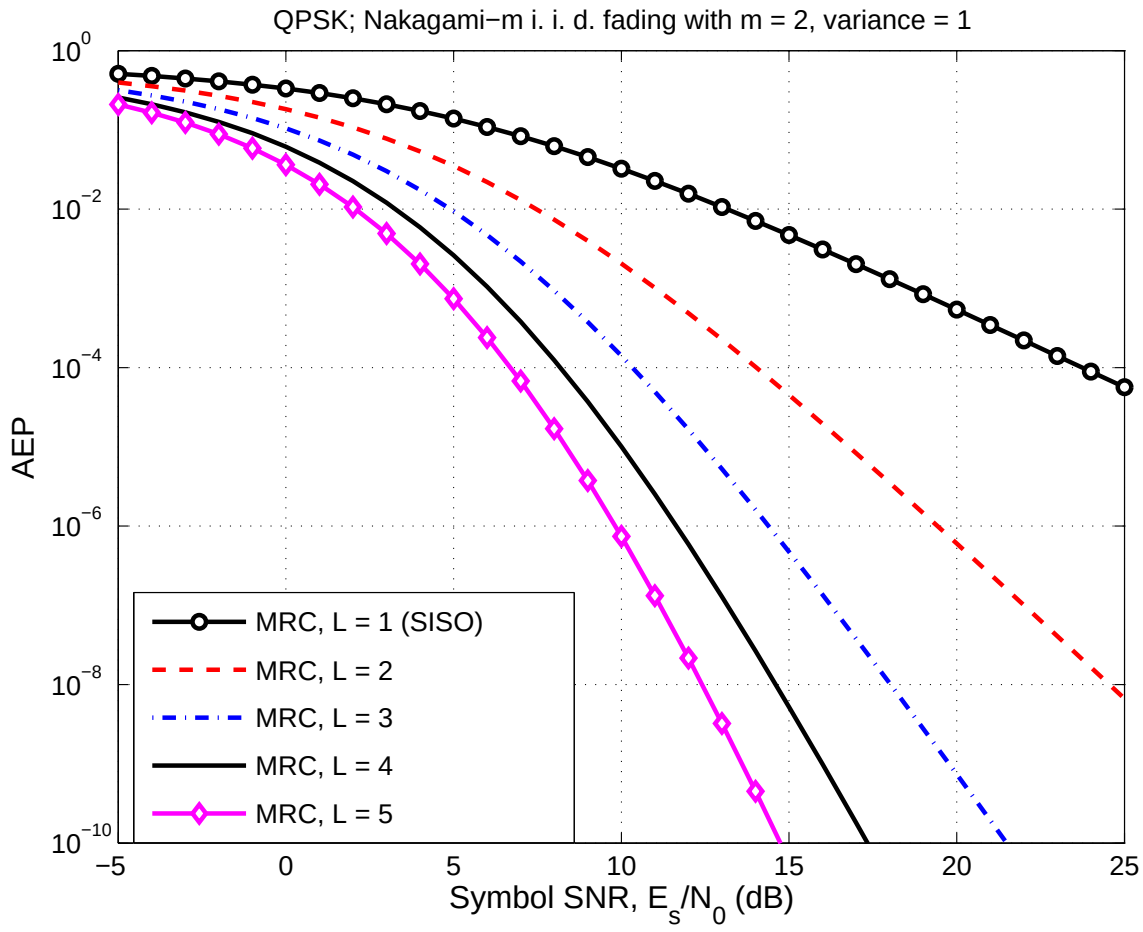

Figure 3.2. AEP vs. SNR per symbol for MRC with perfectly known channel for QPSK transmitted signal and Nakagami-*m* i.i.d. fading branches with $m = 2$ and unit variance.

- the AEP from (2.33), page 16, for non-fading AWGN channel with SNR per symbol equal to $\frac{E_s}{N_0}\,\mathrm{tr}(\mathbf{R}_{\tilde{\mathbf{h}}})$.

For the results shown in Fig. 3.4 the number of branches in MRC is $L = 1, 5, 9, 13, 17$. Notice that, for a fixed $\mathrm{tr}\left(\mathbf{R}_{\tilde{\mathbf{h}}}\right)$, the performance of MRC for an increasing number of i.i.d. fading branches approaches the performance of a non-fading AWGN channel with SNR per symbol $\frac{E_s}{N_0}\,\mathrm{tr}(\mathbf{R}_{\tilde{\mathbf{h}}})$. The explanation follows.

Given $\mathrm{tr}(\mathbf{R}_{\tilde{\mathbf{h}}})$ and i.i.d. Nakagami-*m* (and thus also for Rayleigh) fading, mathematical manipulations of (3.69) yield

$$\lim_{L\to\infty} P_e = \frac{1}{\pi}\int_0^{\frac{M-1}{M}\pi} \exp\left\{-\frac{E_s}{N_0}\,\mathrm{tr}\left(\mathbf{R}_{\tilde{\mathbf{h}}}\right)\,\frac{g_{\mathrm{PSK}}}{\sin^2\phi}\right\} d\phi, \tag{3.70}$$

which is independent of the Nakagami distribution parameter *m*, and, based on (2.33) at page 16, describes the performance for MPSK transmitted signal and non-fading AWGN channel with the SNR per symbol given by $\frac{E_s}{N_0}\,\mathrm{tr}\left(\mathbf{R}_{\tilde{\mathbf{h}}}\right)$. Thus, infinite-order diversity yields a nonfading channel [106, p. 102]. A similar result was obtained in [49, Eq. 20, p. 1857] using a stochastic majorization approach.

3.5.2 Ideal Maximum Average SNR Beamforming (BF)

In practice, received signals at different branches can be correlated. Insufficient antenna inter-element separation or limited scattering [106] in the vicinity of the receiver increases this correlation. RAKE receiver tap signals can also be fairly correlated [104, 123]. Branch correlation degrades MRC performance [34, 123]. When the inter-branch correlation is fairly high, maximum average SNR beamforming (BF) is usually employed [42, 43].

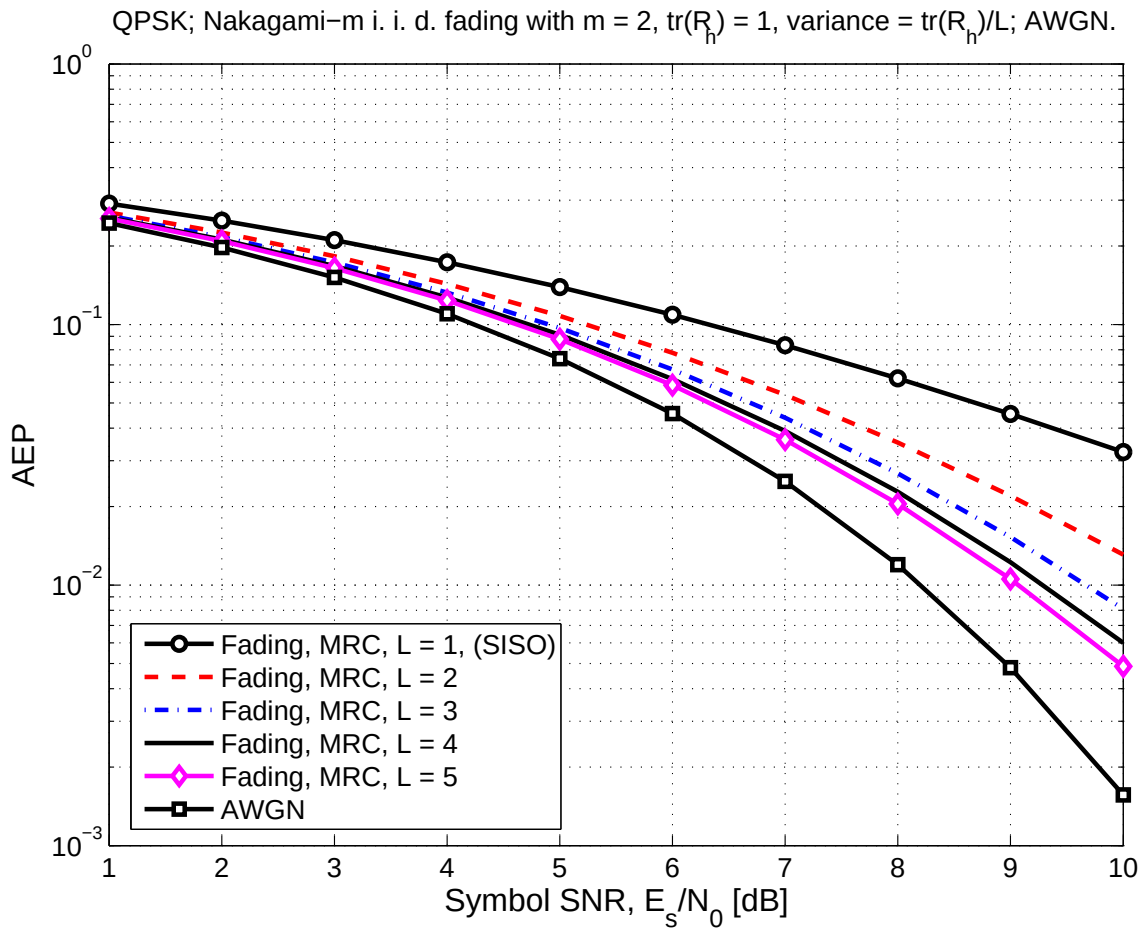

Figure 3.3. Performance of MRC with perfectly known channel for QPSK signal transmitted signal for i.i.d. Nakagami-*m* fading with $m = 2$, fixed $\mathrm{tr}(\mathbf{R}_{\tilde{\mathbf{h}}}) = 1$, and $\sigma^2_{\tilde{h}} = \mathrm{tr}(\mathbf{R}_{\tilde{\mathbf{h}}})/L$; Performance for non-fading AWGN channel with SNR per symbol $\frac{E_s}{N_0}\mathrm{tr}\left(\mathbf{R}_{\tilde{\mathbf{h}}}\right)$; $L = 1:5$.

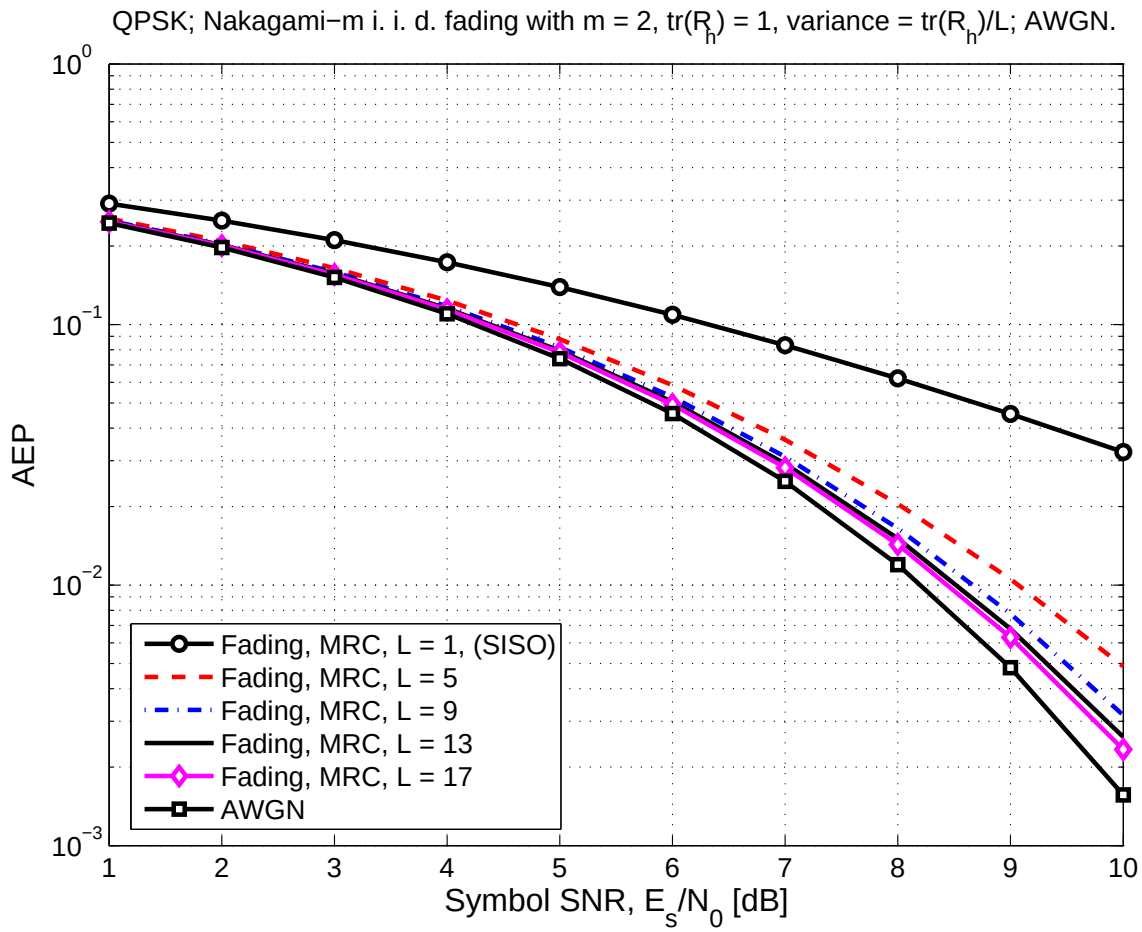

Figure 3.4. Performance for MRC with perfectly known channel for QPSK signal transmitted signal for i.i.d. Nakagami-*m* fading with $m = 2$, fixed $\mathrm{tr}(\mathbf{R}_{\tilde{\mathbf{h}}}) = 1$, and $\sigma^2_{\tilde{h}} = \mathrm{tr}(\mathbf{R}_{\tilde{\mathbf{h}}})/L$; Performance for non-fading AWGN channel with SNR per symbol $\frac{E_s}{N_0}\,\mathrm{tr}\left(\mathbf{R}_{\tilde{\mathbf{h}}}\right)$; $L = 1, 5, 9, 13, 17$.

3.5.2.1 Procedure

As opposed to MRC, in BF the goal is to optimize the average (over fading and noise) SNR, by appropriate combining of the received signal vector $\widetilde{\mathbf{y}}$ in (3.1) with a weight vector $\widetilde{\mathbf{w}}$ as in

$$\widetilde{\mathbf{w}}^H \widetilde{\mathbf{y}} = \sqrt{E_s}\, b\, \widetilde{\mathbf{w}}^H \widetilde{\mathbf{h}} + \widetilde{\mathbf{w}}^H \widetilde{\mathbf{n}}. \tag{3.71}$$

The combiner output power averaged over noise is

$$\begin{aligned} E\{|\widetilde{\mathbf{w}}^H \widetilde{\mathbf{y}}|^2\} &= E_s\, |b|^2\, |\widetilde{\mathbf{w}}^H \widetilde{\mathbf{h}}|^2 + E\{|\widetilde{\mathbf{w}}^H \widetilde{\mathbf{n}}|^2\} && (3.72)\\ &= E_s\, |b|^2\, |\widetilde{\mathbf{w}}^H \widetilde{\mathbf{h}}|^2 + N_0\, \widetilde{\mathbf{w}}^H \widetilde{\mathbf{w}}, && (3.73) \end{aligned}$$

which yields the instantaneous combiner output SNR as

$$\mathrm{SNR}(\widetilde{\mathbf{w}}) \stackrel{\triangle}{=} \frac{E_s}{N_0} \frac{|\widetilde{\mathbf{w}}^H \widetilde{\mathbf{h}}|^2}{\widetilde{\mathbf{w}}^H \widetilde{\mathbf{w}}}. \tag{3.74}$$

The combiner output power, averaging over noise and fading, is

$$\begin{aligned} E\{|\widetilde{\mathbf{w}}^H \widetilde{\mathbf{y}}|^2\} &= E_s\, |b|^2\, E\{|\widetilde{\mathbf{w}}^H \widetilde{\mathbf{h}}|^2\} + E\{|\widetilde{\mathbf{w}}^H \widetilde{\mathbf{n}}|^2\} && (3.75)\\ &= E_s\, \widetilde{\mathbf{w}}^H \mathbf{R}_{\widetilde{\mathbf{h}}} \widetilde{\mathbf{w}} + N_0\, \widetilde{\mathbf{w}}^H \widetilde{\mathbf{w}}, && (3.76) \end{aligned}$$

which yields the output average SNR as

$$\mathrm{SNR}_{\mathrm{avg}}(\widetilde{\mathbf{w}}) \stackrel{\triangle}{=} \frac{E_s}{N_0} \frac{\widetilde{\mathbf{w}}^H \mathbf{R}_{\widetilde{\mathbf{h}}} \widetilde{\mathbf{w}}}{\widetilde{\mathbf{w}}^H \widetilde{\mathbf{w}}}. \tag{3.77}$$

The second ratio in (3.77) is a Rayleigh quotient [64, 78] whose properties yield

$$\frac{E_s}{N_0}\, \lambda_L \le \mathrm{SNR}_{\mathrm{avg}}(\widetilde{\mathbf{w}}) \le \frac{E_s}{N_0}\, \lambda_1, \tag{3.78}$$

where the lower and upper bounds are achieved with $\widetilde{\mathbf{w}} \propto \mathbf{e}_L$ and $\widetilde{\mathbf{w}} \propto \mathbf{e}_1$, respectively. The latter choice thus represents maximum average SNR beamforming (BF).

Consider now the impact of branch decorrelation on BF performance, i.e., on

$$\max_{\widetilde{\mathbf{w}} \in C^L} \mathrm{SNR}_{\mathrm{avg}}(\widetilde{\mathbf{w}}) = \mathrm{SNR}_{\mathrm{avg}}(\mathbf{e}_1) = \frac{E_s}{N_0}\, \lambda_1. \tag{3.79}$$

Using Propositions 1 and 2 from page 54, we deduce that

$$\max_{\widetilde{\mathbf{w}}\in C^L} \mathrm{SNR}_{\mathrm{avg}}(\widetilde{\mathbf{w}}) \in \left[\frac{E_\mathrm{s}}{N_0}\frac{1}{L}\mathrm{tr}(\mathbf{R}_{\widetilde{\mathbf{h}}}), \quad \frac{E_\mathrm{s}}{N_0}\mathrm{tr}(\mathbf{R}_{\widetilde{\mathbf{h}}})\right], \tag{3.80}$$

where the lower and upper bounds are achieved for uncorrelated and coherent branches, respectively. If we denote as *array gain* the increase in average SNR over the SISO case [106, p. 91], since the average SNR for the ith branch is $\check{\bar{\Gamma}}_i \triangleq \frac{E_\mathrm{s}}{N_0}\sigma^2_{\tilde{h}_i}$, it follows that for L coherent branches, BF offers the maximum array gain of [88, p. 1283]

$$G_{A,\max}(L) = 10\log_{10} L \quad [\mathrm{dB}]. \tag{3.81}$$

3.5.2.2 BF Error Probability Analysis based on Output SNR

We now investigate the BF performance for MPSK transmitted signal and Rayleigh fading channel. If we substitute $\widetilde{\mathbf{w}}$ with $\mathbf{e}_1$ in the BF instantaneous SNR expression (3.74), and define the complex-valued random variable $h_1 \triangleq \mathbf{e}_1^H\widetilde{\mathbf{h}}$, which is zero-mean Gaussian, then $\mathrm{SNR}(\mathbf{e}_1)$ is given by

$$\gamma \triangleq \frac{E_\mathrm{s}}{N_0}|h_1|^2, \tag{3.82}$$

which is exponentially distributed [123, Table 2.2, p. 19], with average $\check{\Gamma}_1 \triangleq \frac{E_\mathrm{s}}{N_0}\lambda_1$.

Applying the analysis approach described in Section 3.4.1.1 at page 55, the following AEP expression is obtained for BF [125, p. 17]

$$P_e = \frac{1}{\pi}\int_0^{\frac{M-1}{M}\pi}\left(1+\check{\Gamma}_1\frac{g_{\mathrm{PSK}}}{\sin^2\phi}\right)^{-1}d\phi = \frac{1}{2}\left(1-\sqrt{\frac{\check{\Gamma}_1}{\check{\Gamma}_1+1}}\right). \tag{3.83}$$

To our knowledge, this expression has not been explicitly derived and used in previous research for BF performance evaluation. From (3.79) and (3.80) it follows that BF performance improves with higher branch correlations; it is best for coherent branches, i.e., when the signal arrives from a unique direction, and worst for uncorrelated branches, when the signal arrives

from many distinct directions. MRC is known to perform conversely. Nevertheless, since in practice the branch correlation varies, as described later in this work, due to variable azimuth angle spread [8], a more versatile approach, denoted maximal-ratio eigen-combining (MREC), was introduced and is described further below. MREC relies on the Karhunen-Loève Transform (KLT) [68], which is described next.

3.5.3 The Karhunen-Loève Transform (KLT)

Principal components analysis [52], which uses the Karhunen-Loève Transform (KLT) [68], has established itself in numerous areas [45] as a very effective approach to reduce complexity and improve performance. If a large number of correlated random variables are collected, post-KLT analysis is often considerably simpler [9, 50, 55, 91, 125, 128, 130], since the significant resulting random variables are uncorrelated and usually much fewer. Suitable post-KLT processing of the dominant eigen-modes can improve performance, e.g., in multi-branch wireless receivers [36, 47, 48, 76, 77, 125].

In the seminal work by Comon and Golub [45], numerical eigen-decomposition methods are compared in terms of accuracy, convergence speed, and complexity. The adaptive algorithm described in [45, Section V.G] possesses desirable convergence and tracking capabilities, as well as low complexity, i.e., $O(LN^2)$, where N is the number of eigen-modes of interest. Lower complexity algorithms have been proposed more recently, e.g., the projection approximation subspace tracking (PAST) [151], with complexity $O(LN)$.

In mobile scenarios correlation matrices vary slowly compared to channel fading [8, 36, 69, 130]. Hence, their eigen-decompositions would require infrequent updating, whose execution can thus be distributed over long intervals [1, Section 7.1.1].

3.5.4 Ideal Maximal-Ratio Eigen-Combining (MREC)

Ideal maximal-ratio eigen-combining (MREC) of order N, $1 \leq N \leq L$, consists of two steps:

(Step 1) The $L \times N$, full-column rank, matrix $\mathbf{E}_N \stackrel{\triangle}{=} [\mathbf{e}_1\, \mathbf{e}_2 \ldots \mathbf{e}_N]$ transforms the signal vector from (3.1) into

$$\mathbf{y} = \sqrt{E_s}\, b\, \mathbf{h} + \mathbf{n}, \tag{3.84}$$

where

$$\mathbf{y} \stackrel{\triangle}{=} \mathbf{E}_N^H\, \widetilde{\mathbf{y}}, \tag{3.85}$$

$$\mathbf{h} \stackrel{\triangle}{=} \mathbf{E}_N^H\, \widetilde{\mathbf{h}}, \tag{3.86}$$

$$\mathbf{n} \stackrel{\triangle}{=} \mathbf{E}_N^H\, \widetilde{\mathbf{n}}. \tag{3.87}$$

(Step 2) The elements of the transformed signal vector are linearly combined so as to maximize the instantaneous output SNR (i.e., the maximal-ratio criterion [34]) using

$$\mathbf{w}_{\text{MREC}} = \mathbf{h}. \tag{3.88}$$

Order-L MREC will be referred to as *full MREC*. Then, the following relation holds

$$\widetilde{\mathbf{h}} = \mathbf{E}_L\, \mathbf{h}. \tag{3.89}$$

The elements of the N-dimensional vector $\mathbf{y}$ are denoted as *eigenbranches*. They represent the inner products of the received signal vector, $\widetilde{\mathbf{y}}$, with eigenvectors corresponding to the N largest eigenvalues of $\mathbf{R}_{\widetilde{\mathbf{h}}}$, i.e.,

$$y_i \stackrel{\triangle}{=} \mathbf{e}_i^H\, \widetilde{\mathbf{y}} = \sqrt{E_s}\, b\, h_i + n_i, \tag{3.90}$$

where

$$h_i \stackrel{\triangle}{=} \mathbf{e}_i^H\, \widetilde{\mathbf{h}}, \tag{3.91}$$

$$n_i \triangleq \mathbf{e}_i^H \widetilde{\mathbf{n}}. \tag{3.92}$$

The components of $\mathbf{h}$ are further referred to as channel *eigengains*. They have zero-mean, variances given by

$$\sigma_{h_i}^2 \triangleq E\{|h_i|^2\} = \mathbf{e}_i^H E\{\widetilde{\mathbf{h}}\widetilde{\mathbf{h}}^H\}\mathbf{e}_i = \mathbf{e}_i^H \left[\sum_{l=1}^{N} \lambda_l \mathbf{e}_l \mathbf{e}_l^H\right] \mathbf{e}_i = \sum_{l=1}^{N} \lambda_l \mathbf{e}_i^H \mathbf{e}_l \mathbf{e}_l^H \mathbf{e}_i = \lambda_i, \tag{3.93}$$

and are mutually uncorrelated, because

$$\begin{aligned} E\{h_i h_j^*\} &\triangleq \mathbf{e}_i^H E\{\widetilde{\mathbf{h}}\widetilde{\mathbf{h}}^H\}\mathbf{e}_j = \mathbf{e}_i^H \mathbf{R}_{\widetilde{\mathbf{h}}} \mathbf{e}_j = \mathbf{e}_i^H \left(\sum_{l=1}^{N} \lambda_l \mathbf{e}_l \mathbf{e}_l^H\right) \mathbf{e}_j \\ &= \sum_{l=1}^{N} \lambda_l \mathbf{e}_i^H \mathbf{e}_l \mathbf{e}_l^H \mathbf{e}_j = 0, \quad \forall i \neq j. \end{aligned} \tag{3.94}$$

Thus,

$$\mathbf{R}_{\mathbf{h}} \triangleq E\{\mathbf{h}\mathbf{h}^H\} = \mathbf{\Lambda}_N = \mathrm{diag}\{\lambda_i\}_{i=1}^N, \tag{3.95}$$

for any channel gain distribution [77]. Initial assumptions of Rayleigh fading and zero-mean, complex Gaussian white noise yield

$$\mathbf{h} \sim \mathscr{N}_c(\mathbf{0}, \mathbf{\Lambda}_N), \tag{3.96}$$

so that the eigengains are independent, and

$$\mathbf{n} \sim \mathscr{N}_c(\mathbf{0}, N_0 \mathbf{I}_N). \tag{3.97}$$

so that the transformed noise is temporally and spatially white.

The transformation leading to (3.84) is the Karhunen-Loève Transform (KLT) [68, 77]. Of all possible transforms, the KLT is the optimum (in the least-squares sense) decorrelating transform, packing the largest amount of energy from the original, L-dimensional, signal vector, $\widetilde{\mathbf{y}}$, into the N-dimensional vector $\mathbf{y}$ [68, Section 2.5.7, p. 67], which is desirable for dimension reduction.

Hereafter, the long-term channel parameters $\mathbf{R}_{\widetilde{\mathbf{h}}}$, $\mathbf{\Lambda}_L$, and $\mathbf{E}_L$ are assumed perfectly known because, in practice, enough independent channel samples would be available for an accurate estimation [36]. In this section we also assume that the channel gains are perfectly known.

Then, recovery of a BPSK transmitted symbol, for instance, is attempted with

$$\widehat{b}_{\text{MREC}} = \text{sign}\{\Re\left[\mathbf{w}_{\text{MREC}}^H\,\mathbf{y}\right]\} = \text{sign}\{\Re\left[\mathbf{h}^H\,\mathbf{y}\right]\} \tag{3.98}$$

$$= \text{sign}\{\sqrt{E_\text{s}}\,b\,|\mathbf{h}|^2 + \Re\left[\mathbf{h}^H\,\mathbf{n}\right]\}. \tag{3.99}$$

It is straightforward to show that this symbol detector is actually the maximum likelihood (ML) symbol estimate for the model in (3.84) of the transformed received signal.

3.5.4.1 Ideal-MREC Error Probability Analysis based on Output SNR

The instantaneous SNR of the ith eigenbranch — see (3.90) — is given by

$$\check{\gamma}_i \stackrel{\triangle}{=} \frac{E_\text{s}}{N_0}|h_i|^2, \quad i = 1:N, \tag{3.100}$$

which can be shown to be exponentially distributed, i.e., with p.d.f. [123, p. 19]

$$\text{pdf}(\check{\gamma}_i) = \begin{cases} \frac{1}{\check{\Gamma}_i}\,e^{-\check{\gamma}_i/\check{\Gamma}_i} & , \quad \text{for } \check{\gamma}_i \geq 0, \\ 0 & , \quad \text{otherwise}, \end{cases} \tag{3.101}$$

where

$$\check{\Gamma}_i \stackrel{\triangle}{=} E\{\check{\gamma}_i\} = \frac{E_\text{s}}{N_0}\sigma_{h_i}^2 = \frac{E_\text{s}}{N_0}\lambda_i, \tag{3.102}$$

and m.g.f. [123, Table 2.2, p. 19]

$$M_{\check{\gamma}_i}(s) = \frac{1}{1 - s\check{\Gamma}_i}. \tag{3.103}$$

As in Section 3.5.1.1, page 61, it can be shown that $\mathbf{w}_{\text{MREC}}$ from (3.88) maximizes instantaneous output SNR, i.e., [34]

$$\check{\gamma} = \sum_{i=1}^{N} \check{\gamma}_i, \tag{3.104}$$

justifying the title of "maximal-ratio eigen-combining" [125, 127–130].

Since the eigengains are uncorrelated (this holds regardless of the fading distribution), and since $\check{\gamma}$ satisfies (3.104), the procedure for finding the AEP which was outlined in Section 3.4.1.1, at page 55, can be applied to yield a nonclosed-form, yet simple, finite-limit, AEP expression for MPSK, Rayleigh fading, and ideal MREC as

$$P_e = \frac{1}{\pi} \int_0^{\frac{M-1}{M}\pi} \prod_{i=1}^{N} \left(1 + \check{\Gamma}_i \frac{g_{\text{PSK}}}{\sin^2 \phi} \right)^{-1} d\phi. \tag{3.105}$$

For $L = 1$ the SIMO system reduces to a SISO system, and then the MREC AEP expression (3.105) reduces to the SISO AEP expression, i.e., (3.64), on page 64, written for $L = 1$, and also (2.63), on page 28. Furthermore, BF and order-1 MREC coincide, as can be deduced from their definitions. Then the ideal-MREC AEP expression (3.105), written for $N = 1$, reduces to the ideal-BF AEP expression (3.83), at page 72, as expected.

Let us consider a SISO system with unit-variance channel gain. Let us also consider a 3-branch MREC-based receiver for two cases:

- fully correlated (coherent) channel gains, i.e., the first row and the spectrum of $\mathbf{R}_{\tilde{\mathbf{h}}}$ are given, respectively, by $[1 \quad 1 \quad 1]$ (this implies that all channel gains have unit variance) and $\lambda(\mathbf{R}_{\tilde{\mathbf{h}}}) = \{3, 0, 0\}$;

- correlated gains, with first row and spectrum of $\mathbf{R}_{\tilde{\mathbf{h}}}$ given, respectively, by $[1.\ 0.87\ 0.62]$ (this implies that all channel gains have unit variance; recall from page 52 that we assume a Toeplitz structure for $\mathbf{R}_{\tilde{\mathbf{h}}}$) and $\lambda(\mathbf{R}_{\tilde{\mathbf{h}}}) = \{2.5884, 0.3732, 0.0384\}$.

For QPSK and ideal combining the performance for these cases is depicted in Fig. 3.5 vs. the SNR per bit, which was defined on page 64.

Note from Fig. 3.5 that, for coherent branches, MREC of any order yields the same performance as BF (i.e., order-1 MREC), since potential diversity gain is unavailable. Note also that,

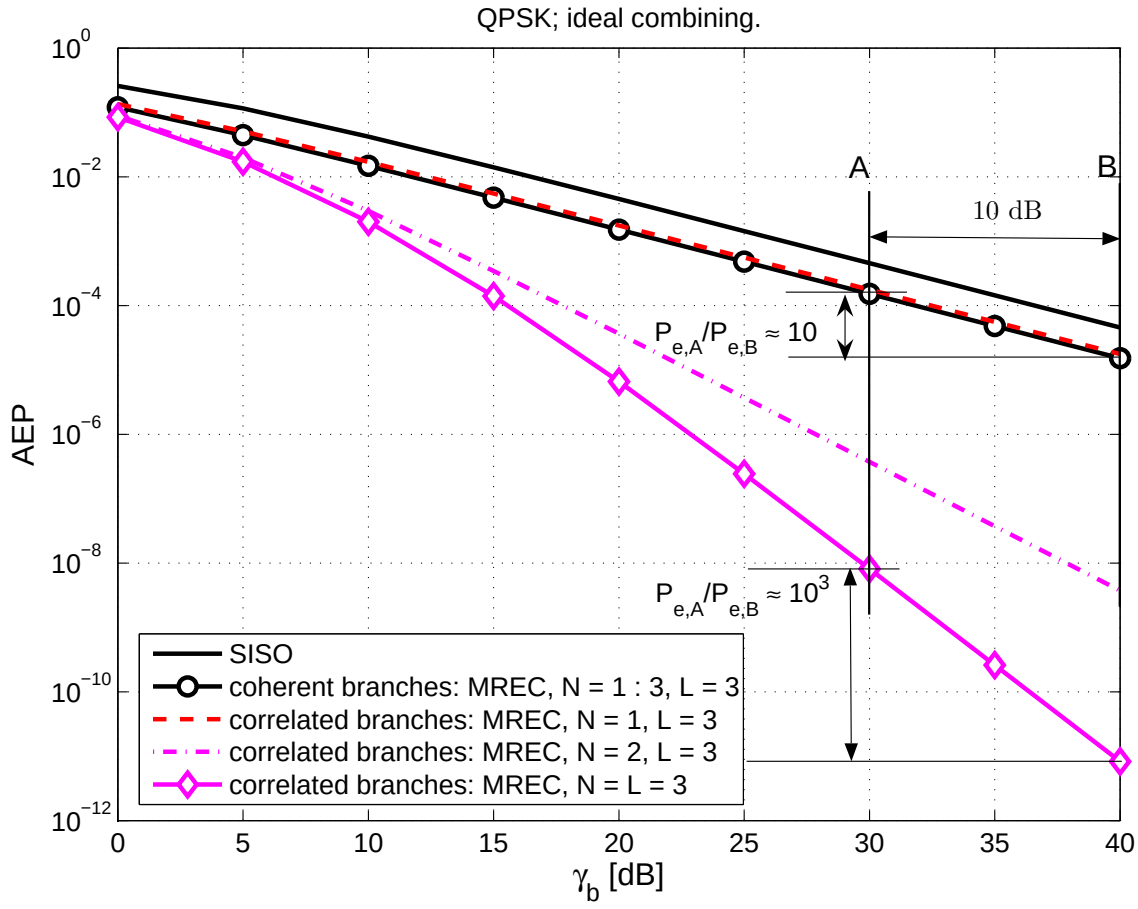

Figure 3.5. AEP vs. SNR per bit, computed for QPSK and perfectly known channel, using (3.105), for a SISO system with unit-variance channel gain, as well as a 3-branch MREC-based SIMO system, for coherent branches, i.e., $\lambda(\mathbf{R}_{\tilde{\mathbf{h}}}) = \{3, 0, 0\}$, and for correlated branches, when $\lambda(\mathbf{R}_{\tilde{\mathbf{h}}}) = \{2.5884, 0.3732, 0.0384\}$.

compared to the SISO case, BF with L branches provides maximum possible array gain [88, p. 1283] of

$$G_{\text{A,max}} \stackrel{\triangle}{=} 10\log_{10} L, \tag{3.106}$$

for coherent branches, which is about 4.8 dB for $L = 3$, at the price of higher receiver complexity. Further, SISO and BF plots are essentially parallel, and the slope reflects a unitary diversity order. As a rule-of-thumb for coherent channel gains, BF performance can readily be deduced by shifting the SISO AEP plot to the left by $10\log_{10} L$ dB.

Fig. 3.5 indicates that, when switching to the case of correlated channel gains described above, BF performance remains largely unaffected. As the correlation decreases further, SISO and BF AEP plots will remain parallel, but channel gain non-coherence will lead to lower array gain, $G_{\text{a}} < G_{\text{A,max}}$, and BF performance will approaches SISO performance.

On the other hand, Fig. 3.5 indicates that for the case of correlated branches described above, MREC with more than $N = 2$ eigenbranches can yield much lower AEP than SISO or BF, due to diversity gain, which yields a steeper slope for the AEP-vs.-SNR plots. Note that order-2 and full MREC yield diversity orders close to 2 and 3, respectively, i.e., as much as MRC would yield with $L = 2, 3$ uncorrelated branches.

For the same case of correlated channel gains, Fig. 3.6 displays for QPSK, the error rates obtained by simulation, and from analysis — see (3.105) — for the SIS/MO systems. These results indicate close agreement between simulation and analysis.

3.5.4.2 Ideal MRC and Full MREC are Performance-Equivalent

Fig. 3.6 also indicates that the performance of MRC, evaluated by simulation, coincides with that of full MREC, evaluated by simulation and by using (3.105), page 77. Recall that this is the case of correlated channel gains. The equivalence of ideal MRC and full MREC was actually demonstrated in [50] based on the equality of the corresponding symbol-detection

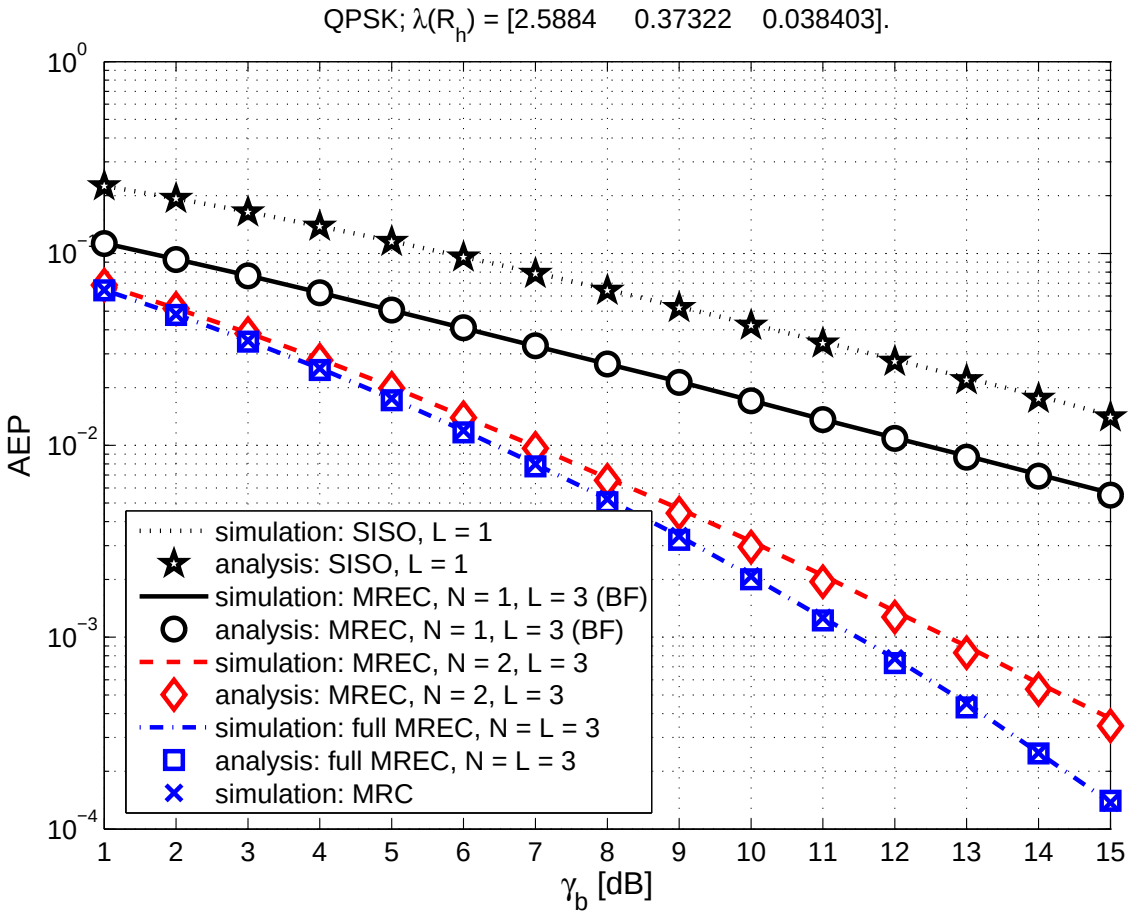

Figure 3.6. Symbol detection performance, for QPSK transmitted symbols, from simulation and (3.105), for SISO and ideal MREC, BF, MRC with $L = 3$ correlated branches, with $\mathbf{R}_{\tilde{\mathbf{h}}}$ spectrum given by $\lambda(\mathbf{R}_{\tilde{\mathbf{h}}}) = \{2.5884, 0.3732, 0.0384\}$.

SNRs. Hence, (3.105), on page 77, with $N = L$, is also an AEP expression for MPSK, Rayleigh fading, and ideal MRC, even when the branches are correlated or unbalanced, i.e., they have distinct variances. On the other hand, the claim made in [55] that a similar performance-equivalence holds for selection combining was disproved (also for equal gain combining) in [91].

Note further that for low SNR in this scenario with $L = 3$ branches with significant correlation, MRC-like performance is possible with order-2 MREC. In the remainder of this work we will evaluate MREC, as superset of MRC and BF, for lower-complexity adaptive receivers in space- and/or frequency-selective channels.

3.5.4.3 Ideal MRC Performs Best/Worst for Uncorrelated/Coherent Channel Gains

In Section 3.5.2.2 at page 72 it was indicated that ideal BF performs best for coherent channel gains, and worst for uncorrelated channel gains. The reverse can be proved for ideal MRC by using (3.105) on page 77, with $N = L$.

3.6 Vector-Channel Estimation using Pilot-Symbol-Aided Modulation (PSAM) and Interpolation

Channel knowledge is imperfect in practice. A simple approach, based on PSAM and interpolation, was described for SISO systems in Section 2.5 on page 33. The SINC PSAM (data-independent, simple, suboptimum, with poor performance at low SNR) and MMSE PSAM (data-dependent, complex, optimum) estimation methods described in Section 2.5 are now generalized for vector channel, and will be employed later for numerical evaluations.

Table 3.1. Interpolation filters for eigenbranch estimation

Interpolation Method	Interpolation Vector
SINC	$[\mathbf{v}_i(m_s)]_t = \mathrm{sinc}(\frac{m_s}{M_s} - t)\frac{\cos[\pi\beta(\frac{m_s}{M_s}-t)]}{1-[2\beta(\frac{m_s}{M_s}-t)]^2} = [\mathbf{v}(m_s)]_t$
MMSE	$\mathbf{v}_i(m_s) = \boldsymbol{\Phi}_i{}^{-1}\boldsymbol{\phi}_i(m_s)$

3.6.1 SINC and MMSE PSAM for MREC

Since the N eigenbranches are independent, their eigengains can be estimated separately. This can significantly reduce complexity for MREC compared to MRC. Drawing on the derivations from Section 2.5, at position $m_\mathrm{s} = 1 : M_\mathrm{s}$ in the currently detected slot of symbols, the estimator of the ith eigenbranch is

$$g_i(0, m_s) = \mathbf{v}_i{}^H(m_s)\,\mathbf{r}_i, \tag{3.107}$$

where $\mathbf{v}_i(m_s)$ is the interpolation filter, and

$$\mathbf{r}_i \stackrel{\triangle}{=} \frac{1}{\sqrt{E_\mathrm{p}}\,b_\mathrm{p}}\,[y_i(-T_1,0)\;y_i\;(-T_1+1,0)\;\ldots\;y_i(0,0)\;\ldots y_i(T_2-1,0)\;y_i(T_2,0)]^\mathrm{T}, \tag{3.108}$$

with

$$y_i(t,0) = \sqrt{E_\mathrm{p}}\;b_\mathrm{p}\;h_i(t,0) + n_i(t,0), \quad t = -T_1 : T_2, \tag{3.109}$$

Table 3.1 provides the interpolation vectors for SINC and MMSE PSAM. The elements of the $T \times T$ matrix $\boldsymbol{\Phi}_i \stackrel{\triangle}{=} E\{\mathbf{r}_i\,\mathbf{r}_i^H\}$, and of the $T \times 1$ vector $\boldsymbol{\phi}_i(m_s) \stackrel{\triangle}{=} E\{\mathbf{r}_i\,h_i^*(0,m_s)\}$ are expressed for Jakes' model of temporal correlation [75] in Table 3.2. Table 3.3 expresses correlations required later in analytical and numerical developments.

Table 3.2. Elements of $\boldsymbol{\Phi}_i$ and $\boldsymbol{\phi}_i(m_s)$, for eigenbranch estimation; $t_1, t_2, t = -T_1 : T_2$

$[\boldsymbol{\Phi}_i]_{t_1+T_1+1,t_2+T_1+1}$	$\lambda_i \, J_0\left(2\pi f_{\mathrm{m}} \lvert t_1 - t_2 \rvert M_s\right) + \frac{N_0}{E_{\mathrm{p}} \lvert b_{\mathrm{p}} \rvert^2} \delta_{t_1,t_2}$
$[\boldsymbol{\phi}_i(m_s)]_{t+T_1+1}$	$\lambda_i \, J_0\left(2\pi f_{\mathrm{m}} \lvert t M_s - m_s \rvert\right)$

Table 3.3. Correlations for eigenbranch estimation

	$g_i(0,m_s) = \mathbf{v}_i{}^H(m_s)\,\mathbf{r}_i, \forall \mathbf{v}_i$	SINC PSAM	MMSE PSAM
$\sigma^2_{h_i g_i}(m_s)$	$\boldsymbol{\phi}_i{}^H(m_s)\,\mathbf{v}_i(m_s)$	$\boldsymbol{\phi}_i^H(m_s)\,\mathbf{v}(m_s)$	$\boldsymbol{\phi}_i^H(m_s)\boldsymbol{\Phi}_i{}^{-1}\boldsymbol{\phi}_i(m_s)$
$\sigma^2_{g_i}(m_s)$	$\mathbf{v}_i{}^H(m_s)\boldsymbol{\Phi}_i\mathbf{v}_i(m_s)$	$\mathbf{v}(m_s)^H\boldsymbol{\Phi}_i\mathbf{v}(m_s)$	$\boldsymbol{\phi}_i^H(m_s)\boldsymbol{\Phi}_i{}^{-1}\boldsymbol{\phi}_i(m_s)$

3.6.2 SINC and MMSE PSAM for MRC

For MMSE PSAM when the branches are uncorrelated, and for SINC PSAM regardless of the branch correlation, we can estimate each of the L channel gains separately, as

$$\widetilde{g}_i(0,m_s) = \widetilde{\mathbf{v}}_i^H(m_s)\widetilde{\mathbf{r}}_i, \tag{3.110}$$

where $\widetilde{\mathbf{v}}_i(m_s)$ is the interpolation filter, described in Table 3.4, and

$$\widetilde{\mathbf{r}}_i \stackrel{\triangle}{=} \frac{1}{\sqrt{E_{\mathrm{p}}}\,b_{\mathrm{p}}}\left[\widetilde{y}_i(-T_1,0)\ \widetilde{y}_i\ (-T_1+1,0)\ \ldots\ \widetilde{y}_i(0,0)\ \ldots \widetilde{y}_i(T_2-1,0)\ \widetilde{y}_i(T_2,0)\right]^{\mathrm{T}}, \tag{3.111}$$

with

$$\widetilde{y}_i(t,0) = \sqrt{E_{\mathrm{p}}}\,b_{\mathrm{p}}\,\widetilde{h}_i(t,0) + \widetilde{n}_i(t,0), \quad t = -T_1 : T_2. \tag{3.112}$$

The elements of the $T \times T$ matrix $\widetilde{\boldsymbol{\Phi}}_i \stackrel{\triangle}{=} E\{\widetilde{\mathbf{r}}_i\,\widetilde{\mathbf{r}}_i^H\}$ and of the $T \times 1$ vector $\widetilde{\boldsymbol{\phi}}_i(m_s) \stackrel{\triangle}{=} E\{\widetilde{\mathbf{r}}_i\widetilde{h}_i^*(0,m_s)\}$ are expressed for Jakes' model of temporal correlation [75] in Table 3.5. Table 3.6 expresses the correlations which will be later required in analytical and numerical developments.

For the more general situation in which the channel gains may be correlated, MMSE estimation is done as follows [28]: given

$$\widetilde{\mathbf{g}}(0,m_{\mathrm{s}}) = \widetilde{\mathbf{G}}^H\widetilde{\mathbf{y}}_{\mathrm{p}}, \tag{3.113}$$

Table 3.4. Interpolation filters for branch estimation

Interpolation Method	Interpolation Vector
SINC	$[\widetilde{\mathbf{v}}_i(m_s)]_t = \text{sinc}(\frac{m_s}{M_s} - t) \frac{\cos[\pi\beta(\frac{m_s}{M_s} - t)]}{1 - [2\beta(\frac{m_s}{M_s} - t)]^2} = [\widetilde{\mathbf{v}}(m_s)]_t$
MMSE (uncorrelated branches)	$\widetilde{\mathbf{v}}_i(m_s) = \widetilde{\mathbf{\Phi}}_i^{-1} \widetilde{\boldsymbol{\phi}}_i(m_s)$

Table 3.5. Elements of $\widetilde{\mathbf{\Phi}}_i$ and $\widetilde{\boldsymbol{\phi}}_i(m_s)$, for branch estimation; $t_1, t_2, t = -T_1 : T_2$

$\left[\widetilde{\mathbf{\Phi}}_i\right]_{t_1+T_1+1, t_2+T_1+1}$	$\sigma^2_{\widetilde{h}_i} J_0(2\pi f_\text{m} \lvert t_1 - t_2 \rvert M_s) + \frac{N_0}{E_\text{p} \lvert b_\text{p} \rvert^2} \delta_{t_1,t_2}$
$\left[\widetilde{\boldsymbol{\phi}}_i(m_s)\right]_{t+T_1+1}$	$\sigma^2_{\widetilde{h}_i} J_0(2\pi f_\text{m} \lvert tM_s - m_s \rvert)$

Table 3.6. Correlations for branch estimation

	$\widetilde{g}_i(0, m_s) = \widetilde{\mathbf{v}}_i^H(m_s) \widetilde{\mathbf{r}}_i, \forall \widetilde{\mathbf{v}}_i$	SINC PSAM	MMSE PSAM
$\sigma^2_{\widetilde{h}_i \widetilde{g}_i}(m_s)$	$\widetilde{\boldsymbol{\phi}}_i^H(m_s) \widetilde{\mathbf{v}}_i(m_s)$	$\widetilde{\boldsymbol{\phi}}_i^H(m_s) \widetilde{\mathbf{v}}(m_s)$	$\widetilde{\boldsymbol{\phi}}_i^H(m_s) \widetilde{\mathbf{\Phi}}_i^{-1} \widetilde{\boldsymbol{\phi}}_i(m_s)$
$\sigma^2_{\widetilde{g}_i}(m_s)$	$\widetilde{\mathbf{v}}_i^H(m_s) \widetilde{\mathbf{\Phi}}_i \widetilde{\mathbf{v}}_i(m_s)$	$\widetilde{\mathbf{v}}(m_s)^H \widetilde{\mathbf{\Phi}}_i \widetilde{\mathbf{v}}(m_s)$	$\widetilde{\boldsymbol{\phi}}_i^H(m_s) \widetilde{\mathbf{\Phi}}_i^{-1} \widetilde{\boldsymbol{\phi}}_i(m_s)$

where

$$\widetilde{\mathbf{y}}_\text{p} \stackrel{\triangle}{=} \left[\widetilde{\mathbf{y}}^\text{T}(-T_1, 0) \quad \widetilde{\mathbf{y}}^\text{T}(-T_1+1, 0) \quad \cdots \quad \widetilde{\mathbf{y}}^\text{T}(T_2-1, 0) \, \widetilde{\mathbf{y}}^\text{T}(T_2, 0)\right]^\text{T}, \tag{3.114}$$

is an LT-dimensional column vector formed with the L-dimensional pilot samples, find

$$arg \min_{\widetilde{G} \in \mathbb{C}^{L \times L}} E\left\{ \left\| \widetilde{\mathbf{h}}(0, m_\text{s}) - \widetilde{\mathbf{g}}(0, m_\text{s}) \right\|^2 \right\}. \tag{3.115}$$

The solution is the well-known Wiener filter, described by [28]

$$\widetilde{\mathbf{G}}_\text{opt}(m_\text{s}) = \mathbf{R}^{-1}_{\widetilde{\mathbf{y}}_\text{p}} \mathbf{R}_{\widetilde{\mathbf{y}}_\text{p} \widetilde{\mathbf{h}}}(m_\text{s}), \tag{3.116}$$

where

$$\mathbf{R}_{\widetilde{\mathbf{y}}_\text{p}} \stackrel{\triangle}{=} E\left\{\widetilde{\mathbf{y}}_\text{p} \widetilde{\mathbf{y}}_\text{p}^H\right\} = E_\text{p} \lvert b_\text{p} \rvert^2 \left[\mathbf{Q} \otimes \mathbf{R}_{\widetilde{\mathbf{h}}}\right] + N_0 \mathbf{I}_{LT}, \text{ is } LT \times LT, \tag{3.117}$$

$$[\mathbf{Q}]_{t_1+T_1+1, t_2+T_1+1} = J_0(2\pi f_\text{m} \lvert t_1 - t_2 \rvert M_s); t_1, t_2 = -T_1 : T_2, \text{ is } T \times T, \tag{3.118}$$

$$\mathbf{R}_{\widetilde{\mathbf{y}}_\mathrm{p}\widetilde{\mathbf{h}}}(m_\mathrm{s}) \triangleq E\left\{\widetilde{\mathbf{y}}_\mathrm{p}\widetilde{\mathbf{h}}^H(0,m_\mathrm{s})\right\} = \sqrt{E_\mathrm{p}}\,b_\mathrm{p}\left[\mathbf{q}(m_\mathrm{s})\otimes\mathbf{R}_{\widetilde{\mathbf{h}}}\right], \text{ is } LT\times L, \quad (3.119)$$

$$[\mathbf{q}(m_\mathrm{s})]_{t+T_1+1} = J_0\left(2\pi f_\mathrm{m}\left|tM_s - m_s\right|\right); t = -T_1 : T_2, \text{ is } T\times 1, \quad (3.120)$$

and the symbol $\otimes$ stands for the Kronecker product [94, pp. 3, 19]. The above expressions were obtained using the fact that temporal and spatial correlations are separable [101, Appendix A.2, pp. 158 – 159] for our channel model, i.e., $\forall t_1, t_2 = -T_1 : T_2,\ i, j = 1 : L$,

$$E\{\widetilde{h}_i(t_1)\widetilde{h}_j^*(t_2)\} = E\{\widetilde{h}_i(t_1)\widetilde{h}_i^*(t_2)\}\,E\{\widetilde{h}_i(t_1)\widetilde{h}_j^*(t_1)\} = J_0\left(2\pi f_\mathrm{m}\left|t_1 - t_2\right|M_s\right)\left(\mathbf{R}_{\widetilde{\mathbf{h}}}\right)_{ij}. \quad (3.121)$$

To conclude this section, note that the channel vectors before and after the KLT, and their respective SINC or MMSE estimators are jointly Gaussian [21, 58, 95, 113, 115].

3.7 Combining Methods for Imperfectly Known Channel

3.7.1 Optimum Eigen-/Combining — Exact MREC, MRC, BF

For zero-mean, jointly-Gaussian $\mathbf{h}$ and $\mathbf{g}$, which is a common assumption also found in [21, 58, 95, 113, 115] since the estimates are obtained from pilot samples, we have that, given $\mathbf{g}$, $\mathbf{h} \sim \mathcal{N}_c(\mathbf{m}, \mathbf{R_e})$, where [81, Appendix 15B, p. 562]

$$\mathbf{m} \triangleq E\{\mathbf{h}|\mathbf{g}\} = E\{\mathbf{h}\mathbf{g}^H\}\left[E\{\mathbf{g}\mathbf{g}^H\}\right]^{-1}\mathbf{g}, \quad (3.122)$$

$$\mathbf{R_e} \triangleq E\{(\mathbf{h}-\mathbf{m})(\mathbf{h}-\mathbf{m})^H|\mathbf{g}\} = \mathbf{R_h} - E\{\mathbf{h}\mathbf{g}^H\}\left[E\{\mathbf{g}\mathbf{g}^H\}\right]^{-1}E\{\mathbf{g}\mathbf{h}^H\}. \quad (3.123)$$

Then, we can write the eigengain vector, in terms of its estimate, as

$$\mathbf{h} = \mathbf{m} + \mathbf{e}, \quad \text{with} \quad \mathbf{e} \sim \mathcal{N}_c(\mathbf{0}, \mathbf{R_e}). \quad (3.124)$$

It can readily be shown that $\mathbf{m}$ and $\mathbf{e}$ are uncorrelated. Substituting (3.124) in the original received signal vector model from (3.84), on page 74, we obtain

$$\mathbf{y} = \sqrt{E_\mathrm{s}}\,b\,\mathbf{m} + \boldsymbol{\nu} \sim \mathcal{N}_c(\sqrt{E_\mathrm{s}}\,b\,\mathbf{m}, \mathbf{R}_{\boldsymbol{\nu}}), \quad (3.125)$$

where, to facilitate subsequent analysis, the channel estimation error effects have been compounded with the receiver noise into the new noise vector

$$\boldsymbol{\nu} \stackrel{\triangle}{=} \sqrt{E_s}\, b\, \mathbf{e} + \mathbf{n} \tag{3.126}$$

whose correlation matrix is given by

$$\mathbf{R}_{\boldsymbol{\nu}} \stackrel{\triangle}{=} E\{\boldsymbol{\nu}\boldsymbol{\nu}^H\} = E_s \mathbf{R}_{\mathbf{e}} + N_0 \mathbf{I}_N, \tag{3.127}$$

for MPSK transmitted symbols.

Maximum-likelihood detection of the transmitted symbol b for the signal model in (3.125) employs the (N-dimensional) eigen-combiner

$$\mathbf{w} = \mathbf{R}_{\boldsymbol{\nu}}^{-1} \mathbf{m}. \tag{3.128}$$

The corresponding symbol decision variable is

$$\mathbf{m}^H \mathbf{R}_{\boldsymbol{\nu}}^{-1} \mathbf{y} = \sqrt{E_s}\, b\, \mathbf{m}^H \mathbf{R}_{\boldsymbol{\nu}}^{-1} \mathbf{m} + \mathbf{m}^H \mathbf{R}_{\boldsymbol{\nu}}^{-1} \boldsymbol{\nu}, \tag{3.129}$$

with $\mathbf{m}^H \mathbf{R}_{\boldsymbol{\nu}}^{-1} \mathbf{m}$ real-valued and positive. Then, the actual symbol detection SNR is

$$\gamma = E_s\, \mathbf{m}^H \mathbf{R}_{\boldsymbol{\nu}}^{-1} \mathbf{m}, \tag{3.130}$$

i.e., maximum. We will therefore refer to this approach as *exact MREC*, to distinguish it from another, suboptimum (approximate MREC), approach described later. For exact MREC, symbol detection performance analysis is possible based on γ, using results from [123, Chapter 8] and the procedure from Section 3.4.1.1, page 55, as shown later in Section 3.10.1, page 107.

The independence property of the eigenbranches is not involved in the above presentation of exact MREC. Therefore, exactly the same technique could be applied for the branches, even when they are correlated, to yield what we refer to herein as *exact MRC*, simply by replacing the notation related to eigen-combining with the corresponding one for combining, i.e., $\mathbf{g}$, $\mathbf{h}$,

$\mathbf{m}$, $\mathbf{e}$, $\boldsymbol{\nu}$, $\mathbf{R}_{\mathbf{e}}$, $\mathbf{y}$, $\mathbf{R}_{\boldsymbol{\nu}}$, $\mathbf{w}$, and γ are replaced with $\widetilde{\mathbf{g}}$, $\widetilde{\mathbf{h}}$, $\widetilde{\mathbf{m}}$, $\widetilde{\mathbf{e}}$, $\widetilde{\mathbf{y}}$, $\widetilde{\boldsymbol{\nu}}$, $\mathbf{R}_{\widetilde{\mathbf{e}}}$, $\mathbf{R}_{\widetilde{\boldsymbol{\nu}}}$, $\widetilde{\mathbf{w}}$, and $\widetilde{\gamma}$, respectively. Exact MRC is described in detail in Appendix B, Section A, on page 209.

Note that the exact-MRC problem is L-dimensional, while the exact-MREC problem is N-dimensional, where N can take any integer value from 1 to L. Exact MRC was studied for MPSK and i.i.d. branches in [113] using the symbol-detection-SNR-based procedure described in Section 3.4.1.1, on page 55, and for correlated branches in [119, 120] using the symbol-decision-variable-based procedure described in Section 3.4.1.2, on page 57.

The definitions of BF and order-1 MREC indicate that they coincide for p.k.c. We further define *exact BF* to stand for *order*-1 *exact MREC*. Thus, performance measures derived subsequently for order-N exact MREC also describe exact BF, after making the substitution $N = 1$.

Let us now continue with the study of exact MREC. The inherent independence of the eigenbranches causes the elements of $\mathbf{g}$ to be independent, and the correlation matrices in (3.122) – (3.127) to be diagonal. Let m_i be the ith element of the vector $\mathbf{m}$ and let $(\mathbf{R}_{\boldsymbol{\nu}})_{i,i}$ be the ith diagonal element of $\mathbf{R}_{\boldsymbol{\nu}}$. Based on (3.122), (3.123), and (3.93) from page 75, we obtain

$$m_i = \frac{\sigma^2_{h_i g_i}}{\sigma^2_{g_i}} g_i, \tag{3.131}$$

$$(\mathbf{R}_{\boldsymbol{\nu}})_{i,i} = E_{\mathrm{s}} \left(\lambda_i - \frac{|\sigma^2_{h_i g_i}|^2}{\sigma^2_{g_i}} \right) + N_0, \tag{3.132}$$

where

$$\sigma^2_{g_i} \triangleq E\{|g_i|^2\}, \tag{3.133}$$

$$\sigma^2_{h_i g_i} \triangleq E\{h_i g_i^*\}. \tag{3.134}$$

Note that in practice the cross-correlation can be complex-valued, “due to the frequency offset

and residual complex interference in the received signal used for channel estimation" [95, Section III.B, p. 3164]. We neglect such impairments throughout this work, and assume real-valued and positive the above cross-correlation from (3.134), as done elsewhere [115, Appendix C] [30, p. 34]. Tables 3.3, 3.2, and 3.1, on page 83, express (3.133) and (3.134) for SINC and MMSE PSAM. For these cases $\sigma^2_{h_i g_i} > 0$ [96, Section III.B, p. 2138].

The exact-MREC output SNR given by (3.130) can then be written as

$$\gamma = E_{\mathrm{s}} \sum_{i=1}^{N} \frac{|m_i|^2}{(\mathbf{R}_{\boldsymbol{\nu}})_{i,i}} = \sum_{i=1}^{N} \gamma_i, \tag{3.135}$$

where γ_i represents the SNR on the ith eigenbranch conditioned on g_i and is given by

$$\gamma_i \stackrel{\triangle}{=} E_{\mathrm{s}} \frac{|m_i|^2}{(\mathbf{R}_{\boldsymbol{\nu}})_{i,i}} = \frac{\frac{E_{\mathrm{s}}}{N_0} \lambda_i |\mu_i|^2}{\frac{E_{\mathrm{s}}}{N_0} \lambda_i \left(1 - |\mu_i|^2\right) + 1} \cdot \frac{|g_i|^2}{\sigma^2_{g_i}}. \tag{3.136}$$

with μ_i being the correlation coefficient of h_i and g_i, defined as in (3.48), on page 60. Again, (3.135) indicates that the combiner in (3.128) yields maximum output SNR, motivating the term "exact MREC" for this approach, by analogy with maximal-ratio combining [34].

Since for Rayleigh fading g_i is Gaussian, the conditioned SNR γ_i from (3.136) is exponentially distributed, with average

$$\Gamma_i \stackrel{\triangle}{=} E\{\gamma_i\} = \frac{\frac{E_{\mathrm{s}}}{N_0} \lambda_i |\mu_i|^2}{\frac{E_{\mathrm{s}}}{N_0} \lambda_i \left(1 - |\mu_i|^2\right) + 1} \geq 0. \tag{3.137}$$

Note that for perfectly known channel (p.k.c.), $\mu_i = 1$, $\forall i = 1 : L$, and the above becomes

$$\check{\Gamma}_i \stackrel{\triangle}{=} E\{\gamma_i\} = \frac{E_{\mathrm{s}}}{N_0} \lambda_i, \tag{3.138}$$

first defined in (3.102) on page 76. Thus, for imperfectly known channel (i.k.c.)

$$\Gamma_i = \frac{\check{\Gamma}_i |\mu_i|^2}{\check{\Gamma}_i \left(1 - |\mu_i|^2\right) + 1} \geq 0. \tag{3.139}$$

From (3.128), (3.131), and (3.132), the individual weights for exact MREC are

$$[\mathbf{w}_N]_i = \frac{1}{\frac{E_{\mathrm{s}}}{N_0} \lambda_i \left(1 - |\mu_i|^2\right) + 1} \frac{\sigma^2_{h_i g_i}}{\sigma^2_{g_i}} g_i, \quad i = 1 : N. \tag{3.140}$$

Unless specified otherwise, the notation γ_b is used hereafter (e.g., on the horizontal axis) on figures showing numerical results derived from simulations or analysis to indicates the average SNR per bit per branch, which, for ideal receivers stands for the actual average SNR per bit per branch, whereas for PSAM-based receivers it stands for the virtual average SNR per bit per branch, to make their comparisons equitable, as described in Section 2.5.3.2, on page 37.

Figs. 3.7 and 3.8 depict the MREC and MRC performance obtained by simulation for ideal combining, as well as for exact combining with SINC and MMSE PSAM, respectively. The channel gains are correlated, with the first row of $\mathbf{R}_{\tilde{\mathbf{h}}}$ given by $[1.0000 \quad 0.8739 \quad 0.6268]$ (this implies that all channel gains have unit variance; recall from page 52 that we assume a Toeplitz structure for $\mathbf{R}_{\tilde{\mathbf{h}}}$), so that the spectrum of $\mathbf{R}_{\tilde{\mathbf{h}}}$ is $\lambda(\mathbf{R}_{\tilde{\mathbf{h}}}) = \{2.5884, 0.3732, 0.0384\}$. Note the large performance gap between exact eigen-/combining for SINC PSAM and ideal eigen-/combining. An improvement is possible with MMSE PSAM.

These figures confirm a previous statement — see Section 3.5.4.2 at page 79 — that ideal MRC and ideal full MREC yield identical performance. Furthermore, Figs. 3.7 and 3.8 indicate that exact MRC and exact full MREC yield the same performance, for both SINC and MMSE PSAM, suggesting that they are performance-equivalent as well. This equivalence is demonstrated later, in Section 3.9.3.3 at page 106.

Finally, these figures demonstrate also for exact eigen-combining that full-MREC performance (i.e., the optimum, MRC, performance) can be attained with low-order MREC, although increasing MREC order is required for higher SNR.

For the same correlation scenario, the exact-MREC performance curves plotted again, for SINC and MMSE PSAM, in Fig. 3.9 show significantly poorer performance with SINC PSAM vs. MMSE PSAM. For example, MMSE interpolation outperforms SINC interpolation by about 1.9, 2, and 2.1 dB, for order-1 MREC, order-2 MREC, and full MREC, respectively. Loss due to inaccurate channel knowledge compounds with more combined terms. Recall,

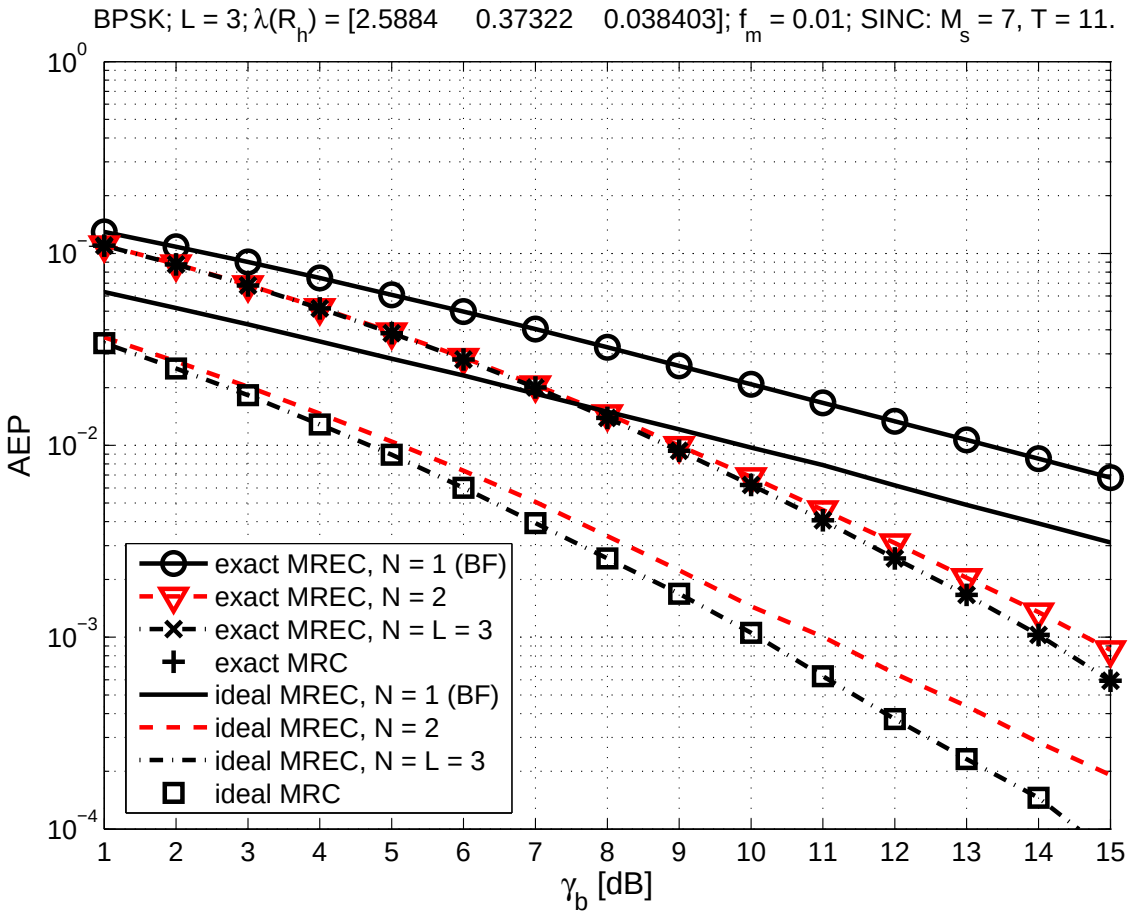

Figure 3.7. AEP vs. SNR per bit, obtained for BPSK by simulation, for exact MREC, BF, and MRC with SINC PSAM ($M_s = 7$, $T = 11$), and for ideal MREC, BF, and MRC; $L = 3$ correlated branches are employed, with $\mathbf{R}_{\tilde{\mathbf{h}}}$ spectrum given by $\lambda(\mathbf{R}_{\tilde{\mathbf{h}}}) = \{2.5884, 0.3732, 0.0384\}$.

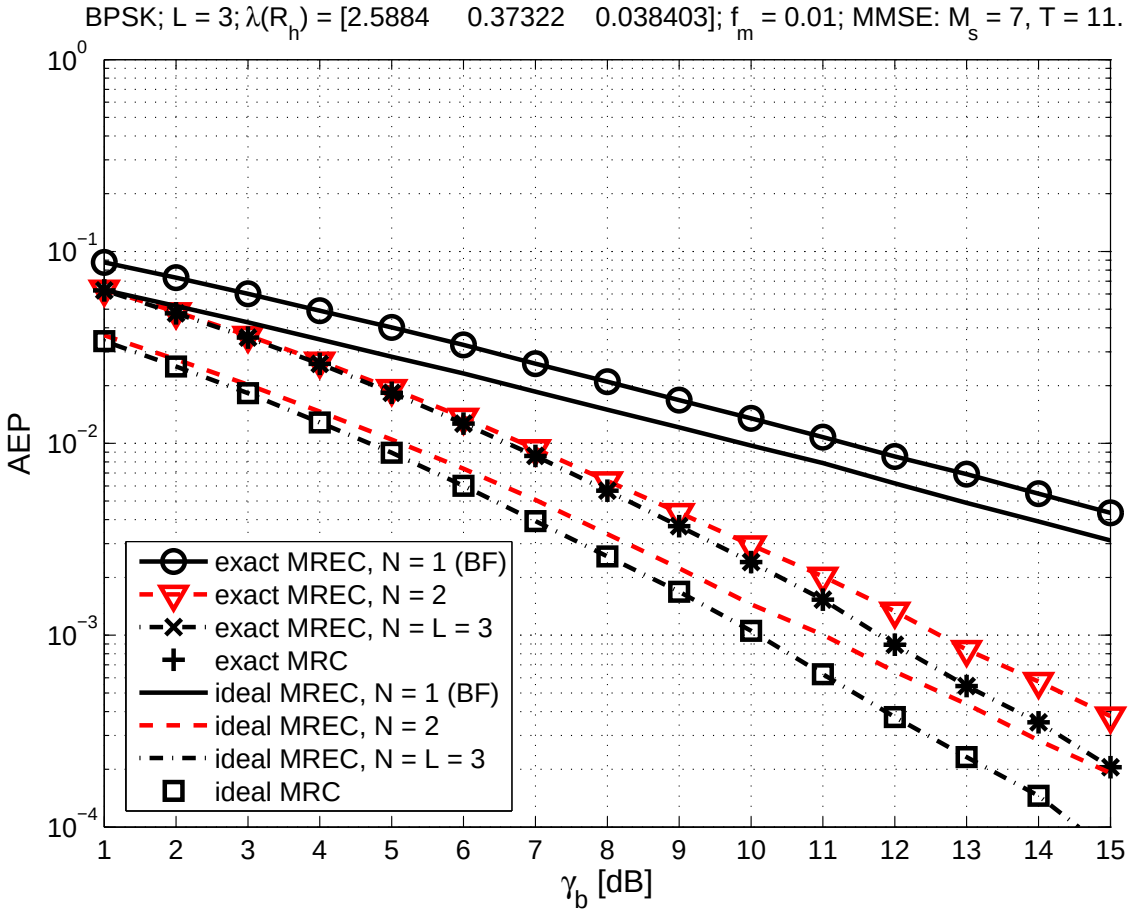

Figure 3.8. AEP vs. SNR per bit, obtained for BPSK by simulation, for exact MREC, BF, and MRC with MMSE PSAM ($M_s = 7$, $T = 11$), and for ideal MREC, BF, and MRC; $L = 3$ correlated branches are employed, with $\mathbf{R}_{\tilde{\mathbf{h}}}$ spectrum given by $\lambda(\mathbf{R}_{\tilde{\mathbf{h}}}) = \{2.5884, 0.3732, 0.0384\}$.

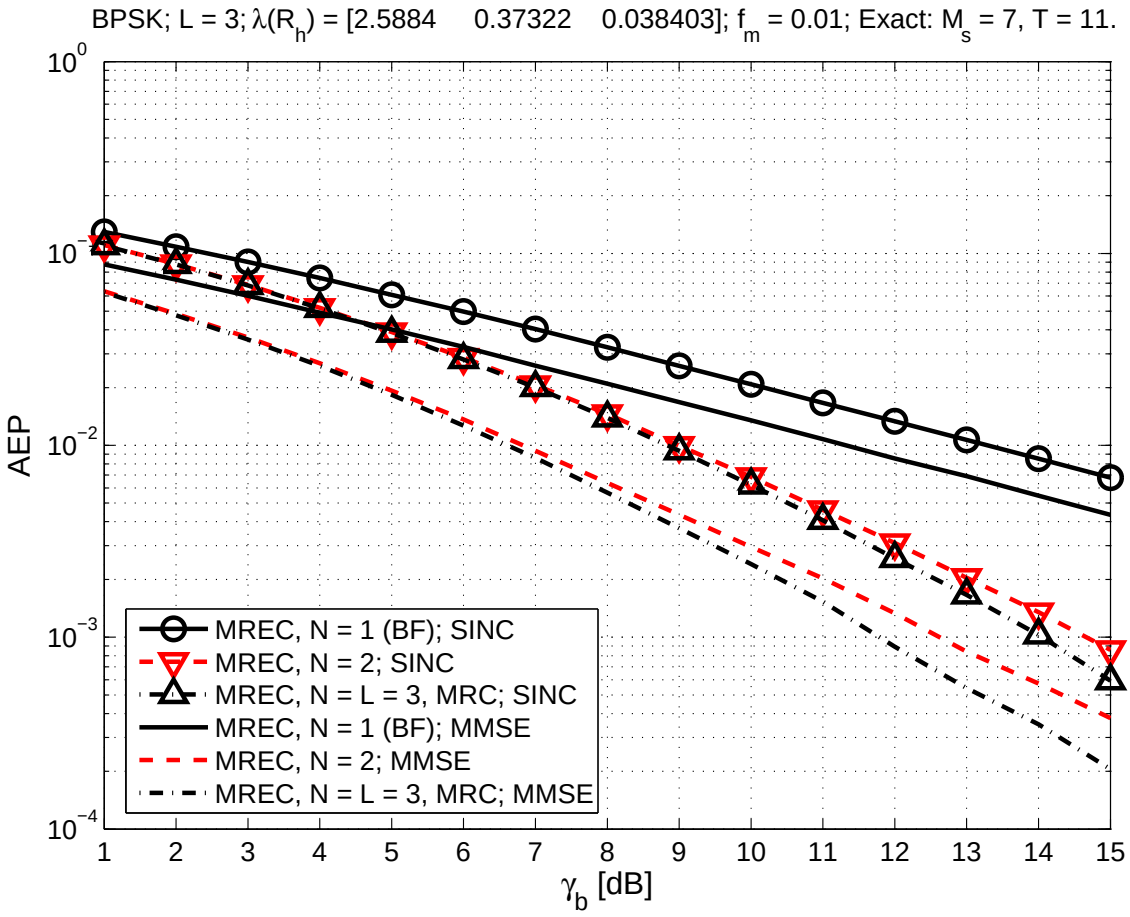

Figure 3.9. AEP vs. SNR per bit, obtained for BPSK by simulation, for exact MREC, BF, MRC, with SINC and MMSE PSAM ($M_s = 7$, $T = 11$); $L = 3$ correlated branches, with $\mathbf{R}_{\tilde{\mathbf{h}}}$ spectrum given by $\lambda(\mathbf{R}_{\tilde{\mathbf{h}}}) = \{2.5884, 0.3732, 0.0384\}$.

however, that SINC PSAM is much simpler than MMSE PSAM, and it does not rely on statistical channel knowledge.

3.7.2 Suboptimum Eigen-/Combining — Approximate MREC, MRC, BF

3.7.2.1 Suboptimum Combining Given Channel Gain Estimates — Approximate MRC

Given the signal model in (3.1) at page 51, when individual channel gains are estimated, the usual symbol detection method proposed and analyzed in the research literature [115, Appendixes B, C] [30, 48, 58] [123, Section 9.9] [20–22, 120] employs the linear combination between the estimate of the channel gain vector

$$\widetilde{\mathbf{g}} \stackrel{\triangle}{=} [\widetilde{g}_1 \quad \widetilde{g}_2 \quad \cdots \quad \widetilde{g}_N]^{\mathrm{T}}, \tag{3.141}$$

and the received signal vector, i.e.,

$$\widetilde{\mathbf{g}}^H \widetilde{\mathbf{y}}. \tag{3.142}$$

Note that the receiver uses the channel gain estimates as if they coincide with the actual gains, which renders this approach suboptimum in general [120, Section III]. Therefore, we refer to it as *approximate MRC* [127, 128, 130].

3.7.2.2 Suboptimum Eigen-combining Given Eigengain Estimates: Approximate MREC

We denote as *approximate MREC* the combining approach in which the N-dimensional transformed signal vector from (3.84) at page 74 is simply linearly combined with the vector comprising the eigenbranch estimates, i.e.,

$$\mathbf{g} \stackrel{\triangle}{=} [g_1 \quad g_2 \quad \cdots \quad g_N]^T. \tag{3.143}$$

Note that, besides g_i, which is a weight for approximate MREC, the weights for exact

MREC, given in (3.140) on page 88, require an additional factor which is a function of channel fading and noise statistics.

Approximate MREC [47, 48, 77, 125, 127, 128] uses for symbol detection the test statistic $\mathbf{g}^H \mathbf{y}$, where $\mathbf{g}$ is given by (3.143). Statistical independence of the eigenbranches allows for a straightforward analysis of approximate MREC [125] based on the approach in [30, 120]. Given eigengain estimates, approximate MREC is suboptimum [120], with an involved AEP expression [125, Eqns. 35, 37], unhelpful for adaptation to varying channel conditions. Moreover, approximate-MREC performance may actually degrade as the number of eigenbranches increases [47, 48, 77, 125, 127].

We define *approximate BF* to be order-1 approximate MREC. Thus, performance measures shown or derived subsequently for order-N approximate MREC also describe approximate-BF performance, after making the substitution $N = 1$.

Figs. 3.10 and 3.11 depict the MREC and MRC performance obtained by simulations for ideal combining, as well as for approximate eigen-/combining with SINC and MMSE PSAM, respectively. The channel gains are correlated, with $[1.0000 \quad 0.8739 \quad 0.6268]$ as the first row of $\mathbf{R}_{\tilde{\mathbf{h}}}$ (which implies that all channel gains have unit variance), so that $\lambda(\mathbf{R}_{\tilde{\mathbf{h}}}) = \{2.5884, 0.3732, 0.0384\}$. Note again that ideal MRC and ideal full MREC yield the same performance. Furthermore, approximate MRC and approximate full MREC yield the same performance for both SINC and MMSE PSAM, suggesting that they are equivalent as well. This equivalence is demonstrated later, in Section 3.9.3.1, on page 105, for SINC PSAM, and in Section 3.9.3.2, on page 105, for MMSE PSAM.

For the same correlation scenario, the approximate-MREC performance curves plotted again, for SINC and MMSE PSAM, in Fig. 3.12 show significantly poorer performance with SINC PSAM vs. MMSE PSAM. For example, MMSE interpolation outperforms SINC interpolation by about 1.9, 2, and 2.1 dB for order-1 MREC (i.e., BF), order-2 MREC, and full

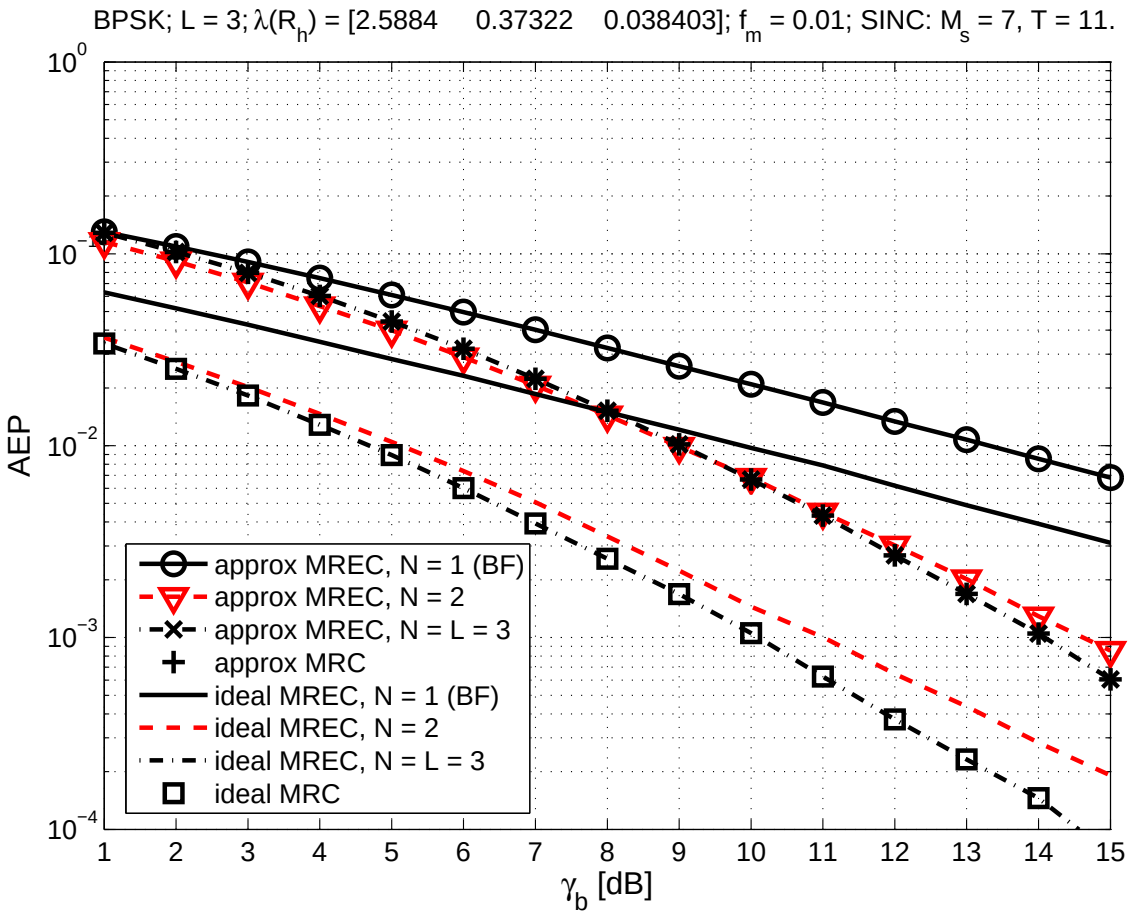

Figure 3.10. AEP vs. SNR per bit, obtained for BPSK by simulation, for approximate MREC, BF, and MRC with SINC PSAM ($M_s = 7$, $T = 11$), and for ideal MREC, BF, and MRC; $L = 3$ correlated branches are employed, with $\mathbf{R}_{\tilde{\mathbf{h}}}$ spectrum given by $\lambda(\mathbf{R}_{\tilde{\mathbf{h}}}) = \{2.5884, 0.3732, 0.0384\}$.

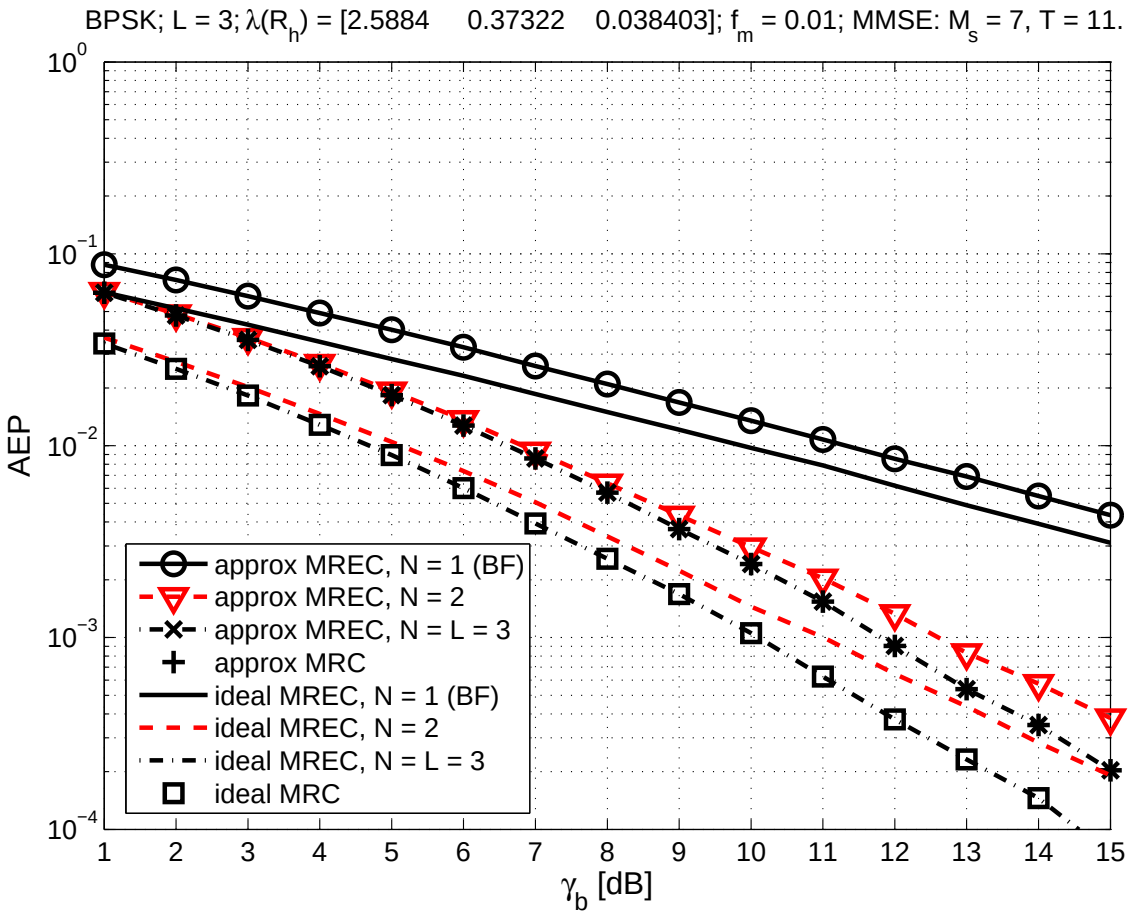

Figure 3.11. AEP vs. SNR per bit, obtained for BPSK by simulation, for approximate MREC, BF, and MRC with MMSE PSAM ($M_s = 7$, $T = 11$), and for ideal MREC, BF, and MRC; $L = 3$ correlated branches are employed, with $\mathbf{R}_{\tilde{\mathbf{h}}}$ spectrum given by $\lambda(\mathbf{R}_{\tilde{\mathbf{h}}}) = \{2.5884, 0.3732, 0.0384\}$.

MREC (i.e., MRC), respectively. Loss due to inaccurate channel knowledge compounds with more combined terms. Recall, however, that SINC PSAM is much simpler than MMSE PSAM, and it does not rely on statistical channel knowledge.

3.7.3 Exact vs. Approximate MREC, for SINC and MMSE PSAM

For the same scenario with correlated branches as above, Figs. 3.13 and 3.14 depict the MREC, BF, and MRC performance for exact and approximate combining for SINC and MMSE PSAM, respectively.

Notice first that approximate and exact BF perform identically, which is expected, because the factor which multiplies the approximate-BF weight g_1 — see (3.143), on page 93 — to yield the exact-BF weight — see (3.140), on page 88 — is real-valued and positive, for both SINC and MMSE interpolation.

Fig. 3.13, which shows results for SINC PSAM, indicates that for approximate eigen-combining the performance can degrade with increasing order. For example, at low SNR, order-2 approximate MREC can outperform full MREC by about 0.5 dB. Larger SNR reverses the relative performance.

The same figure also shows that order-2 exact MREC only very slightly outperforms order-2 approximate MREC at low SNR. However, they perform nearly identically for larger SNR values. On the other hand, at low SNR, order-3 (full) exact MREC outperforms full approximate MREC by about 0.6 dB. Nevertheless, as SNR increases, the performance gap reduces and then disappears. For MMSE PSAM, Fig. 3.14 shows no noticeable performance advantage with exact vs. approximate combining. These results suggest that the performances of approximate and exact combining can be fairly similar.

Finally, Figs. 3.13 and 3.14 both indicate that exact-MREC performance does not degrade with higher order, unlike that of approximate MREC.

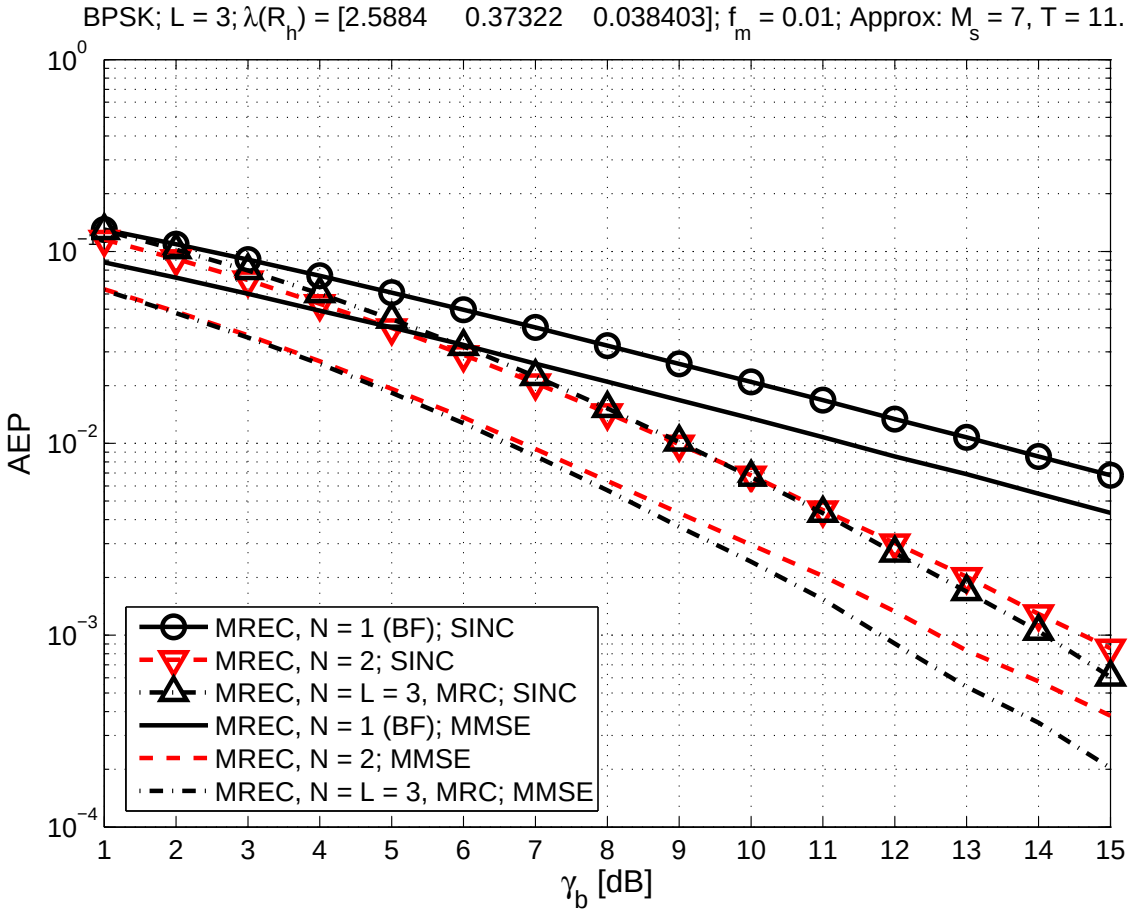

Figure 3.12. AEP vs. SNR per bit, obtained for BPSK by simulation, for approximate MREC, BF, MRC with SINC and MMSE PSAM ($M_s = 7$, $T = 11$); $L = 3$ correlated branches, with $\mathbf{R}_{\tilde{\mathbf{h}}}$ spectrum given by $\lambda(\mathbf{R}_{\tilde{\mathbf{h}}}) = \{2.5884, 0.3732, 0.0384\}$.

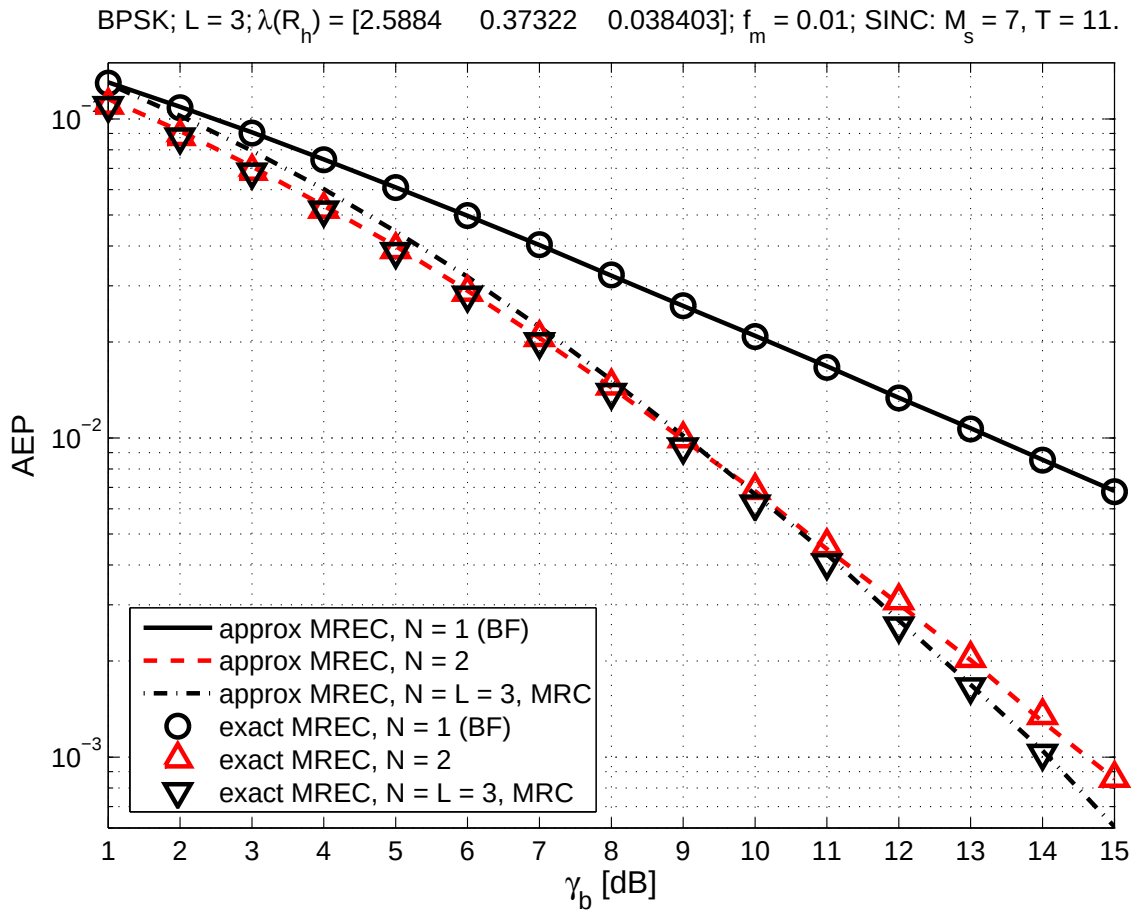

Figure 3.13. AEP vs. SNR per bit, obtained for BPSK by simulation, for exact and approximate MREC, BF, and MRC with SINC PSAM ($M_s = 7$, $T = 11$); $L = 3$ correlated branches are employed, with $\mathbf{R}_{\tilde{\mathbf{h}}}$ spectrum given by $\lambda(\mathbf{R}_{\tilde{\mathbf{h}}}) = \{2.5884, 0.3732, 0.0384\}$.

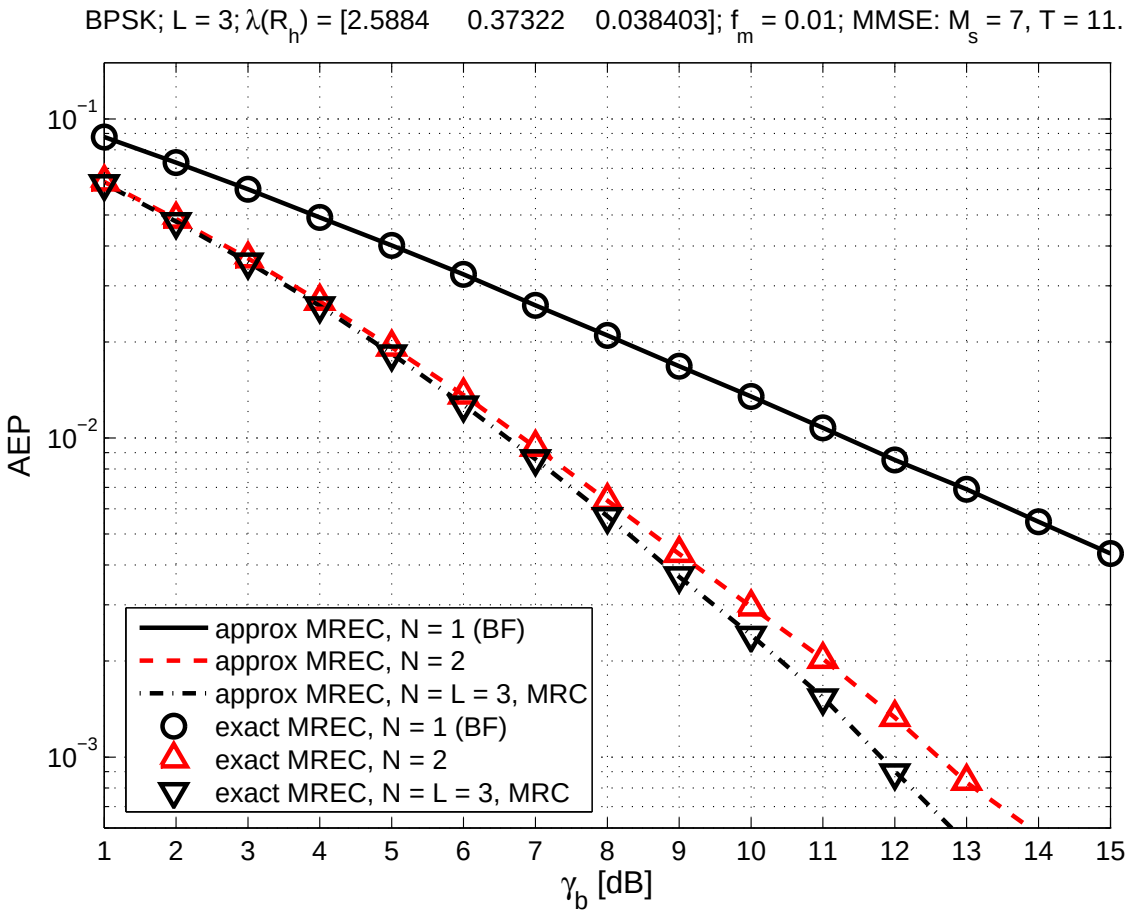

Figure 3.14. AEP vs. SNR per bit, obtained for BPSK by simulation, for exact and approximate MREC, BF, and MRC with MMSE PSAM ($M_s = 7$, $T = 11$); $L = 3$ correlated branches are employed, with $\mathbf{R}_{\tilde{\mathbf{h}}}$ spectrum given by $\lambda(\mathbf{R}_{\tilde{\mathbf{h}}}) = \{2.5884, 0.3732, 0.0384\}$.

3.8 Performance Analysis of MRC for Estimated Branches

3.8.1 Analysis of Approximate MRC

3.8.1.1 Previous Results

Traditionally, approximate-MRC analyses for BPSK modulation and i.i.d. Gaussian branches relied on the characteristic function (c.f.) of the test statistic $\Re\{\widetilde{\mathbf{g}}^H\widetilde{\mathbf{y}}\}$ [30] [115, Appendix C]. Attempts [136, 137] to employ the combiner-output-SNR p.d.f. derived in [58, Eqn. 46] were recently disproved [21, 22, 37, 95, 96]. Very recently, correct analysis was found possible using the so-called "effective" combiner-output SNR [95, Section IV.A] [96, Section IV.B].

For BPSK modulation and i.i.d. branches, the straightforward derivation from [30] relies on Turin's seminal work [142] on the c.f. of a Hermitian quadratic form in complex Gaussian vectors [142, Eqns. 4], and yields a simple closed-form AEP expression [30, Eqn. 59].

In other classical work specifically targeting i.i.d. Rayleigh fading [115, Appendix C], involved derivations yielded a closed-form AEP expression for BPSK [115, Appendix C, Eqn. C-18]. The equivalence between [115, Appendix C, Eqn. C-18] and [30, Eqn. 59] can be proven using [123, Appendix 5A, Eqns. 5A.4]. These expressions generalize to i.k.c. the AEP expression for ideal MRC given by [115, Eqn. 14.4-15].

A finite-limit integral AEP expression [20, Eqn. 19], found by reinterpreting results from [115, Appendix B] [123, Appendix 9A], is claimed to be applicable to BPSK modulation even for non-i.i.d. fading. However, the assumption in [20, Eqn. 2], on the relation between a channel gain and its estimate, can restrict the applicability of these results to the i.i.d. case.

The approach in [30] was rediscovered and applied for non-i.i.d. branches in [120], although explicit AEP expressions were not actually provided. We describe this approach in Section 3.8.1.2, on page 103.

To the best of our knowledge, the most general (i.e., applicable even for correlated and non-identically distributed branches) closed-form AEP expression for approximate MRC for BPSK modulation is [125, Eqn. 37], which we obtained based on eigen-combining, as shown later in Section 3.11.1, starting on page 118. Nevertheless, computer implementation of [125, Eqn. 37] is fairly involved. A similar KLT-based analysis appears in [48], but the case of eigenvalues of $\mathbf{R}_{\tilde{\mathbf{h}}}$ with supra-unitary multiplicity was not considered.

Few results have been published for other PSK constellations for approximate MRC of i.i.d. branches, and they are complicated — see, for instance, the very involved non-closed-form AEP expression [115, Appendix C, Eqn. C-16]. This motivates the much simpler alternative presented in Section 3.11.4, starting on page 125.

For MPSK constellations and non-i.i.d. Ricean fading, [96] computes an upper bound (which becomes tighter for larger M) on the average symbol and bit error probability of approximate MRC [96, Eqn. 3, p. 2138]. Assuming Gray mapping [115, p. 170], the procedure actually yields the exact bit error probability, for BPSK and QPSK. However, since no actual closed-form expression was obtained using this approach for correlated branches in [96], involved numerical evaluation is then required. On the other hand, for Rician i.i.d. branches, [96, Eqn. 3] can be evaluated using the simple finite-limit integral [96, Eqn. 16].

The recent work in [38] targeting independent Ricean fading and allowing for channel gains with different means but the same variance, can yield closed-form bit error probability expressions for BPSK, QPSK, and M-QAM, for PSAM-based channel estimation, by exploiting the Gray bit mapping and basic bit error probability results from [115, Appendix B].

Deriving the AEP for approximate MRC as described in [136] [137, Eqns. 3, 8], by integrating over the combiner-output-SNR p.d.f. tediously expressed by Gans in [58, Eqn. 46], was recently disproved [21, 22, 37, 95, 96]. In fact, such an approach yields a loose error-probability lower bound [21, 22, 37, 95, 96]. AEP expressions obtained as in [136, 137] can thus

seriously underestimate the effect of i.k.c. on diversity systems and even produce misleading performance results [95, 96].

In [22], a correct analysis of approximate MRC for BPSK and i.i.d. Rayleigh fading branches, hinging on the convenient channel gain model originally proposed as [58, Eqn. 16], produced a simple, finite-limit, AEP formula [22, Eqn. 23], which is equivalent to the classical, closed-form, result [30, Eqn. 59].

3.8.1.2 Straightforward Approximate-MRC Analysis for BPSK and Non-I.I.D. Branches

The following analysis approach is based on the original work for i.i.d. complex Gaussian branches from [30] and its extension to non-i.i.d. branches from [120]. Since, for BPSK, the received symbol is decided upon as

$$\widehat{b} = \text{sign}\{\Re\left[\widetilde{\mathbf{g}}^H \widetilde{\mathbf{y}}\right]\}, \tag{3.144}$$

the AEP can be obtained by following the procedure outlined in Section 3.4.1.2, on page 57, after replacing $\mathbf{x}$, $\mathbf{R}$, and $\mathbf{z}$ with $\widetilde{\mathbf{g}}$, $\mathbf{I}_L$, and $\widetilde{\mathbf{y}}$, respectively.

Computing the r.m.g.f. defined in (3.29), on page 57, and expressed in (3.39), on page 59, for the decision variable $\widetilde{q} = \Re\left[\widetilde{\mathbf{g}}^H \widetilde{\mathbf{y}}\right]$ requires knowledge of $\mathbf{R}_{\widetilde{\mathbf{g}}} \stackrel{\triangle}{=} E\{\widetilde{\mathbf{g}}\widetilde{\mathbf{g}}^H\}$, $\mathbf{R}_{\widetilde{\mathbf{g}}\widetilde{\mathbf{y}}} \stackrel{\triangle}{=} E\{\widetilde{\mathbf{g}}\widetilde{\mathbf{y}}^H\}$, $\mathbf{R}_{\widetilde{\mathbf{y}}\widetilde{\mathbf{g}}} \stackrel{\triangle}{=} E\{\widetilde{\mathbf{y}}\widetilde{\mathbf{g}}^H\} = \mathbf{R}^H_{\widetilde{\mathbf{g}}\widetilde{\mathbf{y}}}$, and $\mathbf{R}_{\widetilde{\mathbf{y}}} \stackrel{\triangle}{=} E\{\widetilde{\mathbf{y}}\widetilde{\mathbf{y}}^H\}$ — see (3.40), on page 59. (For SINC and MMSE PSAM, these matrices are expressed in closed-form in Appendix B, Sections B.1.1 and B.1.2, respectively.) These correlation matrices are non-diagonal for correlated branches, which prevents us from expressing in closed-form the poles of the r.m.g.f. of $\widetilde{q}$ — see (3.39), on page 59 — and, thus, for the AEP for approximate MRC. Then, numerical computation of the eigenvalues of the (non-block-diagonal) $2L \times 2L$-matrix $\begin{bmatrix} \mathbf{R}_{\widetilde{\mathbf{g}}\widetilde{\mathbf{y}}} & \mathbf{R}_{\widetilde{\mathbf{g}}} \\ \mathbf{R}_{\widetilde{\mathbf{y}}} & \mathbf{R}_{\widetilde{\mathbf{y}}\widetilde{\mathbf{g}}} \end{bmatrix}$ is required.

3.8.2 Analysis of Exact MRC

Exact MRC, defined in Section 3.7.1, on page 86, and described in detail in Appendix A, uses the combiner $\widetilde{\mathbf{w}} = \mathbf{R}_{\widetilde{\boldsymbol{\nu}}}^{-1}\,\widetilde{\mathbf{m}}$ — with $\widetilde{\mathbf{m}}$ and $\mathbf{R}_{\widetilde{\boldsymbol{\nu}}}$ expressed in Appendix B, Section B.2, for SINC and MMSE PSAM — for the received signal vector from (3.1), on page 51, to yield the instantaneous output SNR

$$\widetilde{\gamma} = E_{\mathrm{s}}\,\widetilde{\mathbf{m}}^{H}\,\mathbf{R}_{\widetilde{\boldsymbol{\nu}}}^{-1}\,\widetilde{\mathbf{m}}. \tag{3.145}$$

The straightforward SNR-based analysis approach outlined in Section 3.4.1.1, on page 55, cannot directly be applied for correlated branches, since $\widetilde{\gamma}$ from (3.145) is not written as a sum of independent SNRs, as required — see (3.23) at page 56. Nevertheless, since the detection variable for exact MRC can be written as $\widetilde{\mathbf{w}}^{H}\widetilde{\mathbf{y}} = \widetilde{\mathbf{m}}^{H}\mathbf{R}_{\widetilde{\boldsymbol{\nu}}}^{-1}\widetilde{\mathbf{y}}$, the BPSK case can be tackled with the method described in Section 3.4.1.2, on page 57, after replacing $\mathbf{x}$, $\mathbf{R}$, and $\mathbf{z}$ with $\widetilde{\mathbf{m}}$, $\mathbf{R}_{\widetilde{\boldsymbol{\nu}}}$, and $\widetilde{\mathbf{y}}$, respectively. The matrices required then to compute the AEP were determined as shown in Appendix B, Section B.2, for both SINC and MMSE PSAM.

3.9 Equivalences between MREC, MRC, BF

3.9.1 Full MREC and MRC Coincide for I.I.D. Branches

Proposition 2 at page 54 indicates that for i.i.d. branches we have $\mathbf{R}_{\widetilde{\mathbf{h}}} = \lambda\,\mathbf{I}_L$. Then, the eigenvectors which make up $\mathbf{E}_L$ can be any set of vectors which form an orthonormal basis in $\mathbb{C}^L$ [26]. Selecting $\mathbf{E}_L = \mathbf{I}_L$ leaves the KLT (for $N = L$) with no impact, and so branches and eigenbranches coincide. Therefore, full MREC and MRC coincide for p.k.c. or i.k.c., optimum or suboptimum combining.

3.9.2 Exact and Approximate BF are Performance-Equivalent

By definition, BF and order-1 MREC coincide for p.k.c., as well as for i.k.c. when either exact or approximate combining is employed. Thus, performance measures derived subsequently for order-N MREC also describe BF, after making the substitution $N = 1$.

Furthermore, if the cross-correlation between the dominant eigengain and its estimate is assumed real-valued and positive [30, p. 34] [115, p. 954] (true for SINC and MMSE PSAM), then the factor which multiplies g_1 in expression (3.140), on page 88, of the weight for exact BF can be disregarded. Thus, exact and approximate BF perform identically for MPSK, which was already noticed, for BPSK, based on simulation results, in Section 3.7.3 — see Fig. 3.13, on page 99, and Fig. 3.14, on page 100.

3.9.3 MRC and Order-L (Full) MREC are Performance-Equivalent

Recall from Section 3.5.4.2, page 79, that for perfectly known channel gains and eigen-gains, (ideal) MRC and full MREC are performance equivalent [9, 50]. In this section we prove that full MREC and MRC are equivalent for both optimum and approximate combining when the gains and eigengains are estimated employing the same method, either SINC or MMSE PSAM.

3.9.3.1 Approximate Eigen-/Combining for SINC PSAM

Using (3.110) from page 83, we can show that, for SINC PSAM, the channel gain vector estimator $\widetilde{\mathbf{g}}$ can be written as

$$\widetilde{\mathbf{g}} = \widetilde{\mathbf{Y}}\widetilde{\mathbf{v}}, \tag{3.146}$$

where $(\widetilde{\mathbf{Y}})_{i,t+T_1+1} \stackrel{\triangle}{=} \frac{1}{\sqrt{E_{\mathrm{p}}\, b_p}}\widetilde{y}_i(t,0),\ i = 1:L, t = -T_1:T_2$. After the KLT with $N = L$ the eigengain estimator $\mathbf{g}$ can be rewritten based on (3.107) from page 82 as

$$\mathbf{g} = \mathbf{Y}\mathbf{v}, \tag{3.147}$$

where $(\mathbf{Y})_{i,t+T_1+1} \stackrel{\triangle}{=} \frac{1}{\sqrt{E_\mathrm{p}}\, b_p} y_i(t,0),\ i = 1:L, t = -T_1 : T_2$. For SINC interpolation $\widetilde{\mathbf{v}} = \mathbf{v}$. Further, since $\mathbf{y} = \mathbf{E}_L^H \widetilde{\mathbf{y}}$, it can be shown that $\mathbf{Y} = \mathbf{E}_L^H \widetilde{\mathbf{Y}}$. Thus,

$$\mathbf{g} = \mathbf{E}_L^H \widetilde{\mathbf{g}}, \tag{3.148}$$

so that

$$\mathbf{g}^H \mathbf{y} = \widetilde{\mathbf{g}}^H \mathbf{E}_L \mathbf{E}_L^H \widetilde{\mathbf{y}} = \widetilde{\mathbf{g}}^H \widetilde{\mathbf{y}}, \tag{3.149}$$

proving that full approximate MREC and approximate MRC are equivalent in terms of symbol detection performance.

3.9.3.2 Approximate Eigen-/Combining for MMSE PSAM

The received signal vector with pilot samples $\widetilde{\mathbf{y}}_\mathrm{p}$ from (3.114), on page 84, can be written as $\widetilde{\mathbf{y}}_\mathrm{p} = \mathbf{E}\,\mathbf{y}_\mathrm{p}$, where $\mathbf{E} \stackrel{\triangle}{=} \mathrm{diag}\{\mathbf{E}_L, \ldots, \mathbf{E}_L\}$ is an $LT \times LT$ block-diagonal, unitary matrix, and $\mathbf{y}_\mathrm{p}$ is the analog, written for the L eigenbranches, of $\widetilde{\mathbf{y}}_\mathrm{p}$. If we define $\mathbf{R}_{\mathbf{y}_\mathrm{p}} \stackrel{\triangle}{=} E\left\{\mathbf{y}_\mathrm{p}\mathbf{y}_\mathrm{p}^H\right\}$, and $\mathbf{R}_{\mathbf{y}_\mathrm{p}\mathbf{h}} \stackrel{\triangle}{=} E\left\{\mathbf{y}_\mathrm{p}\mathbf{h}^H\right\}$, then $\mathbf{R}_{\widetilde{\mathbf{y}}_\mathrm{p}} = \mathbf{E}\,\mathbf{R}_{\mathbf{y}_\mathrm{p}}\,\mathbf{E}^H$, and $\mathbf{R}_{\widetilde{\mathbf{y}}_\mathrm{p}\widetilde{\mathbf{h}}} = \mathbf{E}\,\mathbf{R}_{\mathbf{y}_\mathrm{p}\mathbf{h}}\,\mathbf{E}_L^H$, and from (3.113) and (3.116) we determined that $\widetilde{\mathbf{g}} = \mathbf{E}_L\,\mathbf{G}_\mathrm{opt}^H\,\mathbf{y}_\mathrm{p} = \mathbf{E}_L\,\mathbf{g}$, where $\mathbf{G}_\mathrm{opt} \stackrel{\triangle}{=} \mathbf{R}_{\mathbf{y}_\mathrm{p}}^{-1}\mathbf{R}_{\mathbf{y}_\mathrm{p}\mathbf{h}}$. Thus, the symbol decision variables for approximate MRC and full approximate MREC are equal also for MMSE PSAM.

3.9.3.3 Exact Eigen-/Combining for SINC and MMSE PSAM

Exact MRC implementation is described in Appendix B, Section B.2, on page 213, and exact MREC implementation is described in Section 3.7.1, on page 85. Using the relationship between the eigengains (for $N = L$) and gains, i.e., $\mathbf{h} = \mathbf{E}_L^H \widetilde{\mathbf{h}}$, and the relationship between their estimates obtained above, i.e., $\mathbf{g} = \mathbf{E}_L^H \widetilde{\mathbf{g}}$, we found that $\mathbf{R}_{\boldsymbol{\nu}} = \mathbf{E}_L^H \mathbf{R}_{\widetilde{\boldsymbol{\nu}}} \mathbf{E}_L$, and $\mathbf{m} = \mathbf{E}_L^H \widetilde{\mathbf{m}}$, which yield the relationship between the eigen-combiner for exact full MREC and the combiner for exact MRC as $\mathbf{w} = \mathbf{E}_L^H \widetilde{\mathbf{w}}$. Then, the corresponding conditioned SNRs, i.e., γ from (3.130),

page 86, and $\widetilde{\gamma}$ from (3.145), page 104, are equal, proving the equivalence between exact full MREC and MRC in terms of symbol detection performance.

3.9.4 Exact and Approximate MRC are Performance-Equivalent for I.I.D. Branches

When the branches are i.i.d., full MREC coincides with MRC. Furthermore, the factors which multiply g_i in the expression for exact MREC (also for exact MRC in this case) weights from (3.140), on page 88, are equal. Assuming that they are real-valued and positive as well [30, p. 34] [115, p. 954] (true for SINC and MMSE PSAM), these factors then do not impact exact MRC (full MREC) detection performance, rendering it identical to that of approximate MRC (full MREC). Fig. 3.15 confirms these deductions based on simulations for a scenario with QPSK modulation, $L = 1:3$ i.i.d. branches with unit-variance channel gains, and SINC PSAM channel estimation.

3.10 Performance Analysis of Optimum Eigen-/Combining

3.10.1 Simple, Non-Closed-Form, AEP Expression for Exact MREC

In Section 3.7.1, the signal model developed for exact eigen-combining in (3.125), on page 85, conveniently compounds the channel estimation errors with the receiver noise, to permit an analysis based on the actual symbol detection SNR from (3.130), page 86. Thus, the error probability given the channel eigengain estimates can be computed as [123, Eqn. 8.22, p. 196]

$$P_e(\gamma) = \frac{1}{\pi} \int_0^{\frac{M-1}{M}\pi} \exp\left\{ -\gamma \frac{g_{\text{PSK}}}{\sin^2 \phi} \right\} d\phi, \tag{3.150}$$

where the actual output symbol detection SNR is given by the sum of the individual SNRs, i.e., $\gamma = \sum_{i=1}^{N} \gamma_i$ — see (3.135), on page 88.

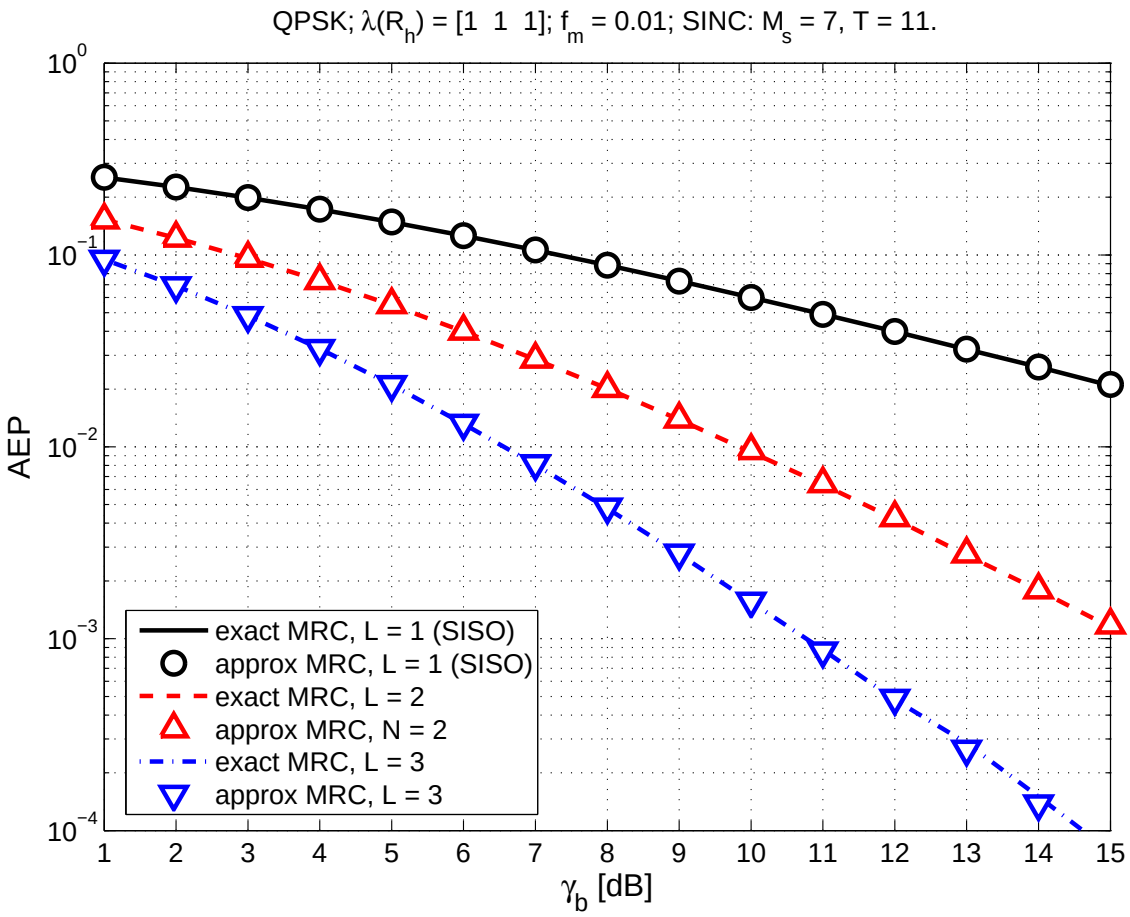

Figure 3.15. AEP vs. SNR per bit, obtained by simulation, for QPSK, approximate and exact MRC of $L = 1 : 3$ i.i.d. branches, with SINC PSAM channel estimation.

For exact MREC, the independence of individual SNR terms γ_i, $i = 1:N$, defined in (3.136), on page 88, along with the above SNR additivity property, allows for a simple, conditioned-SNR-based AEP analysis, along the same lines as in Section 3.4.1.1, page 55. For MPSK transmitted signals and order-N exact MREC, the AEP is then

$$P_{e,N} = \frac{1}{\pi} \int_0^{\frac{M-1}{M}\pi} \prod_{i=1}^{N} \left(1 + \Gamma_i \frac{g_{\text{PSK}}}{\sin^2 \phi}\right)^{-1} d\phi, \tag{3.151}$$

which depends on modulation constellation size, MREC order N, antenna correlation, estimation method and parameters. Note that, since Γ_i, defined in (3.137), on page 88, is positive $\forall i = 1:N$, the performance of exact MREC cannot degrade with higher order. Although (3.151) requires numerical integration, it can be computed easily on a computer. Similar results are possible for other modulations as well as for Rician fading — see Section 3.4.1.1, on page 55.

Consider again the case of $L = 3$, when the channel gains are correlated, with the first row of $\mathbf{R}_{\tilde{\mathbf{h}}}$ given by $[1.0000 \quad 0.8739 \quad 0.6268]$ (this implies that all channel gains have unit variance; recall from page 52 that we assume a Toeplitz structure for $\mathbf{R}_{\tilde{\mathbf{h}}}$), so that $\lambda(\mathbf{R}_{\tilde{\mathbf{h}}}) = \{2.5884, 0.3732, 0.0384\}$. Figs. 3.16 and 3.17 describe, for BPSK, the performance of exact BF, MREC, and MRC, for SINC and MMSE PSAM, respectively, as evaluated with (3.151) and by simulation. These figures indicate the following:

- There is a good agreement between analysis and simulation results.
- MRC and full MREC perform identically.
- MREC performance does not degrade with higher order.
- Full-MREC (i.e., MRC, optimum) performance can be obtained with MREC of lower order for certain SNR ranges. For example, full-MREC performance can be obtained with order-2 MREC for $\gamma_b < 8$ dB for SINC PSAM, and for $\gamma_b < 5$ dB for MMSE PSAM.

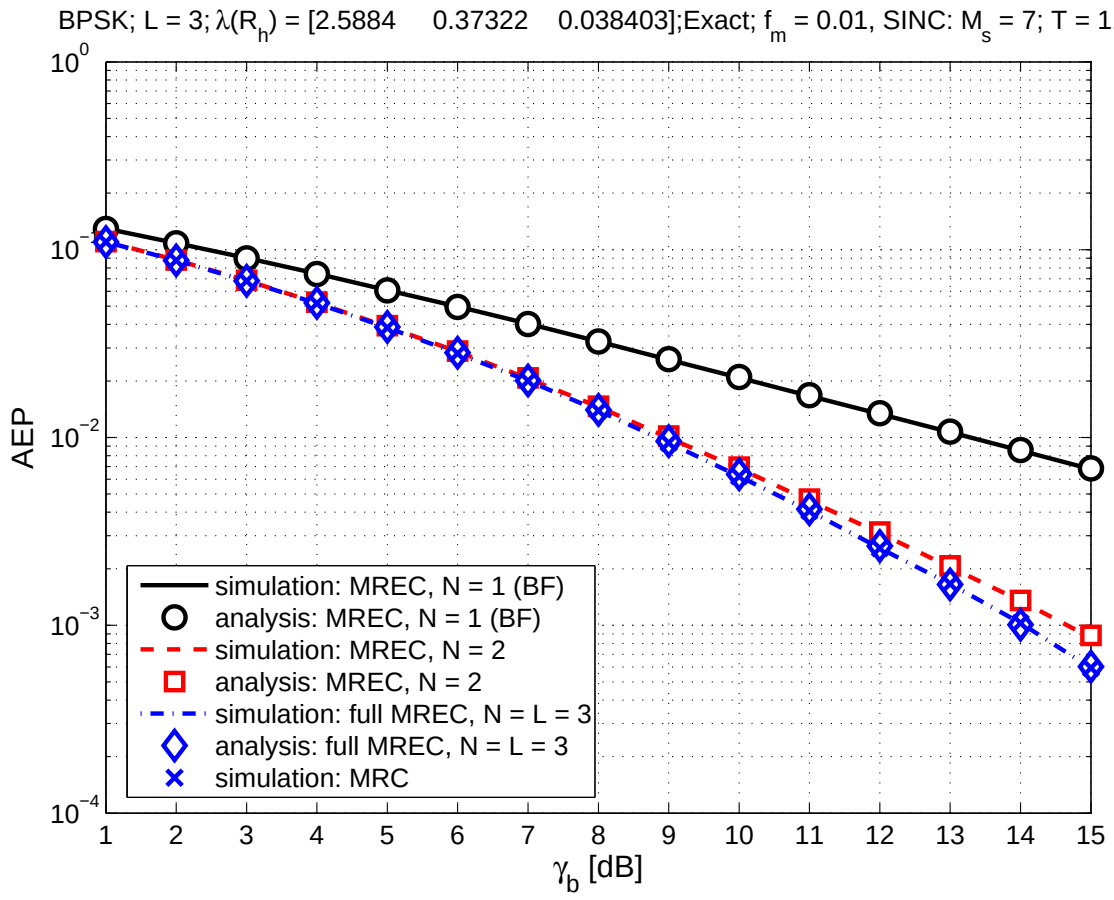

Figure 3.16. AEP vs. SNR per bit, obtained by simulation and from analysis, for BPSK transmitted symbols, for exact BF, MREC, and MRC, with SINC PSAM; $L = 3$ correlated branches are employed, with $\mathbf{R}_{\tilde{\mathbf{h}}}$ spectrum given by $\lambda(\mathbf{R}_{\tilde{\mathbf{h}}}) = \{2.5884, 0.3732, 0.0384\}$.

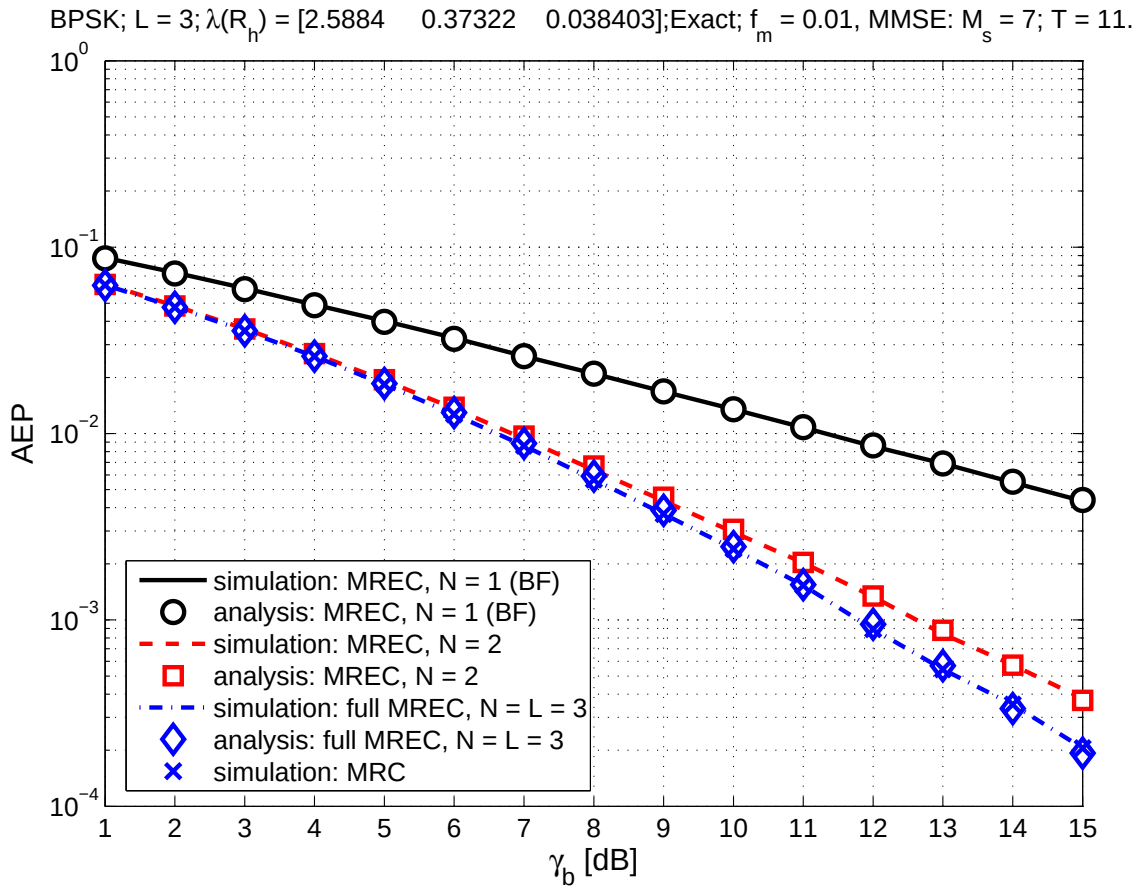

Figure 3.17. AEP vs. SNR per bit, obtained by simulation and from analysis, for BPSK transmitted symbols, for exact BF, MREC, and MRC, with MMSE PSAM; $L = 3$ correlated branches are employed, with $\mathbf{R}_{\tilde{\mathbf{h}}}$ spectrum given by $\lambda(\mathbf{R}_{\tilde{\mathbf{h}}}) = \{2.5884, 0.3732, 0.0384\}$.

3.10.2 Closed-Form AEP Expressions for Exact MREC

Let $\{\Xi_1, \Xi_2, \ldots, \Xi_{N_d}\}$ denote the distinct values in the set $\{\Gamma_1\, g_{\text{PSK}}, \Gamma_2\, g_{\text{PSK}}, \ldots, \Gamma_N\, g_{\text{PSK}}\}$ — which enter the finite-limit integral AEP expression for exact MREC from (3.151), on page 109 — and let r_k denote the algebraic multiplicity of Ξ_k, $k = 1 : N_d$, with $\sum_{k=1}^{N_d} r_k = N$. Then, the r.m.g.f. — defined in (3.29), on page 57 — of exact MREC output SNR γ — see (3.130), on page 86 — is

$$F_\gamma(s) = \prod_{k=1}^{N_d} \left[\frac{1}{1+s\,\Xi_k}\right]^{r_k}. \tag{3.152}$$

We separately consider each case of interest below. The AEP and outage probability (OP) expressions derived next for the case when all eigenvalues of $\mathbf{R}_{\tilde{\mathbf{h}}}$ coincide form the building blocks for the subsequently discussed cases.

3.10.2.1 The Case when All Eigenvalues are Equal

Recall from Section 3.9.1, page 104, that when all eigenvalues of $\mathbf{R}_{\tilde{\mathbf{h}}}$ are equal the eigen-branches coincide with the branches. In this case, $N_d = 1$, $r_1 = N$, and $\Xi_k = \Xi_1 \stackrel{\triangle}{=} \Xi \stackrel{\triangle}{=} \Gamma\, g_{\text{PSK}}$, so that (3.152) reduces to

$$F_\gamma(s) = \frac{1}{(1+s\,\Xi)^N}, \tag{3.153}$$

and the finite-limit integral exact-MREC AEP expression from (3.151) becomes

$$P_{e,N} = \frac{1}{\pi}\int_0^{\frac{M-1}{M}\pi} \left(1+\Xi\,\frac{1}{\sin^2\phi}\right)^{-N} d\,\phi, \tag{3.154}$$

or, in closed-form [123, Appendix 5A, Eqns. 5A.17–19, pp. 127, 128],

$$P_{e,N} = \frac{M-1}{M} - \frac{1}{\pi}\sqrt{\frac{\Xi}{\Xi+1}}\left\{\left(\frac{\pi}{2}+\tan^{-1}\alpha\right)\sum_{n=0}^{N-1}\binom{2n}{n}\frac{1}{[4\,(\Xi+1)]^n}\right.$$
$$\left. +\sin\left(\tan^{-1}\alpha\right)\sum_{n=1}^{N-1}\sum_{i=1}^{n}\frac{T_{i,n}}{(\Xi+1)^n}\left[\cos\left(\tan^{-1}\alpha\right)\right]^{2(n-i)+1}\right\} \tag{3.155}$$

where

$$\alpha \triangleq \sqrt{\frac{\Xi}{\Xi+1}}\left(\tan\frac{\pi}{M}\right)^{-1}, \tag{3.156}$$

$$T_{i,n} \triangleq \frac{\binom{2n}{n}}{\binom{2(n-i)}{n-i}\,4^i\,[2(n-i)+1]}. \tag{3.157}$$

For BPSK this yields [115, Eqn. 14.4-15, p. 825] [123, Appendix 5A, Eqn. 5A.4b]

$$P_{e,N} = \left[\frac{1}{2}(1-\xi)\right]^N \sum_{n=0}^{N-1}\binom{N-1+n}{n}\left[\frac{1}{2}(1+\xi)\right]^n, \tag{3.158}$$

where

$$\xi \triangleq \sqrt{\frac{\Xi}{\Xi+1}} = \sqrt{\frac{\Gamma g_{\text{PSK}}}{\Gamma g_{\text{PSK}}+1}} = \mu\sqrt{\frac{\check{\Gamma} g_{\text{PSK}}}{\check{\Gamma} g_{\text{PSK}}+1}} = \mu\,\check{\xi}, \tag{3.159}$$

with μ being the correlation coefficient between the actual (eigen)gain and its estimate,

$$\check{\xi} \triangleq \sqrt{\frac{\check{\Gamma} g_{\text{PSK}}}{\check{\Gamma} g_{\text{PSK}}+1}}, \tag{3.160}$$

and $\check{\Gamma}$ is the (eigen)branch average SNR for p.k.c., defined in (3.138), on page 88. Using [123, Appendix 5A, Eqns. 5A.4], (3.158) can be shown to be equivalent to

$$P_{e,N} = \frac{1}{2}\left[1-\xi\sum_{n=0}^{N-1}\binom{2n}{n}\left(\frac{1-\xi^2}{4}\right)^n\right]. \tag{3.161}$$

The p.d.f. of γ defined in (3.130), on page 86, can now be derived from (3.153), using (3.30) from page 57, as [115, Eqns. 14.4-12, 13, p. 825]

$$p_\gamma(\gamma) = \frac{\gamma^{N-1}\,e^{-\gamma/\Xi}}{(N-1)!\,\Xi^N}. \tag{3.162}$$

Substituting this into the outage probability definition from (3.50), on page 61, yields

$$P_o = \mathscr{G}\left(N, \frac{\gamma_{\text{th}}}{\Xi}\right), \tag{3.163}$$

where

$$\mathscr{G}(n,x) \triangleq \frac{1}{(n-1)!}\int_0^x e^{-t}\,t^{n-1}\,dt \tag{3.164}$$

is the *incomplete gamma function* [6, Eqn. 6.5.1, p. 260].

3.10.2.2 The Case when Some Eigenvalues are Equal

For multi-branch receivers, some eigenvalues of $\mathbf{R}_{\tilde{\mathbf{h}}}$ can become (nearly) equal [128, Fig. 1] [130, Fig. 1]. Therefore, a separate analysis of this most general case is worthwhile.

Using the partial fraction expansion procedure described in [65, §2.102, pp. 56–57], we can write (3.152) as

$$F_\gamma(s) = \frac{1}{A}\sum_{k=1}^{N_d}\sum_{l=1}^{r_k} c_{k,l}\frac{1}{\left(s+\frac{1}{\Xi_k}\right)^l}, \tag{3.165}$$

where $A \stackrel{\triangle}{=} \prod_{k=1}^{N_d}\Xi_k^{r_k}$, and the factor $c_{k,l}$ is given by

$$c_{k,l} \stackrel{\triangle}{=} \frac{A}{(r_k-l)!}\left\{D_s^{(r_k-l)}\left[F_\gamma(s)\cdot\left(s+\frac{1}{\Xi_k}\right)^{r_k}\right]\right\}\Bigg|_{s=-\frac{1}{\Xi_k}},$$

with $D_s^{(n)}[G(s)] \stackrel{\triangle}{=} \frac{d^n[G(s)]}{ds^n}$, i.e., the nth derivative of $G(s)$.

Based on [18], $c_{k,l}$ can be expressed in the closed-form

$$c_{k,l} = (-1)^{r_k-l}\cdot\sum_{\Omega}\prod_{\substack{j=1\\ j\neq k}}^{N_d} d_j\cdot\left(\frac{1}{\Xi_j}-\frac{1}{\Xi_k}\right)^{-(r_j+i_j)}, \quad k=1:N_d,\ l=1:r_k, \tag{3.166}$$

where Ω stands for the set of integers satisfying $0 \le i_1,\ldots,i_{k-1},i_{k+1},\ldots,i_{N_d} \le r_k-l$ and $i_1+\ldots+i_{k-1}+i_{k+1}+\ldots+i_{N_d} = r_k-l$, and $d_j = \binom{r_j-1+i_j}{i_j}$.

Note that the individual terms of the sum in (3.165) can be recast as the ratio from (3.153). Therefore, we can use results from Section 3.10.2.1 to write the exact-MREC AEP expression for this most general case in the following canonical form

$$P_e = \frac{1}{A}\sum_{k=1}^{N_d}\sum_{l=1}^{r_k} c_{k,l}\cdot\Xi_k^l\cdot I_l(\Xi_k), \tag{3.167}$$

where

$$I_l(\Xi_k) \stackrel{\triangle}{=} \frac{1}{\pi}\int_0^{\frac{M-1}{M}\pi}\left[\frac{\sin^2\phi}{\sin^2\phi+\Xi_k}\right]^l d\phi \tag{3.168}$$

actually coincides with $P_{e,l}$ given by (3.154), and thus is described in closed-form by (3.155) – (3.161), by replacing N, Ξ, ξ, Γ, μ, and $\check{\xi}$ with l, Ξ_k, ξ_k, Γ_k, μ_k, and $\check{\xi}_k$, respectively.

Note that, unlike the non-closed-form exact-MREC AEP expression from (3.151), page 109, the equivalent closed-form AEP expression from (3.167) is very difficult to implement and evaluate on a computer, because the factors $c_{k,l}$ defined in (3.166) depend on the relative magnitudes of the eigenvalues of $\mathbf{R}_{\tilde{\mathbf{h}}}$.

The p.d.f. of γ can now be obtained as the inverse Laplace transform of (3.165), i.e.,

$$p_\gamma(\gamma) = \frac{1}{A}\sum_{k=1}^{N_d}\sum_{l=1}^{r_k} c_{k,l}\cdot\frac{\gamma^{l-1}e^{-\gamma/\Xi_k}}{(l-1)!}, \tag{3.169}$$

using the building blocks provided by (3.153) and (3.162). Substituting this into the outage probability definition from (3.50), on page 61, yields the following general canonical form for the outage probability of exact MREC

$$P_o = \frac{1}{A}\sum_{k=1}^{N_d}\sum_{l=1}^{r_k} c_{k,l}\cdot\Xi_k^l\cdot\mathscr{G}\left(l,\frac{\gamma_{\text{th}}}{\Xi_k}\right), \tag{3.170}$$

where $\mathscr{G}(\cdot,\cdot)$ was defined in (3.164), on page 113.

3.10.2.3 The Case when All Eigenvalues are Distinct

In this case $N_d = N$ and $r_k = 1$, $\forall k = 1:N$, so that (3.165) and (3.166) yield

$$F_\gamma(s) = \sum_{k=1}^{N} R_k\frac{1}{1+s\Xi_k}, \tag{3.171}$$

where

$$R_k = \prod_{j\neq k}^{N}\frac{\Xi_k}{\Xi_k-\Xi_j}. \tag{3.172}$$

Then, from (3.171), using (3.153) and (3.158) for $N=1$, we obtain

$$P_e = \frac{1}{2}\sum_{k=1}^{N} R_k\cdot(1-\xi_k), \tag{3.173}$$

which, for p.k.c., uncorrelated branches, and BPSK, reduces to the MRC AEP-formula [115, Eqn. 14.5-28, p. 845].

In this case, the p.d.f. of γ, given in (3.169), becomes [89, Eqn. (10-60), p. 308]

$$p_\gamma(\gamma) = \sum_{k=1}^{N} R_k \frac{1}{\Xi_k} e^{-\gamma/\Xi_k}, \tag{3.174}$$

which, for p.k.c., reduces to [115, Eqn. 14.5-26, p. 847]. Then, the OP is given by

$$P_o = \sum_{k=1}^{N} R_k \left(1 - e^{-\gamma_{\text{th}}/\Xi_k}\right). \tag{3.175}$$

3.10.3 Exact-MREC Analysis Results Specialized to Exact BF and MRC

For $N = 1$, exact MREC reduces to exact BF, for which (3.151), on page 109, is then a non-closed-form, but finite-limit integral, average error probability expression. This can be recast in closed-form as described in Section 3.10.2.1 at page 112. Thus, the exact-BF AEP for MPSK and arbitrarily correlated Rayleigh fading is given by the following expressions:

$$P_e = \frac{1}{\pi} \int_0^{\frac{M-1}{M}\pi} \left(1 + \Gamma_1 \frac{g_{\text{PSK}}}{\sin^2\phi}\right)^{-1} d\phi = \frac{1}{2}\left(1 - \sqrt{\frac{\Gamma_1 g_{\text{PSK}}}{\Gamma_1 g_{\text{PSK}} + 1}}\right). \tag{3.176}$$

Due to the equivalence demonstrated in Section 3.9.3.3, page 106, between full MREC and MRC, it follows that (3.151), page 109, with $N = L$, also describes exact-MRC performance, for non-i.i.d. branches. The equivalent closed-form average error probability expressions derived above for exact MREC also hold for exact MRC, after the $N = L$ substitution.

Similarly, we can obtain exact-BF and exact-MRC OP expressions from the ones derived above for exact MREC. We have thus unified the treatment of exact MREC, BF, and MRC, for which we obtained new, simple non-closed-form as well as more involved closed-form performance-measure expressions that cover most cases of interest in terms of channel estimation procedure, and relative channel gain eigenvalue magnitudes. They are useful in optimum eigen-/combining performance evaluation given statistical information about the noise and fading, as well as for MREC adaptation, as shown later.

3.10.4 Exact-MREC Analysis Results Specialized to Ideal MREC, BF, and MRC

3.10.4.1 Exact-MREC Analysis Results Specialized to Ideal MREC

Perfectly known eigengains implies that $\mu_i = 1, \forall i = 1 : L$. Then the average effective eigen-branch SNR Γ_i defined for i.k.c. in (3.137), on page 88, reduces to the average actual eigen-branch SNR $\check{\Gamma}_i$ defined for p.k.c. in (3.138), on page 88, and the nonclosed-form AEP expression for exact MREC from (3.151), on page 109, reduces to the expression for ideal MREC, already determined in (3.105), on page 77. Thus, the closed-form AEP expressions derived in Section 3.10.2, starting at page 112, for optimum MREC for i.k.c. yield corresponding closed-form AEP expressions for ideal MREC by simply replacing Γ_i with $\check{\Gamma}_i$. Similarly, we can obtain ideal-MRC OP expressions from the ones derived above for exact MREC. We thus unified the treatment of optimum eigen-combining for i.k.c. and p.k.c.

3.10.4.2 Exact-MREC Analysis Results Specialized to Ideal BF and MRC

By definition, BF is order-1 MREC. Therefore, the AEP and OP expressions derived above for exact order-N MREC characterize, by substituting $N = 1$ and by replacing Γ_i with $\check{\Gamma}_i$, ideal BF.

Since full MREC and MRC are equivalent for p.k.c. [50], the AEP and OP expressions derived above for exact order-N MREC reduce, by substituting $N = L$ and by replacing Γ_i with $\check{\Gamma}_i$, to the AEP and OP expressions for ideal MRC. Evidently, for p.k.c. and uncorrelated branches, Eqn. (3.151), on page 109, reduces to the MRC AEP expression already derived in (3.63), on page 63.

3.11 Performance Analysis of Suboptimum Eigen-/Combining

3.11.1 Performance Analysis of Approximate MREC

Approximate MREC was described in Section 3.7.2.2, on page 93. Approximate-MREC error probability analysis for BPSK relies on the approach described in Section 3.4.1.2, on page 57, by replacing **x**, **z**, and **R** with **g**, **y**, and $\mathbf{I}_N$, respectively. Recall that **g**, defined in (3.143), on page 93, is the estimate of the N-dimensional eigengain vector from (3.86), on page 74, and **y** is the transformed signal vector defined in (3.84), on page 74. The symbol-detection variable for approximate MREC is $q = \mathbf{g}^H \mathbf{y}$, whose r.m.g.f. can be written based on (3.42) – (3.47), as

$$F_q(s) = \prod_{k=1}^{N} \frac{1}{\left[-a_k^2 (s - s_{k,1})(s + s_{k,2})\right]} \tag{3.177}$$

where

$$a_k^2 = \frac{E_\mathrm{s} \left(\sigma_{g_k h_k}^2\right)^2}{4\Gamma_k} = \frac{1}{4} N_0 \sigma_{g_k}^2 \left[1 + (1 - \mu_k^2)\breve{\Gamma}_k\right] > 0, \tag{3.178}$$

with Γ_k given by (3.137), on page 88, the relation between Γ_k and $\breve{\Gamma}_k$ described by (3.139), on page 88, and

$$s_{k,1} = \frac{2}{\sqrt{E_\mathrm{s}}\, \sigma_{g_k h_k}^2} \cdot \frac{\xi_k}{1 - \xi_k} = \frac{2\breve{\xi}_k}{\sqrt{E_\mathrm{s}\, \sigma_{h_k}^2\, \sigma_{g_k}^2}} \cdot \frac{1}{1 - \mu_k \breve{\xi}_k} > 0, \tag{3.179}$$

$$s_{k,2} = \frac{2}{\sqrt{E_\mathrm{s}}\, \sigma_{g_k h_k}^2} \cdot \frac{\xi_k}{1 + \xi_k} = \frac{2\breve{\xi}_k}{\sqrt{E_\mathrm{s}\, \sigma_{h_k}^2\, \sigma_{g_k}^2}} \cdot \frac{1}{1 + \mu_k \breve{\xi}_k} > 0, \tag{3.180}$$

with $\breve{\xi}_k$ given by (3.160), on page 113, (for BPSK, $g_{\mathrm{PSK}} = 1$), and the relation between ξ_k and $\breve{\xi}_k$ given by (3.159), on page 113.

Again, we consider separately three particular situations.

3.11.1.1 The Case when Some Eigenvalues are Equal

Assuming that some of the eigen-branches may have identical parameters, the r.m.g.f. of q becomes

$$F_q(s) = \prod_{k=1}^{N_d} \frac{1}{\left[-a_k^2(s-s_{k,1})(s+s_{k,2})\right]^{r_k}}, \tag{3.181}$$

which we conveniently rewrite as

$$F_q(s) = \frac{1}{B} \prod_{p=1}^{2N_d} \frac{1}{(s+\sigma_p)^{\rho_p}}, \tag{3.182}$$

where

$$B \triangleq \prod_{k=1}^{N_d} (-a_k^2)^{r_k}, \tag{3.183}$$

$$\sigma_p \triangleq \begin{cases} -s_{p,1} \quad , \quad \rho_p = r_p, & \text{for } p = 1 : N_d, \\ s_{p-N_d,2} \quad , \quad \rho_p = r_{p-N_d}, & \text{for } p = N_d+1 : 2N_d. \end{cases} \tag{3.184}$$

As in Section 3.10.2.2, we obtain, based on [65, §2.102, pp. 56–57], the following partial fraction expansion:

$$F_q(s) = \frac{1}{B} \sum_{p=1}^{2N_d} \sum_{l=1}^{\rho_p} c_{p,l} \frac{1}{(s+\sigma_p)^l}, \tag{3.185}$$

with

$$\begin{aligned} c_{p,l} &\triangleq \frac{B}{(\rho_p - l)!} \left\{ D_s^{(\rho_p - l)} \left[F_q(s) \cdot (s+\sigma_p)^{\rho_p} \right] \right\} \Big|_{s=-\sigma_p}, \\ &= (-1)^{\rho_p - l} \cdot \sum_{\Psi} \prod_{\substack{j=1 \\ j \neq p}}^{2N_d} \delta_j \cdot \frac{1}{\left(\sigma_j - \sigma_p\right)^{(\rho_j + i_j)}}, \end{aligned} \tag{3.186}$$

where Ψ stands for the set of integers satisfying $0 \leq i_1, \ldots, i_{p-1}, i_{p+1}, \ldots, i_{2N_d} \leq \rho_p - l$ and $i_1 + \ldots + i_{p-1} + i_{p+1} + \ldots + i_{2N_d} = \rho_p - l$, and $\delta_j = \binom{\rho_j - 1 + i_j}{i_j}$.

The p.d.f. of q, obtained as the inverse Laplace transform of $F_q(s)$ from (3.185), is

$$p_q(q) = \frac{1}{B} \sum_{k=1}^{N_d} \sum_{l=1}^{r_k} \left[-\frac{c_{k,l}}{(l-1)!} q^{l-1} e^{s_{k,1} q} u(-q) + \frac{c_{k+N_d,l}}{(l-1)!} q^{l-1} e^{-s_{k,2} q} u(q) \right], \tag{3.187}$$

where $u(q)$ is the unit-step function, i.e., $u(q) = 0$ for $q < 0$, and $u(q) = 1$ for $q \geq 0$. Since $P_e = \int_{-\infty}^{0} p_q(q)\, dq$, only the first term from the above $p_q(q)$ expression affects the P_e, which then becomes

$$\begin{aligned} P_e &= \frac{1}{B} \sum_{k=1}^{N_d} \sum_{l=1}^{r_k} c_{k,l} \cdot \left[-\frac{1}{s_{k,1}} \right]^l \\ &= \frac{1}{B} \sum_{k=1}^{N_d} \sum_{l=1}^{r_k} c_{k,l} \cdot \left[-\frac{\sqrt{E_s}\, \sigma^2_{g_k h_k}}{2} \cdot \frac{1-\xi_k}{\xi_k} \right]^l \qquad (3.188) \\ &= \frac{1}{B} \sum_{k=1}^{N_d} \sum_{l=1}^{r_k} c_{k,l} \cdot \left[-\frac{\sqrt{E_s\, \sigma^2_{h_k}\, \sigma^2_{g_k}}}{\breve{\xi}_k} \cdot \frac{1-\mu_k \breve{\xi}_k}{2} \right]^l . \qquad (3.189) \end{aligned}$$

This novel formula is applicable for arbitrary channel gain correlations.

Consider again $L = 3$, with correlated channel gains, and the first row of $\mathbf{R}_{\tilde{\mathbf{h}}}$ given by $[1.0000 \quad 0.8739 \quad 0.6268]$ (this implies that all channel gains have unit variance; recall from page 52 that we assume a Toeplitz structure for $\mathbf{R}_{\tilde{\mathbf{h}}}$) so that $\lambda(\mathbf{R}_{\tilde{\mathbf{h}}}) = \{2.5884, 0.3732, 0.0384\}$. For this case, Figs. 3.18 and 3.19 describe the performance of approximate BF, MREC, and MRC for SINC and MMSE PSAM, respectively, as evaluated from (3.189) and by simulation. These figures indicate a good agreement between analysis and simulation results. They validate our statement that approximate MRC and approximate full MREC coincide in terms of performance — see Sections 3.9.3.1 and 3.9.3.2. Furthermore, Fig. 3.18 confirms that approximate-MREC performance can degrade with increasing order: in this example, order-2 MREC outperforms full MREC (and thus approximate MRC), for $\gamma_b < 8$ dB. Actually, for this SNR range, Fig. 3.13, on page 99, shows that order-2 approximate MREC has near-optimum performance, i.e., the performance of exact full MREC (and thus exact MRC).

As inter-branch correlation changes — slowly, relative to fading, in typical scenarios [8, 130] — eigenvalues of $\mathbf{R}_{\tilde{\mathbf{h}}}$ can become nearly equal [128, Fig. 1] [130, Fig. 1]. This changes the multiplicities within the spectrum of $\mathbf{R}_{\tilde{\mathbf{h}}}$, i.e., r_k from (3.181). Then, the factors $c_{p,l}$, $p = 1 : N_d$, need to be accordingly re-computed, with the cumbersome expression from (3.186).

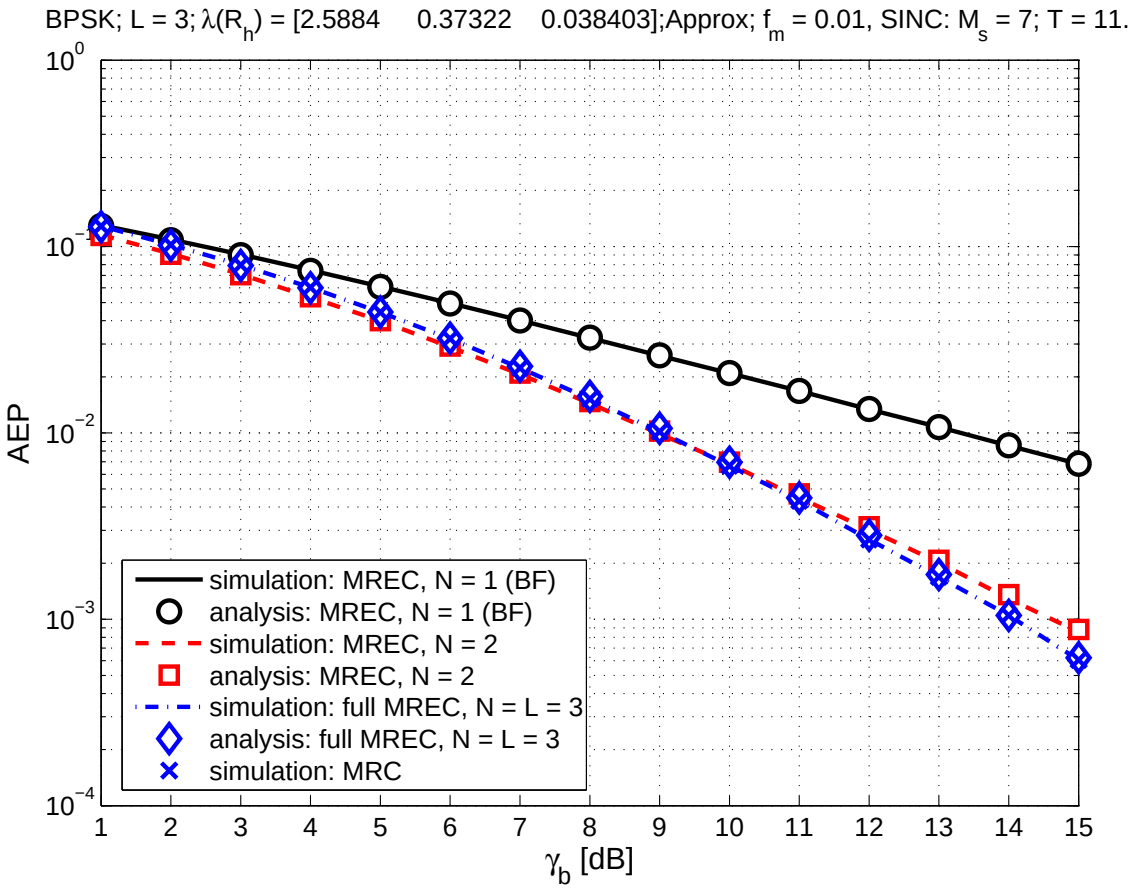

Figure 3.18. AEP vs. SNR per bit, obtained analytically, from (3.189), and by simulation, for BPSK transmitted symbols, for approximate BF, MREC, and MRC, with SINC PSAM; $L = 3$ correlated branches are employed, with $\mathbf{R}_{\tilde{\mathbf{h}}}$ spectrum given by $\lambda(\mathbf{R}_{\tilde{\mathbf{h}}}) = \{2.5884, 0.3732, 0.0384\}$.

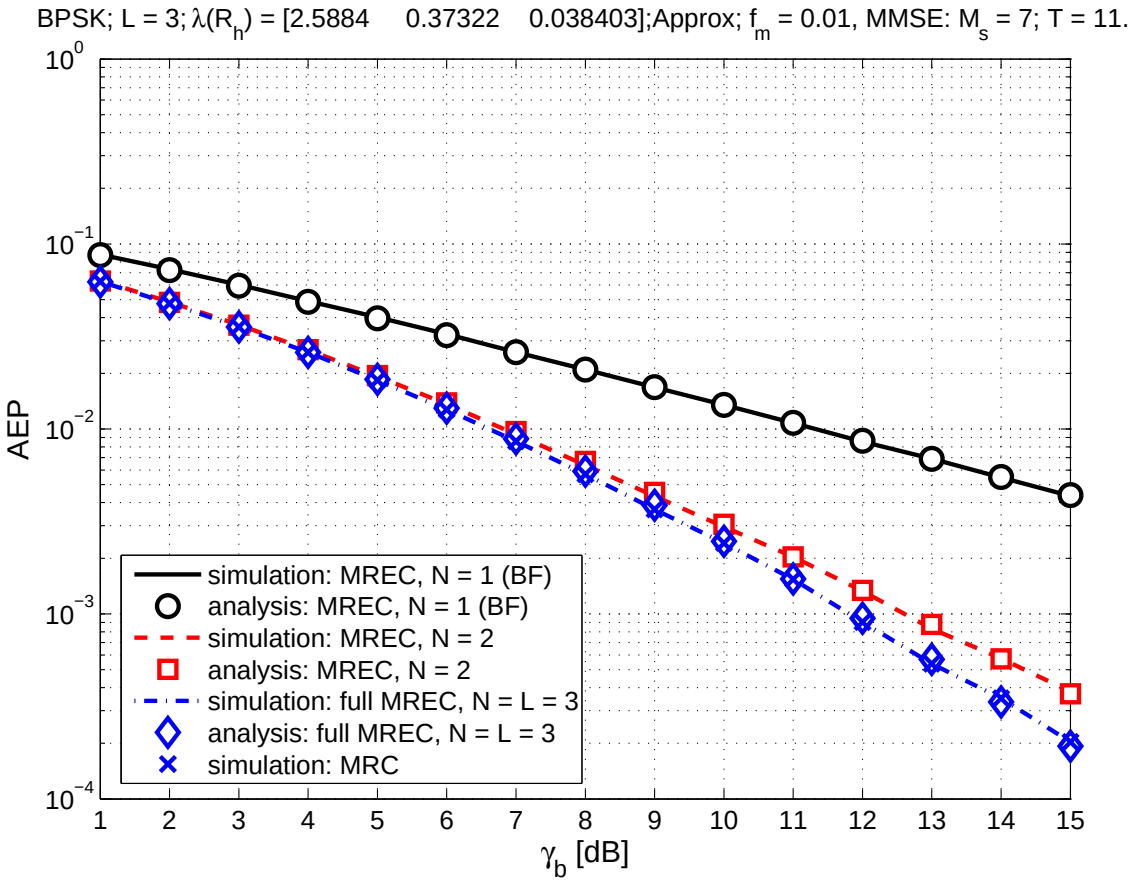

Figure 3.19. AEP vs. SNR per bit, obtained analytically, from (3.189), and by simulation, for BPSK transmitted symbols, for approximate BF, MREC, and MRC, with MMSE PSAM; $L = 3$ correlated branches are employed, with $\mathbf{R}_{\tilde{\mathbf{h}}}$ spectrum given by $\lambda(\mathbf{R}_{\tilde{\mathbf{h}}}) = \{2.5884, 0.3732, 0.0384\}$.

3.11.1.2 The Case when All Eigenvalues are Equal

Proposition 2, on page 54, states that equal eigenvalues implies i.i.d. branches. That is, eigen-branches coincide with branches. In this case we can drop the index k because $k = N_d = 1$ ($r_1 = N$). Manipulating (3.188) and (3.189) using a version of (3.186) specialized to this case, we obtain

$$\begin{aligned} P_e &= \left[\frac{1}{2}(1-\xi)\right]^N \sum_{n=0}^{N-1} \binom{N-1+n}{n} \left[\frac{1}{2}(1+\xi)\right]^n \\ &= \left[\frac{1}{2}\left(1-\mu\,\breve{\xi}\right)\right]^N \sum_{n=0}^{N-1} \binom{N-1+n}{n} \left[\frac{1}{2}\left(1+\mu\,\breve{\xi}\right)\right]^n . \end{aligned} \tag{3.190}$$

This can be shown to coincide with [30, Eqn. 59, p. 39]. Using [123, Appendix 5A, Eqns. 5A.4], (3.190) can be shown to be equivalent to [115, Appendix C, Eqn. C-18]. For p.k.c. gains we have $\mu = 1$ and (3.190) reduces to the well-known result [115, Eqn. (14.4-15)].

3.11.1.3 The Case when All Eigenvalues are Distinct

In this case $N_d = N$, and $r_k = 1$, $\forall k = 1 : N$, so that (3.188), (3.189) and (3.186) yield

$$P_e = \frac{1}{2}\sum_{k=1}^{N} S_k \cdot (1-\xi_k) = \frac{1}{2}\sum_{k=1}^{N} S_k \cdot \left(1-\mu_k\,\breve{\xi}_k\right), \tag{3.191}$$

where

$$S_k = \prod_{\substack{j=1 \\ j\neq k}}^{N} \frac{1}{\left[-a_j^2(s_{k,1}-s_{j,1})(s_{k,1}+s_{j,2})\right]}. \tag{3.192}$$

Note that, for $N = L$, this result generalizes previous results from [89, p. 308] which were obtained specifically for p.k.c. and MRC of correlated gains whose correlation matrix has only distinct eigenvalues.

Eqn. (3.191) is similar to [48, Eqn. 16, p. 421] which was derived specifically for MREC with unequal eigen-gain variances (eigenvalues), and ML estimation. Obviously, such expression fails to produce useful results when some eigenvalues can become nearly-equal — see [125, Fig. 2] — making our AEP expression (3.189) strictly necessary.

3.11.2 Approximate-MREC Analysis Results Specialized to Approximate BF and MRC

For $N = 1$, approximate MREC reduces to approximate BF, by definition. Then, a new approximate-BF AEP expression is (3.190) for $N = 1$. That coincides with the exact-BF AEP expression (3.176), on page 116. This confirms the equivalence between exact and approximate BF, stated in Section 3.9.2 at page 105.

For SINC and MMSE PSAM, we proved in Sections 3.9.3.1 and 3.9.3.2, respectively, that full approximate MREC and approximate MRC are performance-equivalent. Therefore, the above approximate-MREC analysis results, for $N = L$, apply to approximate MRC. To the best of our knowledge, Eqn. (3.188), on page 120, which we first derived in [125], is the most encompassing AEP expression available for BPSK and approximate MRC of branches with arbitrarily correlated Rayleigh fading channel gains.

Although in closed-form, the AEP expression from (3.188) has a tedious computer implementation, as opposed to the exact-MREC AEP expression we derived in (3.151), on page 109.

3.11.3 Approximate-MREC Analysis Results Specialized to Ideal MREC, BF, and MRC

The approximate-MREC AEP expressions derived in Section 3.11.1, starting on page 118, can be specialized to produce corresponding AEP expressions for ideal MREC, BF and MRC, by simply substituting $\mu_i = 1$, and $N = 1$ or $N = L$, accordingly. The results coincide with expressions derived earlier in this work specifically for those special cases.

3.11.4 Novel Performance Measures for Approximate MRC of I.I.D. Branches

As stated in Section 3.9.1, page 104, the KLT has no effect on i.i.d. branches. Gains and eigengains, branches and eigenbranches, combining and eigen-combining then coincide. Furthermore, the factors which multiply $\widetilde{g}_i$, to produce the exact-MRC weights from (3.140), page 88, are equal $\forall i = 1 : L$. Since this common factor is real-valued and positive as well, exact MRC reduces to approximate MRC, whose ith weight is simply given by $\widetilde{g}_i$ — see (3.141), page 93. Therefore, exact-MRC analysis results (i.e., AEP and OP expressions) obtained earlier for MPSK and i.i.d. channel gains also characterize approximate MRC performance.

For MPSK transmitted signal and exact MRC, the symbol error probability conditioned on the channel gain estimates can be written as (3.150)

$$P_e(\gamma) = \frac{1}{\pi}\int_0^{\frac{M-1}{M}\pi} \exp\left\{-\gamma\frac{g_{\text{PSK}}}{\sin^2\phi}\right\} d\phi, \tag{3.193}$$

where $\gamma = \sum_{i=1}^{L}\gamma_i$, and the conditioned SNR for the ith branch, γ_i, is given by (3.136), on page 88. For i.i.d. branches the above applies for approximate MRC, and can be used to derive average error probability or outage probability expressions as described next.

3.11.4.1 Approximate-MRC AEP For MPSK, I.I.D. Branches

The simple m.g.f.-based procedure described in Section 3.4.1.1, page 55, can now be employed as in Section 3.10.1, page 107, to produce the following simple, finite-limit integral, AEP expression for MPSK and exact MRC of i.i.d. branches

$$P_e = \frac{1}{\pi}\int_0^{\frac{M-1}{M}\pi} \left(1+\Gamma\frac{g_{\text{PSK}}}{\sin^2\phi}\right)^{-L} d\phi, \tag{3.194}$$

where $\Gamma \stackrel{\triangle}{=} \Gamma_1 = \Gamma_2 = \ldots = \Gamma_L > 0$, and Γ_i is the average effective SNR per branch, defined in (3.137), page 88. Since the branches are i.i.d., the above applies to approximate MRC as

well. To the best of our knowledge, (3.194) is the simplest expression available for this case. Note now that, unlike for correlated channel gains, the performance of MRC with (estimated) i.i.d. channel gains, cannot degrade by increasing the number of branches, because $\Gamma > 0$.

Using [123, Appendix 5A, Eqn. 5A.4b] for $M = 2$, Eqn. (3.194) can be shown to reduce to previous results for BPSK and approximate MRC of i.i.d. Rayleigh fading branches [30, Eqn. 59] [115, Appendix C, Eqn. C-18] [21, Eqn. 23]. However, it is not known whether the analysis methods in [21, 30, 125] can be generalized for MPSK.

For MPSK modulation, the new approximate-MRC AEP expression (3.194) is much simpler than the incomplete, non-closed-form, alternative [115, Appendix C, Eqn. C-16]. A closed-form equivalent of (3.194) can be obtained as described for exact combining in Section 3.10.2.1, page 112, by replacing N with L in Eqns. (3.154) – (3.157). For BPSK, this reduces to (3.158), or equivalently, to (3.161), and also to the expression obtained specifically for this case using approximate eigen-combining analysis, in (3.190), on page 123. Now note the coincidence between (3.158), on page 113, and (3.190), on page 123, which are, respectively, the exact- and approximate-MRC AEP expressions we derived for i.i.d. branches. This confirms our earlier statement that exact and approximate MRC coincide for i.i.d. branches.

Figs. 3.20 and 3.21 display the average symbol error probability for MPSK with $M = 2, 4, 8, 16, 64, 256$, approximate/exact MRC of $L = 5$ i.i.d. branches, for SINC and MMSE PSAM, respectively. Using the approximate relationship [115, Eqn. 5.2-62, p. 271] [123, Eqn. 8.7, p. 195] between the bit and symbol error probabilities, which is valid for Gray mapping at large symbol SNR, along with (3.194), we plot the average bit error probability for MPSK and approximate MRC of i.i.d. branches in Figs. 3.22 and 3.23.

For Rayleigh fading and p.k.c. it can be shown that BPSK and QPSK yield the same bit error probability [115, p. 832]. Figs. 3.22 and 3.23 indicate that bit error performance for BPSK and QPSK remains similar even for estimated channel gains estimation. Nevertheless,

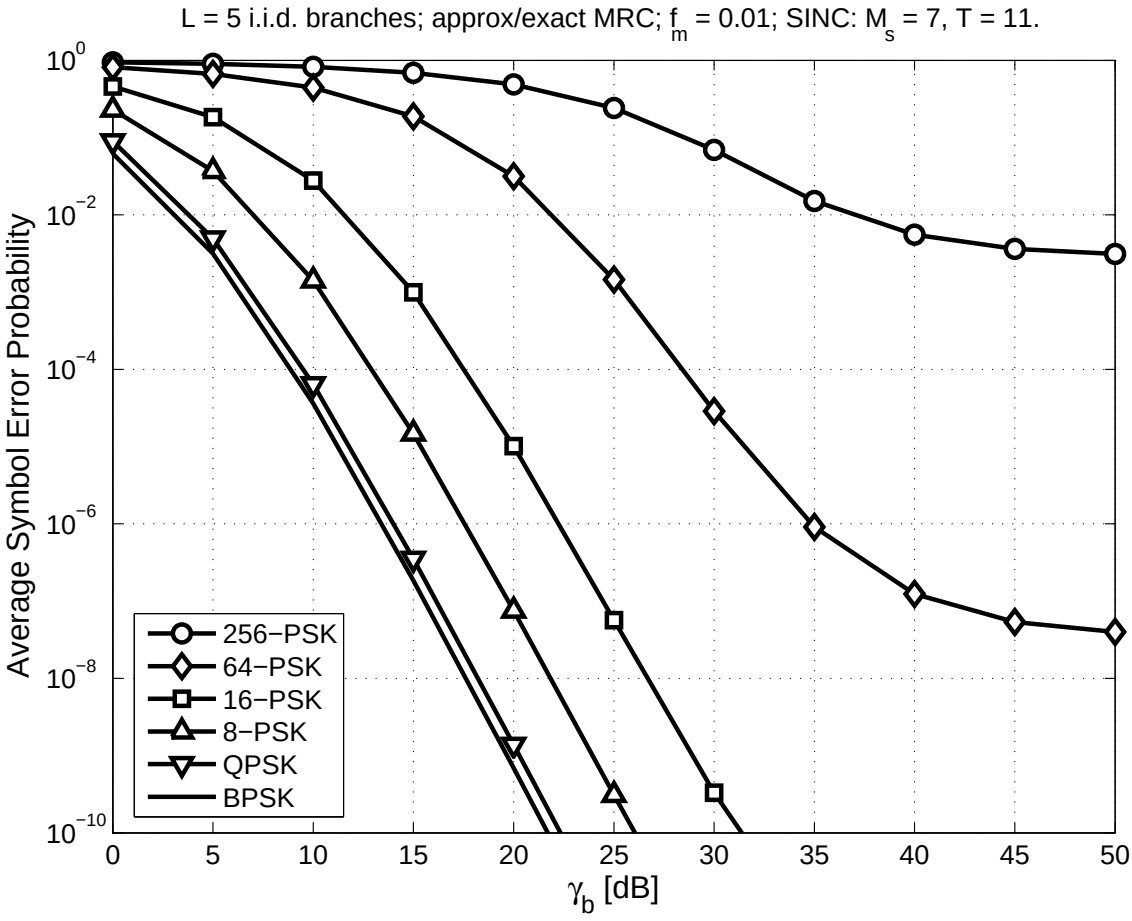

Figure 3.20. Average symbol error probability vs. SNR per bit, for approximate and exact MRC of $L = 5$ i.i.d. branches and SINC PSAM.

smaller constellations will yield lower error floors.

3.11.4.2 Approximate-MRC Outage Probability Expression For MPSK, I.I.D. Branches

Since approximate MRC coincides with exact MRC for i.i.d. branches, we can use the p.d.f. of the actual symbol detection SNR $\widetilde{\gamma}$ given by (3.162) on page 113, to derive its outage probability, as given by (3.163), on page 113. To the best of our knowledge, this result is much simpler and more accurate than previous results, e.g., the infinite-limit integral expression [95, Eqn.

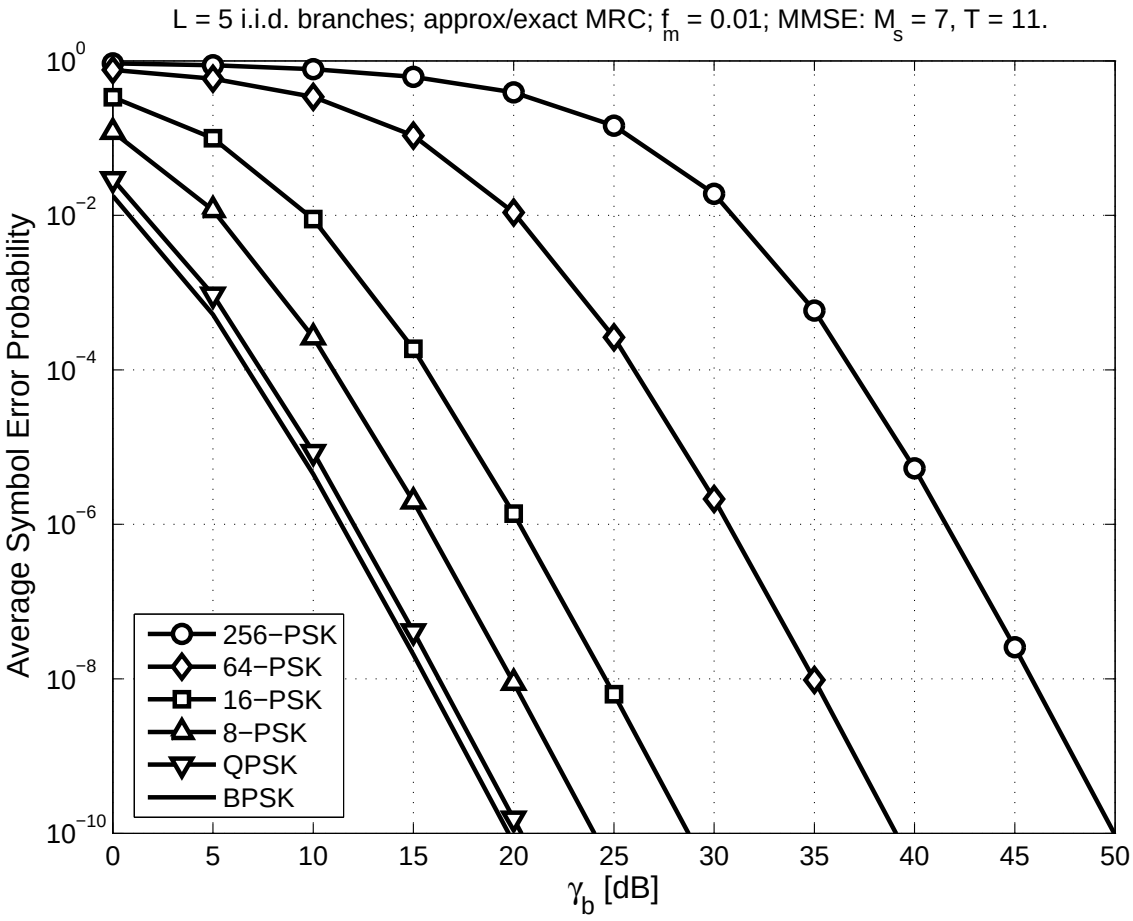

Figure 3.21. Average symbol error probability vs. SNR per bit, for approximate and exact MRC of $L = 5$ i.i.d. branches and MMSE PSAM.

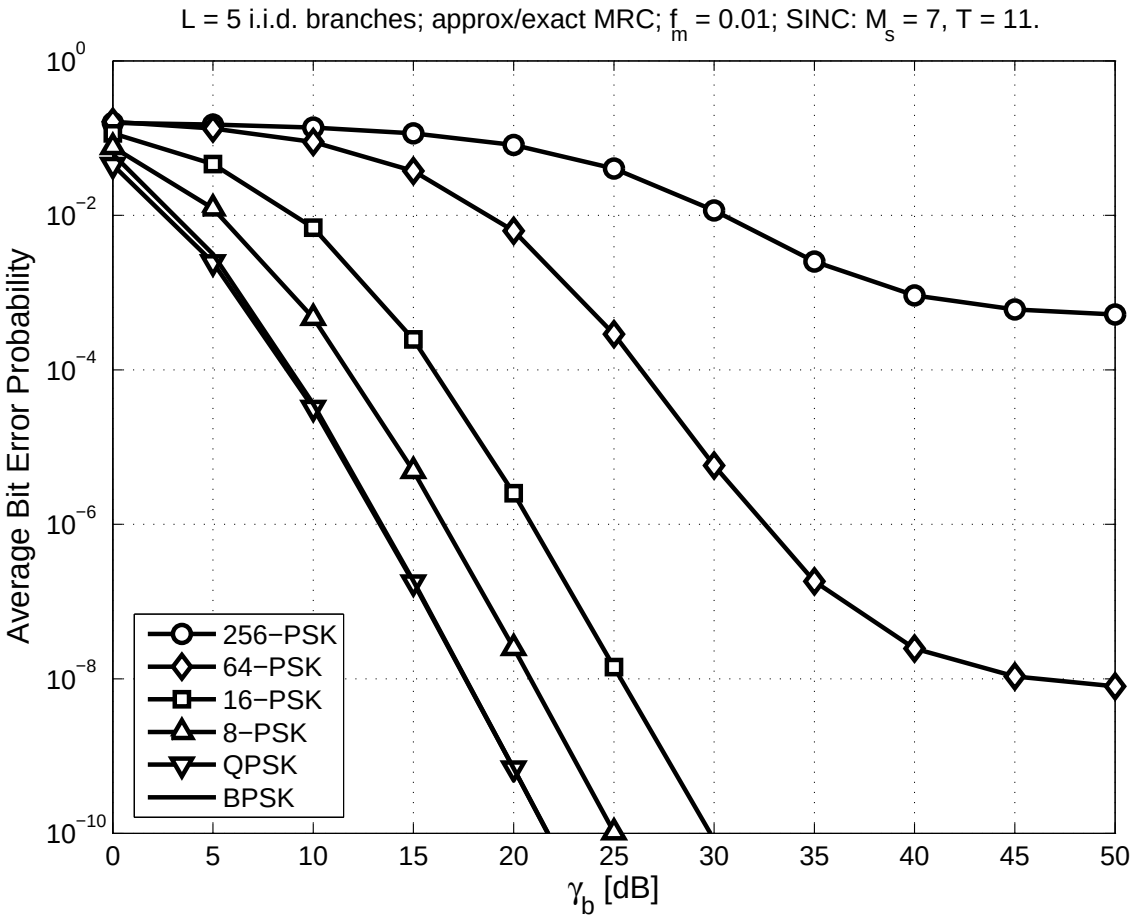

Figure 3.22. Average bit error probability vs. SNR per bit, for approximate and exact MRC of $L = 5$ i.i.d. branches and SINC PSAM.

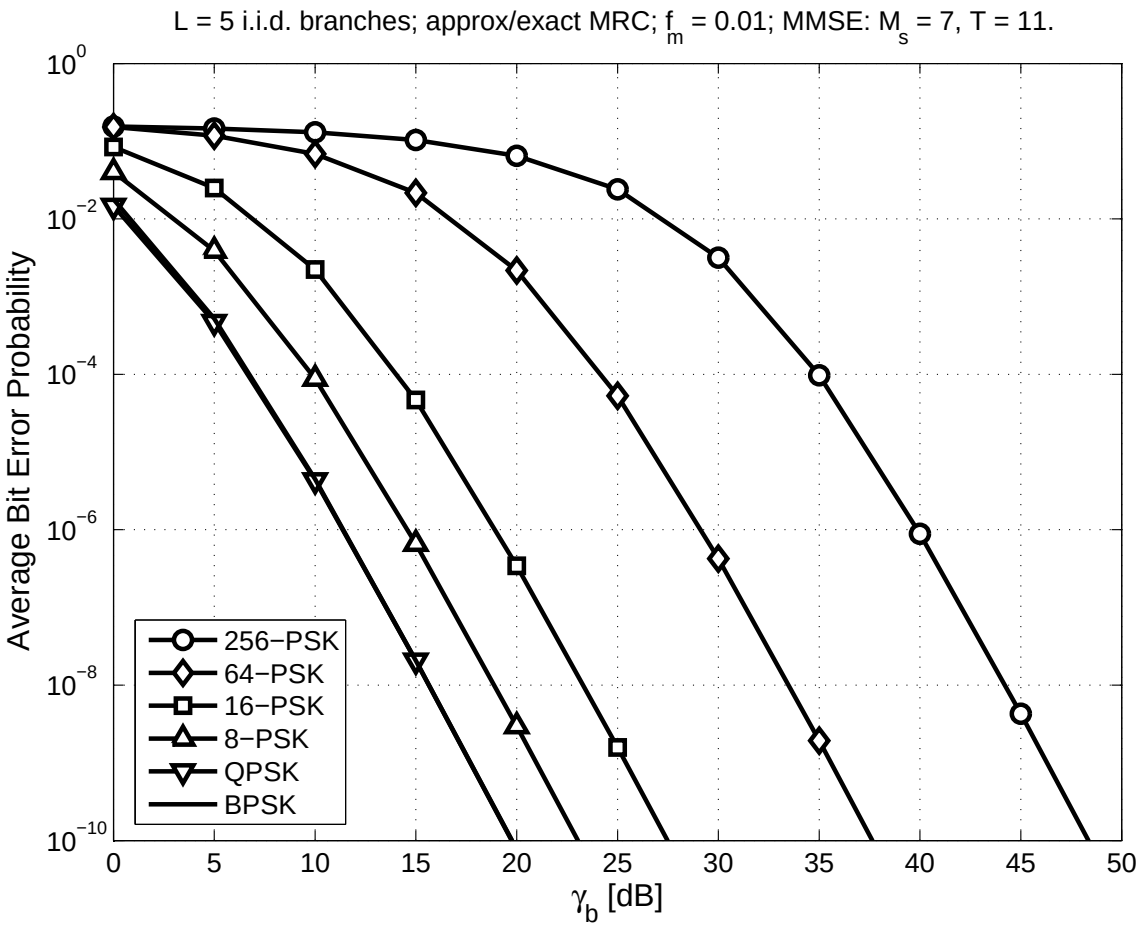

Figure 3.23. Average bit error probability vs. SNR per bit, for approximate and exact MRC of $L = 5$ i.i.d. branches and MMSE PSAM.

20], which is only an upper bound on the outage probability.

3.11.4.3 Comparison with Previous Work

We noticed intriguing similarities and differences between our exact-MRC-based analysis of approximate MRC — described above — and previous results from [21] [95].

First, at the end of their approximate-MRC analysis for BPSK, the authors of [21] defined the "effective SNR due to Gaussian errors" in [21, Eqn. 22], which then enters a closed-form AEP expression [21, Eqn. 23]. We found that their "effective" SNR coincides with our Γ, defined in (3.137), which enters our simple, finite-limit integral, AEP expression from (3.194), written for BPSK. Therefore, [21, Eqn. 23] is equivalent to our (3.190), and [30, Eqn. 59] [115, Appendix C, Eqn. C-18].

Furthermore, a cumbersome relation between the channel gain and its estimate [21, Eqn. 8] — originally proposed in [58, Eqn. 16] — is actually equivalent to (3.124), on page 85. However, [21] did not focus on the "effective" SNR conditioned on the channel gain estimates, which we defined in (3.130), on page 86, and then used to obtain (3.194). Our approach presented above is simpler and works for any MPSK constellation because the channel gain estimation error — contained in vector $\mathbf{e}$ from (3.124), page 85 — is considered as noise in our working signal model (3.125), page 85, unlike in [21].

In [95, Section IV.A], an approximate-MRC analysis approach for i.i.d. branches and MPSK is presented. Relying on [58, Eqn. 16], this approach compounds the channel estimation errors with the receiver noise and employs the "effective" SNR conditioned on the channel gain estimates for performance analysis based on the m.g.f. of this SNR. Nevertheless, only an upper bound on the average symbol error probability is provided for MPSK, although exact bit error probability expressions are also claimed possible, for BPSK and QPSK (with Gray mapping). Note that results from [95] can be employed to extend our error and outage probability analysis

Table 3.7. Numerical complexity (no. of complex multiplications/additions) for L branches

Combining method	Interpolation method	MRC	order-N MREC
approximate	SINC	$L(T+1)$	$N(L+T+1)$
	MMSE	$L(LT+1)$	$N(L+T+1)$
exact	SINC	$L(L+T+1)$	$N(L+T+2)$
	MMSE	$L(LT+L+1)$	$N(L+T+2)$

for Ricean channel fading.

3.12 BF, MREC, and MRC — a Complexity Comparison

The numerical complexities of MRC and order-N MREC, in terms of the number of complex multiplications/additions required per symbol for KLT, interpolation, and combining, were determined as shown in Table 3.7. As SINC interpolation is data-independent, while MMSE interpolation as well as channel gain correlation matrix eigen-decomposition depend only on channel statistics, which change much more slowly than the fading, their computations are not included [1, 8, 130].

The complexity expressions from Table 3.7 were evaluated for $L = 5$ and $T = 11$, and the results are plotted in Fig. 3.24, allowing for the following complexity comparison of MREC, MRC, and BF, for SINC/MMSE interpolation and approximate/exact combining:

i) MREC complexity is not higher with MMSE interpolation than with SINC interpolation, since the eigengains can be estimated independently, as shown in (3.107), on page 82. On the other hand, MRC complexity increases several-fold for MMSE interpolation compared to SINC interpolation, because correlated branches are estimated independently for SINC PSAM, as shown in (3.110), on page 83, but concurrently for MMSE PSAM,

as shown in (3.113), on page 83.

ii) For the same reason as above, MREC complexity is not significantly larger with exact combining compared to approximate combining. For MRC, the relative increase in complexity for exact vs. approximate combining is larger when SINC interpolation is employed.

iii) MREC complexity increases linearly with order, so that BF is the least complex.

iv) for MMSE PSAM, MRC is several times more complex than full MREC — due to the way estimation takes place — although they are equivalent in performance. For SINC PSAM and exact combining, MRC and full MREC have similar complexity, while for approximate combining, MRC can be less complex than high-order MREC.

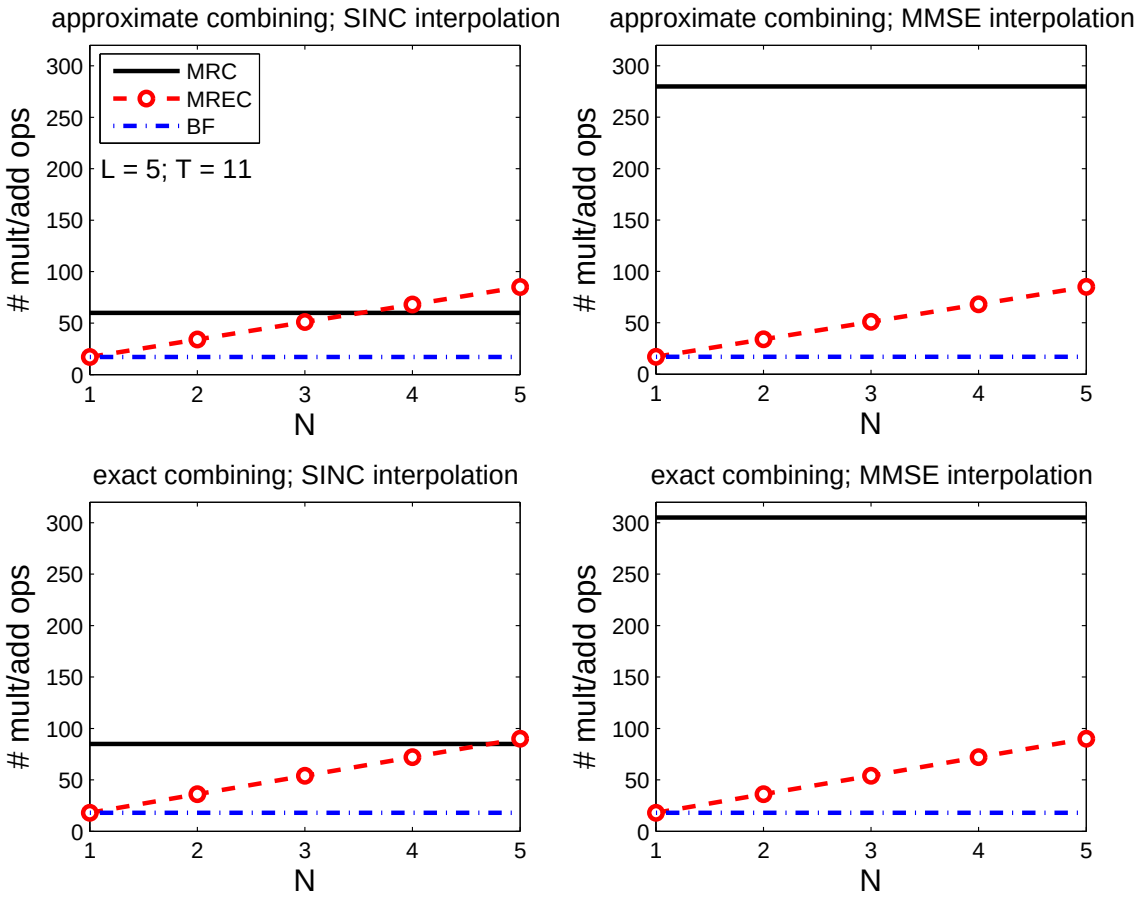

Figure 3.24. Numerical complexity (in terms of the number of complex multiplications and additions) required per symbol for MRC, MREC, and BF, for $L = 5$, $T = 11$.

Chapter 4

MREC Performance–Complexity Tradeoff for Realistic Scenarios

4.1 Chapter Overview

In the previous chapter we provided symbol-detection performance comparisons between BF, MRC, and MREC for artificially selected sets of inter-branch correlations. Furthermore, the complexity comparison was limited since it did not relate to the channel conditions or performance. In this chapter we make comparisons that are more representative of what happens in actual practice. Using computer evaluations, we compare the performance and complexity of these combiners for typical scenarios, for Laplacian power azimuth spectrum (p.a.s.) with slowly varying log-normal distributed azimuth angle spread (AS). MREC performance–complexity tradeoffs are found to provide high performance for significant computational savings. The next chapter will take our comparison to the more practical level of fixed-point implementation.

4.2 Azimuth Angle Spread Model

4.2.1 Laplacian Power Azimuth Spectrum and Azimuth Angle Spread

In wireless communications, wave scattering [60,75,89,106,116,140] induces azimuthal angle dispersion or spread, which has been thoroughly characterized in recognition of its important effect on performance [2,8,53,56,98,106,108,109,131,145].

The channel's spatial selectivity, i.e., the antenna decorrelation [101,117,118], is affected by the power azimuth spectrum (p.a.s.), which can be defined as [8,108,109]

$$P(\theta) = \int E\left\{ \sum_{p} |\alpha_p|^2 \, \delta(\theta - \theta_p, \tau - \tau_p) \right\} d\tau, \tag{4.1}$$

where the summation terms correspond to the multiple arriving signal paths, with α_p, θ_p, and τ_p being the complex-valued gain, angle of arrival (AoA), and time delay, respectively, for the pth arriving path. The averaging is over the path gains, and $\delta(\cdot)$ represents the Dirac delta function. The angles are measured with respect to antenna broadside, i.e., the line perpendicular to the line that connects the antenna elements, for a uniform linear array (ULA).

Let us consider a truncated Laplacian p.a.s., which is described by [118]

$$P(\theta) = \begin{cases} \frac{1}{1-\exp\left\{-\frac{\pi}{\sigma/\sqrt{2}}\right\}} \cdot \frac{1}{2\cdot\sigma/\sqrt{2}} \cdot \exp\left\{-\frac{|\theta-\theta_c|}{\sigma/\sqrt{2}}\right\} & , \quad \text{for } \theta \in [\theta_c - \pi, \theta_c + \pi] \\ 0 & , \quad \text{otherwise,} \end{cases} \tag{4.2}$$

where θ_c is the average AoA, while σ approximates the p.a.s. root second central moment [108], and is hereafter referred to as *azimuth spread* (AS) [8,118]. The Laplacian p.a.s. accurately models actual radio channel measurements for rural, sub/urban, and indoor scenarios [2,8,108,109,131].

Mathematical operations similar to those shown in [117, Appendix] [118], lead to the following expressions for the real and imaginary parts of the (m,n)th element of $\mathbf{R}_{\tilde{\mathbf{h}}}$ for a ULA:

$$\Re\{(\mathbf{R}_{\tilde{\mathbf{h}}})_{m,n}\} \;=\; J_0(z_{m,n}) + 2\sum_{k=1}^{\infty} J_{2k}(z_{m,n}) \cdot \frac{\cos(2k\,\theta_c)}{1 + \left[2k\,\sigma/\sqrt{2}\right]^2} \tag{4.3}$$

$$\Im\{(\mathbf{R}_{\tilde{\mathbf{h}}})_{m,n}\} \;=\; \frac{1+\exp\left\{-\frac{\pi}{\sigma/\sqrt{2}}\right\}}{1-\exp\left\{-\frac{\pi}{\sigma/\sqrt{2}}\right\}} \cdot 2\sum_{k=0}^{\infty} J_{2k+1}(z_{m,n}) \cdot \frac{\sin[(2k+1)\,\theta_c]}{1+\left[(2k+1)\,\sigma/\sqrt{2}\right]^2}, \quad (4.4)$$

where $J_i(z)$ is the ith-order Bessel function of the first kind [6, §9.1.21, p. 360], given by

$$J_i(x) \stackrel{\triangle}{=} \frac{1}{\pi}\int_0^{\pi} \cos(x\sin\theta - i\,\theta)d\,\theta, \quad (4.5)$$

$z_{m,n} \stackrel{\triangle}{=} \pi\,(m-n)\,\frac{d}{\lambda_c/2}$, d is the distance between adjacent sensors in the array, and λ_c is the wavelength of the carrier signal; we will refer to $d_n \stackrel{\triangle}{=} \frac{d}{\lambda_c/2}$ as normalized inter-element distance. Unless specified otherwise, numerical results shown in this work assume $d_n = 1$ and $\theta_c = 0$; the latter yields real-valued inter-element correlation. Note that the above correlation expressions, used for numerical results shown hereafter, yield unitary autocorrelations for the channel gains as well as a Toeplitz structure for $\mathbf{R}_{\tilde{\mathbf{h}}}$ for a ULA.

For numerical results shown hereafter the channel gain vector samples were generated as in [106, Section 3.6], assuming separable temporal and spatial correlations [101, Section 2.2.2, and Appendix A] [106, Section 3.6]. First, spatially independent and temporally correlated Gaussian samples are produced using the procedure from [153], as described in Section 2.4.1, page 16. The output vector is then left-multiplied by the square root of the correlation matrix computed with (4.3) and (4.4), yielding the intended spatial and temporal statistics.

4.2.2 Azimuth Spread Effect on Antenna Correlation

Note that antenna correlation is a function of the p.a.s. type [117, 118], AS, normalized inter-element distance $d_n = \frac{d}{\lambda_c/2}$, and average AoA θ_c. The AS depends on the environment as well as antenna array location and height [8, 108, 109, 131], and varies more slowly than the channel gains [8].

Consider a ULA with $L = 5$ elements and normalized inter-element distance $d_n = 1$, i.e., the physical distance equals half the carrier wavelength. Then, for $\theta_c = 0°$, Fig. 4.1 shows the

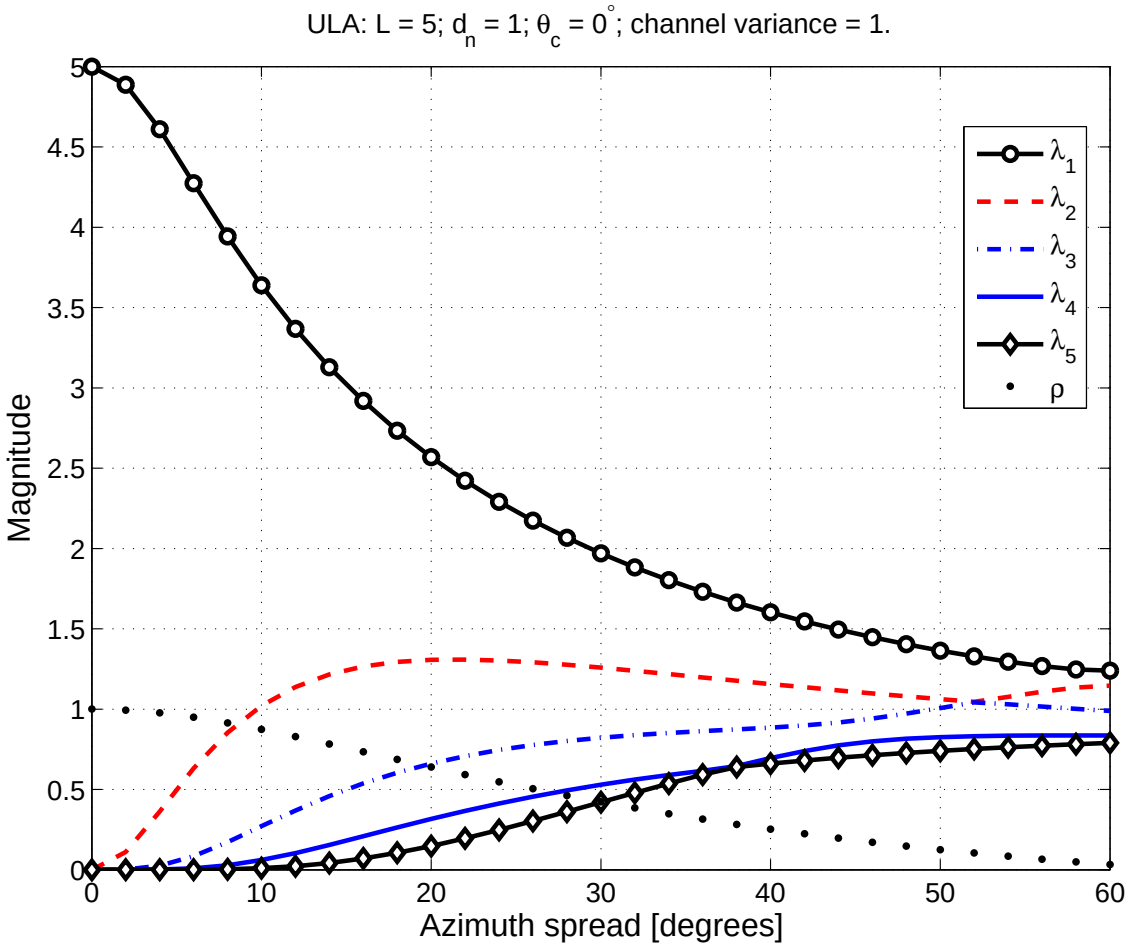

Figure 4.1. Correlation between adjacent ULA elements and the eigenvalues of the $\mathbf{R}_{\tilde{\mathbf{h}}}$, for $d_{\mathrm{n}} = 1$, $\theta_c = 0^{\circ}$, and Laplacian power azimuth spectrum.

correlation, ρ, between any two adjacent antennas, computed with (4.3), and the eigenvalues, $\lambda_i, i = 1 : L$, of the channel gain correlation matrix, $\mathbf{R}_{\tilde{\mathbf{h}}}$. On the horizontal axis we represented AS.

Notice the AS impact on antenna correlation and thus on relative eigenvalue magnitudes. For small AS, the received signals are highly correlated, and the received intended-signal energy, proportional to $\mathrm{tr}(\mathbf{R}_{\tilde{\mathbf{h}}})$, is concentrated along the first few eigen-directions. Then, the

channel is said to be spatially non-selective [101, Section 2.2.2, p. 37], and the available diversity gain is small [77]. When AS increases, antenna correlation decreases, and the energy is distributed more uniformly along all eigen-directions. Then, the channel becomes spatially more selective and higher diversity gain becomes available.

Let us now complete the discussion on the effects of the channel scattering and antenna geometry on inter-element correlation. Fig. 4.2 shows faster correlation decrease with increasing inter-element distance, for larger AS. For a compact antenna array with $d_{\mathrm{n}} = 1$, AS $< 20^{\circ}$ produces inter-element correlation greater than 0.5, which is significantly high, i.e., it leads to severe diversity gain reductions [63,123]. For AS $< 10^{\circ}$, correlation remains high even for normalized distances as large as $d_{\mathrm{n}} = 3$. Fig. 4.3 indicates that the correlation coefficient tends to increase with increasing mean-AoA. This was also observed for uniform p.a.s. in [101, Section 2.2.2] [117] and for Gaussian and Laplacian p.a.s. in [139].

4.2.3 Azimuth Spread Model for Typical Urban Scenario

It was found by measurement that the AS depends on the environment, antenna array location and height, and is time-varying [8, 53, 56, 98, 108, 109, 131, 145]. Measurements for typical suburban and urban scenarios [8] have shown that the base-station AS — measured in degrees — can be well modeled as a random variable with log-normal distribution, i.e.,

$$\mathrm{AS} = 10^{\varepsilon x + \mu}; \quad x \sim \mathscr{N}(0,1). \tag{4.6}$$

This model was also proposed by the 3rd Generation Partnership Project (3GPP) [2] for channel simulation purposes.

In this work we will present numerical results for the typical urban (TU) scenario measured in [8] and described in Table 4.1, for which $\varepsilon = 0.47$, and $\mu = 0.74$. Then, the AS takes predominantly small-to-moderate values, e.g., $\Pr(1^{\circ} < AS < 20^{\circ}) \approx 0.8$ [2, 8, 106, 108].

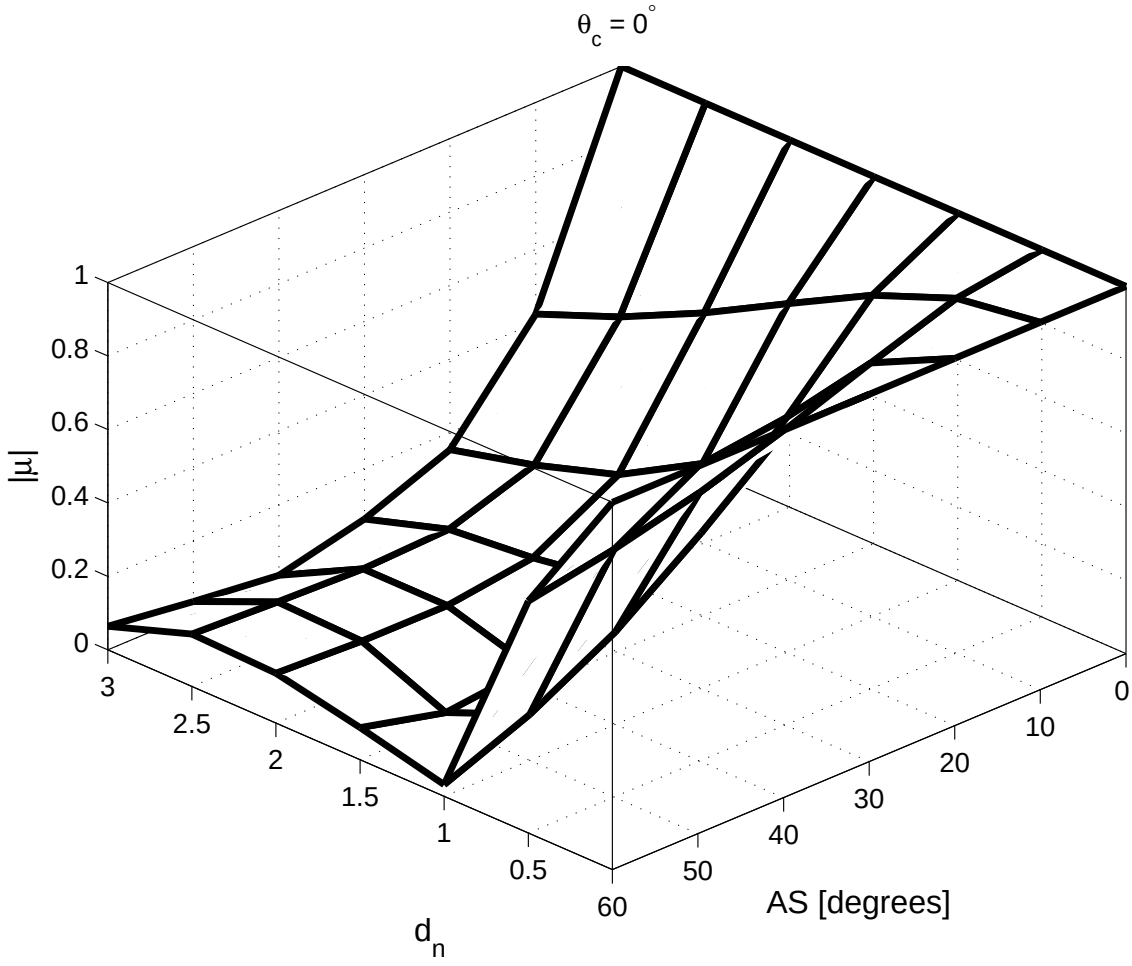

Figure 4.2. Correlation coefficient vs. normalized inter-element distance, d_{n}, and AS; Laplacian power azimuth spectrum, mean AoA $\theta_c = 0^{\circ}$.

Table 4.1. Typical urban (TU) scenario: Aarhus, Denmark [8]

buildings height/distribution	4 – 6 floors/uniform density
street layout	irregular
line of sight	not present
mobile station – base station distance	0.2 to 1.1 km
antenna location/height	above rooftop level/32 m-high

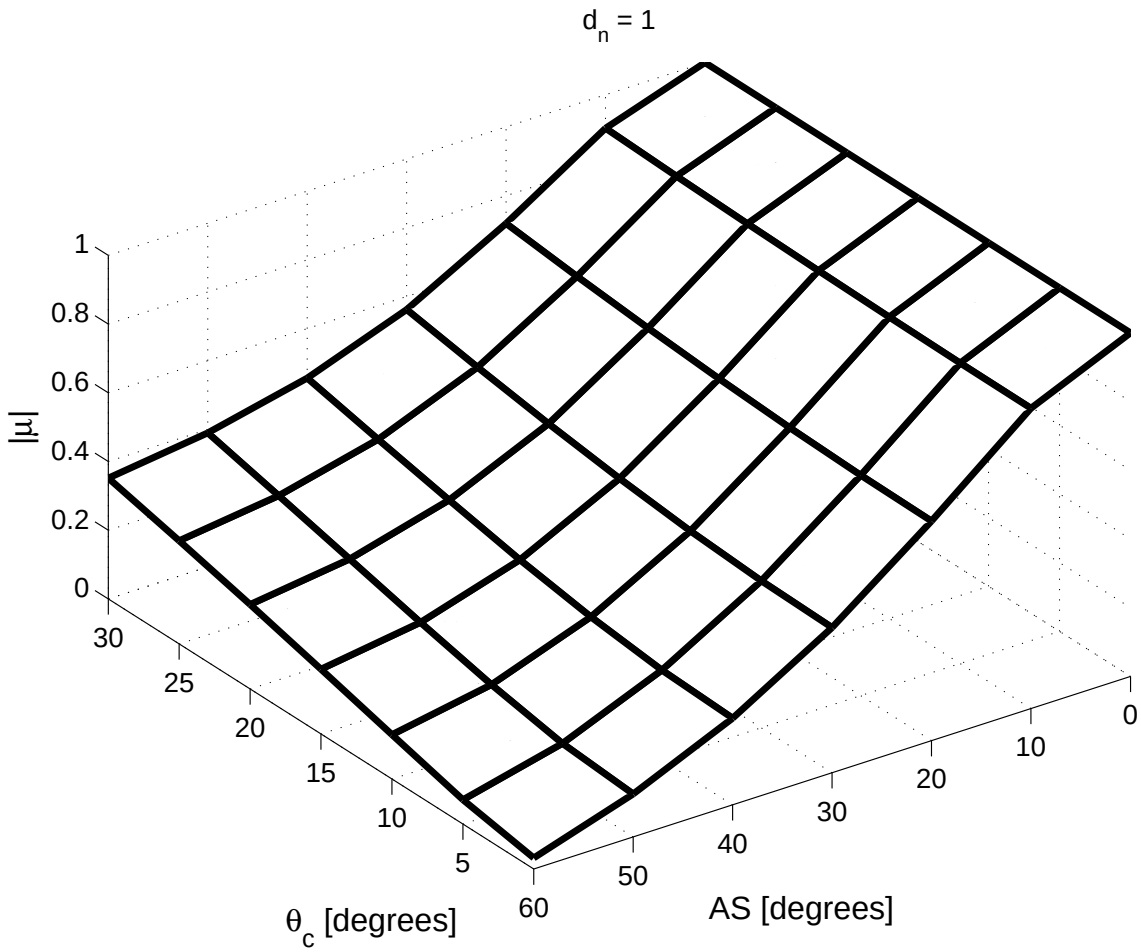

Figure 4.3. Correlation coefficient for adjacent antenna elements vs. mean AoA, θ_c, and AS; Laplacian power azimuth spectrum, normalized inter-element distance $d_{\mathrm{n}} = 1$.

Table 4.2. Mobile, channel, and receiver (channel estimation) parameters

	Parameter	Value
Mobile	Mobile speed	$v = 16.67$ m/s $= 60$ km/h
	BPSK transmitted symbol rate	$f_s = 10$ ksps
	Carrier frequency	$f_c = 1.8$ GHz
	Pilot symbol period [39, Sect. III.C]	$M_s = 39$
Channel	Maximum Doppler frequency	$f_D = 100$ Hz
	Normalized maximum Doppler frequency	$f_m = f_D / f_s = 0.01$
	Channel coherence time [116, Eqn. 4.40.b]	$T_c \approx 1.8$ ms
	Channel coherence distance	$d_c = v T_c \approx 30$ mm
Receiver	Interpolator size [39, Sect. III.D]	$T = 11$

Mobile station displacement causes AS variations [8, 98, 109]. For TU scenarios, the expression for the spatial correlation of the AS was empirically determined as [8]

$$\rho_{AS}(d) = e^{-d/d_{AS}}, \tag{4.7}$$

where d is the distance traveled by the mobile station, and d_{AS} is the AS *decorrelation distance*, i.e., the distance over which the AS correlation decreases by a factor of two. Comparing d_{AS}, measured in [8] for the TU scenario at $d_{AS} = 50$ m, with the fading coherence distance d_c, computed for the typical system parameter values from Table 4.2 at $d_c \approx 0.03$ m, we conclude that the AS variation is much slower (by 3 orders of magnitude) than the fading. The parameter values from Table 4.2 have been employed for the numerical results shown throughout this chapter.

4.3 BF, MRC, and MREC Performance and Complexity Comparison for Non-Random AS

Let us consider a SIMO communication system for which the transmitter, channel, antenna, and receiver parameters take the values set above. Hereafter, for plotting numerical results we employ the actual average SNR per symbol, defined in (2.79), on page 37. Since unit variance channel gains are assumed, this SNR will actually stand for E_s/N_0.

Then, the top subplot in Fig. 4.4 shows again the correlation of channel gains at adjacent antenna elements, and the eigenvalues of $\mathbf{R}_{\tilde{\mathbf{h}}}$, vs. the AS. The middle subplot shows the average error probability (AEP) for exact MREC, computed using (3.151), on page 109, for BPSK, $E_s/N_0 = 5$ dB, and MMSE PSAM. The lines indicating the worst and the best performance correspond to BF and MRC, respectively.

As also noticed in previous work [36, 42, 47, 77], BF performance degrades with increasing AS, because it relies on branch coherence, as opposed to available diversity gain. On the other hand, MRC employed at very low AS performs similarly to BF, for about 16 times higher complexity, as Table 3.7, on page 132, indicates.

For larger AS, Fig. 4.4 shows that MREC of order-2 or more, which exploits available diversity gain, can greatly outperform BF. Actually, for small-to-moderate AS, e.g., $1^\circ < \text{AS} < 20^\circ$, low-order MREC can perform as well as the much more complex MRC (performance-equivalent to full MREC). For example, Fig. 4.4, along with Table 3.7 and Fig. 3.24 from Section 3.12, on page 132, indicate that MRC-like performance can instead be attained with MREC of appropriately-selected order, for the important complexity savings shown in Table 4.3.

Recall from Section 4.2.3, on page 139, that the AS takes predominantly small-to-moderate values, e.g., $\Pr(1^\circ < AS < 20^\circ) \approx 0.8$ [8, 108], for the TU scenario under consideration. Then, Fig. 4.4 and Table 4.3 suggests that MREC with adaptive order selection can yield significant

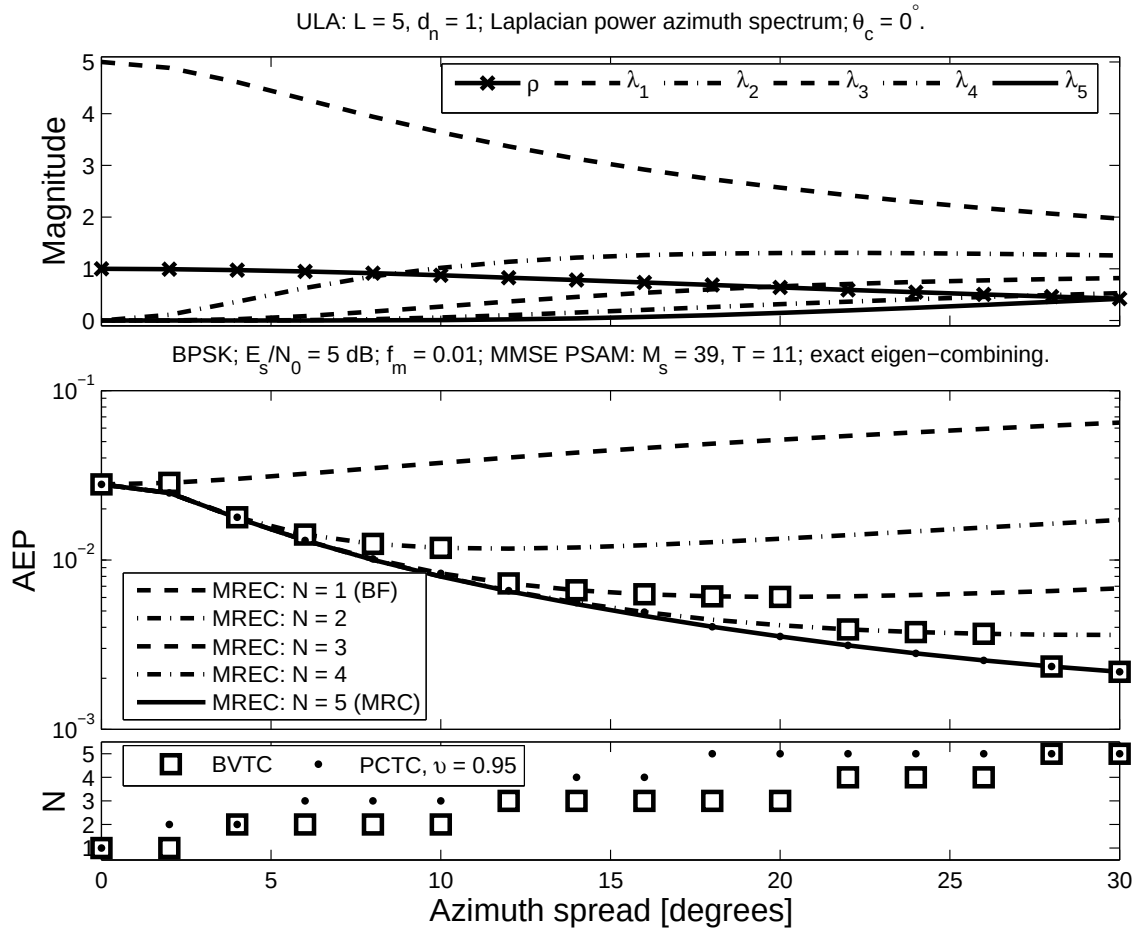

Figure 4.4. Top: fading correlation for adjacent antenna elements, ρ, and channel correlation matrix eigenvalues, $\lambda_i, i = 1 : L$; Middle: exact-MREC AEPs obtained with (3.151), on page 109, for BPSK and MMSE PSAM eigengain estimation; BF performs poorly for non-zero AS; MRC-like performance can be achieved with MREC, at much lower complexity; Bottom: MREC order selected with criteria described in Section 4.4.

Table 4.3. Computational savings available with exact MREC vs. exact MRC.

Azimuth spread range	MREC order	Savings
AS $\in [0^\circ, 6^\circ)$	N = 2	88%
AS $\in [6^\circ, 12^\circ)$	N = 3	82%
AS $\in [12^\circ, 18^\circ)$	N = 4	76%
AS $> 18^\circ$	N = L = 5	70%

performance gains and complexity savings over BF and MRC, respectively.

4.4 Order Selection for MREC

4.4.1 Previous Criteria

Drawing on previous results on reduced-dimension eigen-combining [76, 77], a possible criterion for MREC adaptation is

$$\min_{N=1:L} E\left\{E_s \cdot \|\mathbf{\Pi}_{L-N}\widetilde{\mathbf{h}}\|^2 + \|\mathbf{\Pi}_N \widetilde{\mathbf{n}}\|^2\right\}, \tag{4.8}$$

where $\|\cdot\|$ stands for Euclidian norm, $\mathbf{\Pi}_N \stackrel{\triangle}{=} \mathbf{E}_N \mathbf{E}_N^H$ is the orthogonal projection on the subspace spanned by the columns of $\mathbf{E}_N$, and $\mathbf{\Pi}_{L-N} \stackrel{\triangle}{=} \mathbf{I}_L - \mathbf{\Pi}_N$. This criterion is equivalent to

$$\min_{N=1:L}\left[E_s \cdot \sum_{i=N+1}^{L} \lambda_i + N_0 \cdot N\right] \tag{4.9}$$

and is better known as the *bias–variance tradeoff* criterion [77] (BVTC) because (4.9) balances the loss incurred by removing the weakest $(L-N)$ intended-signal contributions (the first term) against the residual-noise contribution (the second term). Although applicable for both approximate-MREC [77] and exact-MREC, the BVTC does not account for the actual combining approach, Doppler rate, channel estimation method and its parameters (M_s, T).

Furthermore, the BVTC requires knowledge of the smallest eigenvalues, which might not be estimated accurately.

To ensure that the selected order depends on the estimation method and its parameters, Dietrich *et al*. [47] applied the following MMSE criterion (MMSEC)

$$\min_{N=1:L} E\left\{\|\widetilde{\mathbf{h}}-\mathbf{E}_N\,\mathbf{g}\|^2\right\} \tag{4.10}$$

for approximate-MREC order selection. However, the MMSEC does not necessarily minimize the AEP for maximum-likelihood eigengain estimation [47, Section VI] or for SINC PSAM [127, Fig. 4]. Furthermore, the MMSEC cannot reduce the problem dimension for MMSE PSAM, regardless of antenna correlation, symbol SNR, or fading rate [127, Section V].

A common, important, BVTC and MMSEC drawback is disregard of the ensuing MREC complexity and symbol-detection performance. These criteria can thus 1) waste processing resources on inaccurately estimating insignificant eigengains and on high-dimensional combining, or 2) ignore eigen-directions with needed performance-enhancing potential.

4.4.2 Proposed Performance–Complexity Tradeoff Criterion (PCTC)

For Rayleigh fading and MPSK, the exact-MREC AEP given by (3.151), on page 109, is a non-increasing function of the MREC order, N. Further, since $\sin^2\phi \leq 1$, Eqn. (3.151) implies

$$P_{e,N} \leq \frac{P_{e,N-1}}{1+\Gamma_N \cdot \sin^2\frac{\pi}{M}}, \tag{4.11}$$

i.e., order-N MREC will guarantee an AEP decrease by the factor $\left[1+\Gamma_N \cdot \sin^2\frac{\pi}{M}\right]$ over order-$(N-1)$ MREC. This decrease is larger for smaller signal constellation sizes as well as for larger Γ_N. However, this improvement may not be worth the extra computational complexity of estimating the additional eigengain. Therefore, we propose the following performance–complexity tradeoff criterion (PCTC): use the Nth eigenbranch only if it guarantees

$$P_{e,N} \leq \upsilon \cdot P_{e,N-1}, \tag{4.12}$$

where $\upsilon \in (0,1)$ is a design parameter chosen based on eigengain estimation complexity and receiver processing load. A *sufficient* condition for (4.12) to hold is that

$$\Gamma_N \geq \Gamma_c \stackrel{\triangle}{=} \frac{\left(\upsilon^{-1}-1\right)}{\sin^2 \frac{\pi}{M}}, \tag{4.13}$$

where Γ_c is the *cutoff* average effective SNR. (The derivation of the *necessary* condition for (4.12) is not tractable). The PCTC selects as MREC order the largest value of N for which (4.13) holds. (Note that, unlike the BVTC-based approach, the PCTC may not require knowledge of weak eigenvalues, whose estimates may be inaccurate.) When the channel conditions are so poor that $\Gamma_2 \not\geq \Gamma_c$, the receiver will deploy BF. Otherwise, higher-order MREC is selected. For very good channel conditions, the MREC order N output by our criterion may approach or equal L. The above PCTC needs to be supplemented with a condition for switching from order-N MREC to MRC only if MREC complexity can become higher than MRC complexity, which is not the case for numerical results shown next.

In Fig. 4.4, on page 144, the lower subplot shows the MREC order selected with the PCTC for $\upsilon = 0.95$, and with the BVTC. The corresponding AEP values for adapted MREC appear in the middle subplot. For this choice of υ, the proposed PCTC can outperform the BVTC, at the price of higher complexity. The situation may reverse when complexity is more important, i.e., for smaller υ imposed in the PCTC. The effectiveness of the PCTC-based MREC is evident at $\mathrm{AS} = 10^\circ$, where MREC yields almost the same (lowest) AEP for $3 \leq N \leq L = 5$, but $N = 3$ is selected, to minimize complexity. The BVTC selects $N = 2$, even though the performance may be unacceptable and sufficient processing resources may still be available. The SNR thresholds for a PCTC-based MREC receiver can be adapted to the base station load, so that they increase before the signal processing resources are exhausted, thus yielding higher user capacity and graceful performance degradation.

4.5 BF, MRC, and MREC Performance and Complexity Comparison for Random AS

For the same settings as selected earlier in this chapter, and the TU scenario described in Table 4.1, on page 140, we generated $10,000$ independent log-normal AS samples using (4.6), on page 139. The AS average and standard deviation were 9.76° and 13.43°, respectively. The correlation matrix $\mathbf{R}_{\tilde{\mathbf{h}}}$ and its eigenvalues were computed at every AS sample, and the exact-MREC AEP was computed using (3.151), on page 109, for MMSE PSAM.

Then, Fig. 4.5 shows results after averaging over the AS samples. The upper subplot indicates that PCTC-based MREC can significantly outperform BF, e.g., by almost 5 dB at AEP $= 10^{-2}$, and more than 7 dB at AEP $\approx 10^{-3}$. The AEP plots for MREC of order $N = 3,4$ are not shown because they almost overlap the full-MREC AEP plot. Note that higher MREC order is selected with both BVTC and PCTC for increasing SNR.

Fig. 4.5, along with Table 3.7, on page 132, indicate that, for symbol-SNR in the range $[0 \text{ dB}, 10 \text{ dB}]$, PCTC-based adaptive exact MREC achieves optimum performance (i.e., the exact-MRC performance) for about $80\% - 90\%$ lower complexity than that of exact MRC.

Finally, Fig. 4.6 displays, in the top subplot, the AS for the considered TU scenario computed using (4.6) and (4.7). The mobile station travels a 125 m distance in 7.5 s and transmits $75,000$ symbols. To emulate actual updating, $\mathbf{R}_{\tilde{\mathbf{h}}}$ and its eigenstructure are recalculated once every $d_{\text{AS}}/20 = 2.5$ m (or 1500 symbols). Over this distance there is small AS variation. For the results shown in this chapter the slot length was selected as $M_{\text{s}} = 39$, which, for $f_{\text{m}} = 0.01$, satisfies the condition from (2.76), on page 36. Referring back to Fig. 2.4 and our comments on page 23, we learn that channel gain samples separated by 39 symbols are nearly uncorrelated. Therefore, within the frame of 1500 symbols there is a sufficient number of uncorrelated pilot samples to allow for accurate eigen-structure estimation, e.g., as in [100, 101].

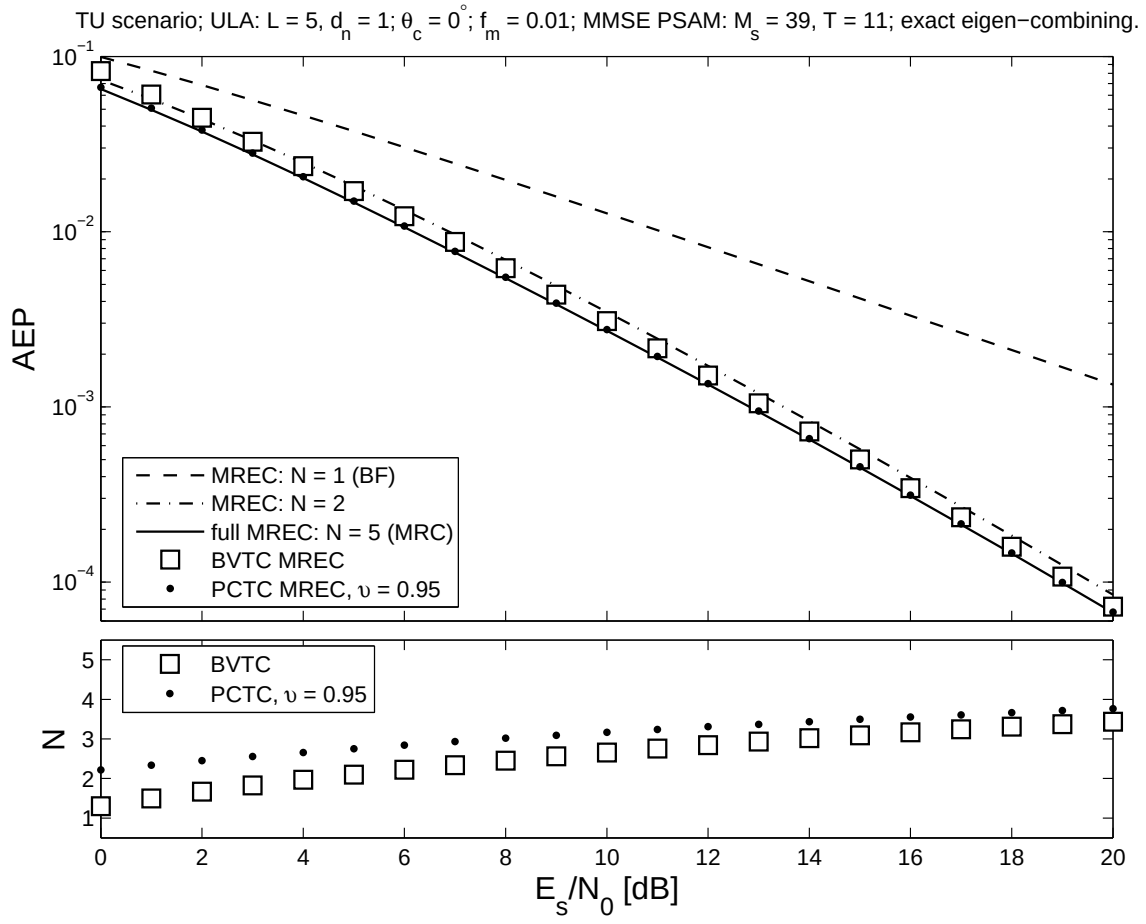

Figure 4.5. Top: AEP for BPSK, MMSE PSAM, and exact MREC vs. the SNR per symbol; Bottom: average MREC order selected with discussed criteria. These results are averages over 10,000 independent samples of log-normal AS for the TU scenario under consideration.

Fig. 4.6 shows in the middle subplot the BF, MRC, and adaptive MREC AEPs evaluated using (3.151), on page 109, after each eigenstructure update. The bottom subplot shows the MREC orders selected adaptively with the applicable criteria described in Section 4.4. Note that adaptive, PCTC-based, MREC can lead to significant performance gain and complexity reduction over BF and MRC, respectively.

Numerical results we present in [127], as well as later in Section 5.2.4, on page 179, indicate that our PCTC from (4.13) is effective also for approximate-MREC adaptation. This is somewhat expected, since the performance gap between exact and approximate eigen-combining can be fairly narrow — see our comments on Figs. 3.13 and 3.14 in Section 3.7.3.

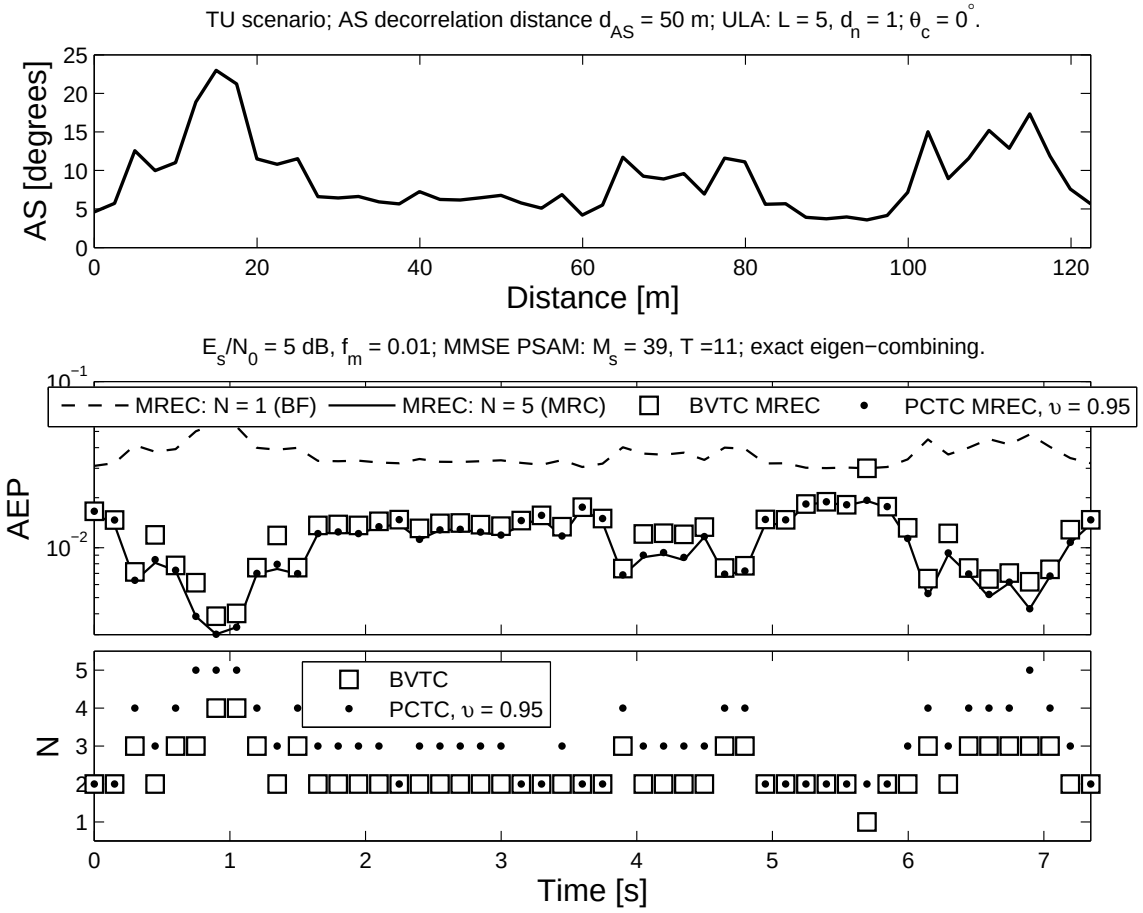

Figure 4.6. Top: AS vs. distance traveled by mobile station, for the TU scenario; Middle: AEP for BPSK, MMSE PSAM, and exact BF, MRC, and adaptive MREC, vs. time; Bottom: adaptively-selected MREC order vs. time. The PCTC adaptively selects the MREC order which ensures the best performance for a designer-approved complexity level.

Chapter 5

FPGA-based Communications Receivers

5.0.1 Chapter Overview

In the previous chapters we have shown that enhanced, multi-branch, receivers can significantly outperform the conventional, single-branch, receiver. However, the performance gains obtainable with multi-branch receivers employing maximum average SNR beamforming (BF) or maximal-ratio combining (MRC) vary with the channel gain correlations, although computational complexity remains constant. Our preceding analysis and simulations suggest that the complexity of maximal-ratio eigen-combining (MREC) can be effectively adjusted to these variations, while achieving required performance.

Based on our work from [129], in this chapter we first overview the advantages of field-program-mable gate arrays (FPGAs) over other processing devices, and describe an Altera® FPGA-based design environment. Then, we present our FPGA-based implementations of conventional and enhanced (BF, MRC, MREC) receiver algorithms. These designs are compared in terms of error rate performance as well as chip resource usage and power consumption. We will show that FPGA-based eigenmode-monitoring receivers can adapt to channel statistics variations, for high-performing, efficient, inexpensive, smart antenna array embedded systems.

5.1 Field-Programmable Gate Arrays (FPGAs)

5.1.1 FPGA vs. DSP and ASIC

Traditionally, SISO digital communications transceivers have been implemented on digital signal processors (DSPs) and application-specific integrated circuits (ASICs). Currently, wireless communications systems are fast evolving towards highly complex, multi-branch transceivers which will yield much higher data rates. These transceivers' requirements for speed and flexibility can surpass the capabilities of DSPs and ASICs.

Unlike general-purpose microprocessors employed in computers [86, Chapter 2], DSPs [86, Chapter 3] comprise specialized hardware multiply-accumulate block(s), as well as memory and bus structure that allow for efficient and frequent data access [13]. Customization of these on-chip DSP resources is generally not possible.

Although DSPs can offer high computation precision and wide dynamic range through floating-point number representation, data-buses are usually very wide relative to the actual requirements. In practice, optimum representation-wordlength requirements vary [70], and are usually much smaller than those offered by current DSPs. Furthermore, the fixed number of available multiply-accumulate blocks can seriously limit the speed of DSP-based implementations of multi-branch communications algorithms, which are commonly highly parallelizable. Finally, embedded memory can speed up processing but consumes power. Since for DSPs the amount of on-chip storage space is fixed at fabrication, processing may be slowed due to frequent external-memory access, or power may be consumed by unused on-chip memory [13].

On the other hand, ASICs yield fast and power-efficient implementations for a given task because 1) parallelizable operations can be implemented for simultaneous execution on functionally-parallel hardware blocks, and 2) the internal structure is designed to exactly suit requirements. In [111] the authors present the ASIC implementation of a 4×4 MIMO orthogonal

frequency division multiplexing (OFDM) wireless local area network (WLAN) transceiver relevant to the IEEE 802.11n standard, achieving data rates of 192 Mbps in a 20-MHz channel, i.e., 9.6 bits/s/Hz spectral efficiency. This MIMO implementation was found to require 6.5 times larger chip area over the SISO implementation. In [54], the ASIC implementation of an OFDM smart antenna receiver is proved to compare favorably with its DSP counterpart.

However, implemented ASIC designs are inflexible [54] because they are hardwired for specific tasks. More importantly, ASIC design and production are time-consuming and extremely expensive for chips not produced in very large numbers, due to very high non-recurring engineering cost.

Field-programmable gate arrays (FPGAs) can offer ASIC-like speed (through hardware parallelism) and DSP-like flexibility (through reprogrammability), as well as simple, model-based, design flows [11, pp. 55 - 56] [17]. FPGAs can thus outpace DSPs (e.g., by an order of magnitude in [72]), through parallel hardware execution, at a small fraction of the ASIC design and implementation effort and cost. Therefore, FPGAs are drawing ever increasing interest from designers of future-generation mobile and fixed wireless communications systems. A flurry of reports on FPGA-based prototyping of enhanced communications transceivers (MIMO, OFDM, ST coding, multiplexing, multi-user detection — MUD, WCDMA, etc.) and of MIMO channel-measurement test-beds have appeared recently — see, for instance, the current EURASIP "*Journal on Applied Signal Processing*" volume, and the upcoming "Special Issue on Field-Programmable Gate Arrays in Embedded Systems", of the "*EURASIP Journal on Embedded Systems*", to appear in the 4th quarter of 2006.

Unlike DSPs or ASICs, FPGA fabric can be reconfigured because its internal structure is only partially fixed at fabrication, leaving to the application designer the wiring for the intended task. FPGA designs can thus benefit from data-matching bus widths, optimum on-chip

storage space and multiply-accumulate resources that can support extensive functional parallelism [13]. Furthermore, FPGA reconfigurability and design flow simplicity [11, pp. 55 - 56] can significantly shorten design and production, and thus time-to-market. FPGAs tend to be slower and to consume more power than ASICs [54]. Nevertheless, FPGA reconfigurability can eliminate the risks of faulty design or fabrication risks. Furthermore, FPGA-based implementations improve platform adaptability and thus longevity. In an era of fast-changing wireless communications standards, applications, and markets, FPGAs can facilitate design upgrades even for systems already in operation.

FPGAs are especially well-suited for embedded communications systems (e.g., cellular system base station line cards, or mobile stations) because, beside a reconfigurable area of logical elements (LEs), they can also incorporate large amounts of memory, high-speed DSP blocks, clock-management circuitry, high-speed input/output (I/O), as well as support for external memory, high-speed networking, and communications bus standards [15]. For a small share of the resources, soft processors (i.e., processors downloaded into the FPGA fabric) can be included within the FPGA fabric as well [97].

Furthermore, once an FPGA design has been thoroughly tested it can be migrated into equivalent structured-ASIC, e.g., the Altera® HardCopy™ devices [10], which can yield higher speed for more than 50% in power consumption reduction and up to 90% in cost reduction, compared to FPGA counterparts [10, 41]. Note further that the powerful Quartus II package is the only software tool required throughout the Altera® FPGA-based design and migration to structured-ASIC.

As already mentioned, FPGA on-chip feature richness, as well as their reprogrammability and simple design flow (which allows for rapid design-improving iterations) have already established these devices as prime candidates for expeditious prototyping of advanced communications signal processing algorithms. Their combination with DSPs and ASICs can also

be advantageous. For example, in [67] FPGAs and DSPs implement the receiver in a Bell Labs Layered Space-Time (BLAST) MIMO architecture for the Universal Mobile Telecommunications System (UMTS). Implemented in FPGAs were processing-intensive tasks, such as channel estimation, finger assignment, and RAKE receiver, whereas DSPs were employed for MIMO decoding. A DSP/FPGA architecture was also demonstrated in [66] for rapid prototyping of wideband code-division multiple access (WCDMA) downlink. Therein, FPGAs implement the high-rate front-end. Channel estimation is shown to consume more than one fourth of the FPGA resources. DSPs handle symbol-level processing, control operations, matrix inversions, and matrix-vector multiplications. Note that in [66] DSP-based channel estimation proved too slow. A ten-fold speed-up from the FPGA led to adequate channel tracking.

Time-critical, highly-parallelizable applications which can benefit from FPGA implementations have recently been identified also in other areas such as image processing [72], speech processing [144], and even in bio-informatics [97, 143].

5.1.2 FPGA Power Usage Considerations

Competitive line-powered embedded systems demand low-cost power supplies and cooling devices [121, 135]. Devices operating at high temperatures can become unreliable. Finally, designs for portable products aim for the longest possible battery life, emphasizing power-efficiency importance in embedded systems.

Although power-efficiency has continuously improved through FPGA evolution, these devices are still important power consumers [82]. Consistently underutilized designs can only exacerbate this situation [31, 121, 135, 150].

Static, dynamic, and interface (I/O) power losses occur in FPGAs [31, 110, 121, 135, 150]. Hereafter we will neglect interface (I/O) power losses since they are relatively small [110]. Static (stand-by) power is consumed by the chip when no input signals are exercised [121].

This loss occurs due to transistor leakage, which is frequency-independent, but highly dependent on junction temperature and transistor size. Static power has been increasing (exponentially, at processes below 0.25 μm [135]) with each finer semiconductor technology to become the dominant loss component in current chips. This is a concern for designers of portable embedded systems which spend long intervals in stand-by mode [121].

Dynamic power, consumed in normal operation through charging and discharging of the internal capacitive loads, is proportional to gate output load, square of the supply voltage, clock frequency, and gate switching activity [31, 121, 135, 150]. Although the supply voltage has decreased significantly in newer process technologies, high operating frequencies can still yield significant dynamic power losses [121]. A tight power budget may thus limit clock speed [121].

FPGA chips are judiciously fabricated to minimize power losses [31,121,124,135]. Nonetheless, effective use of dedicated on-chip resources (e.g., DSP blocks, memory) increases speed, and can reduce power consumption by up to 45% [82]. Power-aware compilation, synthesis, and fitting are also recommended to further reduce losses [82]. Intellectual Property (IP) modules, which are generally parameterizable and optimized in terms of resource and power consumption, are available from FPGA vendors and third-parties, for a wide range of applications: filtering, image encoding/decoding, modulation, encryption, error-correction, etc. [13].

Application design can also enhance power-efficiency. For example, dynamic power usage can be reduced by turning off unnecessary chip sections using gated clocks [31, 51, 121, 124]. Since the clock signal network can account for up to 40% of the dynamic power consumption [51], due to fast switching and long paths [82], clock gating as close as possible to the clock source can yield significant savings. Nevertheless, clock-gating can introduce or increase clock-skew [32], which complicates clock-tree design [24]. Therefore, manual gating needs to be done very carefully — see [14] for Altera®-recommended clock-gating procedures. Research on clock-gating automation shows promising results [24, 32].

Apart from the obvious option of selecting the smallest FPGA which would fit the intended design, static power consumption can also be reduced by adaptively redistributing temporally-unused on-chip resources for other tasks, which would otherwise use other FPGAs, as shown later in this chapter, in Sections 5.2.3 and 5.2.4.

5.1.3 FPGA-based Development System Description

The analysis in this chapter is based on the system shown in Fig. 5.1, which was provided by CMC Microsystems (www.cmc.ca). The Altera® DSP Development Kit Stratix™ Professional Edition [16], which comprises the Stratix™ EP1S80 DSP development board, is built around the Stratix™ EP1S80B956C6 FPGA chip [15], and comes with the DSP Builder interface [12] to the Quartus II design flow [14].

Quartus II provides a comprehensive design, synthesis, and analysis environment for system-on-a-programmable-chip (SOPC) applications. DSP Builder helps create the hardware representation of the required digital signal processing functions using the MATLAB® and Simulink® user-friendly algorithm-development environments, for shorter design and implementation cycles. MATLAB® functions and native Simulink® blocks can be combined with Altera® DSP Builder library blocks (see Fig. 5.1), to create FPGA designs simulable under Simulink®. For automated design flow, the "Signal Compiler" block, which is at the core of DSP Builder, can generate hardware description language (HDL) code as well as scripts for Quartus II-based synthesis and fitting from within Simulink®. Furthermore, the DSP Builder "Hardware-in-the-loop" (HIL) block enables chip programming and hardware–software co-simulation.

For the designs described further below, we relied on Quartus II reports on resource usage, e.g., the number of logic elements (LEs), chip pins, and dedicated DSP blocks. Static and dynamic power losses were estimated using the Quartus II PowerPlay Analyzer (dynamic power was estimated for default toggle rates of 12.5%).

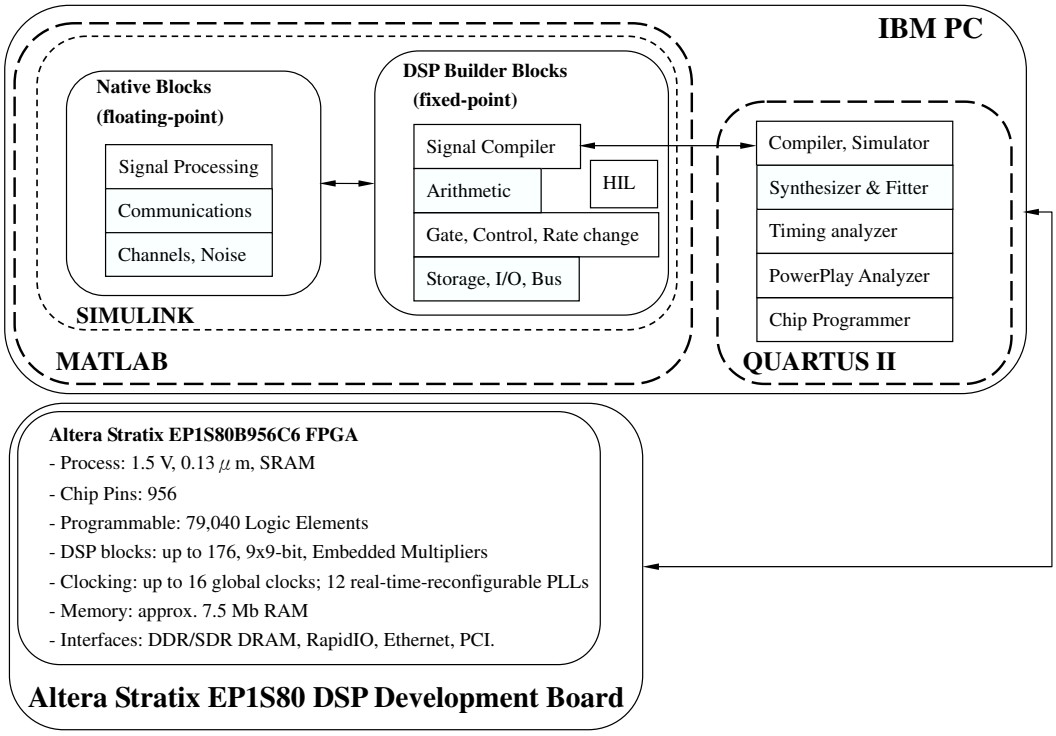

Figure 5.1. FPGA development system hardware and software.

5.2 FPGA-based Receiver Implementations

Enhanced, i.e., multi-branch, receivers employing maximum average SNR beamforming (BF) or maximal-ratio combining (MRC) can generate antenna and diversity gain, respectively, which vary with the channel gain correlations. Such algorithms can however require much larger computational volumes than the conventional, single-branch, receiver [129]. This translates into high on-chip resource requirements and thus power consumption, which also remain constant although receiver performance changes with varying channel statistics [129]. Our preceding analysis and simulations suggest that the complexity of maximal-ratio eigen-combining (MREC) can be effectively adjusted to these variations, while achieving required performance.

In the following, we describe conventional and enhanced (BF, MRC, MREC) receiver algorithm implementations. The designs are compared in terms of average error rate performance for BPSK transmission, as well as chip-resource usage and power consumption. We will show that FPGA-based eigenmode-monitoring receivers can adapt to channel statistics variations, for high-performing, inexpensive, smart antenna array embedded systems.

For the system shown in Fig. 5.1 we focus on FPGA-based receiver algorithm implementation, assuming availability of digitized received signals. The transmitted signal and channel/receiver impairments, i.e., noise and temporally- and spatially-correlated fading, are generated in MATLAB® and Simulink®. Various receiver algorithms were simulated as well as run from the FPGA through DSP Builder HIL. Computer simulations and the corresponding hardware/software HIL co-simulations were found to perform identically. Note that computations done in MATLAB® or with native Simulink® blocks are very precise, due to floating-point number representation. On the other hand, DSP Builder relies on fixed-point representation, which can limit the dynamic range and can introduce quantization noise [70].

For the numerical results shown hereafter a Rayleigh fading channel is assumed that follows the well-established Jakes' model [75] for temporal correlation — see Section 2.4.1, on

page 16. The Doppler spread is $f_{\mathrm{D}} = 100$ Hz, and the transmission rate is $f_{\mathrm{s}} = 10$ kbps, so that the normalized Doppler spread is $f_{\mathrm{m}} = 0.01$ Hz. PSAM with slot length $M_{\mathrm{s}} = 7$ (1 pilot symbol followed by 6 information-encoding symbols) is combined with SINC interpolation over $T = 11$ slots ($T_1 = T_2 = 5$), for channel estimation. The SINC interpolation coefficients are computed as shown in Table 3.4, on page 84. The ULA with $d_{\mathrm{n}} = 1$ is assumed to provide the received signals for the enhanced receivers.

5.2.1 Conventional, Single-Branch, vs. Enhanced, Multi-Branch, MRC Receivers

In this section, a conventional single-branch receiver and an enhanced MRC receiver with $L = 2$ i.i.d. branches are considered. For BPSK, p.k.c., as well as i.k.c. for SINC PSAM, the AEP is evaluated employing the simple, finite-limit integral, approximate-MRC AEP expression from (3.194), on page 125. Then, for i.k.c., FPGA-based designs were simulated as well as hardware–software co-simulated. For the latter, the receiver design is compiled and then downloaded into the FPGA chip. Afterwards, received signals emulated using MATLAB® are processed online by the programmed FPGA. The channel gain estimation root mean square error (RMSE) is determined from theory [127], simulations, and HIL implementations.

In terms of the representation precision within the FPGA, for the computer-simulated received signal, $\widetilde{\mathbf{y}}$, two cases are evaluated in this section: 1) 8 bits for the integer part and 8 bits for the fractional part — this case is denoted further with 8.8; 2) the 4.4 case. Note that for signed representation the left-most bit indicates the sign of the number: 0 indicates a positive, 1 indicates a negative.

BPSK modulation is done in the simulated transmitter so that b in the signal models is $+1$ when a 0 information bit is transmitted, and -1 when a 1 bit is transmitted. Thus, in the receiver the detected bit is simply the sign bit of the test variable.

For a conventional, single-branch receiver, with received signal $\widetilde{y}_1$ and channel gain estimate $\widetilde{g}_1$, the detected symbol is the sign bit of

$$\Re(\widetilde{g}_1^* \widetilde{y}_1). \tag{5.1}$$

For dual-branch approximate MRC — see Section 3.7.2.1, on page 93 — the detected symbol is the sign bit of

$$\Re(\widetilde{\mathbf{g}}^H \widetilde{\mathbf{y}}) = \Re(\widetilde{g}_1^* \widetilde{y}_1) + \Re(\widetilde{g}_2^* \widetilde{y}_2). \tag{5.2}$$

The Simulink®/DSP Builder design which implements

$$\Re(\widetilde{g}_1^* \widetilde{y}_1) = \Re(\widetilde{g}_1)\,\Re(\widetilde{y}_1) + \Im(\widetilde{g}_1)\,\Im(\widetilde{y}_1) \tag{5.3}$$

for the 8.8 case is reproduced in the upper part of Fig. 5.2, along with the "SINC Interpolator" block which outputs $\Re(\widetilde{g}_1)$. The lower part of the figure details our "SINC Interpolator" design, for detected symbol position $m = 1$. (Symbols appear without the tilde due to Simulink® editing limitations).

The "Shift Taps" DSP Builder blocks shown at the top of the figure delay the received signal by $(T_1 + 1)\, M_\mathrm{s} = 42$ samples, aligning it with the corresponding channel estimate. The "Multiply Add" block then computes $\Re(\widetilde{g}_1^* \widetilde{y}_1)$. A similar design was implemented for the second branch of the MRC receiver.

Since the DSP Builder blocks "Sum of Products" in the "SINC Interpolator" design require integer input and coefficients, binary shifting of the received signal and interpolator coefficients is required. The "SINC Interpolator" "Shift Taps" block outputs $\Re(\widetilde{\mathbf{r}}_1)$ for the vector with pilot samples $\widetilde{\mathbf{r}}_1$ from (3.111), on page 83. The "Parallel Adder/Subtractor" outputs $\Re(\widetilde{g}_1)$, computed as in (3.110), on page 83. The latter is then used for combining, as shown in the upper part of the figure.

Channel estimation can thus be very demanding resource-wise, especially for multi-branch receivers. Based on (2.76), on page 36, channel fading with $f_\mathrm{m} = 0.01$ allows for slot length as

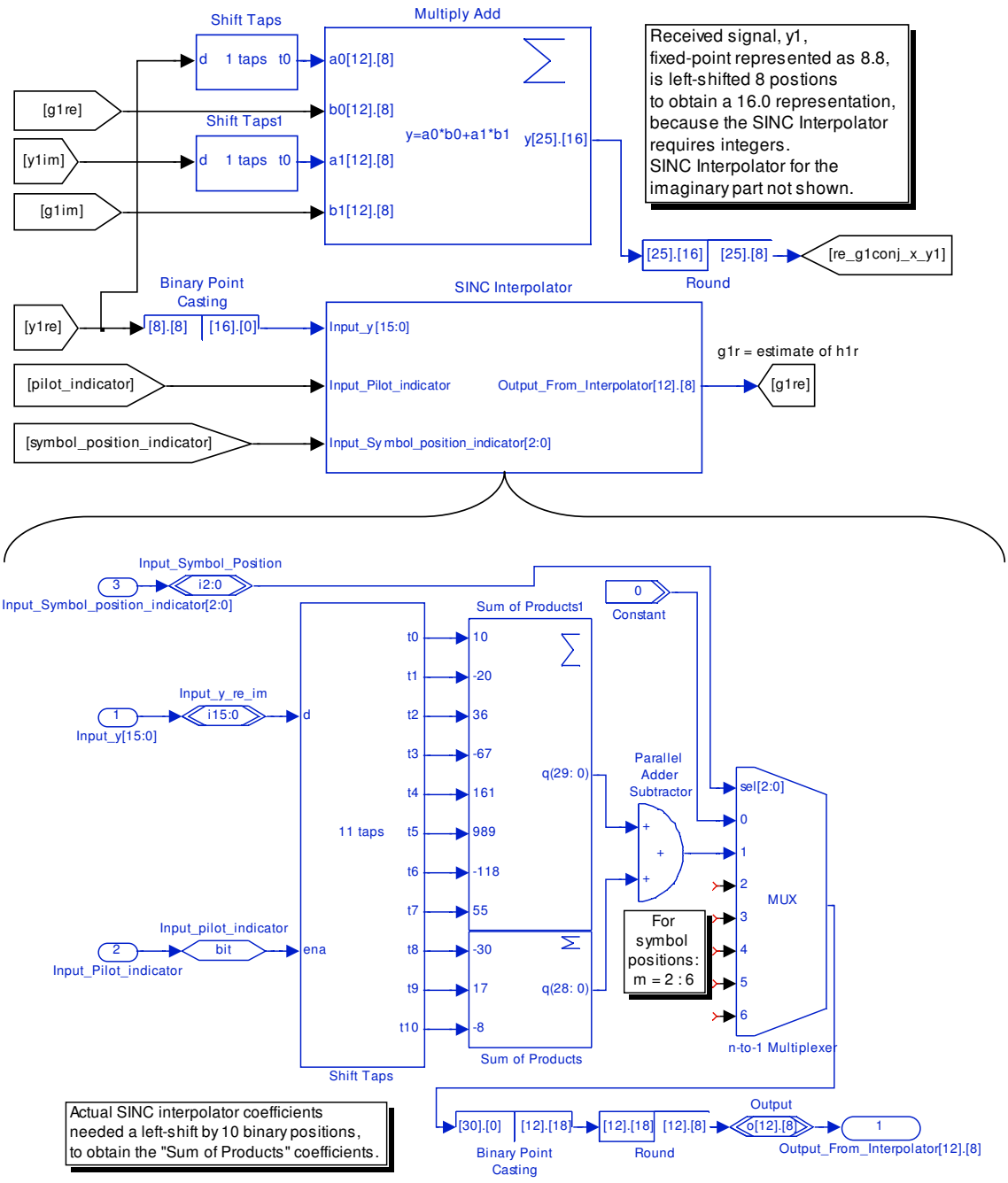

Figure 5.2. Simulink® model detail with DSP Builder blocks implementing channel gain estimation (through SINC interpolation) for MRC.

large as $M_s \leq 50$. However, this would mean that the "Sum of Product" and "Parallel Adder" blocks of the "SINC Interpolator" design would have to be repeated 49 times, thus consuming a large amount of FPGA resources. To reduce complexity, we traded off throughput by selecting $M_s = 7$ for all designs presented hereafter.

The RMSE subplot in Fig. 5.3 indicates that for 4.4 and 8.8 fixed-point initial representation of the received signal in FPGA, channel estimation accuracy does not visibly degrade compared to floating-point (computer) computation. Nevertheless, the lower subplots show that fixed-point computation with fixed-point narrow word (i.e., poor precision, narrow dynamic range) can significantly degrade performance, an effect which cumulates with more branches.

Fig. 5.3 also indicates that the performance degradation (i.e., about 3.4 dB) which occurs for a conventional receiver due to i.k.c. can be successfully compensated for with an FPGA-based dual-branch MRC, due to its diversity gain. Confidence intervals for all these results are very tight, since $10,000$ slots, i.e., $60,000$ data symbols, were detected.

For designs discussed hereafter we settled for the 8.8 representation case, since it was found to offer a fair compromise between representation accuracy/dynamic range (i.e., receiver performance) and FPGA resource utilization. Furthermore, DSP Builder was instructed to allocate hardwired DSP circuitry embedded into the reconfigurable FPGA fabric, which yields more efficient chip utilization [15, 54].

Quartus II reports on FPGA resource (i.e., LEs, chip pins, and DSP blocks) usage, maximum allowable clock frequency, and dynamic power usage, as shown in Table 5.1. The estimated static power loss is 1.395 W. Note that, for the performance advantage shown in Fig. 5.3 over the conventional receiver, denoted herein as MRC, $L = 1$, dual-branch MRC nearly doubles resource requirements and dynamic power loss. Since the MRC performance gradient diminishes with increasing number of branches [123], implementation/operational costs can be minimized either with tightly-matched chips or through clock gating of excess resources.

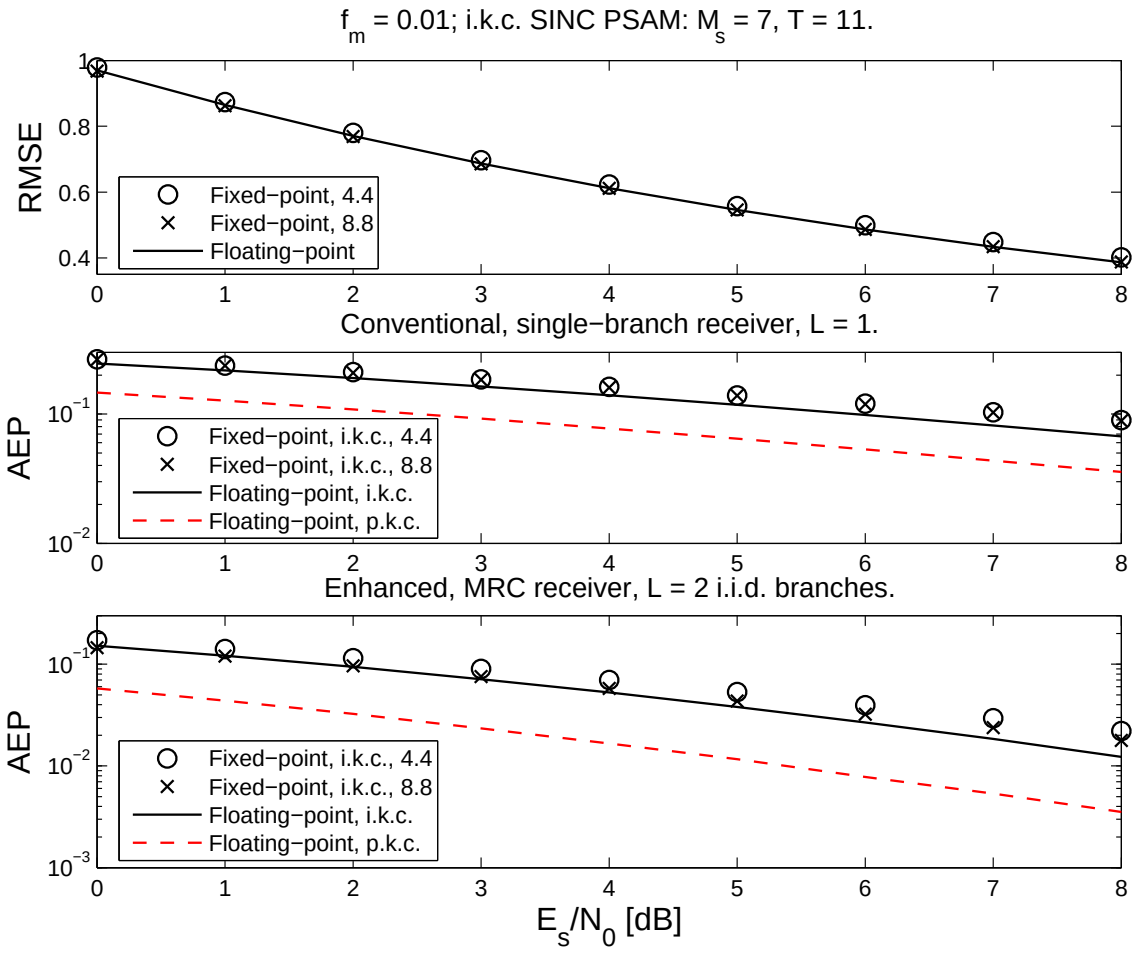

Figure 5.3. Top: RMSE for channel gain estimates. Middle and bottom: Performance of the conventional, single-branch, receiver, and of the dual-branch MRC receiver for various computer- and FPGA-based implementations. Fixed-point results correspond to both DSP Builder-based simulations and HIL implementations.

Table 5.1. Resource usage for 8.8 implementation of MRC, BF, and adaptive MREC

Method	LEs [out of 79,040]	Pins [692]	DSP [176]	Clock Frequency [MHz]	Dynamic Power [mW]
MRC L = 1	13,227 16.73%	43 6.21%	16 9.09%	41.06	69.35
MRC L = 2	26,478 33.49%	83 11.99%	32 18.18%	38.56	119.67
MRC L = 3	39,731 50.27%	123 17.77%	48 27.27%	38.35	169.78
MRC L = 4	55,983 70.83%	167 24.13%	64 36.36%	36.74	221.62
BF L = 4	13,457 17.02%	259 37.43%	48 27.27%	40.57	74.95
BVTC MREC L = 4, N = 1	13,458 17.02%	262 37.86%	48 27.27%	41.15	74.95
BVTC MREC L = 4, N = 2	26,940 34.08%	358 51.73%	96 54.54%	39.73	130.89
BVTC MREC L = 4, N = 3	40,423 51.14%	454 65.60%	144 81.81%	39.09	186.64
BVTC MREC L = 4, N = 4	55,847 70.66%	550 79.48%	176 100%	38.82	244.64
EVTC MREC L = 4, N = 1	13,561 17.16%	424 61.27%	48 27.27%	41.09	75.67
EVTC MREC L = 4, N = 2	27,372 34.63%	524 75.72%	96 54.54%	39.14	132.95
EVTC MREC L = 4, N = 3	40,983 51.85%	624 90.17%	144 81.81%	35.43	189.23

In the above MRC receiver design, channel gains on different branches were considered statistically independent, for simplicity. As already mentioned, this is rarely the case in practice [8]. Although scattering is richer around the mobile than around the base station, mobile antenna array size limitations can still lead to large inter-branch correlation, i.e., scarce diversity gain availability. Then, adaptive MREC [127, 130] may provide more suitable tradeoffs between performance and resource/power utilization, as shown next.

5.2.2 Enhanced, MREC, Receiver Design: the Case of a Single User Processed per FPGA Chip

5.2.2.1 Adaptive BVTC-based MREC implementation

We extended the previously-discussed FPGA-based MRC receiver design to support L = 4 branches, and also designed the stand-alone BF receiver as well as the MREC receiver adapted using the bias-variance tradeoff criterion (BVTC) described in Section 4.4.1, on page 145. Implementation details for a BVTC MREC receiver are provided in Fig. 5.4. See Table 5.1 for the resource and power usage report.

Note that the stand-alone BF implementation takes about as many resources as order-1 MREC takes in the BVTC MREC implementation since these two designs are almost identical. Furthermore, MRC can in principle be obtained from a MREC design by bypassing the KLT. Thus, an MREC design can readily be reconfigured (even during operation, on-the-fly) to implement BF or MRC instead.

For a more relevant resource/power usage and performance evaluation, we consider the azimuth spread (AS) model and the typical urban scenario (from the base-station perspective) discussed in Section 4.2, on page 136, and apply the conventional and enhanced receiver combining algorithms (after estimating channel gains and eigengains as in Section 3.6, page 81)

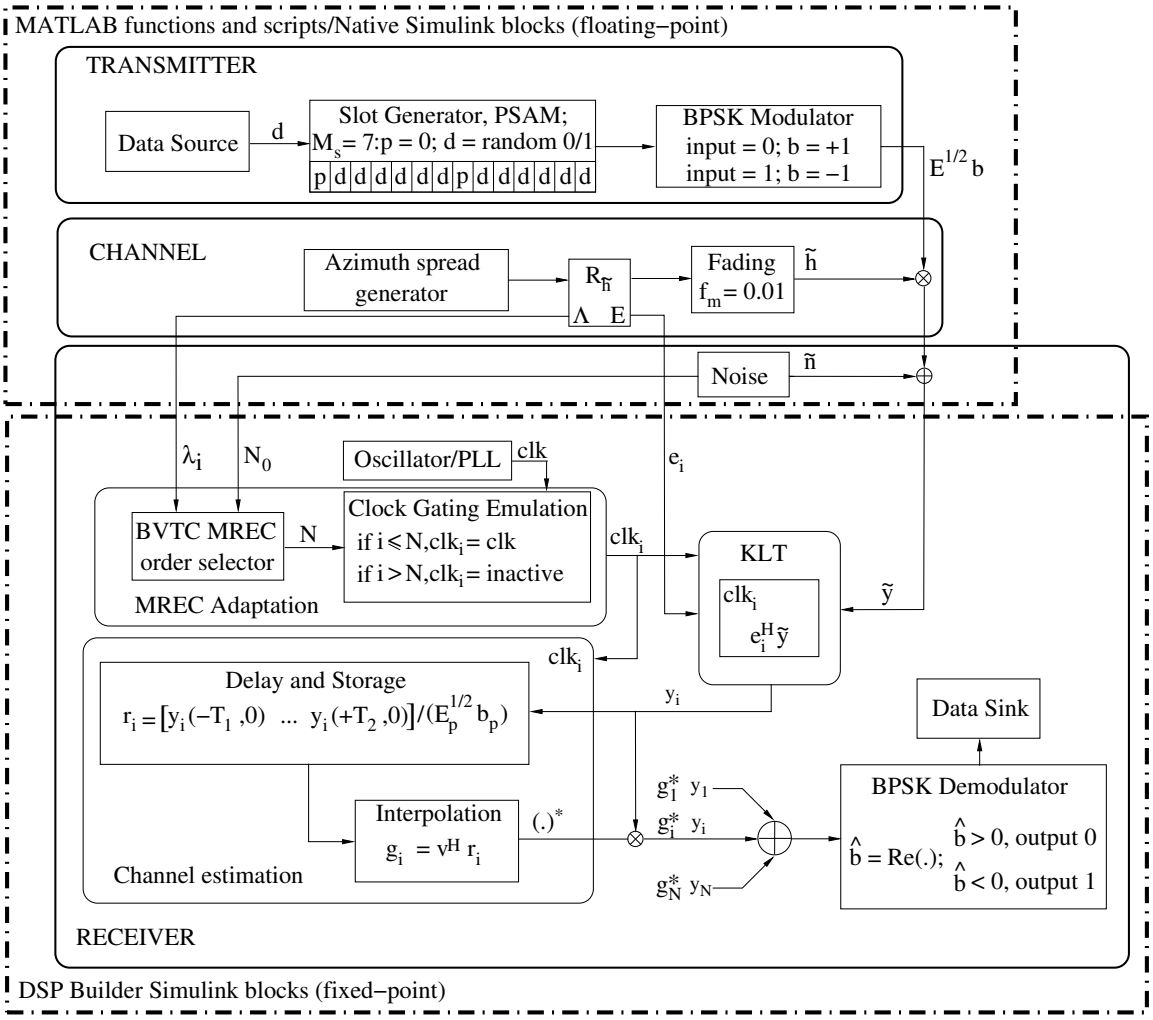

Figure 5.4. Transmitter, channel, and FPGA-based BVTC MREC receiver.

to detect the transmitted symbols. Using MATLAB® scripts and functions as well as native Simulink® blocks, the actual log-normal distributed and temporally correlated AS sequence is simulated for realistic Laplacian power azimuth spectrum (p.a.s.) and then employed to compute the spatial correlation matrix and its eigen-decomposition — see Fig 5.4. The computed correlation matrix $\mathbf{R}_{\tilde{\mathbf{h}}}$ inputs a customized Simulink® "Multipath Rayleigh Fading Channel" block, to simulate $L = 4$ correlated branches.

In an actual embedded receiver, the channel correlation matrix and its eigenvalue decomposition could be updated by a processor. For instance, Altera® claims that their Nios II® soft processor consumes only about 5% of a large FPGA. Furthermore, third-party floating-point libraries for this processor can yield the dynamic range and numerical precision required for accurate eigen-decomposition. Recently, FPGA implementations of eigenvalue decompositions have also been described [40] and even made available as IP cores [7].

5.2.2.2 Performance Comparison of Conventional and Enhanced Receivers

We selected a correlation update period (frame duration) of 0.14 s, which corresponds to a distance of roughly 2.3 m traveled by the mobile. As discussed in Section 4.5, page 148, the AS remains relatively constant over this interval [8], allowing for sufficient time and uncorrelated samples for eigenstructure updating.

The top subplot in Fig. 5.5 depicts an AS sequence generated using the model described in Section 4.2.3, page 139. The predominantly small-to-moderate AS values indicate that we should often expect significant spatial correlation, i.e., small available diversity gain. Performance enhancement can then arise from BF array gain. Occasionally however, the AS can also become fairly large (see also the top-right subplot in Fig. 5.8, on page 177, for AS produced in an independent trial), but then the available diversity gain cannot benefit BF performance. On the other hand, significant diversity gain may be available too infrequently to justify permanent

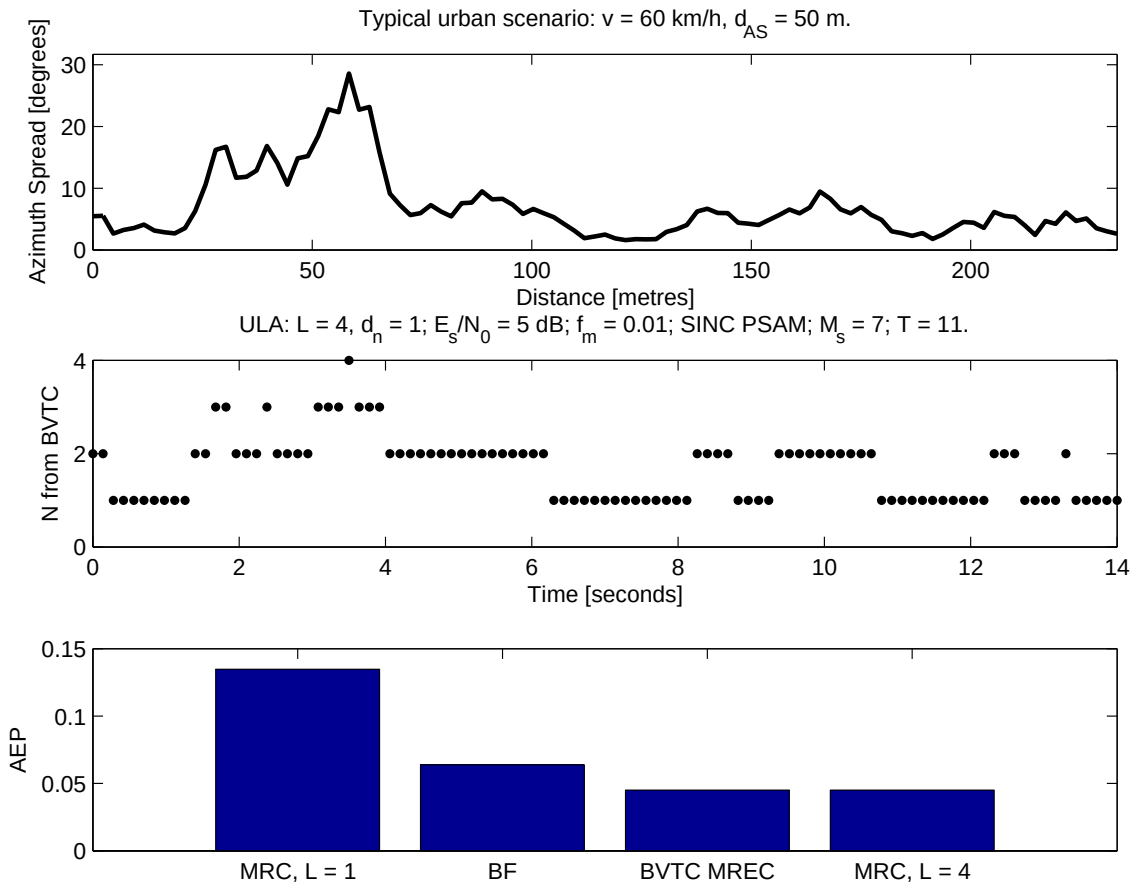

Figure 5.5. Azimuth spread (AS) sequence, MREC order selected with the BVTC, and AEP performance (averaging over the AS trial) for the conventional receiver (MRC, $L = 1$) and the enhanced receivers (BF, MRC, and BVTC MREC).

use of an MRC receiver. As we shall see, an FPGA-based MREC receiver can provide, for a channel with slowly-varying statistics, flexibility that yields affordable performance.

For an FPGA-based BVTC adaptive MREC receiver the unnecessary eigenbranch processing modules (e.p.m.) can be virtually turned off using the clock gating technique discussed in Section 5.1.2, page 156, to reduce dynamic power loss, while necessary eigenbranches can be implemented to run in parallel, for high speed. Exempting weak eigenbranches can also benefit performance (for approximate MREC and SINC PSAM — see Section 3.7.3, on page 97).

Further, as mentioned earlier, a MREC implementation can easily be reduced to stand-alone BF or MRC implementations, if required, either at system setup or during operation.

Unfortunately, clock gating is unavailable through DSP Builder, although possible from Quartus II. Therefore, clock gating was only emulated in DSP Builder, for the BVTC MREC implementation depicted in Fig. 5.4. First, non-adaptive MREC designs with $N = 1:4$ eigen-branches were compiled to determine their resource usage (shown in Table 5.1, page 166). Then, after each eigenstructure update during the BVTC MREC simulation, we stored the MREC order output by the BVTC, and disconnected unused e.p.m. from the active structure. Finally, average resource usage was computed.

The middle subplot in Fig. 5.5 displays the MREC order selected adaptively using the BVTC. The lower subplot presents the AEP averaged over the AS trial for the conventional and enhanced receivers. Notice that, for $L = 4$, MRC and BVTC adaptive MREC slightly outperform BF, and greatly outperform the single-branch receiver.

5.2.2.3 Resource Requirements and Power Consumption Comparison of Conventional and Enhanced Receivers

For the same typical urban scenario and system parameters, Fig. 5.6 shows resource usage, in percentage points of the total available on the Altera® chip, and dynamic power consumption, all averaged over 8 AS trials, for the conventional receiver, and the enhanced ones, i.e., BF, MRC, and BVTC MREC, for $L = 4$ branches. In each trial, the AS samples have correlation given by (4.7), on page 142, and the AS sequences are independent between trials.

Fig. 5.6 (upper-left subplot) indicates that BF occupies an equal share of FPGA programmable fabric (i.e., logical elements — LEs) as the conventional receiver, since eigen-decomposition does not take place on the FPGA for our designs. For soft-processor-based eigen-decomposition, BF (and MREC) would require as many chip pins as MRC (with $L = 4$), as

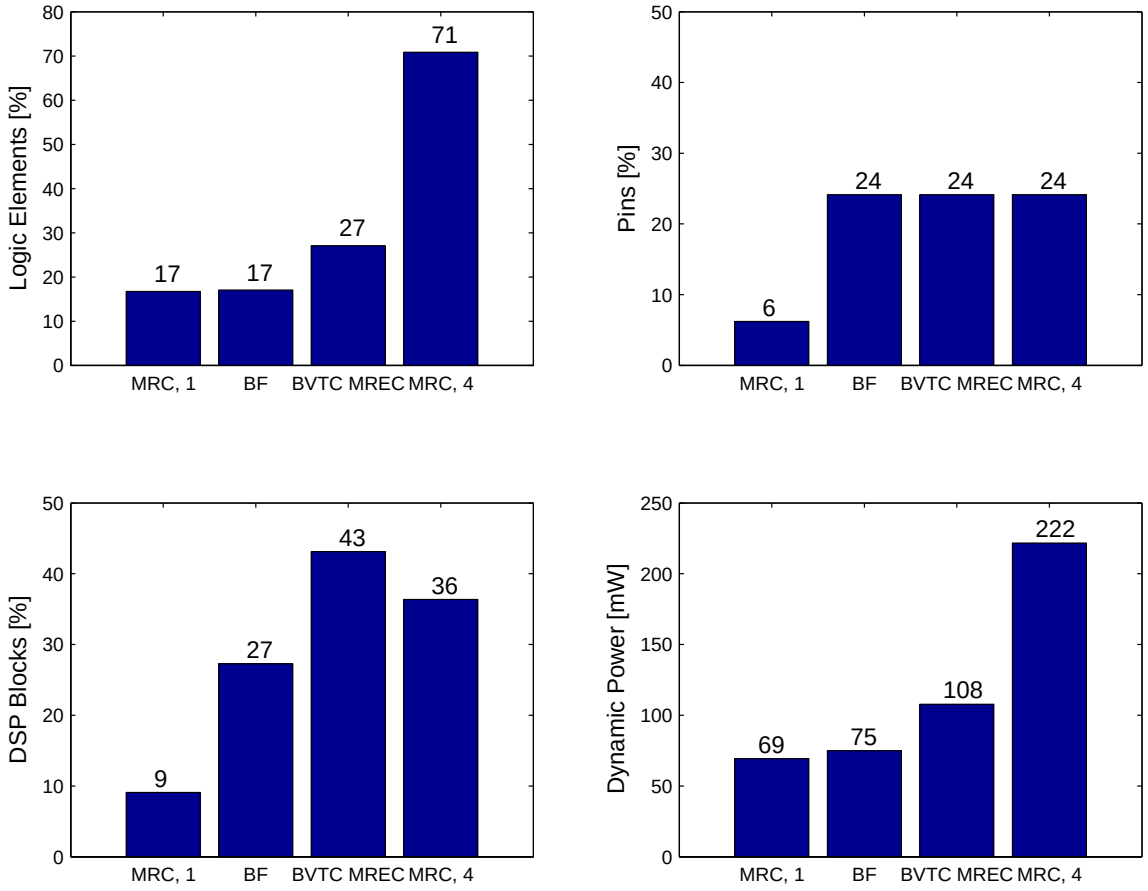

Figure 5.6. Average resource and dynamic power usage for BF, BVTC MREC, and MRC, over 8 trials with mutually independent azimuth spread sequences.

shown in the upper-right subplot of Fig. 5.6.

Due to the required KLT, BF occupies 3 times more DSP blocks than the conventional receiver, yet since these on-chip resources are power-efficient, BF does not consume much more power — see the bottom-right subplot in Fig. 5.6. On the other hand, resource and power usage for MRC scale almost linearly with the number of branches.

BVTC adaptive MREC appears to provide more judicious resource usage. In average, it takes about 60% more LEs than BF, and about 2.6 times fewer than MRC, and the same number of chip pins (for eigen-decomposition executed on-chip). Due to the KLT, more DSP blocks are needed than in stand-alone BF or MRC. BVTC MREC consumes about 40% more dynamic power than BF, but less than half as much as MRC.

5.2.2.4 Further Results and Discussion

Fig. 5.7 shows performance and total (dynamic + static) power used by a cellular operator's large network of base stations similar to the one described in [135], averaging again over the 8 independent AS trials mentioned above. The single-branch receiver consumes least yet performs poorly. For performance similar to BF and BVTC MREC, MRC (with $L = 4$) doubles dynamic power loss. BF and BVTC MREC appear to provide a better tradeoff. Recall however that a compact ULA with $d_{\mathrm{n}} = 1$ is considered. For larger inter-element distances (feasible at base stations), MREC with more than one eigenbranch can significantly outperform BF.

Note that the branch correlation can become large even at the mobile stations, due to limited antenna spacing and AS [2]. Then, an FPGA-based BVTC MREC receiver employing clock gating will achieve near-optimum performance, and longer battery life than with MRC.

From the base station perspective, Fig. 5.5 (middle subplot) indicates that, frequently, only one or two, out of the four implemented, eigenbranches are actually employed for BVTC MREC for that particular AS sequence, due to its small-to-moderate values. Similar results

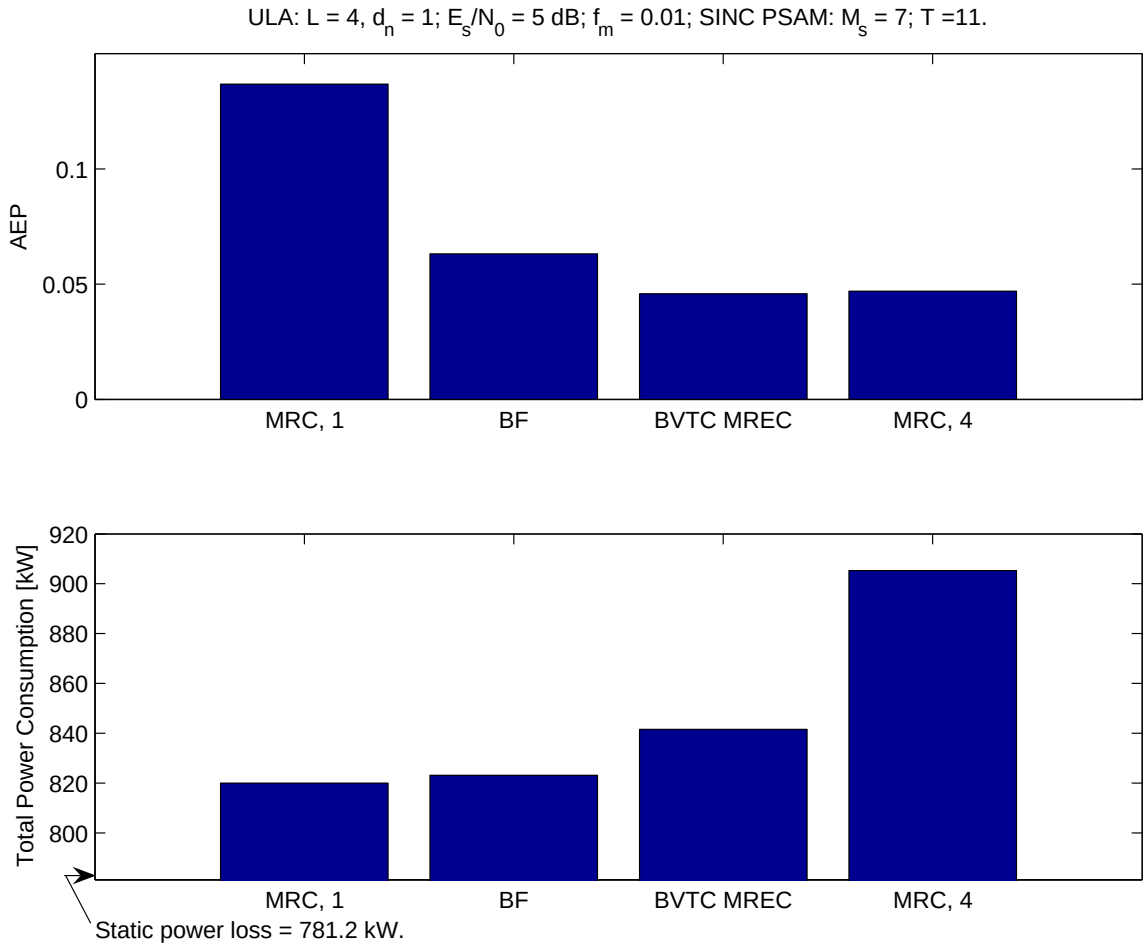

Figure 5.7. AEP and total (static + dynamic) power consumption for BF, BVTC MREC, and MRC, averaged over 8 independent azimuth spread trials.

were obtained in other trials for independent AS sequences. Then, large amounts of FPGA resources go unused, saving dynamic power if clock gating is used, but still consuming significant amounts of static power, as indicated in Fig. 5.7.

Hence, adaptively allocating on-chip resources to process signals from several active users may significantly increase base-station user processing capacity, or, equivalently, reduce the required number of FPGA chips per base station, lowering both hardware cost and static power losses. As shown earlier BVTC is appropriate for saving dynamic power (through clock gating) when the FPGA resources are allocated to a single user. Since BVTC output only depends on the statistics of channel and noise experienced by each of the users, and not resource availability or ensuing MREC complexity, BVTC is not suitable when the same FPGA needs to be shared between users. Possible paths towards such multi-user implementations are described next.

5.2.3 Enhanced, MREC Receiver Design: Simple Procedure for Processing Multiple Users per FPGA Chip

Assume that signals received (independently, without interference) with L antennas from N_{u} mobile stations need to be processed at a base station with only $N_{\mathrm{e}} \ll N_{\mathrm{u}} L$ available e.p.m. Then, a control algorithm determines the dominant N_{e} eigenmodes among all transmitting mobiles, and allocates available resources accordingly. For instance, if a receiving antenna array system with $L = 4$ elements has only $N_{\mathrm{e}} = 3$ available e.p.m. while $N_{\mathrm{u}} = 2$, the available resources are allocated as follows: if the 3 largest eigenvalues (out of $N_{\mathrm{u}} L = 8$) are such that two correspond to User 1, and one to User 2, then two e.p.m. are allocated to process the received signal vector from User 1, and the other available e.p.m. is allocated to User 2. This approach to selecting eigenbranches for MREC is hereafter denoted as the *eigenvalue-based tradeoff criterion* (EVTC), and MREC adapted based on EVTC is referred to as EVTC MREC.

EVTC-based adaptive MREC can provide more consistent use of the FPGA chip, compared to BVTC MREC. We propose to efficiently exploit a total of 3 eigenbranch processing modules, which fit into our FPGA, to process concurrently the signals received with L = 4 branches from two mobiles (without interference). Rather than permanently allotting chip processing resources to a certain user (which may or may not need to use them, depending on channel conditions), herein we will adaptively deploy these resources to simultaneously detect the symbols transmitted from two mobiles.

Resource usage information for EVTC MREC when $N = 1:3$ eigenbranches are selected can be found in Table 5.1, on page 166. Note that the BVTC and EVTC MREC implementations differ significantly only in the required number of chip pins. The larger number of pins required for EVTC MREC (to input the received signals from two mobiles, and — in our implementation — the eigenvectors) limits to 3 the possible number of implemented eigenbranches. Larger N_e leads to unsuccessful compilation. Mutually independent AS sequences for the signals arriving at the base station from the two mobile stations were simulated, as shown in the top subplots of Fig. 5.8. The MREC orders selected with the EVTC for each of the users are shown in the middle subplots. The lower subplots indicate that EVTC MREC can perform remarkably close to the enhanced receivers discussed previously.

The upper-left subplot in Fig. 5.9 indicates that our FPGA would not fit concurrent four-branch MRC implementations for the two users. On the other hand, the successfully-compiled two-user EVTC MREC implementation with $N_e = 3$ requires about half of the dynamic power consumed by MRC, for similar performance. Furthermore, since EVTC MREC allows for effective concurrent processing of two users on a single FPGA, it yields a two-fold reduction in static power consumption or a doubling of the base station user processing capacity. Thus, both implementation and operational costs can be drastically reduced with EVTC MREC.

Ideally, an FPGA-based embedded receiver would comprise 1) several FPGAs programmed

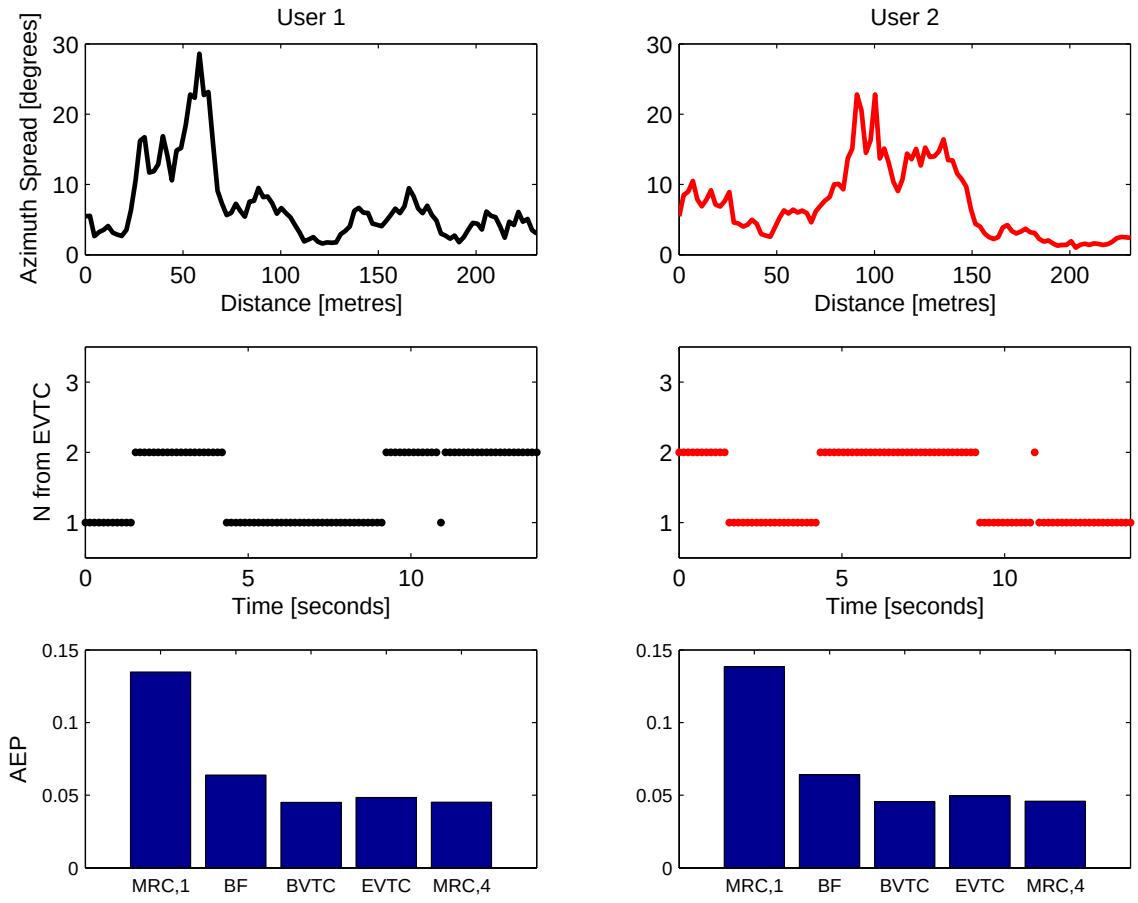

Figure 5.8. Azimuth spread, EVTC MREC order, and corresponding AEP performance for the conventional and enhanced receivers (approximate eigen-/combining); for EVTC MREC, the two users continuously share the FPGA chip.

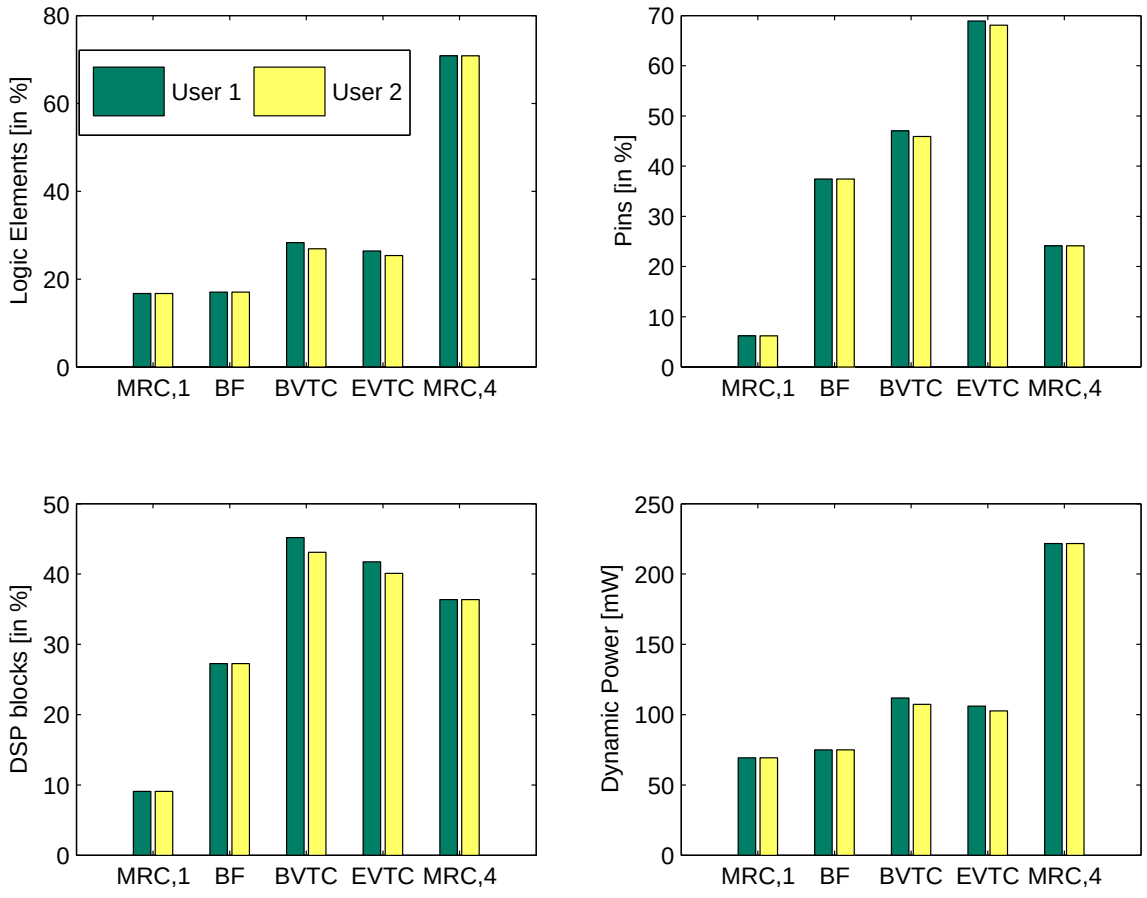

Figure 5.9. Resource usage (in percentage of total available), and dynamic power consumption for the conventional and enhanced receivers (approximate eigen-/combining); for EVTC MREC, the two users continuosly share the FPGA chip.

for KLT, channel estimation, signal combining, and symbol detection, and 2) a device (DSP, FPGA, soft-processor) monitoring each user's channel conditions (i.e., eigenmodes) to adaptively allocate the minimum resource share that offers the required performance. At the beginning of each frame, the monitoring device browses a user hierarchy and the information about their channel conditions, and allocates the FPGA resources accordingly. Several users whose respective received signals are highly correlated can share the e.p.m. on a single FPGA. If the AS for one of these users later widens significantly (yielding more available diversity gain), a larger share of the FPGA resources can be allocated accordingly, if better performance is required. This yields an efficient, performance- and power-aware, antenna array receiver. Such implementations could use MREC adaptation based on the performance–complexity tradeoff criterion (PCTC) — see Section 4.4.2, on page 146 — as described next.

5.2.4 PCTC-based MREC receiver designs

5.2.4.1 PCTC-based MREC Receiver Designs for Continuously-Active Users

We assume again that $N_{\mathrm{e}} = 3$ e.p.m. are available on a base-station FPGA chip, to process the signals received with a ULA with $L = 4$ from $N_{\mathrm{u}} = 2$ users.

Let us suppose that each active user is allotted one e.p.m. by default. The PCTC performance improvement thresholds from (4.12), page 146, were selected as $\upsilon_1 = 0.8$ and $\upsilon_2 = 0.7$. Based on (4.13), on page 147, these yield the corresponding cutoff average effective SNRs as $\Gamma_{c,\text{User 1}} \approx -6$ dB and $\Gamma_{c,\text{User 2}} \approx -3.7$ dB. Then, at the beginning of each frame, the remaining e.p.m. is allocated as indicated in Table 5.2. Thus, User 1 has higher priority than User 2 in adding an e.p.m., and a lower cutoff SNR as well. Note that when applied for approximate-MREC adaptation, the PCTC requires very careful selection of its cutoff SNR, since an extra e.p.m may actually degrade performance, though not significantly — see discussion on page 97.

For the same scenario as for the results shown in Fig. 5.8 on page 177, but different AS trials

Table 5.2. Resource allocation procedure for PCTC MREC.

if $\Gamma_{2,\text{User 1}} \geq \Gamma_{c,\text{User 1}}$
then allocate available e.p.m. to User 1
else if $\Gamma_{2,\text{User 2}} \geq \Gamma_{c,\text{User 2}}$
then allocate available e.p.m. to User 2
otherwise leave e.p.m. unallocated, to save dynamic power.

for the two users, Fig. 5.10 shows in the top subplot the AS sequences. The middle subplot shows the orders selected with the PCTC-based procedure indicated in Table 5.2. The bottom subplots show the average (over the AS trial, and thus also over the fading) AEP performance for approximate eigen-/combining. A detail with the AS sequences and the corresponding MREC orders selected for each user appears in Fig. 5.11. When the AS for both users was small enough, the extra e.p.m. is not allocated, which can yield power savings in implementations which also employ clock gating. On the other hand, User 2 is allocated 2 e.p.m. only when the diversity gain is not available for User 1.

Higher priority for User 1 was effective: it yields $\text{BER}_1 = 0.0534$ vs. $\text{BER}_2 = 0.0623$ — see the bottom subplots in Fig. 5.8 — even though $E\{\text{AS}_1\} \approx 3.9^\circ < E\{\text{AS}_2\} \approx 10^\circ$. PCTC MREC yields the same performance for User 1 as BVTC MREC. For User 2, BVTC MREC outperforms PCTC MREC, due to wide AS and resource restrictioning in PCTC MREC.

These observations are supported by the resource-usage results from Fig. 5.12. For User 2, the BVTC selects higher MREC order than PCTC, and thus BVTC MREC requires more resources compared to PCTC MREC. For User 1, BVTC and PCTC have about the same resource requirements (pins excepted). Finally, PCTC MREC halves the dynamic and static power consumption as well, compared to MRC.

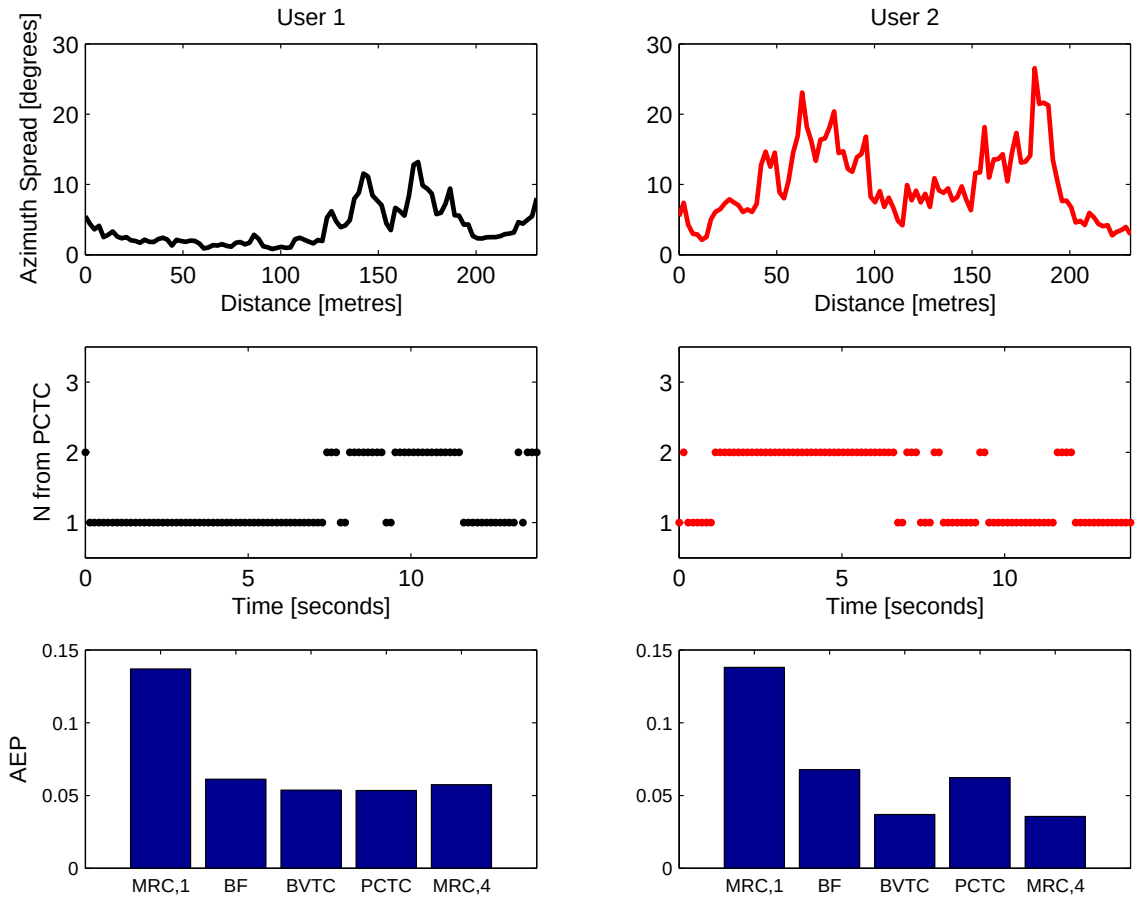

Figure 5.10. Azimuth spread, PCTC MREC order, and corresponding AEP performance for the conventional and enhanced receivers (approximate eigen-/combining); for PCTC MREC, the two users continuously share the FPGA chip.

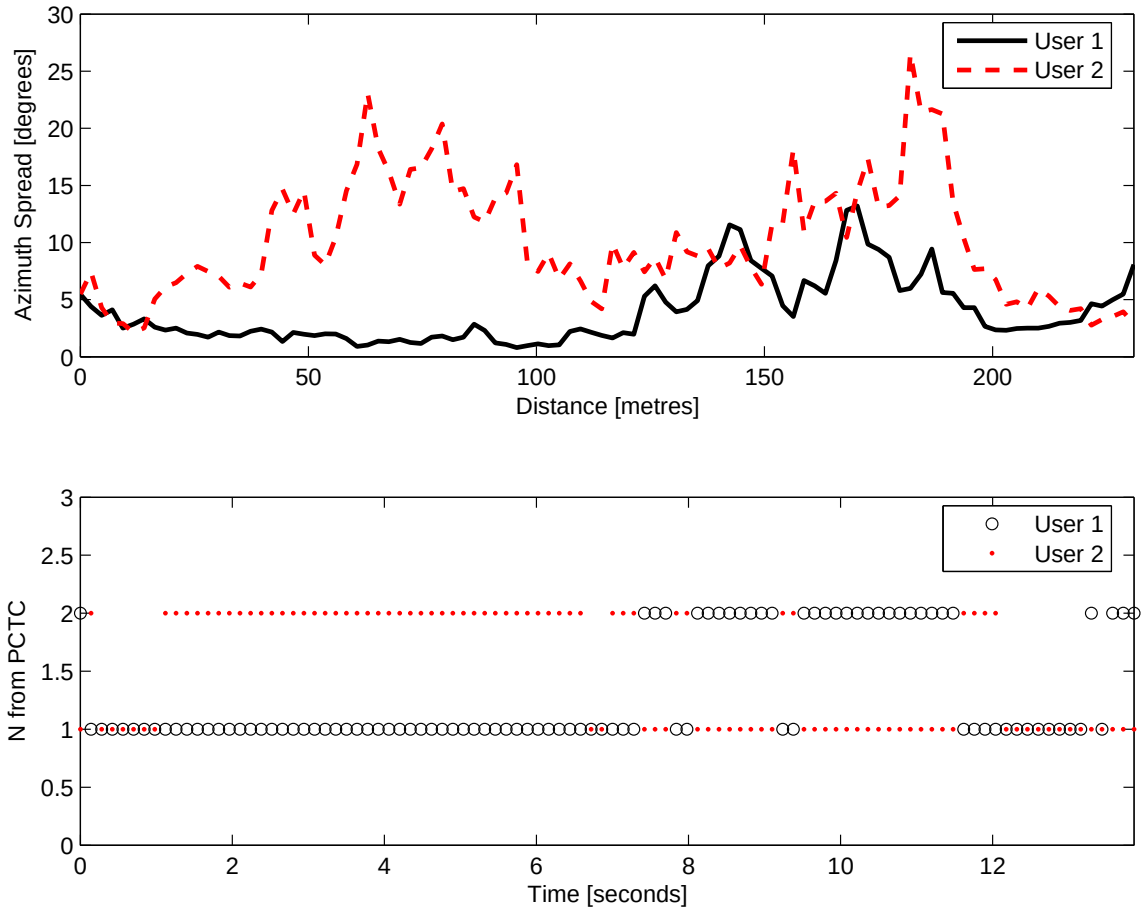

Figure 5.11. Azimuth spread, and PCTC MREC order when two users continuously share the FPGA chip.

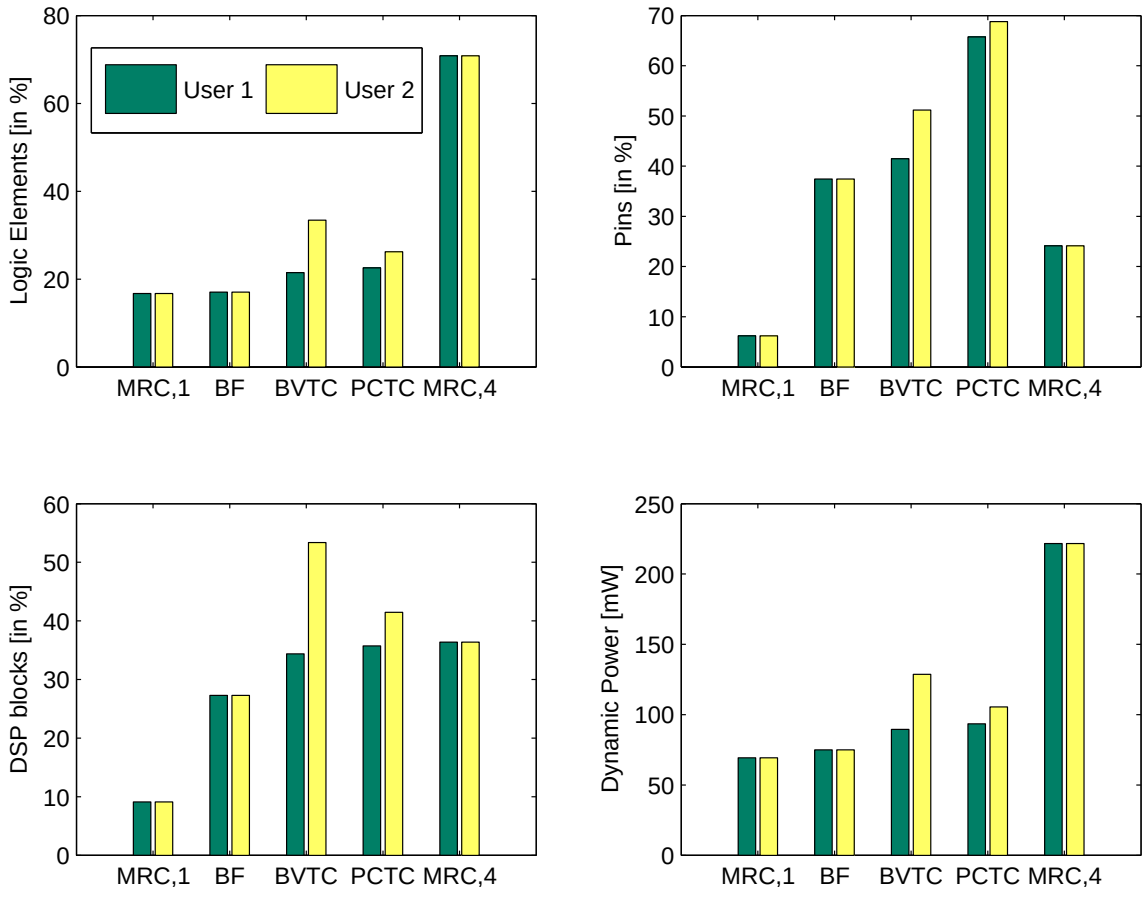

Figure 5.12. Resource usage (in percentage of total available), and dynamic power consumption, for the conventional and enhanced receivers (approximate eigen-/combining); for PCTC MREC, the two users continuously share the FPGA chip.

5.2.4.2 PCTC-based MREC Receiver Designs for Intermittently-Active Users

For the same settings as above but different AS sequences, shown in Fig. 5.13 (top subplot), consider User 1 transmitting continuously (such as a voice user), while User 2 is only active in the interval $[3.5\text{ s}, 10.5\text{ s}]$ (such as a data user). Note that User 2 could have transmission durations as short as a frame. We employ the PCTC discussed in Section 4.4.2, page 146, to distribute FPGA resources between users using the procedure from Table 5.2, on page 180.

If only User 1 is actively transmitting, we set $\upsilon_1 = 0.95$, i.e., $\Gamma_{c,\text{User 1}} = -12.8$ dB, which means that the control algorithm will readily allocate new resources. When User 2 becomes active as well, we set $\upsilon_2 = 0.7$, i.e., $\Gamma_{c,\text{User 2}} = -3.7$ dB, and $\upsilon_1 = 0.8$, i.e., $\Gamma_{c,\text{User 1}} = -6$ dB.

The selected MREC orders are displayed in Fig. 5.13 (middle subplot). A detail of the AS sequences and the PCTC orders is shown in Fig. 5.14. The average AEP is shown in Fig. 5.13 (bottom subplot) for this implementation of PCTC MREC, as well as for the conventional receiver and other enhanced receivers presented earlier. Note that, although $E\{\text{AS}_1\} \approx 4.9^\circ < E\{\text{AS}_2\} \approx 14.3^\circ$, the average (over the AS trial) AEP performance is slightly better for User 1 than for User 2, i.e., $\text{BER}_1 = 0.0637$ and $\text{BER}_2 = 0.0702$.

Figs. 5.13 and 5.15 indicate that, for User 1, BVTC MREC outperforms, and requires fewer resources, than PCTC MREC, which is due to the fact that for approximate eigen-combining, using more eigenbranches in low AS can actually yield poorer performance. Thus, a more conservative (i.e., lower) υ value would be advisable for User 1 when User 2 was not transmitting.

Fig. 5.15 also shows a much lower resource requirement for PCTC MREC for User 2 compared to User 1, which is expected since User 2 is active only half of the time.

In conclusion, although FPGA-based implementations of BF and MRC antenna array receivers outperform the single-branch receiver, the performance gain may not always justify the

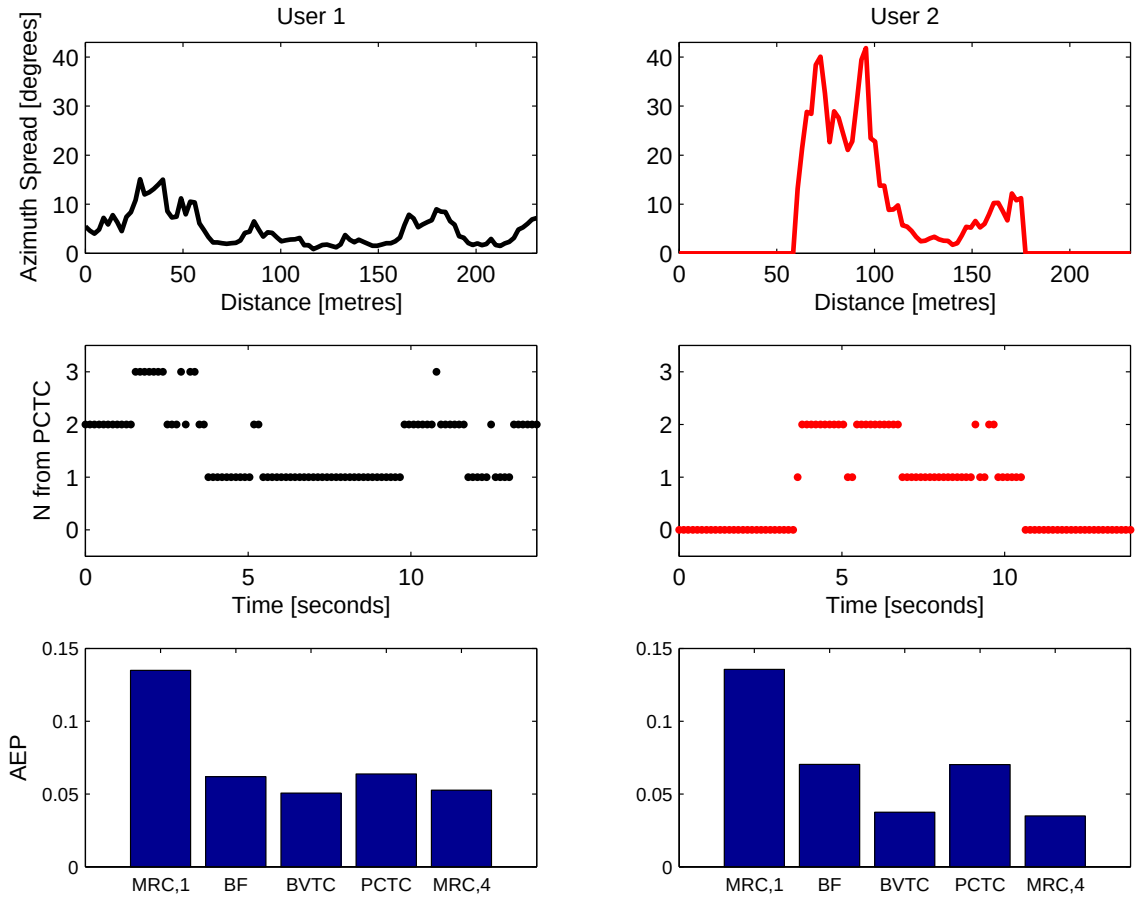

Figure 5.13. Azimuth spread, PCTC MREC order, and corresponding AEP performance for the conventional and enhanced receivers (approximate eigen-/combining); for PCTC MREC, the two users intermittently share the FPGA chip. User 2 enters the system at time 3.5 s, and exits at 10.5 s.

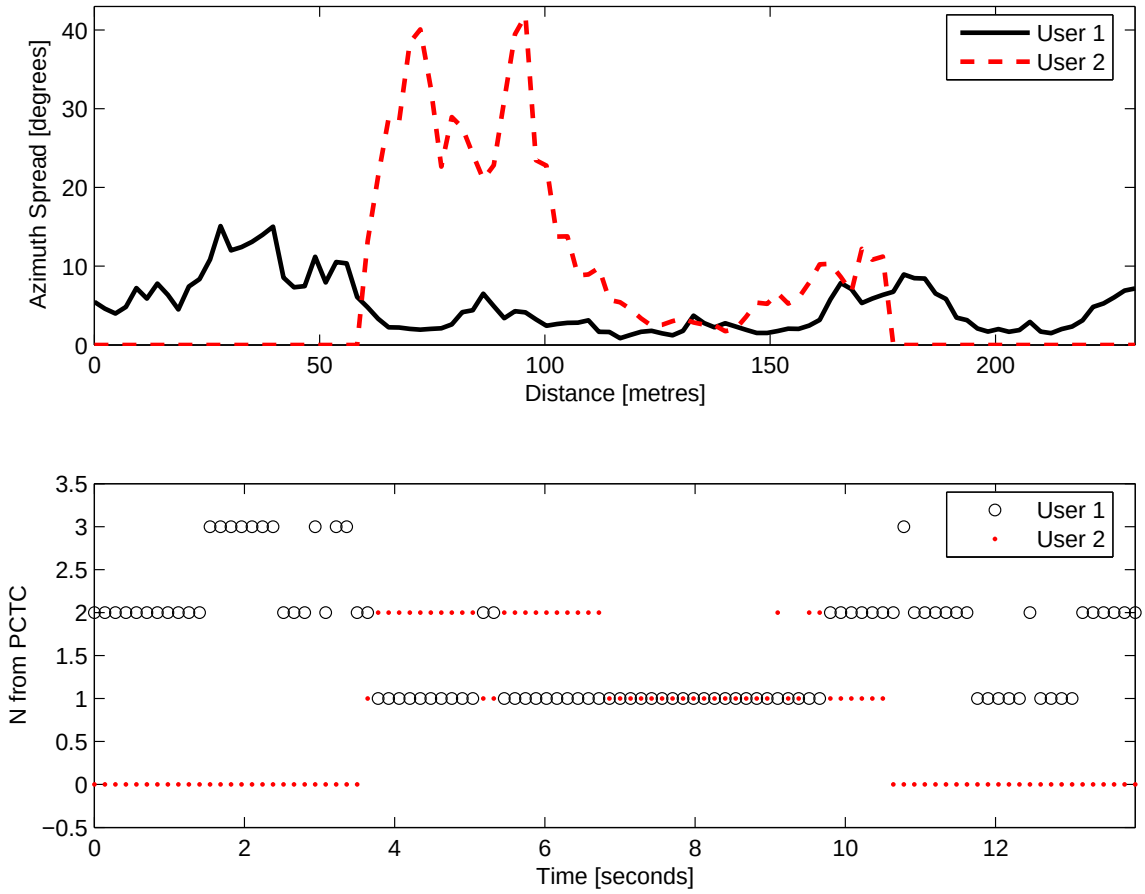

Figure 5.14. Azimuth spread, and PCTC MREC order when two users intermittently share the FPGA chip. User 2 enters the system at time 3.5 s, and exits at 10.5 s.

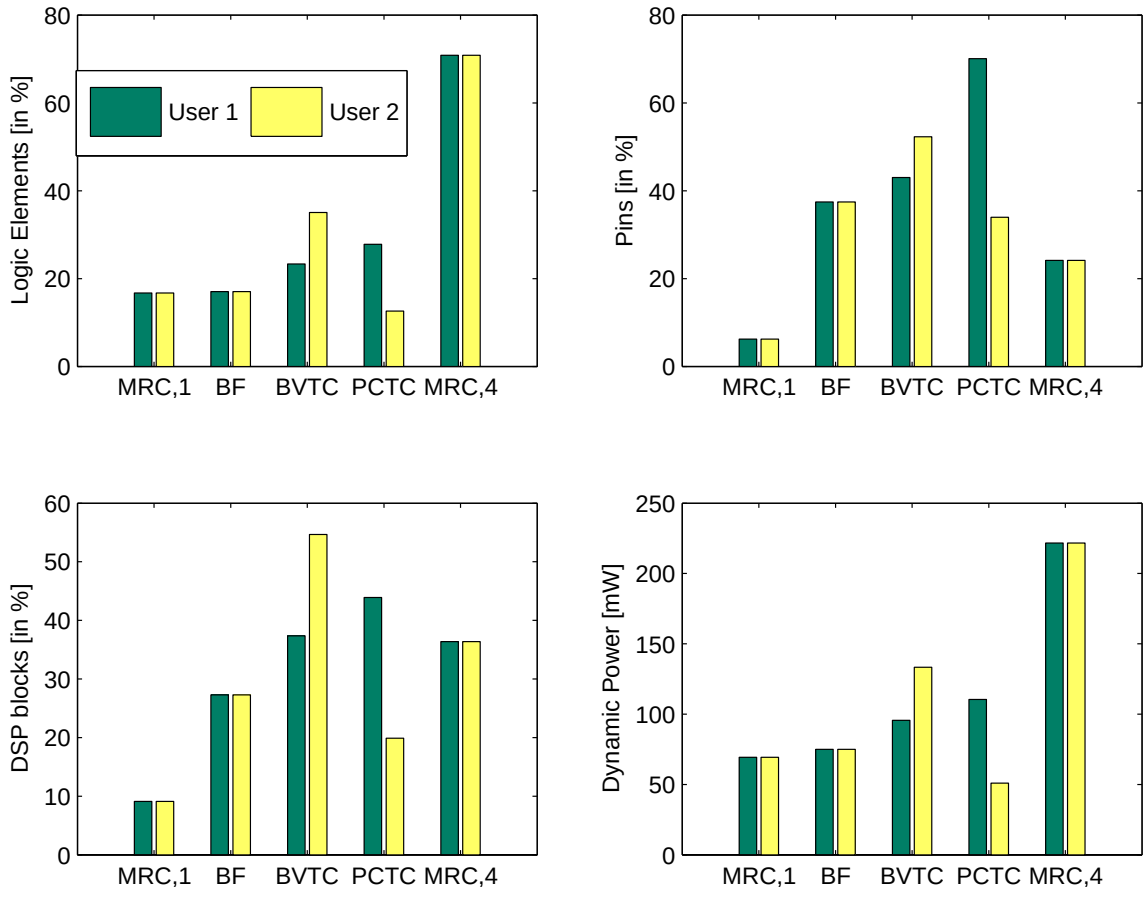

Figure 5.15. Resource usage (in percentage of total available), and dynamic power consumption for the conventional and enhanced receivers (approximate eigen-/combining); for PCTC MREC, the two users intermittently share the FPGA chip. User 2 enters the system at time 3.5 s, and exits at 10.5 s.

additional implementation and operational costs. Adaptive algorithms which track the slowly-varying dominant channel eigenmodes can yield smarter, performance- and power-aware, antenna arrays. A two-fold user-processing capacity increase, or power consumption decrease, is possible, for a typical urban scenario. FPGAs can thus yield very efficient implementations of adaptive receivers which are based on parallelizable algorithms, for 3G systems.

Chapter 6

Eigen-/Combining for CDMA Systems

6.1 Chapter Overview

In this chapter we first introduce the code-division multiple access [140, 155] (CDMA) concept and its application to multi-branch receivers. We then present the CDMA transmitted signal model and despreading techniques for the received signal. A practical implementation method for optimum combining is subsequently proposed and demonstrated. Finally, optimum eigen-combining — which takes advantage of fading gain correlation to reduce problem dimensionality — is described, along with its implementation.

6.2 Multi-Branch CDMA Receiver Background

CDMA uses codes to distinguish among transmitters within the same frequency band in order to increase user capacity [140, 155]. This multiple access technique is employed in 2nd generation (2G) and 3rd generation (3G) wireless communications systems [33, 71, 132, 134].

The RAKE receiver [63, Chapter 13] [114] is readily applicable in CDMA systems subjected to frequency selectivity [100]. Such a multi-branch receiver has been proposed for

CDMA systems to yield a form of frequency diversity gain. Nevertheless, recent comprehensive measurement results described in [104] for macrocellular, microcellular, and indoor wideband channels indicate that RAKE temporal taps can be highly correlated, thus drastically limiting the potential diversity gain.

Over the past decade a significant effort has also been devoted to the evaluation of antenna-array-based CDMA systems employing statistical beamforming or diversity combining or both [33, Chapter 3] [35,36] [42,43,83] [100,101] [134, Chapter 3]. When the processing gain (PG) is large and when the power control is accurate, CDMA interference can be approximated as spatially white [101]. However, in 3G systems the processing gain is variable and can be low, which yields non-white interference. Then, maximum average (over fading) signal-to-noise ratio (SNR) beamforming has been shown to be outperformed by maximum average signal-to-interference-plus-noise (SINR) beamforming [43]. The maximal-ratio combining (MRC) CDMA antenna array receiver, which disregards the interference, is suboptimum as well [101]. On the other hand, optimum combining [123, Chapter 10] [148] limits the degrading effect of interference-plus-noise and enhances the intended signal (to the extent allowed by the number of receiver branches).

Naguib [100, 101] proposed a practical approach to optimum combining for CDMA systems with base-station antenna array [101, Section 3.2.2], and studied the effect of temporal and spatial fading correlation caused, respectively, by user motion and azimuth spread (for uniform power azimuth spectrum) [101, Chapter 4]. The interference-cancelation properties of antenna array combining were shown to significantly improve the symbol-detection performance and user capacity [101, Chapter 6] over the single-antenna receiver. On the other hand, in [141] imposed power control accuracy restrictions for CDMA have been alleviated using directional instead of omnidirectional antennas. Lower sensitivity to imperfect power control in CDMA with base station antenna arrays is also demonstrated in [138], using a smart-antenna test-bed.

Note, however, that besides the channel gain vector for the intended user, which is the weight vector for MRC, optimum combining [123, Chapter 10] [148] also requires the inverse of the interference-plus-noise correlation matrix [123, Section 10.1.1, p. 439]. This matrix was computed in [100, 101] using the front-end (spread) received signal, which is generally represented with low numerical precision [74,122]. Furthermore, the approach from [100,101] depends on the chip-pulse waveform actually employed. Finally, estimation of channel gain vector for the intended user and the corresponding inverse interference-plus-noise correlation matrix can be computationally expensive in actual practice, when the channel gains are varying, e.g., on the order of the square of the number of branches [101, Tables 4.3, 4.4].

In [43], maximum average SINR beamforming has been suboptimally implemented for the CDMA uplink, by direct recursive updating of the combiner, for a computational load linear in the number of antenna elements. The algorithm greatly outperforms the single-antenna receiver, and the antenna array receiver which assumes white interference. Nevertheless, this approach was also designed for a specific, idealized, chip-pulse waveform, and has poor convergence properties.

RAKE processing has already been integrated with optimum (average and instantaneous — relative to the fading) array signal processing [43, 101], in order to take advantage of frequency diversity gain as well as space diversity gain and array gain. Nevertheless, the signals received at RAKE taps and antenna elements can be highly correlated [2,42,43,101,104,123]. Furthermore, normalized correlation values around $+0.5$ between delay spread and azimuth spread have been measured [8, Table IV] (this correlation value was also proposed by the 3GPP for channel simulations [2]), which indicates that space and frequency diversity gains are significantly correlated as well [8]. Thus, multi-branch CDMA signal processing algorithms could benefit by adapting their complexity to actual channel statistics, through eigencombining [35,36,42,83].

6.3 CDMA Transmitted Signal Model

Consider a generic asynchronous CDMA cellular system, with a base station antenna array receiving signals from N_{u} mobiles from the same cell. Suppose that the baseband signal transmitted by the intended mobile is

$$s(t) = b(t)\,c(t), \tag{6.1}$$

where $b(t) = \sum_{-\infty}^{+\infty} b(k) \cdot \Pi(t - kT_s)$ is the information-encoding signal, with $b(k)$ i.i.d. equiprobable BPSK symbols (± 1), modulating the rectangular symbol-pulse waveform $\Pi(t)$ of duration T_{s} [19, Section 2.5.1, p. 21]. (BPSK symbols are, for example, transmitted in the uplink of the UMTS Frequency Division Duplex (FDD) [5]. Nevertheless, the following results are readily extendable to MPSK constellations.) Further, $c(t) = \sum_{-\infty}^{+\infty} c(n) \cdot p(t - nT_{\mathrm{c}})$ is a user-specific spreading signal made of i.i.d. equiprobable BPSK chips, $c(n)$, modulating the chip-pulse waveform, $p(t)$, of duration T_{c}.

The processing (or spreading) gain of the system is defined as $\mathrm{PG} \stackrel{\Delta}{=} T_{\mathrm{s}}/T_{\mathrm{c}}$, and represents the factor by which the bandwidth of the information-bearing signal $b(t)$ is enlarged, or spread, using the chip signal, $c(t)$. It also represents the factor by which the intended signal is boosted relative to the interferers by despreading, at the receiver. The energy transmitted per symbol, E_{s}, and the energy transmitted per chip, E_{c}, are related through $E_{\mathrm{s}} = PG \cdot E_{\mathrm{c}}$.

We make the common "narrowband system" assumption [100] [106, p. 35] that the signal propagation time between antennas is equivalent to a phase shift. This holds approximately when the carrier frequency is much larger than the bandwidth of the transmitted signal, $s(t)$.

6.4 CDMA Received-Signal Despreading Methods

Despreading the received CDMA signal to the original, i.e., data, bandwidth has traditionally been done using the code-filtering approach [100, 101] described below. More recently, a despreading method useful in the computation of the interference-plus-noise correlation matrix, and entitled signal-cancelation despreading, was proposed in [93], and is described further below.

6.4.1 Code-Filtering Despreading

After the receiver filter matched to the transmitted chip-pulse waveform, and synchronized on the intended transmitter, the signal vector sampled at the lth chip, $l = 1 : PG$, within a symbol b, can be written as

$$\widetilde{\mathbf{y}}(l) = \sqrt{E_{\mathrm{c}}}\, b \widetilde{\mathbf{h}}\, c(l) + \widetilde{\mathbf{u}}(l), \tag{6.2}$$

where $\widetilde{\mathbf{h}}$ is the L-dimensional Rayleigh fading channel gain vector corresponding to the intended user, assumed to remain constant over several symbols [100] [101, Section 3.2.2]. Above, $\widetilde{\mathbf{u}}(l)$ is the interference-plus-noise signal vector, given by

$$\widetilde{\mathbf{u}}(l) = \sum_{m=1}^{N_{\mathrm{u}}} \sqrt{E_{\mathrm{c}}}\, b_m \widetilde{\mathbf{h}}_m\, c_m(l) + \widetilde{\mathbf{n}}(l), \tag{6.3}$$

where b_m, $\widetilde{\mathbf{h}}_m$, and $c_m(l)$ represent the transmitted symbol, channel gain vector, and chip sequence, respectively, for the mth interfering mobile, and $\widetilde{\mathbf{n}}(l)$ is the receiver noise vector, which is assumed to be zero-mean, complex Gaussian, temporally and spatially white. The channel gains, transmitted symbols and chips are assumed mutually uncorrelated between different mobiles.

Hereafter, the term "short-term averaging" will stand for temporal averaging over the longest period wherein the channel gains can be assumed constant. In terms of ensemble averaging,

we assume that this operation is equivalent to averaging over the noise, chips, and symbols. "Long-term averaging" will stand for averaging over the longest period in which the channel fading statistics remain constant. In terms of ensemble averaging, we assume that this operation is equivalent to averaging over noise, chips, symbols, and the channel fading gains.

For the traditional *code-filtering* despreading approach [100, 101], $\widetilde{\mathbf{y}}(l)$ given by (6.2) is correlated with the intended mobile's spreading sequence, as follows

$$\begin{aligned}\widetilde{\mathbf{y}} &= \sum_{l=1}^{PG} c(l)\,\widetilde{\mathbf{y}}(l) = \sqrt{E_{\mathrm{c}}}\,b\,\widetilde{\mathbf{h}} \sum_{l=1}^{PG} \underbrace{c(l)^2}_{=1} + \sum_{l=1}^{PG} c(l)\,\widetilde{\mathbf{u}}(l) \\ &= PG\sqrt{E_{\mathrm{c}}}\,b\,\widetilde{\mathbf{h}} + \widetilde{\mathbf{u}}_{\mathrm{cf}} = \sqrt{PG}\,\sqrt{E_{\mathrm{s}}}\,b\,\widetilde{\mathbf{h}} + \widetilde{\mathbf{u}}_{\mathrm{cf}}, \end{aligned} \tag{6.4}$$

where the interference-plus-noise term is

$$\widetilde{\mathbf{u}}_{\mathrm{cf}} \stackrel{\triangle}{=} \sum_{l=1}^{PG} c(l)\,\widetilde{\mathbf{u}}(l). \tag{6.5}$$

Note that the correlation matrix of this vector depends on the chip-pulse waveform actually used [93, 100, 101].

6.4.2 Signal-Cancelation Despreading

Despreading the received signal for the intended user using the chip sequence obtained from the original one as follows [93, Eqn. 7]

$$d(l) = (-1)^{l-1}\,c(l),\ l = 1 : PG, \tag{6.6}$$

yields the despread signal

$$\begin{aligned}\widetilde{\mathbf{z}} &= \sum_{l=1}^{PG} d(l)\,\widetilde{\mathbf{y}}(l) \\ &= \sqrt{E_{\mathrm{c}}}\,b\,\widetilde{\mathbf{h}} \underbrace{\sum_{l=1}^{PG} (-1)^{l-1} c(l)^2}_{=0,\,\text{for even PG}} + \sum_{l=1}^{PG} d(l)\,\widetilde{\mathbf{u}}(l). \end{aligned} \tag{6.7}$$

Note the null contribution of the intended signal to $\widetilde{\mathbf{z}}$, justifying the title of *signal-cancelation* despreading for this method [93].

Interestingly, it can readily be shown that the statistics of the signal-cancelation despreading output $\widetilde{\mathbf{z}}$ from (6.7) coincide with those of the code-filtering interference-plus-noise, $\widetilde{\mathbf{u}}_{\text{cf}}$ from (6.5), i.e., $E\{\widetilde{\mathbf{u}}_{\text{cf}}\widetilde{\mathbf{u}}_{\text{cf}}\} = \mathbf{R}_{\widetilde{\mathbf{z}}}$ [93]. Then, (6.4) yields

$$\mathbf{R}_{\widetilde{\mathbf{y}}} = PG \cdot E_{\text{s}} \cdot E\{\widetilde{\mathbf{h}}\widetilde{\mathbf{h}}^H\} + \mathbf{R}_{\widetilde{\mathbf{z}}}, \tag{6.8}$$

where averaging is over the noise, chips, symbols, and, can be over the channel gains as well.

6.5 Optimum Eigen-/Combining

6.5.1 Optimum Beamforming

For the code-filtering signal model from (6.4), the maximum average SINR beamformer [43, Section III.A] is the vector $\widetilde{\mathbf{w}} \in \mathbb{C}^L$ which maximizes

$$\text{SINR}(\widetilde{\mathbf{w}}) \stackrel{\triangle}{=} \frac{\text{PG} \cdot E_{\text{s}} \cdot \widetilde{\mathbf{w}}^H \mathbf{R}_{\widetilde{\mathbf{h}}} \widetilde{\mathbf{w}}}{\widetilde{\mathbf{w}}^H E\{\widetilde{\mathbf{u}}_{\text{cf}}\widetilde{\mathbf{u}}_{\text{cf}}\}\widetilde{\mathbf{w}}}, \tag{6.9}$$

i.e.,

$$arg \max_{\widetilde{\mathbf{w}} \in \mathbb{C}^L} \frac{\widetilde{\mathbf{w}}^H \mathbf{R}_{\widetilde{\mathbf{h}}} \widetilde{\mathbf{w}}}{\widetilde{\mathbf{w}}^H \mathbf{R}_{\widetilde{\mathbf{z}}} \widetilde{\mathbf{w}}}, \text{ or } \frac{\widetilde{\mathbf{w}}^H \left(\mathbf{R}_{\widetilde{\mathbf{y}}} - \mathbf{R}_{\widetilde{\mathbf{z}}}\right) \widetilde{\mathbf{w}}}{\widetilde{\mathbf{w}}^H \mathbf{R}_{\widetilde{\mathbf{z}}} \widetilde{\mathbf{w}}}, \text{ or } \frac{\widetilde{\mathbf{w}}^H \mathbf{R}_{\widetilde{\mathbf{y}}} \widetilde{\mathbf{w}}}{\widetilde{\mathbf{w}}^H \mathbf{R}_{\widetilde{\mathbf{z}}} \widetilde{\mathbf{w}}}. \tag{6.10}$$

Since the interference-plus-noise correlation matrix $\mathbf{R}_{\widetilde{\mathbf{z}}}$ is a positive definite matrix, there exists a positive definite matrix $\mathbf{R}_{\widetilde{\mathbf{z}}}^{1/2}$ such that $\mathbf{R}_{\widetilde{\mathbf{z}}} = \mathbf{R}_{\widetilde{\mathbf{z}}}^{1/2} \mathbf{R}_{\widetilde{\mathbf{z}}}^{1/2}$, which is called the square-root decomposition of $\mathbf{R}_{\widetilde{\mathbf{z}}}$ [94, ¶9.12.3(2), p. 155] [64, ¶. 11.2-4, p. 395] [101]. The optimum beamformer from (6.10) is then given by

$$\widetilde{\mathbf{w}}_{\text{BF}} = \mathbf{R}_{\widetilde{\mathbf{z}}}^{-1/2} \mathbf{d}\left(\mathbf{R}_{\widetilde{\mathbf{z}}}^{-1/2} (\mathbf{R}_{\widetilde{\mathbf{y}}} - \mathbf{R}_{\widetilde{\mathbf{z}}}) \mathbf{R}_{\widetilde{\mathbf{z}}}^{-1/2}\right) = \mathbf{R}_{\widetilde{\mathbf{z}}}^{-1/2} \mathbf{d}\left(\mathbf{R}_{\widetilde{\mathbf{z}}}^{-1/2} \mathbf{R}_{\widetilde{\mathbf{y}}} \mathbf{R}_{\widetilde{\mathbf{z}}}^{-1/2}\right), \tag{6.11}$$

where $\mathbf{d}(\cdot)$ represents the dominant eigenvector of the enclosed matrix.

For spatially-white interference this reduces to $\mathbf{d}\left(\mathbf{R}_{\widetilde{\mathbf{y}}}\right)$, which actually coincides with $\mathbf{d}\left(\mathbf{R}_{\widetilde{\mathbf{h}}}\right)$ — see Section 3.5.2.1, on page 71, where maximum average SNR beamforming is discussed. For nonfading channel, $\mathbf{d}\left(\mathbf{R}_{\widetilde{\mathbf{h}}}\right) \propto \widetilde{\mathbf{h}}$, and maximum SNR beamforming actually reduces to maximal-ratio combining (MRC) — see Section 3.5.1.1, on page 61.

In order to solve the above problem in practice, $\mathbf{R}_{\widetilde{\mathbf{z}}}^{-1/2}$ can be updated directly from samples of $\widetilde{\mathbf{z}}$ using the square-root updating algorithm described in [100, Table 1, p. 1517], with complexity order $\mathscr{O}(L^2)$. The required dominant eigenvector can be computed using the *Power Method* [64] [101, Section 4.1.1], of complexity order $\mathscr{O}(L^2)$. A direct, but approximate, recursion for the optimum beamformer [43, Eqn. 28, p. 812] reduces complexity to $\mathscr{O}(L)$. Since the execution of these matrix and vector operations can be distributed over a long period (i.e., the period in which the channel statistics remain relatively constant), they do not represent a considerable computational burden [1, 35, 36].

6.5.2 Optimum Combining

For the despread signal model from (6.4), maximizing the SINR defined as in (6.9), now without averaging over the fading, yields the optimum combiner

$$\widetilde{\mathbf{w}} = \left[E\{\widetilde{\mathbf{u}}_{\mathrm{cf}}\widetilde{\mathbf{u}}_{\mathrm{cf}}\}\right]^{-1}\widetilde{\mathbf{h}} = \left[E\{\widetilde{\mathbf{z}}\widetilde{\mathbf{z}}\}\right]^{-1}\widetilde{\mathbf{h}}, \tag{6.12}$$

and then the BPSK symbol can be detected as $\widehat{b} = \mathrm{sign}\{\Re\left[\widetilde{\mathbf{w}}^H\widetilde{\mathbf{y}}\right]\}$.

Recursive estimation of the short-term $\mathbf{R}_{\widetilde{\mathbf{z}}}^{-1}$ from samples of $\widetilde{\mathbf{z}}$ can use the approach described in [100, 101], i.e., update $\mathbf{R}_{\widetilde{\mathbf{z}}}^{-1/2}$ and then compute $\mathbf{R}_{\widetilde{\mathbf{z}}}^{-1} = \mathbf{R}_{\widetilde{\mathbf{z}}}^{-1/2}\mathbf{R}_{\widetilde{\mathbf{z}}}^{-1/2}$. On the other hand, exploiting the short-term version of (6.8) yields $\widetilde{\mathbf{h}}\widetilde{\mathbf{h}}^H \propto \mathbf{R}_{\widetilde{\mathbf{y}}} - \mathbf{R}_{\widetilde{\mathbf{z}}}$. Hence, $\widetilde{\mathbf{h}}$, required for (6.12), is the dominant eigenvector of $\mathbf{d}\left(\mathbf{R}_{\widetilde{\mathbf{y}}} - \mathbf{R}_{\widetilde{\mathbf{z}}}\right)$, which is computable using the *Power Method* [64] [101, Section 4.1.1], of complexity order $\mathscr{O}(L^2)$.

Fig. 6.1 describes CDMA optimum combining, which requires channel-rate and symbol-rate operations involving L-dimensional vectors and $L \times L$ matrices. Hence, the data rate and the number L of receiver branches are limited by the complexity involved by the computation of the combiner from (6.12). Described further below is an eigen-combining approach that can reduce the channel-rate and symbol-rate processing volume and can improve performance [36].

Note that the proposed combining method makes no direct use of the spread (pre-correlation) received signal vector. This is important since its numerical representation precision is usually very limited [74, 122]. Further benefits of signal-cancelation despreading are described next.

6.5.3 Numerical Results for Nonfading Scenario

As in [126], a simplified scenario with zero azimuth spread is considered, i.e., with fully correlated channel gain vector components (which differ only by a deterministic phase, related to the corresponding AoA) for each user [99]. The terms "combining" and "beamforming" are then interchangeable. Assuming no temporal fading as well, the required correlation matrices were computed using their theoretical expressions given by [126, Eqns. 3 – 7]

$$\mathbf{R}_{\tilde{\mathbf{y}}} = \mathrm{PG}\, E_{\mathrm{s}}\, \widetilde{\mathbf{h}}\widetilde{\mathbf{h}}^{H} + \xi \sum_{m=1}^{N_{\mathrm{u}}} E_{\mathrm{s}}\, \widetilde{\mathbf{h}}_m \widetilde{\mathbf{h}}_m^{H} + \zeta\, N_0\, \mathbf{I}, \tag{6.13}$$

$$\mathbf{R}_{\tilde{\mathbf{z}}} = \xi \sum_{m=1}^{N_{\mathrm{u}}} E_{\mathrm{s}}\, \widetilde{\mathbf{h}}_m \widetilde{\mathbf{h}}_m^{H} + \zeta\, N_0\, \mathbf{I}, \tag{6.14}$$

where ξ and ζ depend on the chip-pulse waveform. Note that $\mathbf{R}_{\tilde{\mathbf{z}}}$ coincides with the $\mathbf{R}_{\tilde{\mathbf{y}}}$ component corresponding to the interference-plus-noise, regardless of the chip-pulse waveform. On the other hand, the required dominant eigenvectors were estimated using the Power Method.

For the numerical results presented next we also assume rectangular chip-pulse waveform and $PG = 128$. The intended signal arrives with power 0 dB from AoA 0° (i.e., antenna broadside), while interfering signals arrive from up to 8 users, with power 10 dB from AoAs $\pm 5^\circ$, $\pm 15^\circ$, $\pm 25^\circ$, $\pm 35^\circ$.

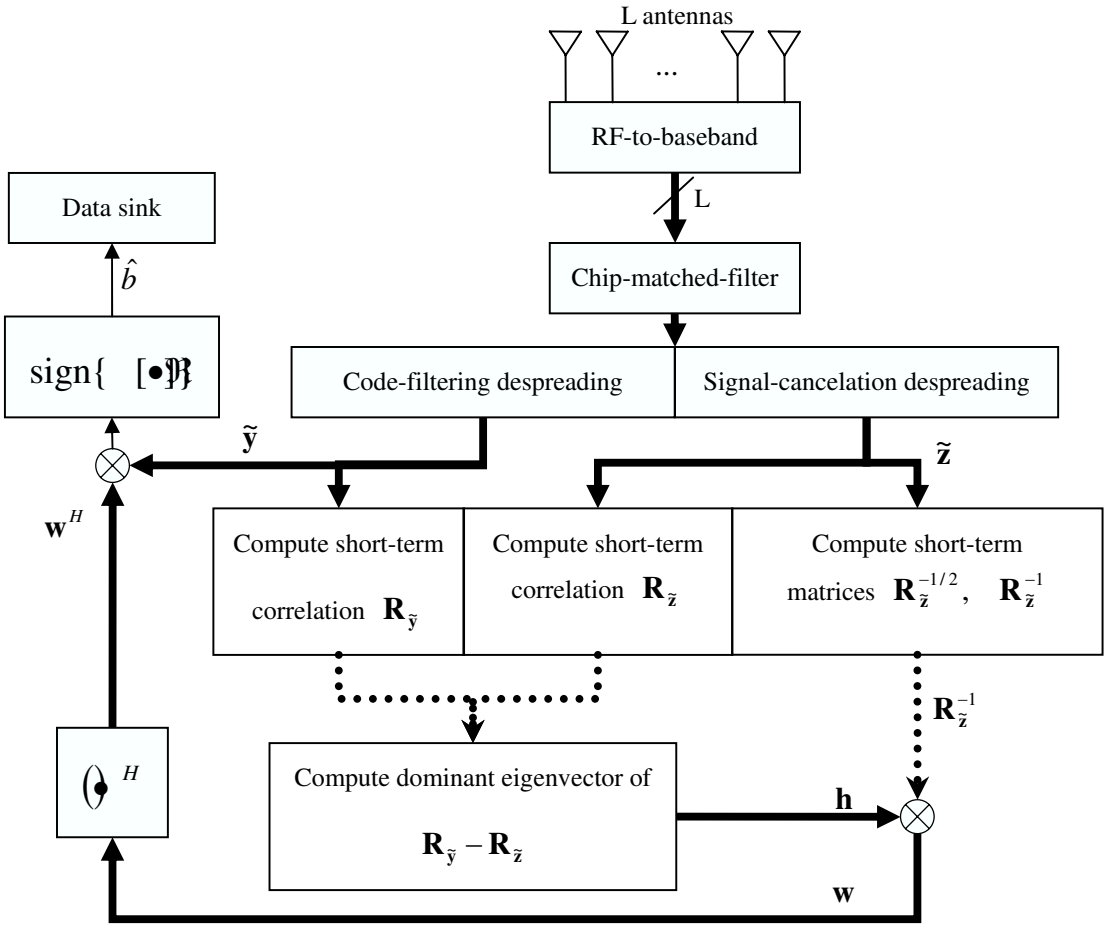

Figure 6.1. Combining for CDMA systems using jointly code-filtering and signal-cancelation despreading.

Fig. 6.2 shows poor performance for the beamforming (combining) approach proposed by Naguib in [100,101] — which computes the optimum beamformer (combiner) using the spread signal and the code-filtering output — compared to theoretical maximum SINR beamforming, and even the suboptimum maximum-SNR beamforming (which assumes white interference). The degradation is due to the fact that Naguib's approach [100,101] assumes an idealized band-limited chip-pulse waveform, and is suboptimum otherwise. Our method using the signal-cancelation and code-filtering despread signals yields SINR very close to that of theoretical maximum SINR beamforming, because it is independent of the chip-pulse waveform.

Fig. 6.3 shows that the beamforming approach proposed by Choi *et al.* in [43], which also uses the spread signal and the code-filtering output, yields much slower convergence to the optimum beamformer than our approach. Furthermore, the number of PM iterations required for convergence in Choi's method increases significantly when strong interferers are added to the system, while for our approach this number remains almost constant. The improvement is due to the fact that our proposal computes the dominant eigenvector for a near-unitary-rank matrix, while Choi's method [43] employs a higher-rank matrix with more interferers.

These results indicate that, even when the degrading effect of poor quantization precision for the front-end, i.e., spread, signal is not included, the proposed signal-cancelation-based approaches are more accurate and faster-converging than previous proposals [43, 101].

6.5.4 Optimum Eigen-Combining

The long-term $\mathbf{R}_{\widetilde{\mathbf{z}}}^{-1/2}$ can also be updated recursively by applying the square-root updating algorithm from [100, 101]. Then, the interference-plus-noise component of the code-filtering signal described by (6.4) can be whitened in long-term as follows

$$\begin{aligned} \widetilde{\mathbf{y}}_{\mathrm{w}} &\triangleq \mathbf{R}_{\widetilde{\mathbf{z}}}^{-1/2}\widetilde{\mathbf{y}} = \sqrt{PG}\cdot\sqrt{E_{\mathrm{s}}}\, b\, \mathbf{R}_{\widetilde{\mathbf{z}}}^{-1/2}\,\widetilde{\mathbf{h}} + \mathbf{R}_{\widetilde{\mathbf{z}}}^{-1/2}\widetilde{\mathbf{u}}_{\mathrm{cf}} \\ &= \sqrt{PG}\cdot\sqrt{E_{\mathrm{s}}}\, b\,\widetilde{\mathbf{h}}_{\mathrm{w}} + \widetilde{\mathbf{u}}_{\mathrm{w}}, \end{aligned} \tag{6.15}$$

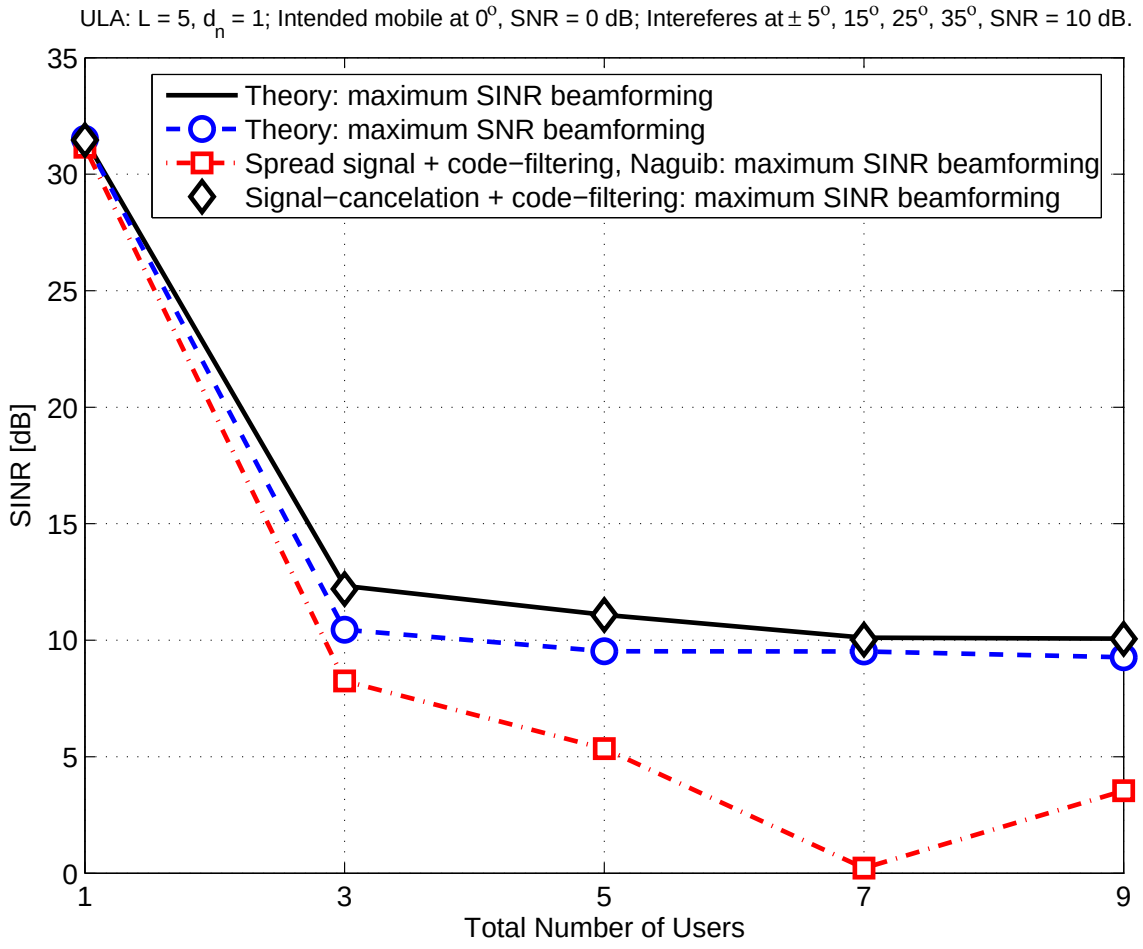

Figure 6.2. SINR achieved by beamforming approaches vs. the number of signal sources, for rectangular chip-pulse waveform

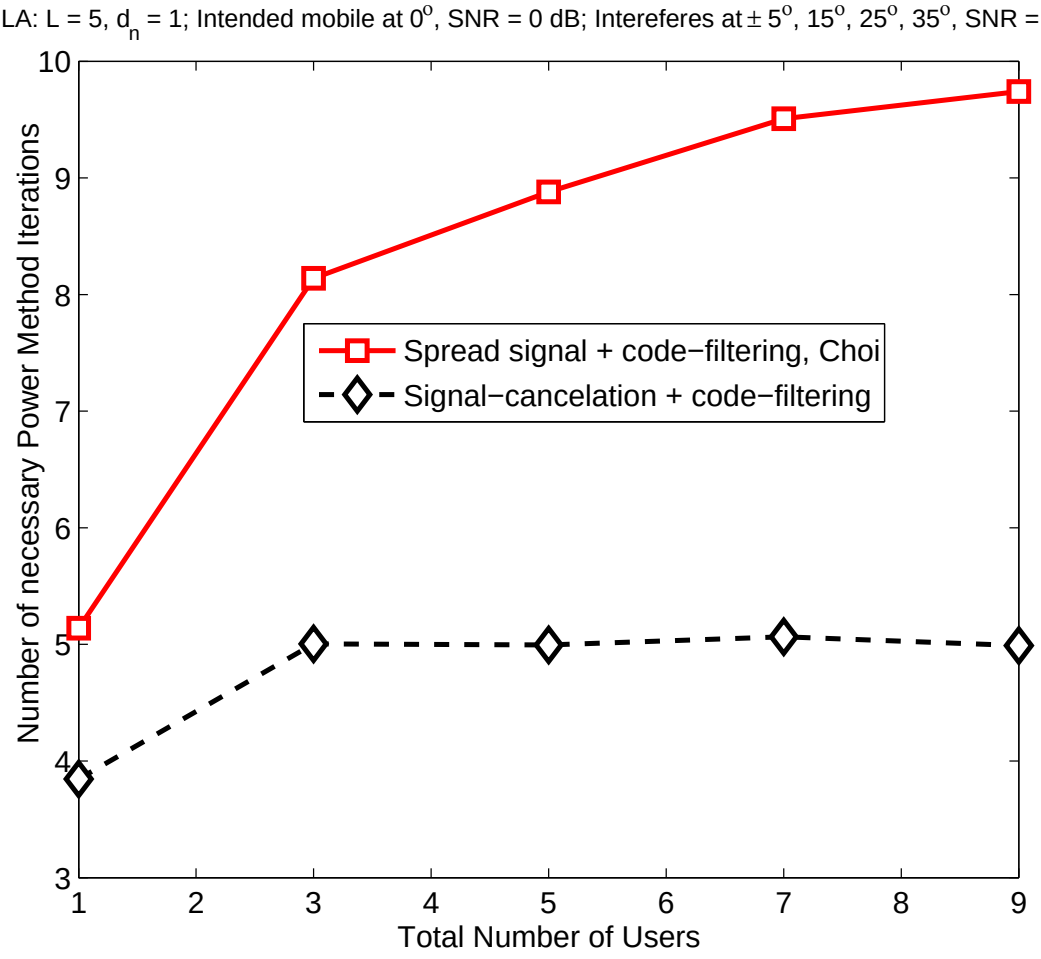

Figure 6.3. Number of Power Method iterations required for beamforming approaches vs. the number of signal sources, for rectangular chip-pulse waveform

where $\widetilde{\mathbf{h}}_{\mathrm{w}} \stackrel{\triangle}{=} \mathbf{R}_{\widetilde{\mathbf{z}}}^{-1/2}\widetilde{\mathbf{h}}$, and $\widetilde{\mathbf{u}}_{\mathrm{w}} \stackrel{\triangle}{=} \mathbf{R}_{\widetilde{\mathbf{z}}}^{-1/2}\widetilde{\mathbf{u}}_{\mathrm{cf}}$ has long-term-uncorrelated, unit-variance components, so that

$$\mathbf{R}_{\widetilde{\mathbf{y}}_{\mathrm{w}}} \stackrel{\triangle}{=} E\{\widetilde{\mathbf{y}}_{\mathrm{w}}\widetilde{\mathbf{y}}_{\mathrm{w}}^{H}\} = \mathbf{R}_{\widetilde{\mathbf{z}}}^{-1/2}\mathbf{R}_{\widetilde{\mathbf{y}}}\mathbf{R}_{\widetilde{\mathbf{z}}}^{-1/2} = PG\cdot E_{\mathrm{s}}\cdot\mathbf{R}_{\widetilde{\mathbf{h}}_{\mathrm{w}}} + \mathbf{I}_{\mathrm{L}}. \tag{6.16}$$

Employing the same matrix $\mathbf{R}_{\widetilde{\mathbf{z}}}^{-1/2}$ as above to multiply the signal-cancelation output $\widetilde{\mathbf{z}}$ from (6.7) yields

$$\widetilde{\mathbf{z}}_{\mathrm{w}} \;\stackrel{\triangle}{=}\; \mathbf{R}_{\widetilde{\mathbf{z}}}^{-1/2}\widetilde{\mathbf{z}}, \tag{6.17}$$

with long-term-uncorrelated, unit-variance components.

The KLT of the signal from (6.15), using the N dominant eigenvectors from the eigen-decomposition $\mathbf{R}_{\widetilde{\mathbf{h}}_{\mathrm{w}}} = \mathbf{E}_{\mathrm{L}}\,\mathbf{\Lambda}_{\mathrm{L}}\,\mathbf{E}_{\mathrm{L}}^{H}$, produces

$$\mathbf{y}_{\mathrm{w},N} \;\stackrel{\triangle}{=}\; \mathbf{E}_{N}^{H}\widetilde{\mathbf{y}}_{\mathrm{w}} = \sqrt{PG}\,\sqrt{E_{\mathrm{s}}}\,b\,\mathbf{h}_{\mathrm{w},N} + \mathbf{u}_{w,N}, \tag{6.18}$$

where $\mathbf{h}_{\mathrm{w},N} \stackrel{\triangle}{=} \mathbf{E}_{N}^{H}\widetilde{\mathbf{h}}_{\mathrm{w}}$ and $\mathbf{u}_{w,N} \stackrel{\triangle}{=} \mathbf{E}_{N}^{H}\widetilde{\mathbf{u}}_{\mathrm{w}}$. Define further

$$\mathbf{z}_{\mathrm{w},N} \;\stackrel{\triangle}{=}\; \mathbf{E}_{N}^{H}\widetilde{\mathbf{z}}_{\mathrm{w}}. \tag{6.19}$$

Since the correlation matrices of $\widetilde{\mathbf{u}}_{\mathrm{cf}}$ and $\widetilde{\mathbf{z}}$ coincide, so do those of $\mathbf{u}_{w,N}$ and $\mathbf{z}_{\mathrm{w},N}$.

The above procedure can be streamlined as follows. Using temporally-uncorrelated samples of $\widetilde{\mathbf{y}}$ and $\widetilde{\mathbf{z}}$, the long-term $\mathbf{R}_{\widetilde{\mathbf{y}}}$ and $\mathbf{R}_{\widetilde{\mathbf{z}}}^{-1/2}$ can be updated. Then, the eigen-decomposition of $\mathbf{R}_{\widetilde{\mathbf{y}}_{\mathrm{w}}} = \mathbf{R}_{\widetilde{\mathbf{z}}}^{-1/2}\mathbf{R}_{\widetilde{\mathbf{y}}}\mathbf{R}_{\widetilde{\mathbf{z}}}^{-1/2}$ provides $\mathbf{E}_N$, which is then used at each symbol, for dimension reduction, as follows:

$$\mathbf{y}_{\mathrm{w},N} \;\stackrel{\triangle}{=}\; \mathbf{E}_{N}^{H}\,\mathbf{R}_{\widetilde{\mathbf{z}}}^{-1/2}\widetilde{\mathbf{y}}, \tag{6.20}$$

$$\mathbf{z}_{\mathrm{w},N} \;\stackrel{\triangle}{=}\; \mathbf{E}_{N}^{H}\,\mathbf{R}_{\widetilde{\mathbf{z}}}^{-1/2}\widetilde{\mathbf{z}}. \tag{6.21}$$

The (short-term) optimum combiner for the signal vector described by (6.18) or (6.20) is

$$\mathbf{w}_N = \left[E\{\mathbf{z}_{w,N}\,\mathbf{z}_{w,N}^{H}\}\right]^{-1}\mathbf{h}_{\mathrm{w},N}, \tag{6.22}$$

and the detected BPSK symbol is $\widehat{b}_N = \text{sign}\{\Re\left[\mathbf{w}_N^H \mathbf{y}_{\text{w},N}\right]\}$.

In practice, the inverse short-term correlation matrix from (6.22) can be estimated from samples of $\mathbf{z}_{w,N}$ given by (6.21), using the square-root updating algorithm from [100, Table 1, p. 1517]. On the other hand, exploiting (6.20) for short-term averaging yields

$$\mathbf{R}_{\mathbf{y}_{\text{w},N}} = PG \cdot E_{\text{s}} \cdot \mathbf{h}_{\text{w},N}\, \mathbf{h}_{\text{w},N}^H + \mathbf{R}_{\mathbf{z}_{\text{w},N}}. \tag{6.23}$$

Hence, the N-dimensional vector $\mathbf{h}_{\text{w},N}$ required for combining is $\mathbf{d}\left(\mathbf{R}_{\mathbf{y}_{\text{w},N}} - \mathbf{R}_{\mathbf{z}_{\text{w},N}}\right)$.

A diagram of the described eigen-combining method for a CDMA system is presented in Fig. 6.4. Note that most channel-rate and symbol-rate processing now involves $N \times N$ matrices and N-dimensional vectors. Only the KLT from (6.20) and (6.21) requires symbol-rate multiplication of a long-term $N \times L$ matrix with an L-dimensional vector. Since the long-term correlation matrices are changing very slowly compared to the short-term ones, and since in practice it is expected that $N \ll L$ [35, 36], eigen-combining is expected to significantly reduce complexity over combining. Furthermore, eigen-combining without the weak eigen-modes can lead to significant performance improvements for CDMA [35, 36]. The eigen-combining approach described above also avoids direct use of the spread signal vector, thus promising improved performance, independently of the chip-pulse-waveform independence, as well as faster convergence.

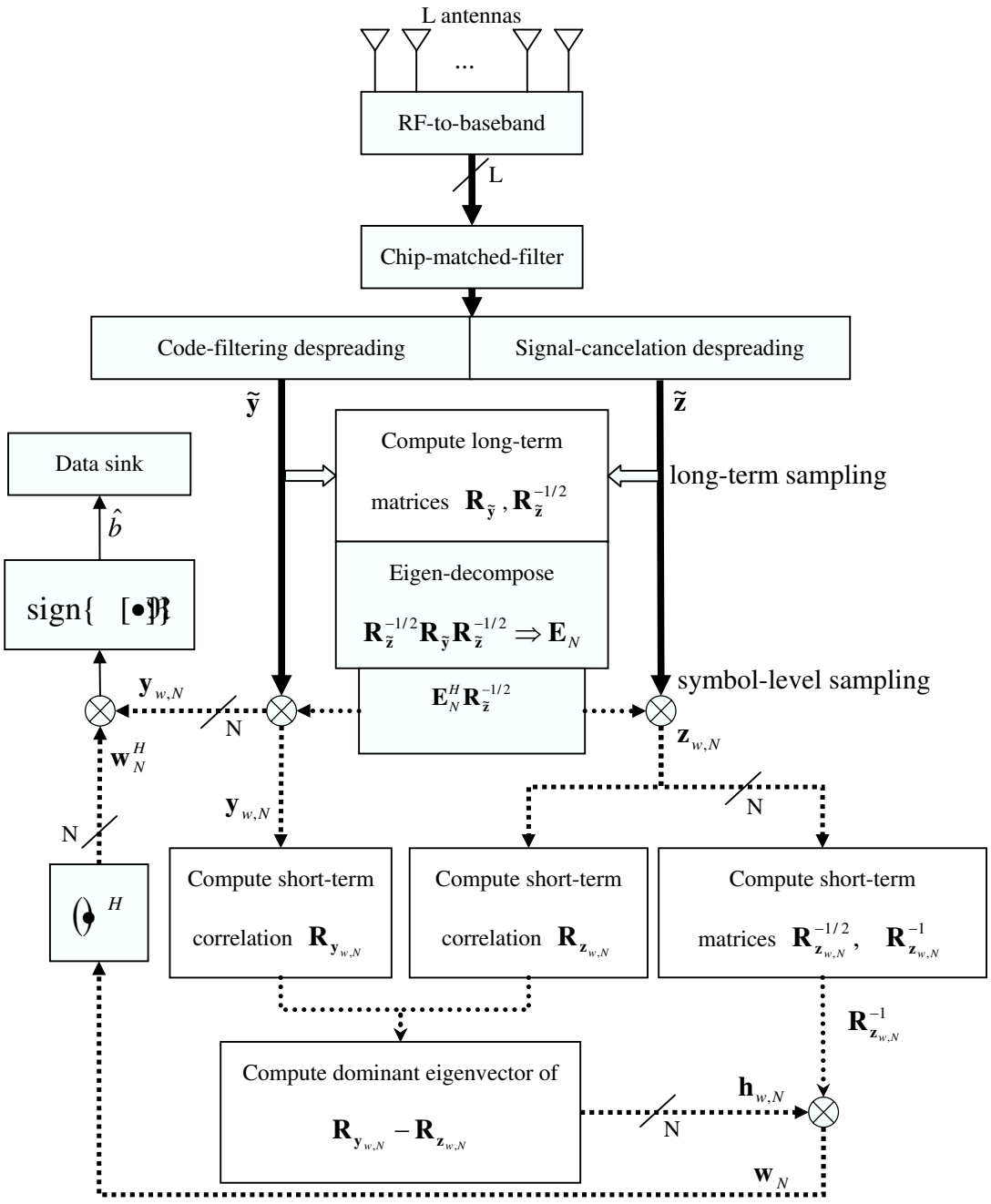

Figure 6.4. Eigen-combining for CDMA systems using jointly code-filtering and signal-cancelation despreading.

Chapter 7

Summary, Conclusions, and Future Work

Below, we provide an account of the results of this work and then outline a few envisioned further research directions.

7.1 Summary and Conclusions

Chapter 2 provides the background information on the conventional SISO wireless communications system, wherein receiver noise, channel fading, and estimation inaccuracy can yield very poor performance.

The first part of Chapter 3 shows that SIMO systems employing statistical beamforming (BF) and maximal-ratio combining (MRC) can significantly improve symbol-detection performance, due to array and diversity gains. Chapter 3 introduces the concept of maximal-ratio eigen-combining (MREC). The derivation of symbol-detection performance measures is described for MREC with perfectly known channels. Since MREC is a superset of BF and MRC, MREC performance measures apply to BF and MRC, as special cases. Optimum and suboptimum approaches are described for the case of imperfectly known channels. A finite-limit-integral — i.e., non-closed-form — yet easily computable and analytically more convenient, average error probability (AEP) expression is derived for optimum (exact) MREC, while a

more involved closed-form AEP expression is derived for suboptimum (approximate) MREC. These expressions are proven applicable for BF and MRC as special cases, and they serve to evaluate the relative performance of these receivers. Finally, a numerical complexity comparison of exact and approximate BF, MRC, and MREC is provided.

In Chapter 4, a realistic spatial channel correlation model is described, relying on the Laplacian power azimuth spectrum with random, log-normally-distributed azimuth angle spread, for typical urban scenarios. The adaptation of MREC to actual channel statistics, performance requirements, and complexity load is investigated. Smarter antenna arrays employing MREC promise performance enhancements and complexity reductions over BF and MRC for typical cellular scenarios with varying azimuth angle spreads. Gains of almost 5 dB at AEP $= 10^{-2}$, and more than 7 dB at AEP $= 10^{-3}$ are found possible with MREC over BF with a uniform linear array with 5 elements, and half-wavelength inter-element distance. Furthermore, for symbol-SNR in the $[0\text{ dB}, 10\text{ dB}]$ range, the proposed performance-complexity-tradeoff-criterion-based adaptive exact MREC achieves optimum performance (i.e., the exact-MRC performance) with about $80\% - 90\%$ lower complexity than that of exact MRC.

Chapter 5 describes actual fixed-point implementations of SISO and SIMO (BF, MRC, and MREC) baseband receivers on a field-programmable gate array (FPGA). These devices have been chosen due to their great potential for hardware parallelism, which perfectly suits the requirements of current- and future-generation communications signal processing. Their reprogrammability represents a significant advantage for fast prototyping of new algorithms, as well as for keeping up with standard, application, and market changes, even after system deployment. FPGA-based implementations of smarter, MREC-based, antenna arrays are found to achieve near-optimum performance while doubling user processing capacity, or, equivalently, halving resource and power consumption requirements, compared to MRC.

In Chapter 6 beamforming, combining, and eigen-combining are considered for code-division multiple access (CDMA) systems. We describe the traditional code-filtering signal despreading approach as well as a newer approach referred to as signal-cancelation despreading. The latter is found instrumental in computing accurately the interference-plus-noise correlation matrix for any chip-pulse waveform. We propose the joint exploitation of these despreading methods for optimum combining at CDMA antenna arrays, and demonstrate beamforming performance improvements. In order to further improve performance and reduce complexity, an approach to optimum eigen-combining for smarter CDMA antenna arrays is described.

7.2 Related Future Research Directions

Although extensive comparisons of BF, MRC, and MREC in terms of symbol-detection performance, algorithm complexity, as well as resource and power consumption for realistic scenarios — based on analysis, simulations, and actual fixed-point implementations — have been provided in this thesis, investigation of eigen-combining for a wider range of channel models at the base station and the mobile station, for fixed and mobile wireless communications is needed. Furthermore, fixed-point implementation which incorporates the eigen-decomposition required for eigen-combining is necessary for more definitive conclusions on real-world applicability.

The application of eigen-combining for CDMA systems is also of interest, as its application across antennas and RAKE taps, employing the signal-cancelation despreading technique, promises to yield truly cost-efficient multi-branch receivers achieving near-optimum performance.

Eigen-combining for MIMO systems is of great interest. Work is required on the adaptive joint receiver-transmitter selection of the most appropriate eigen-combining orders which

would provide the intended performance for the lowest cost in terms of transceiver resource and power consumption, while simultaneously adapting the modulation to the channel condition and user requirements.

Appendix A

Implementation of Exact MRC

Assuming that $\widetilde{\mathbf{h}}$ and $\widetilde{\mathbf{g}}$ are zero-mean, jointly-Gaussian, the channel gain vector $\widetilde{\mathbf{h}}$ conditioned on its estimate $\widetilde{\mathbf{g}}$ is Gaussian with mean and correlation given by [81, Appendix 15B, p. 562]

$$\widetilde{\mathbf{m}} \triangleq E\{\widetilde{\mathbf{h}}|\widetilde{\mathbf{g}}\} = E\{\widetilde{\mathbf{h}}\widetilde{\mathbf{g}}^H\}\left[E\{\widetilde{\mathbf{g}}\widetilde{\mathbf{g}}^H\}\right]^{-1}\widetilde{\mathbf{g}}, \tag{A.1}$$

$$\mathbf{R}_{\widetilde{\mathbf{e}}} \triangleq E\{(\widetilde{\mathbf{h}}-\widetilde{\mathbf{m}})(\widetilde{\mathbf{h}}-\widetilde{\mathbf{m}})^H|\widetilde{\mathbf{g}}\} = \mathbf{R}_{\widetilde{\mathbf{h}}} - E\{\widetilde{\mathbf{h}}\widetilde{\mathbf{g}}^H\}\left[E\{\widetilde{\mathbf{g}}\widetilde{\mathbf{g}}^H\}\right]^{-1}E\{\widetilde{\mathbf{g}}\widetilde{\mathbf{h}}^H\}. \tag{A.2}$$

We can then write the channel gain vector, conditioned on its estimate, as

$$\widetilde{\mathbf{h}} = \widetilde{\mathbf{m}} + \widetilde{\mathbf{e}}, \quad \text{with} \quad \widetilde{\mathbf{e}} \sim \mathscr{N}_c(\mathbf{0}, \mathbf{R}_{\widetilde{\mathbf{e}}}), \tag{A.3}$$

so that the received signal vector from (3.1), on page 51, can be rewritten as

$$\widetilde{\mathbf{y}} = \sqrt{E_\mathrm{s}}\, b\, \widetilde{\mathbf{m}} + \widetilde{\boldsymbol{\nu}} \sim \mathscr{N}_c(\sqrt{E_\mathrm{s}}\, b\, \widetilde{\mathbf{m}}, \mathbf{R}_{\widetilde{\boldsymbol{\nu}}}), \tag{A.4}$$

where

$$\widetilde{\boldsymbol{\nu}} \triangleq \sqrt{E_\mathrm{s}}\, b\, \widetilde{\mathbf{e}} + \widetilde{\mathbf{n}}, \tag{A.5}$$

and

$$\mathbf{R}_{\widetilde{\boldsymbol{\nu}}} \triangleq E\{\widetilde{\boldsymbol{\nu}}\widetilde{\boldsymbol{\nu}}^H\} = E_\mathrm{s}\,|b|^2\,\mathbf{R}_{\widetilde{\mathbf{e}}} + N_0\,\mathbf{I}_L. \tag{A.6}$$

The signal model in (A.4) conveniently compounds receiver noise and channel estimation error into the vector $\widetilde{\boldsymbol{\nu}}$. The corresponding optimum combiner is

$$\widetilde{\mathbf{w}} = \mathbf{R}_{\widetilde{\boldsymbol{\nu}}}^{-1}\,\widetilde{\mathbf{m}}, \tag{A.7}$$

which yields maximum SNR, given by

$$\widetilde{\gamma} = E_{\mathrm{s}}\,\widetilde{\mathbf{m}}^{H}\,\mathbf{R}_{\widetilde{\boldsymbol{\nu}}}^{-1}\,\widetilde{\mathbf{m}}. \tag{A.8}$$

Appendix B

Correlation Matrices Required for MRC

In this appendix we provide expressions for correlation matrices required in the implementation and performance analysis of approximate and exact MRC — see Section 3.8.1, on page 101, Section 3.8.2, on page 104, and Appendix A.

B.1 Correlations Required for Approximate MRC

The test-variable-based performance analysis method described in Section 3.4.1.2, on page 57, requires for approximate MRC the matrices expressed below for SINC and MMSE PSAM.

B.1.1 The Case of SINC PSAM Channel Estimation

Based on details from Section 3.6.2, on page 83, for SINC PSAM, the following hold:

- $\left(\mathbf{R}_{\widetilde{\mathbf{g}}}(m_{\mathrm{s}})\right)_{i,j} \stackrel{\triangle}{=} E\{\widetilde{g}_i(0,m_{\mathrm{s}})\,\widetilde{g}_j^*(0,m_{\mathrm{s}})\} = \widetilde{\mathbf{v}}(m_{\mathrm{s}})^{\mathrm{T}}\left\{\left(\mathbf{R}_{\widetilde{\mathbf{h}}}\right)_{i,j}\mathbf{Q} + \frac{N_0}{E_{\mathrm{p}}|b_p|^2}\mathbf{I}_T\right\}\widetilde{\mathbf{v}}(m_{\mathrm{s}})$, with the real-valued SINC interpolation vector $\widetilde{\mathbf{v}}(m_{\mathrm{s}})$ given in Table 3.4, on page 84, and the $T \times T$ real-valued matrix $\mathbf{Q}$ defined in (3.118), on page 84.

- $\left(\mathbf{R}_{\widetilde{\mathbf{g}}\widetilde{\mathbf{y}}}(m_{\mathrm{s}})\right)_{i,j} \stackrel{\triangle}{=} E\{\widetilde{g}_i(0,m_{\mathrm{s}})\,\widetilde{y}_j^*(0,m_{\mathrm{s}})\} = \sqrt{E_{\mathrm{s}}}\,b^* \cdot \left(\mathbf{R}_{\widetilde{\mathbf{h}}}\right)_{i,j}\widetilde{\mathbf{v}}(m_{\mathrm{s}})^{\mathrm{T}}\mathbf{q}(m_{\mathrm{s}})$,
  $\left(\mathbf{R}_{\widetilde{\mathbf{y}}\widetilde{\mathbf{g}}}(m_{\mathrm{s}})\right)_{i,j} \stackrel{\triangle}{=} E\{\widetilde{y}_i(0,m_{\mathrm{s}})\,\widetilde{g}_j^*(0,m_{\mathrm{s}})\} = \sqrt{E_{\mathrm{s}}}\,b \cdot \left(\mathbf{R}_{\widetilde{\mathbf{h}}}\right)_{i,j}\widetilde{\mathbf{v}}(m_{\mathrm{s}})^{\mathrm{T}}\mathbf{q}(m_{\mathrm{s}})$,

with the T-dimensional, real-valued vector $\mathbf{q}(m_{\mathrm{s}})$ defined in (3.120) at page 85. Thus,
$\mathbf{R}_{\widetilde{\mathbf{g}}\widetilde{\mathbf{y}}}(m_{\mathrm{s}}) \stackrel{\triangle}{=} E\{\widetilde{\mathbf{g}}(0,m_{\mathrm{s}})\widetilde{\mathbf{y}}^H(0,m_{\mathrm{s}})\} = \sqrt{E_{\mathrm{s}}}\,b^*\,\mathbf{R}_{\widetilde{\mathbf{h}}}\widetilde{\mathbf{v}}(m_{\mathrm{s}})^{\mathrm{T}}\mathbf{q}(m_{\mathrm{s}})$,
$\mathbf{R}_{\widetilde{\mathbf{y}}\widetilde{\mathbf{g}}}(m_{\mathrm{s}}) \stackrel{\triangle}{=} E\{\widetilde{\mathbf{y}}(0,m_{\mathrm{s}})\widetilde{\mathbf{g}}^H(0,m_{\mathrm{s}})\} = \sqrt{E_{\mathrm{s}}}\,b\,\mathbf{R}_{\widetilde{\mathbf{h}}}\widetilde{\mathbf{v}}(m_{\mathrm{s}})^{\mathrm{T}}\mathbf{q}(m_{\mathrm{s}})$.

- $\left(\mathbf{R}_{\widetilde{\mathbf{y}}}\right)_{i,j} \stackrel{\triangle}{=} E\{\widetilde{y}_i\widetilde{y}_j^*\} = E_{\mathrm{s}}\,|b|^2\,\left(\mathbf{R}_{\widetilde{\mathbf{h}}}\right)_{i,j} + N_0$, i.e., $\mathbf{R}_{\widetilde{\mathbf{y}}} = E_{\mathrm{s}}\,|b|^2\,\mathbf{R}_{\widetilde{\mathbf{h}}} + N_0$, which, evidently, does not depend on estimation.

B.1.2 The Case of MMSE PSAM Channel Estimation

MMSE PSAM branch estimation is described in Section 3.6.2, on page 83. Using (3.116)–(3.120) from page 84, we get the channel gain vector estimate as $\widetilde{\mathbf{g}}(0,m_{\mathrm{s}}) = \widetilde{\mathbf{G}}_{\mathrm{opt}}^H(m_{\mathrm{s}})\widetilde{\mathbf{y}}_{\mathrm{p}} = \mathbf{R}^H_{\widetilde{\mathbf{y}}_{\mathrm{p}}\widetilde{\mathbf{h}}}(m_{\mathrm{s}})\,\mathbf{R}^{-1}_{\widetilde{\mathbf{y}}_{\mathrm{p}}}\widetilde{\mathbf{y}}_{\mathrm{p}}$, which requires the following correlation matrices:

- $\mathbf{R}_{\widetilde{\mathbf{y}}_{\mathrm{p}}}$ and $\mathbf{R}_{\widetilde{\mathbf{y}}_{\mathrm{p}}\widetilde{\mathbf{h}}}(m_{\mathrm{s}})$, expressed in (3.117) and (3.119), respectively, at page 85.

- $\mathbf{R}^H_{\widetilde{\mathbf{y}}_{\mathrm{p}}\widetilde{\mathbf{h}}}(m_{\mathrm{s}}) = \sqrt{E_{\mathrm{p}}}\,b_{\mathrm{p}}^*\,\left[\mathbf{q}^{\mathrm{T}}(m_{\mathrm{s}})\otimes\mathbf{R}_{\widetilde{\mathbf{h}}}\right]$, obtained from (3.119) using a Kronecker product property [94, Section 2.4, §10.a, p. 19].

MMSE-PSAM-based approximate-MRC analysis requires the following correlation matrices:

- $\mathbf{R}_{\widetilde{\mathbf{g}}}(m_{\mathrm{s}}) \stackrel{\triangle}{=} E\{\widetilde{\mathbf{g}}(0,m_{\mathrm{s}})\widetilde{\mathbf{g}}^H(0,m_{\mathrm{s}})\} = \mathbf{R}^H_{\widetilde{\mathbf{y}}_{\mathrm{p}}\widetilde{\mathbf{h}}}(m_{\mathrm{s}})\,\mathbf{R}^{-1}_{\widetilde{\mathbf{y}}_{\mathrm{p}}}\mathbf{R}_{\widetilde{\mathbf{y}}_{\mathrm{p}}\widetilde{\mathbf{h}}}(m_{\mathrm{s}})$.

- $\mathbf{R}_{\widetilde{\mathbf{g}}\widetilde{\mathbf{y}}}(m_{\mathrm{s}}) \stackrel{\triangle}{=} E\{\widetilde{\mathbf{g}}(0,m_{\mathrm{s}})\widetilde{\mathbf{y}}^H(0,m_{\mathrm{s}})\} = \sqrt{E_{\mathrm{s}}}\,b^*\,\mathbf{R}_{\widetilde{\mathbf{g}}\widetilde{\mathbf{h}}}(m_{\mathrm{s}}) = \sqrt{E_{\mathrm{s}}}\,b^*\,\widetilde{\mathbf{G}}^H_{\mathrm{opt}}(m_{\mathrm{s}})\,\mathbf{R}_{\widetilde{\mathbf{y}}_{\mathrm{p}}\widetilde{\mathbf{h}}}(m_{\mathrm{s}}) =$
  $= \sqrt{E_{\mathrm{s}}}\,b^*\,\mathbf{R}^H_{\widetilde{\mathbf{y}}_{\mathrm{p}}\widetilde{\mathbf{h}}}(m_{\mathrm{s}})\,\mathbf{R}^{-1}_{\widetilde{\mathbf{y}}_{\mathrm{p}}}\mathbf{R}_{\widetilde{\mathbf{y}}_{\mathrm{p}}\widetilde{\mathbf{h}}}(m_{\mathrm{s}}) = \sqrt{E_{\mathrm{s}}}\,b^*\,\mathbf{R}_{\widetilde{\mathbf{g}}}(m_{\mathrm{s}})$.

- it follows that for MMSE PSAM $\mathbf{R}_{\widetilde{\mathbf{g}}}(m_{\mathrm{s}}) = \mathbf{R}_{\widetilde{\mathbf{g}}\widetilde{\mathbf{h}}}(m_{\mathrm{s}})$, which is a well-known property of MMSE estimates, also known as the orthogonality principle [81, p. 386] [102, p. 177].

B.2 Correlations Required for Exact MRC

As shown in Appendix A, implementation of exact MRC requires the calculation of the optimum combiner given by $\widetilde{\mathbf{w}}(0,m_{\mathrm{s}}) = \mathbf{R}_{\widetilde{\boldsymbol{\nu}}}^{-1}(m_{\mathrm{s}})\,\widetilde{\mathbf{m}}(0,m_{\mathrm{s}})$. From (A.1), we have

$$\widetilde{\mathbf{m}}(0,m_{\mathrm{s}}) = \mathbf{R}_{\widetilde{\mathbf{h}}\widetilde{\mathbf{g}}}(m_{\mathrm{s}})\,\mathbf{R}_{\widetilde{\mathbf{g}}}^{-1}(m_{\mathrm{s}})\,\widetilde{\mathbf{g}}(0,m_{\mathrm{s}}), \tag{B.1}$$

and from (A.2) and (A.6) we have

$$\mathbf{R}_{\widetilde{\boldsymbol{\nu}}}(m_{\mathrm{s}}) = E_{\mathrm{s}}\,|b|^2\,\left[\mathbf{R}_{\widetilde{\mathbf{h}}} - \mathbf{R}_{\widetilde{\mathbf{h}}\widetilde{\mathbf{g}}}(m_{\mathrm{s}})\,\mathbf{R}_{\widetilde{\mathbf{g}}}^{-1}(m_{\mathrm{s}})\,\mathbf{R}_{\widetilde{\mathbf{g}}\widetilde{\mathbf{h}}}(m_{\mathrm{s}})\right] + N_0\,\mathbf{I}_L. \tag{B.2}$$

The test-variable-based performance analysis method described in Section 3.4.1.2, starting on page 57, requires for exact MRC the matrices $\mathbf{R}_{\widetilde{\mathbf{m}}}(m_{\mathrm{s}})$, $\mathbf{R}_{\widetilde{\mathbf{m}}\widetilde{\mathbf{y}}}(m_{\mathrm{s}})$, $\mathbf{R}_{\widetilde{\mathbf{y}}\widetilde{\mathbf{m}}}(m_{\mathrm{s}})$, which can be expressed as follows:

- $\mathbf{R}_{\widetilde{\mathbf{m}}}(m_{\mathrm{s}}) = \mathbf{R}_{\widetilde{\mathbf{h}}\widetilde{\mathbf{g}}}(m_{\mathrm{s}})\,\mathbf{R}_{\widetilde{\mathbf{g}}}^{-1}(m_{\mathrm{s}})\,\mathbf{R}_{\widetilde{\mathbf{g}}\widetilde{\mathbf{h}}}(m_{\mathrm{s}})$
- $\mathbf{R}_{\widetilde{\mathbf{m}}\widetilde{\mathbf{y}}}(m_{\mathrm{s}}) = \mathbf{R}_{\widetilde{\mathbf{h}}\widetilde{\mathbf{g}}}(m_{\mathrm{s}})\,\mathbf{R}_{\widetilde{\mathbf{g}}}^{-1}(m_{\mathrm{s}})\,\mathbf{R}_{\widetilde{\mathbf{g}}\widetilde{\mathbf{y}}}(m_{\mathrm{s}})$
- $\mathbf{R}_{\widetilde{\mathbf{y}}\widetilde{\mathbf{m}}}(m_{\mathrm{s}}) = \mathbf{R}_{\widetilde{\mathbf{m}}\widetilde{\mathbf{y}}}^{H}(m_{\mathrm{s}}) = \mathbf{R}_{\widetilde{\mathbf{y}}\widetilde{\mathbf{g}}}(m_{\mathrm{s}})\,\mathbf{R}_{\widetilde{\mathbf{g}}}^{-1}(m_{\mathrm{s}})\,\mathbf{R}_{\widetilde{\mathbf{g}}\widetilde{\mathbf{h}}}(m_{\mathrm{s}})$.

For SINC PSAM, $\mathbf{R}_{\widetilde{\mathbf{g}}}(m_{\mathrm{s}})$ and $\mathbf{R}_{\widetilde{\mathbf{g}}\widetilde{\mathbf{y}}}(m_{\mathrm{s}})$ have been expressed in Section B.1.1. Then, the remaining correlations needed in (B.1) and (B.2) are given by $\mathbf{R}_{\widetilde{\mathbf{h}}\widetilde{\mathbf{g}}}(m_{\mathrm{s}}) = \mathbf{R}_{\widetilde{\mathbf{g}}\widetilde{\mathbf{y}}}(m_{\mathrm{s}})/(\sqrt{E_{\mathrm{s}}}\,b)$ and $\mathbf{R}_{\widetilde{\mathbf{g}}\widetilde{\mathbf{h}}}(m_{\mathrm{s}}) = \mathbf{R}_{\widetilde{\mathbf{h}}\widetilde{\mathbf{g}}}^{H}(m_{\mathrm{s}})$.

For MMSE PSAM we have from Section B.1.2 that $\mathbf{R}_{\widetilde{\mathbf{g}}}(m_{\mathrm{s}}) = \mathbf{R}_{\widetilde{\mathbf{g}}\widetilde{\mathbf{h}}}(m_{\mathrm{s}}) = \mathbf{R}_{\widetilde{\mathbf{h}}\widetilde{\mathbf{g}}}(m_{\mathrm{s}})$, which reduces (B.1) to $\widetilde{\mathbf{m}}(0,m_{\mathrm{s}}) = \widetilde{\mathbf{g}}(0,m_{\mathrm{s}})$, and (B.2) to $\mathbf{R}_{\widetilde{\boldsymbol{\nu}}}(m_{\mathrm{s}}) = E_{\mathrm{s}}\,|b|^2\,\left[\mathbf{R}_{\widetilde{\mathbf{h}}} - \mathbf{R}_{\widetilde{\mathbf{g}}}(m_{\mathrm{s}})\right] + N_0\,\mathbf{I}_L$, with $\mathbf{R}_{\widetilde{\mathbf{g}}}(m_{\mathrm{s}})$ expressed in Section B.1.2. Furthermore, $\mathbf{R}_{\widetilde{\mathbf{m}}}(m_{\mathrm{s}}) = \mathbf{R}_{\widetilde{\mathbf{g}}}(m_{\mathrm{s}})$, $\mathbf{R}_{\widetilde{\mathbf{m}}\widetilde{\mathbf{y}}}(m_{\mathrm{s}}) = \mathbf{R}_{\widetilde{\mathbf{g}}\widetilde{\mathbf{y}}}(m_{\mathrm{s}})$, and $\mathbf{R}_{\widetilde{\mathbf{y}}\widetilde{\mathbf{m}}}(m_{\mathrm{s}}) = \mathbf{R}_{\widetilde{\mathbf{m}}\widetilde{\mathbf{y}}}^{H}(m_{\mathrm{s}}) = \mathbf{R}_{\widetilde{\mathbf{y}}\widetilde{\mathbf{g}}}(m_{\mathrm{s}})$, with $\mathbf{R}_{\widetilde{\mathbf{g}}\widetilde{\mathbf{y}}}(m_{\mathrm{s}})$ also expressed in Section B.1.2.

Bibliography

[1] “Siemens. Text proposal for RAN WG1 report on Tx diversity solutions for multiple antennas,” 3rd Generation Partnership Project (3GPP), TSG RAN WG1, Tech. Rep. TSGR1 15 R1-00-1126, 2000.

[2] “Technical Specification Group Radio Access Network. Spatial Channel Model for Multiple Input Multiple Output (MIMO) Simulations, Release 6,” 3rd Generation Partnership Project (3GPP), Tech. Rep. TS 25.996, 6.1.0, 2003.

[3] “Technical Specification Group Radio Access Network. Multiple-Input Multiple Output in UTRA, Release 7,” 3rd Generation Partnership Project (3GPP), Tech. Rep. TS 25.876, 1.8.0, 2005.

[4] “Technical Specification Group Radio Access Network. Physical Layer Procedures (FDD), Release 7,” 3rd Generation Partnership Project (3GPP), Tech. Rep. TS 25.214, 7.0.0, 2006.

[5] “Technical Specification Group Radio Access Network. Spreading and Modulation (FDD), Release 7,” 3rd Generation Partnership Project (3GPP), Tech. Rep. TS 25.213, 7.0.0, 2006.

[6] M. Abramowitz and I. A. Stegun, Eds., *Handbook of Mathematical Functions with Formulas, Graphs and Mathematical Tables*. New York, NY 10014: Dover Publications, Inc., 1995.

[7] "AccelWare linear algebra core generators," White Paper, Accelchip. [Online]. Available: http://www.accelchip.com/papers.html

[8] A. Algans, K. I. Pedersen, and P. E. Mogensen, "Experimental analysis of the joint statistical properties of azimuth spread, delay spread, and shadow fading," *IEEE Journal on Selected Areas in Communications*, vol. 20, no. 3, pp. 523–531, April 2002.

[9] M.-S. Alouini, A. Scaglione, and G. B. Giannakis, "PCC: principal components combining for dense correlated multipath fading environments," in *Proc. IEEE Vehicular Technology Conference, (VTC '00)*, vol. 5, September 2000, pp. 2510–2517.

[10] HardCopy^{tm} series handbook. Altera, Inc. San Jose, CA. [Online]. Available: http://www.altera.com/literature

[11] Application note 311: ASIC to FPGA design methodology and guidelines. Altera, Inc. San Jose, CA. [Online]. Available: http://www.altera.com/literature

[12] DSP builder reference manual. Altera, Inc. San Jose, CA. [Online]. Available: http://www.altera.com/literature

[13] "FPGAs provide reconfigurable DSP solutions," White Paper, Altera, Inc. [Online]. Available: http://www.altera.com/literature

[14] Quartus II handbook. Altera, Inc. San Jose, CA. [Online]. Available: http://www.altera.com/literature

[15] Stratix device handbook. Altera, Inc. San Jose, CA. [Online]. Available: http://www.altera.com/literature

[16] Stratix EP1S80 DSP development board user guide. Altera, Inc. San Jose, CA. [Online]. Available: http://www.altera.com/literature

[17] "Implementing OFDM using Altera intellectual property," White Paper, Altera, Inc., Mar. 2001. [Online]. Available: http://www.altera.com/literature

[18] S. V. Amari and R. B. Misra, "Closed-form expressions for distribution of sum of exponential random variables," *IEEE Transactions on Reliability*, vol. 46, no. 4, pp. 519 – 522, December 1997.

[19] A. Ambardar, *Analog and Digital Signal Processing*. Boston, MA: PWS Publishing Company, 1995.

[20] R. Annavajjala, "A simple approach to error probability with binary signaling over generalized fading channels with maximal ratio combining and noisy channel estimates," *IEEE Transactions on Wireless Communications*, vol. 4, no. 2, pp. 380–383, March 2005.

[21] R. Annavajjala and L. B. Milstein, "On the performance of diversity combining schemes on Rayleigh fading channels with noisy channel estimates," in *Proc. IEEE Military Communications Conference, (MILCOM '03)*, vol. 1, October 2003, pp. 320 – 325.

[22] ——, "Performance analysis of linear diversity-combining schemes on Rayleigh fading channels with binary signaling and gaussian weighting errors," *IEEE Transactions on Wireless Communications*, vol. 4, no. 5, pp. 2267–2278, September 2005.

[23] S. Applebaum, "Adaptive arrays," *IEEE Transactions on Antennas and Propagation*, vol. 24, no. 5, pp. 585 – 598, September 1976.

[24] P. Babighian, L. Benini, and E. Macii, "A scalable ODC-based algorithm for RTL insertion of gated clocks," in *Proc. Design, Automation and Test in Europe Conference and Exhibition, (DATE '04)*, vol. 1, February 2004, pp. 500 – 505.

[25] K. E. Baddour and N. C. Beaulieu, "Autoregressive models for fading channel simulation," in *Proc. IEEE Global Telecommunications Conference, (GLOBECOM '01)*, vol. 2, November 2001, pp. 1187 – 1192.

[26] Z. Bai, J. Demmel, J. Dongarra, A. Ruhe, and H. van de Vorst, Eds., *Templates for the Solution of Algebraic Eigenvalue Problems: A Practical Guide*. Philadelphia, PA: SIAM, 2000.

[27] R. Baines and D. Pulley, "A total cost approach to evaluating different reconfigurable architectures for baseband processing in wireless receivers," *IEEE Communications Magazine*, vol. 41, no. 1, pp. 105–113, January 2003.

[28] M.-A. R. Baissas and A. M. Sayeed, "Pilot-based estimation of time-varying multipath channels for coherent CDMA receivers," *IEEE Transactions on Signal Processing*, vol. 50, no. 8, pp. 2037–2049, August 2002.

[29] C. A. Balanis, *Antenna Theory. Analysis and Design*, 2nd ed. New York, NY: John Wiley and Sons, 1997.

[30] P. Bello and B. D. Nelin, "Predetection diversity combining with selectively fading channels," *IEEE Transactions on Communications*, vol. 10, no. 1, pp. 32–42, March 1962.

[31] L. Benini, G. D. Micheli, and E. Macii, "Designing low-power circuits: practical recipes," *IEEE Circuits and Systems Magazine*, vol. 1, no. 1, pp. 6 – 25, 2001.

[32] L. Benini, P. Siegel, and G. D. Micheli, “Saving power by synthesizing gated clocks for sequential circuits,” *IEEE Design and Test of Computers*, vol. 11, no. 4, pp. 32 – 41, 1994.

[33] J. S. Blogh and L. Hanzo, *Third-Generation Systems and Intelligent Wireless Networking: Smart Antennas and Adaptive Modulation*. Chichester, West Sussex, England: John Wiley and Sons, 2002.

[34] D. G. Brennan, “Linear diversity combining techniques,” *Proceedings of the IEEE*, vol. 91, no. 2, pp. 331 – 356, February 2003.

[35] C. Brunner, “Efficient space-time processing schemes for WCDMA,” Ph.D. dissertation, Munich Technical University, Germany, 2000.

[36] C. Brunner, W. Utschick, and J. A. Nossek, “Exploiting the short-term and long-term channel properties in space and time: eigenbeamforming concepts for the BS in WCDMA,” *European Transactions on Telecommunications. Special Issue on Smart Antennas*, vol. 12, no. 5, pp. 365–378, 2001.

[37] L. Cao and N. C. Beaulieu, “Bit error rate analysis of hybrid selection/maximal-ratio diversity combining with channel estimation error,” in *Proc. IEEE Global Telecommunications Conference, (GLOBECOM ’04)*, vol. 1, November/December 2004, pp. 446–451.

[38] ——, “Closed-form BER results for MRC diversity with channel estimation errors in Ricean fading channels,” *IEEE Transactions on Wireless Communications*, vol. 4, no. 4, pp. 1440–1447, July 2005.

[39] J. K. Cavers, "An analysis of pilot symbol assisted modulation for Rayleigh fading channels," *IEEE Transactions on Vehicular Technology*, vol. 40, no. 4, pp. 686 – 693, November 1991.

[40] T. Cesear and R. Uribe, "Exploration of least-squares solutions of linear systems of equations with fixed-point arithmetic hardware," in *Software Defined Radio Technical Conference, (SDR '05)*, November. [Online]. Available: http://www.accelchip.com/files/whitepapers

[41] R. Chawla, "ASIC prototyping in 90-nm FPGAs," in *User2User Mentor Graphics International User Conference, (U2U '05)*, May 2005. [Online]. Available: http://www.altera.com/literature

[42] J. Choi and S. Choi, "Diversity gain for CDMA systems equipped with antenna arrays," *IEEE Transactions on Vehicular Technology*, vol. 52, no. 3, pp. 720–725, May 2003.

[43] S. Choi, J. Choi, H.-J. Im, and B. Choi, "A novel adaptive beamforming algorithm for antenna array CDMA systems with strong interferers," *IEEE Transactions on Vehicular Technology*, vol. 51, no. 5, pp. 808–816, September 2002.

[44] A. Clapton, Ed., *Future Mobile Networks: 3G and Beyond*. London, UK: Institution of Electrical Engineers, 2001.

[45] P. Common and G. H. Golub, "Tracking a few extreme singular values and vectors in signal processing," *Proceedings of the IEEE*, vol. 78, no. 8, pp. 1327–1343, August 1990.

[46] J. W. Craig, "A new, simple and exact result for calculating the probability of error for two-dimensional signal constellations," in *Proc. IEEE Military Communications Conference, (MILCOM '91)*, vol. 2, 1991, pp. 571 – 575.

[47] F. Dietrich and W. Utschick, "On the effective spatio-temporal rank of wireless communication channels," in *Proc. 13th IEEE International Symposium on Personal, Indoor and Mobile Radio Communications, (PIMRC '02)*, vol. 5, 2002, pp. 1982–1986.

[48] F. A. Dietrich and W. Utschick, "Maximum ratio combining of correlated Rayleigh fading channels with imperfectly known channel," *IEEE Communications Letters*, vol. 7, no. 9, pp. 419–421, September 2003.

[49] D. V. Djonin and V. K. Bhargava, "On the influence of the power profile on diversity combining schemes," *IEEE Transactions on Wireless Communications*, vol. 3, no. 5, pp. 1854 – 1861, September 2004.

[50] X. Dong and N. Beaulieu, "Optimal maximal ratio combining with correlated diversity branches," *IEEE Communications Letters*, vol. 6, no. 1, pp. 22–24, January 2002.

[51] M. Donno, A. Ivaldi, L. Benini, and E. Macii, "Clock-tree power optimization based on RTL clock-gating," in *Proc. Design Automation Conference, (DAC '03)*, June 2003, pp. 622–627.

[52] G. H. Dunteman, *Principal Components Analysis*, ser. Sage University Papers on Quantitative Applications in the Social Sciences, 69. Beverly Hills, CA: SAGE Publications, 1989.

[53] G. D. Durgin, *Space-Time Wireless Channels*. Upper Saddle River, NJ: Prentice Hall, PTR, 2003.

[54] C. Ebeling, C. Fisher, G. Xing, M. Shen, and H. Liu, "Implementing an OFDM receiver on the RaPiD reconfigurable architecture," *IEEE Transactions on Computers*, vol. 53, no. 11, pp. 1436–1448, November 2004.

[55] L. Fang, G. Bi, and A. C. Kot, "New method of performance analysis for diversity reception with correlated Rayleigh-fading signals," *IEEE Transactions on Vehicular Technology*, vol. 49, no. 5, pp. 1807 – 1812, September 2000.

[56] B. H. Fleury, "First- and second-order characterization of direction dispersion and space selectivity in the radio channel," *IEEE Transactions on Information Theory*, vol. 46, no. 6, pp. 2027–2044, September 2000.

[57] G. J. Foschini and M. J. Gans, "On limits of wireless communications in a fading environment when using multiple antennas," *Wireless Personal Communications*, vol. 6, no. 3, pp. 311–335, March 1998.

[58] M. J. Gans, "The effect of Gaussian error in maximal ratio combiners," *IEEE Transactions on Communications*, vol. 19, no. 4, pp. 492–500, August 1971.

[59] J. J. Gerbrands, "On the relationships between SVD, KLT and PCA," *Pattern Recognition*, vol. 14, no. 1-6, pp. 375–381, 1981.

[60] A. B. Gershman and N. D. Sidiropoulos, Eds., *Space-Time Processing for MIMO Communications*. Chichester, West Sussex, England: John Wiley and Sons, 2005.

[61] L. C. Godara, Ed., *Handbook of Antennas in Wireless Communications*. Boca Raton, FL: CRC Press, 2002.

[62] L. C. Godara, *Smart Antennas*. Boca Raton, FL: CRC Press, 2004.

[63] A. Goldsmith, *Wireless communications*. New York, NY: Cambridge University Press, 2005.

[64] G. H. Golub and C. F. van Loan, *Matrix Computations*. New York, NY: The John Hopkins University Press, 2000.

[65] I. S. Gradshteyn and I. M. Ryzhik, *Table of Integrals, Series, and Products*, 4th ed. New York, NY: Academic Press, 1965.

[66] M. Guillaud, A. Burg, L. Mailaender, B. Haller, M. Rupp, and E. Beck, "From basic concept to real-time implementation: prototyping WCDMA downlink receiver algorithms — a case study," in *Conference Record of the Thirty-Fourth Asilomar Conference on Signals, Systems and Computers*, vol. 1, November 2000, pp. 84 – 88.

[67] M. Guillaud, A. Burg, M. Rupp, E. Beck, and S. Das, "Rapid prototyping design of a 4×4 BLAST-over-UMTS system," in *Conference Record of the Thirty-Fifth Asilomar Conference on Signals, Systems and Computers*, vol. 2, November 2001, pp. 1256–1260.

[68] R. A. Haddad and T. W. Parsons, *Digital Signal Processing: Theory, Applications, And Hardware*. New York, NY: Computer Science Press, an imprint of W. H. Freeman and Co., 1991.

[69] J. S. Hammerschmidt, "*Adaptive Space and Space-Time Signal Processing for High-Rate Mobile Data Receivers*," Ph.D. dissertation, Stanford University, 1999.

[70] K. Han and B. L. Evans, "Optimum wordlength search using sensitivity information," *EURASIP Journal on Applied Signal Processing*, vol. 2006, pp. 1–14, 2006.

[71] H. Holma and A. Toskala, Eds., *WCDMA for UMTS: Radio Access for Third Generation Mobile Communications*, 2nd ed. Chichester, West Sussex, England: John Wiley and Sons, 2002.

[72] B. L. Hutchings and B. E. Nelson, "Gigaop DSP on FPGA," in *Proc. IEEE International Conference on Acoustics, Speech, and Signal Processing, (ICASSP '01)*, vol. 2, May 2001, pp. 885–888.

[73] *Standard for Local and Metropolitan Area Networks. Part 16: Air Interface for Fixed Broadband Wireless Access Systems*, IEEE Std. 802.16, 2004.

[74] H.-J. Im, S. Choi, B. Choi, H. Kim, and J. Choi, "A survey of essential problems in the design of smart antenna system," *Microwave and Optical Technology Letters*, vol. 33, no. 1, pp. 31–34, April 2002.

[75] W. C. Jakes, Ed., *Microwave Mobile Communications*. New York, NY: John Wiley and Sons, 1974.

[76] J. Jelitto, M. Bronzel, and G. P. Fettweis, "From smart antennas to reduced-dimension space-time processing," *Frequenz, Journal of Telecommunications*, vol. 55, no. 5/6, pp. 165–170, May/June 2001.

[77] J. Jelitto and G. Fettweis, "Reduced dimension space-time processing for multi-antenna wireless systems," *IEEE Wireless Communications*, vol. 9, no. 6, pp. 18–25, December 2002.

[78] D. H. Johnson and D. E. Dudgeon, *Array Signal Processing: Concepts and techniques*. Englewood Cliffs, New Jersey: Prentice Hall, 1993.

[79] T. Kaiser, "When will smart antennas be ready for the market? part I," *IEEE Signal Processing Magazine*, vol. 22, no. 2, pp. 87 – 92, March 2005.

[80] ——, "When will smart antennas be ready for the market? part II – results," *IEEE Signal Processing Magazine*, vol. 22, no. 6, pp. 174 – 176, November 2005.

[81] S. M. Kay, *Fundamentals of Statistical Signal Processing*. Englewood Cliffs, New Jersey 07632: Prentice Hall, 1993.

[82] M. Khan, “Power optimization in FPGA designs,” in *Synopsis Users Group Conference, (SNUG ’06)*, March 2006. [Online]. Available: http://www.altera.com/literature

[83] M. Kim, W.-C. Lee, J. Choi, and S. Choi, “Adaptive beamforming technique based on eigen-space method for a smart antenna in IS2000 1X environment,” in *IEEE Antennas and Propagation Society International Symposium*, vol. 1, June 2002, pp. 118 – 121.

[84] Y.-C. Ko, M.-S. Alouini, and M. K. Simon, “Outage probability of diversity systems over generalized fading channels,” *IEEE Transactions on Communications*, vol. 48, no. 11, pp. 1783–1787, November 2000.

[85] S. Kokoska and D. Zwillinger, *CRC Standard Probability and Statistics Tables and Formulae. Student Edition.* Boca Raton, FL: Chapman and Hall/CRC, 2000.

[86] V. Korneev and A. Kiselev, *Modern Microprocessors*, 3rd ed. Hingham, MA: Charles River Media, 2004.

[87] H. Krim and M. Viberg, “Two decades of array signal processing research: the parametric approach,” *IEEE Signal Processing Magazine*, vol. 13, no. 4, pp. 67 – 94, July 1996.

[88] A. Kuchar, M. Tangemann, and E. Bonek, “A real-time DOA-based smart antenna processor,” *IEEE Transactions on Vehicular Technology*, vol. 51, no. 6, pp. 1279 – 1293, November 2002.

[89] W. C. Y. Lee, *Mobile Communications Engineering*. Englewood Cliffs, New Jersey: McGraw-Hill, 1982.

[90] N. W. K. Lo, D. D. Falconer, and A. U. H. Sheikh, “Adaptive equalization and diversity combining for mobile radio using interpolated channel estimates,” *IEEE Transactions on Vehicular Technology*, vol. 40, no. 3, pp. 636 – 645, August 1991.

[91] S. Loyka, C. Tellambura, A. Kouki, A. Annamalai, and F. Gagnon, “Comments on ’New method of performance analysis for diversity reception with correlated Rayleigh-fading signals’,” *IEEE Transactions Vehicular Technology*, vol. 52, no. 6, pp. 725–726, May 2003.

[92] W. Lu, Ed., *Broadband Wireless Mobile: 3G and Beyond*. Chichester, West Sussex, England: John Wiley and Sons, 2002.

[93] T. Luo and S. D. Blostein, “Using signal cancelation for optimum beamforming in a cellular CDMA system,” in *Proc. IEEE International Conference on Acoustics, Speech, and Signal Processing, (ICASSP ’98)*, vol. 4, May 1998, pp. 2493–2496.

[94] H. Lutkepohl, *Handbook of Matrices*. New York, NY: John Wiley and Sons, 1996.

[95] Y. Ma, R. Schober, and S. Pasupathy, “Effect of imperfect channel estimation on MRC diversity in fading channels,” in *Proc. IEEE International Conference on Communications, (ICC ’04)*, vol. 6, June 2004, pp. 3163–3167.

[96] ——, “Effect of channel estimation errors on MRC diversity in Rician fading channels,” *IEEE Transactions on Vehicular Technology*, vol. 54, no. 6, pp. 2137–2142, November 2005.

[97] T. S. T. Mak and K. P. Lam, “Embedded computation of maximum-likelihood phylogeny inference using platform FPGA,” in *Proc. IEEE Computational Systems Bioinformatics Conference, (CSB ’04)*, August 2004, pp. 512–514.

[98] P. E. Mogensen, K. I. Pedersen, P. Leth-Espensen, B. Fleury, F. Frederiksen, K. Olesen, and S. L. Larsen, “Preliminary measurement results from an adaptive antenna array testbed for GSM/UMTS,” in *Proc. IEEE Vehicular Technology Conference, (VTC ’97)*, vol. 3, May 1997, pp. 1592–1596.

[99] R. A. Monzingo and T. W. Miller, *Introduction to Adaptive Arrays*. New York: John Wiley and Sons, 1980.

[100] A. F. Naguib, "Recursive adaptive beamforming for wireless CDMA," in *Proc. IEEE International Conference on Communications, (ICC '95)*, vol. 3, June 1995, pp. 1515 – 1519.

[101] ——, "*Adaptive Antennas for CDMA Wireless Networks*," Ph.D. dissertation, Stanford University, 1995.

[102] A. Papoulis, *Probability, Random Variables and Stochastic Processes*, 4th ed. Boston, MA: McGraw-Hill, 2001.

[103] B. N. Parlett, *The Symmetric Eigenvalue Problem*, ser. Classics in Applied Mathematics. Philadelphia, PA: SIAM, 1998.

[104] F. Patenaude, J. Lodge, and J.-Y. Chouinard, "Eigen analysis of wide-band fading channel impulse responses," *IEEE Transactions on Vehicular Technology*, vol. 48, no. 2, pp. 593 – 606, March 1999.

[105] M. Patzold, U. Killat, and F. Laue, "A deterministic signal simulation model for Suzuki processes with application to a shadow Rayleigh land mobile radio channel," *IEEE Transactions on Vehicular Technology*, vol. 45, no. 2, pp. 318 – 331, May 1996.

[106] A. Paulraj, R. Nabar, and D. Gore, *Introduction to Space-Time Wireless Communications*. Cambridge, UK: Cambridge University Press, 2005.

[107] A. J. Paulraj and C. B. Papadias, "Space-time processing for wireless communications," *IEEE Signal Processing Magazine*, vol. 14, no. 6, pp. 49 – 83, November 1997.

[108] K. I. Pedersen, P. E. Mogensen, and B. H. Fleury, "A stochastic model of the temporal and azimuthal dispersion seen at the base station in outdoor propagation environments," *IEEE Transactions on Vehicular Technology*, vol. 49, no. 2, pp. 437–447, March 2000.

[109] K. Pedersen, P. Mogensen, and B. Fleury, "Spatial channel characteristics in outdoor environments and their impact on BS antenna system performance," in *Proc. IEEE Vehicular Technology Conference, (VTC '98)*, vol. 2, May 1998, pp. 719 – 723.

[110] R. Pelt and M. Lee, "Low-power software-defined radio design using FPGAs," in *Software Defined Radio Technical Conference, (SDR '05)*, November 2005. [Online]. Available: http://www.altera.com/literature

[111] D. Perels, S. Haene, P. Luethi, A. Burg, W. Fichtner, H. Bolcskei, and N. Felber, "ASIC implementation of a MIMO-OFDM transceiver for 192 Mbps WLANs," in *Proc. European Solid-State Device Research Conference, (ESSCIRC '05)*, September 2005, pp. 215 – 218.

[112] S. U. Pillai, *Array Signal Processing*. New York, NY: Springer-Verlag, 1989.

[113] P. Polydorou and P. Ho, "Error performance of MPSK with diversity combining in non-uniform Rayleigh fading and non-ideal channel estimation," in *Proc. IEEE Vehicular Technology Conference, (VTC '00)*, vol. 1, 2000, pp. 627 – 631.

[114] R. Price and P. E. Green, "A communication technique for multipath channels," *Proceedings of the IEEE*, vol. 46, no. 3, pp. 555–570, March 1958.

[115] J. G. Proakis, *Digital Communications*, 4th ed. New York, NY: McGraw-Hill, Inc., 2001.

[116] T. S. Rappaport, *Wireless Communications. Principles and Practice*. Prentice Hall PTR, 1996.

[117] J. Salz and J. H. Winters, "Effect of fading correlation on adaptive arrays in digital mobile radio," *IEEE Transactions on Vehicular Technology*, vol. 43, no. 4, pp. 1049–1057, November 1994.

[118] L. Schumacher, K. I. Pedersen, and P. E. Mogensen, "From antenna spacings to theoretical capacities - guidelines for simulating MIMO systems," in *Proc. 13th IEEE International Symposium on Personal, Indoor and Mobile Radio Communications, (PIMRC '02)*, vol. 2, September 2002, pp. 587 – 592.

[119] D. K. Shamain, "*Capacity Enhancing Techniques for Code Division Multiple Access Systems*," Ph.D. dissertation, University of California, San Diego, 2001.

[120] D. K. Shamain and L. B. Milstein, "Detection with spatial diversity using noisy channel estimates in a correlated fading channel," in *Proc. IEEE Military Communications Conference, (MILCOM '02)*, vol. 1, 2002, pp. 691 – 696.

[121] S. Sharp, "Conquering the three challenges of power consumption," *XCell Journal*, vol. Second Quarter, 2005.

[122] S. Sheng and R. Brodersen, *Low Power CMOS Wireless Communications. A Wideband CDMA System Design*. Boston/Dordrecht/London: Kluwer Academic Publishers, 1998.

[123] M. K. Simon and M.-S. Alouini, *Digital Communication over Fading Channels. A Unified Approach to Performance Analysis*. Baltimore, Maryland: John Wiley and Sons, 2000.

[124] T. Simunic, L. Benini, and G. D. Micheli, "Energy-efficient design of battery-powered embedded systems," *IEEE Transactions on VLSI Systems*, vol. 9, no. 1, pp. 15 – 28, February 2001.

[125] C. Siriteanu and S. D. Blostein, "Maximal-ratio eigen-combining: a performance analysis," *Canadian Journal of Electrical and Computer Engineering*, vol. 29, no. 1/2, pp. 15–22, January–April 2004.

[126] ——, "Optimum beamforming for CDMA systems with signal-cancelation despreading," in *Proc. 22nd Biennial Symposium on Communications, Kingston, Canada*, 2004, pp. 451–453.

[127] ——, "Performance of smart antenna arrays with maximal-ratio eigen-combining," Queen's University, Department of Electrical and Computer Engineering, Kingston, Ontario, Canada, Tech. Rep. 0401, Jan. 2004. [Online]. Available: http://ipcl.ee.queensu.ca

[128] ——, "Smart antenna arrays for correlated and imperfectly-estimated Rayleigh fading channels," in *Proc. IEEE International Conference on Communications, (ICC '04)*, vol. 5, 2004, pp. 2757 – 2761.

[129] ——, "FPGA-based communications receivers for smart antenna array embedded systems," *EURASIP Journal on Embedded Systems, Special Issue on Field-Programmable Gate Arrays in Embedded Systems*, 4th Quarter, 2006 2006.

[130] ——, "Maximal-ratio eigen-combining for smarter antenna arrays," *IEEE Transactions on Wireless Communications*, in press.

[131] Q. H. Spencer, B. D. Jeffs, M. A. Jensen, and A. L. Swindlehurst, "Modeling the statistical time and angle of arrival characteristics of an indoor multipath channel," *IEEE Journal on Selected Areas in Communications*, vol. 18, no. 3, pp. 347–360, March 2000.

[132] R. Steele, C.-C. Lee, and P. Gould, *GSM, cdmaOne and 3G systems.* Chichester, UK: John Wiley and Sons, 2001.

[133] G. L. Stuber, *Principles of Mobile Communications*. Norwell, MA: Kluwer Academic Publishers, 2002.

[134] F. Swarts, P. van Rooyen, I. Oppermann, and M. P. Lotter, Eds., *CDMA Techniques for Third Generation Mobile Systems*. Norwell, MA: Kluwer Academic Publishers, 1999.

[135] A. Telikepalli, "Performance vs. power: getting the best of both worlds," *XCell Journal*, vol. Third Quarter, 2005.

[136] B. R. Tomiuk, "*Effects of imperfect maximal ratio combining on digital communications*," Ph.D. dissertation, Queen's University, 2002.

[137] B. R. Tomiuk, N. C. Beaulieu, and A. A. Abu-Dayya, "General forms for maximal ratio diversity with weighting errors," *IEEE Transactions on Communications*, vol. 47, no. 4, pp. 488–492, Apr. 1999.

[138] M. Torlak and G. Xu, "Performance of CDMA smart antenna systems," in *Conference Record of the Twenty-Ninth Asilomar Conference on Signals, Systems and Computers*, vol. 1, 1995, pp. 383 – 387.

[139] J.-A. Tsai, R. M. Buehrer, and B. D. Woerner, "The impact of AOA energy distribution on the spatial fading correlation of linear antenna array," in *Proc. IEEE Vehicular Technology Conference, (VTC '02)*, vol. 2, May 2002, pp. 933–937.

[140] D. Tse and P. Viswanath, *Fundamentals of Wireless Communication*. Cambridge, UK: Cambridge University Press, 2005.

[141] G. V. Tsoulos, M. A. Beach, and S. C. Swales, "Performance enhancement of DS-CDMA microcellular networks with adaptive antennas," in *Proc. IEEE Vehicular Technology Conference, (VTC '96)*, vol. 2, 1996, pp. 1086 – 1090.

[142] G. L. Turin, “The characteristic function of Hermitian quadratic forms in complex normal random variables,” *Biometrika*, vol. 47, no. 1/2, pp. 199 – 201, June 1960.

[143] T. VanCourt, Y. Gu, V. Mundada, and M. Herbordt, “Rigid molecule docking: FPGA reconfiguration for alternative force laws,” *EURASIP Journal on Applied Signal Processing*, vol. 2006, pp. 1–10, 2006.

[144] F. L. Vargas, R. D. R. Fagundes, and D. B. Junior, “A FPGA-based Viterbi algorithm implementation for speech recognition systems,” in *Proc. IEEE International Conference on Acoustics, Speech, and Signal Processing, (ICASSP ’01)*, vol. 2, May 2001, pp. 1217–1220.

[145] R. Vaughan and J. B. Andersen, *Channels, Propagation and Antennas for Mobile Communications*. London, UK: The Institution of Electrical Engineers, 2003.

[146] P. D. Welch, “The use of fast Fourier transform for the estimation of power spectra: A method based on time averaging over short, modified periodograms,” *IEEE Transactions on Audio and Electroacoustics*, vol. AU-15, no. 2, pp. 70 – 73, June 1967.

[147] B. Widrow, P. E. Mantey, L. J. Griffiths, and B. B. Goode, “Adaptive antenna systems,” *Proceedings of the IEEE*, vol. 55, no. 12, pp. 2143 – 2159, December 1967.

[148] J. H. Winters, “Optimum combining in digital mobile radio with cochannel interference,” *IEEE Transactions on Vehicular Technology*, vol. 33, no. 3, pp. 144 – 155, August 1984.

[149] Virtex-5 LX platform overview. Xilinx, Inc. San Jose, CA. [Online]. Available: http://direct.xilinx.com/bvdocs/publications

[150] A. Yang, “Design techniques to reduce power consumption,” *XCell Journal*, vol. Third Quarter, 2005.

[151] B. Yang, “Projection approximation subspace tracking,” *IEEE Transactions on Signal Processing*, vol. 43, no. 1, pp. 95 – 107, January 1995.

[152] D. J. Young, “*The generation of correlated Rayleigh random variates by discrete Fourier transform and quality measures for random variate generation* ,” Master’s thesis, Dept. of Electrical and Computer Engineering, Queen’s University, 1997.

[153] D. J. Young and N. C. Beaulieu, “The generation of correlated Rayleigh random variates by inverse discrete Fourier transform,” *IEEE Transactions on Communications*, vol. 48, no. 7, pp. 1114 – 1127, July 2000.

[154] S. Zhou and G. B. Giannakis, “Optimal transmitter eigen-beamforming and space-time block coding based on channel correlations,” *IEEE Transactions on Information Theory*, vol. 49, no. 7, pp. 1673 – 1690, July 2003.

[155] K. S. Zigangirov, *Theory of Code Division Multiple Access Communication*, ser. IEEE Series on Digital and Mobile Communication, J. B. Anderson, Ed. New York, NY: John Wiley and Sons, 2004.